Application of Molecular Tagging Velocimetry to Study Laminar Flow and Laminar-to-Turbulent Transition in Hypersonic Boundary Layers

---

A Dissertation

Presented to

the faculty of the School of Engineering and Applied Science

University of Virginia

---

in partial fulfillment

of the requirements for the degree

Doctor of Philosophy

by

Brett F. Bathel

August

2013

APPROVAL SHEET

The dissertation

is submitted in partial fulfillment of the requirements

for the degree of

Doctor of Philosophy

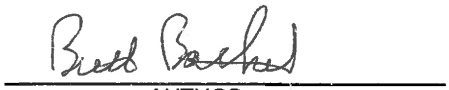

AUTHOR

The dissertation has been read and approved by the examining committee:

Christopher P. Goyne

Advisor

Paul M. Danehy

James C. McDaniel

Harsha K. Chelliah

Mool C. Gupta

Accepted for the School of Engineering and Applied Science:

Dean, School of Engineering and Applied Science

August

2013

Abstract

This dissertation provides a comprehensive summary of quantitative streamwise velocity measurements in hypersonic boundary layers in a large-scale hypersonic test facility. These measurements are used to study the behavior of streamwise velocity in laminar hypersonic boundary layers and hypersonic boundary layers undergoing transition-to-turbulence. These measurements are made with and without the presence of an isolated cylindrical roughness element on a 20° wedge model. This dissertation provides a review of the theory of boundary layer transition-to-turbulence and of laser-induced fluorescence, which is the mechanism used to measure streamwise velocity non-intrusively. In addition to the streamwise velocity data, a comprehensive image processing method and uncertainty analysis method are presented.

The studies in this dissertation also detail the development of two fluorescence-based forms of the Molecular Tagging Velocimetry (MTV) technique for use at NASA Langley Research Center. The first is a single-laser excitation technique using fluorescence of nitric oxide (NO). The second is a three-laser technique where nitrogen dioxide (NO_2) is dissociated with a high-intensity laser into NO and oxygen (O), with subsequent probing of NO fluorescence. The measurements presented in this dissertation are the first quantitative non-intrusive flowfield velocimetry measurements obtained in NASA Langley Research Center's 31-Inch Mach 10 Air Tunnel.

Acknowledgements

There are many people to thank for their support and assistance over the course of my studies. Without these individuals, I would not have been blessed with the opportunities I have had.

I am grateful to Dr. Paul Danehy at NASA Langley Research Center for giving me the opportunity to pursue a PhD at NASA. Dr. Danehy has been an excellent example of what a research engineer should be: he is a great co-worker, a hard worker, a smart worker, and a self-motivated worker. I am also grateful to Dr. Christopher Goyne at the University of Virginia. Dr. Goyne has been an excellent guide and mentor throughout the PhD process. I have enjoyed working with him in the past and look forward to working with him in the future.

I would have been completely lost without the help and friendship of Dr. Jennifer Inman and Mr. Stephen Jones at NASA Langley Research Center. They make it so that I am excited to come into work

every day. I would also like to thank my branch head, Mr. Tom Jones, and assistant branch head, Mr. William "Tony" Humphreys, for their support. Thanks to the branch administrative support assistant, Ms. Geraldine Tucker, for her helpfulness and positive attitude. I would like to thank my current and former NASA colleagues Dr. Craig Johansen, Dr. Shann Rufer, Ms. Karen Berger, and Dr. Sarah Tedder for their help and support. I would also like to thank Dr. Robert Bryant for providing me with my first opportunity to work at NASA Langley Research Center in 2004.

I am grateful to the members of my PhD committee for the time, guidance, and effort they have given throughout my studies: Dr. James McDaniel, Dr. Mool Gupta, and Dr. Harsha Chelliah. I would also like to thank Ms. Laura Troutman in the Mechanical and Aerospace Engineering Department for her assistance over the past several years.

I am especially grateful to Dr. Albert Ratner at the University of Iowa for providing my very first opportunity to participate in a research project. He truly opened a new world of opportunity for me. I am thankful for the friendship of Dr. Yun Huang that began at the University of Iowa and continues to this day.

I want to acknowledge my church family, both at Berean Baptist Church in Boone, Iowa, and at Colonial Baptist Church in Virginia Beach, Virginia. Their prayers and support have been greatly appreciated.

Great thanks go to the biggest role models in my life, my parents, Mr. Henry "Fred" Bathel and Mrs. Janice Bathel. Anything I have accomplished and may accomplish is a result of the guidance and love they have given to me over the course of my life. They each consistently demonstrate a Christian walk and work ethic that I strive to follow. I must also include thanks to my siblings, Mr. Mark Bathel and Ms. Megan Bathel, who themselves are excellent Christian examples. Many thanks also to my grandmother, Mrs. Ruth Bathel, for her love and support as well as that from my departed grandparents, Mr. Roy Bathel and Mr. and Mrs. James Farrell.

Finally, and most importantly, I must thank God. All of my earthly accomplishments are nothing compared to the salvation I have received through Jesus Christ.

Trust in the LORD with all thine heart, and lean not unto thine own understanding. In all thy ways acknowledge Him, and He shall direct thy paths. Proverbs 3:5-6

Contents

List of Figures

Chapter 1

Chapter 2

Chapter 5

Chapter 6

List of Tables

Chapter 2

Chapter 3

Chapter 4

Chapter 5

Chapter 6

Nomenclature

$\boldsymbol{A}$	=	spatial uncertainty fitting parameter, μm
A	=	area
A_{21}	=	Einstein A coefficient for spontaneous emission, s^{-1}
A_{Slot}	=	seeding slot area, mm^2
AoA	=	angle-of-attack
a	=	Voigt a parameter
a_{CF}	=	correction factor fitting parameter
$\boldsymbol{B}$	=	spatial uncertainty fitting parameter, μm
B_{12}	=	Einstein B coefficient for stimulated absorption, cm/W·s
B_{21}	=	Einstein B coefficient for stimulated emission, cm/W·s
B_i	=	background signal in i^{th} exposure, counts
b_{CF}	=	correction factor fitting parameter
$\boldsymbol{C}$	=	spatial uncertainty fitting parameter
C_f	=	skin friction coefficient
C_h	=	convective heat transfer coefficient
C_{hFR}	=	convective heat transfer coefficient at stagnation point on hemisphere
C_H	=	Stanton number
C_{Loss}	=	loss coefficient of gas supply tube
CCD	=	charge coupled device
CF	=	correction factor
CFD	=	computational fluid dynamics

c	=	speed of light, m/s
c_{CF}	=	correction factor fitting parameter
$\boldsymbol{D}$	=	center of Gaussian-like fit to intensity data
D	=	differential operator, $\partial/\partial y$, m^{-1}
DNS	=	direct numerical simulation
D_f	=	viscous drag, N
D_{Line}	=	diameter of gas supply tube, mm
E	=	lower energy state
F_J	=	rotational energy, J
$FWHM$	=	full-width at half maximum
f_B	=	Boltzmann fraction
G	=	overlap integral
G_i	=	Gaussian-like fit to fluorescence signal in i^{th} exposure, counts
G_v	=	vibrational energy, J
g	=	degeneracy
h	=	Planck's constant, J·s
I	=	irradiance, W/m^2
I_{sat}	=	saturation irradiance, W/m^2
I_v	=	spectral irradiance, $W/m^2/cm^{-1}$
J	=	rotational quantum number
Kn	=	Knudsen number
k	=	roughness height, mm
k_B	=	Boltzmann's constant, J/K
k_s	=	absorption coefficient, m^{-1}
L	=	length of excited NO molecule train
L_{Line}	=	gas supply tube length, m
L_{Slot}	=	gas supply slot length, mm
L_v	=	laser-line shape, $1/cm^{-1}$

LIF	=	laser-induced fluorescence
M	=	Mach number
$\bar{M}$	=	mean magnification, mm/pixel
MTV	=	molecular tagging velocimetry
m	=	mass
$\dot{m}$	=	mass flow rate, mg/s
N	=	number of measurements
N_i	=	noise in i^{th} exposure, counts
N_s	=	number density of absorbing species, molecules/m^3
N_T	=	total number density, molecules/m^3
NO	=	nitric oxide
NO_2	=	nitrogen dioxide
P	=	pressure, Pa
P_i	=	peak in i^{th} exposure, counts
PLIF	=	planar laser-induced fluorescence
PMT	=	photomultiplier tube
Q_{21}	=	collisional quenching rate constant, s^{-1}
Q_{pre}	=	predissocation rate constant, s^{-1}
Q_{ion}	=	ionization rate constant, s^{-1}
Q	=	surface heat transfer rate, $W/m^2 \cdot s$
R	=	gas constant
Re_k	=	roughness Reynolds number, $\rho_k U_k k/\mu_w$
$\mathcal{R}$	=	profile matrix scaled time parameter
r	=	build up time of excited state, s
$\mathcal{r}$	=	profile matrix time dimension
S	=	signal
SCCM	=	standard cubic centimeters per minute, cm^3/minute
SLPM	=	standard liters per minute, L^3/minute

SNR	=	signal-to-noise ratio
T	=	temperature, K
TSP	=	temperature sensitive paint
t	=	time, s
t_{add}	=	additional delay, ns
t_{E1}	=	first exposure duration, ns
t_{E2}	=	second exposure duration, ns
t_{GD}	=	gate delay, ns
t_{GW}	=	intensifier gate width, ns
$t_{N-1,95\%}$	=	student t-statistic at 95% confidence for N measurements
t_P	=	probe laser duration, ns
U	=	streamwise component of velocity, m/s
$\overline{U}$	=	mean streamwise component of velocity, m/s
U'	=	fluctuating component of streamwise velocity, m/s
u	=	uncertainty
V	=	wall-normal component of velocity, m/s
$V(a,x)$	=	Voigt integral function
V_i	=	valley in i^{th} exposure, counts
v	=	vibrational quantum number
$v_{s,i}$	=	mean relative velocity, m/s
W	=	width of correlation window, pixels
W_{12}	=	stimulated absorption rate constant, s^{-1}
W_{Slot}	=	width of seeding slot, mm
x	=	streamwise spatial coordinate, mm
$\tilde{x}$	=	Voigt Doppler broadening parameter
Y_v	=	line-shape function
y	=	wall-normal spatial coordinate, mm
$\tilde{y}$	=	Voigt integration parameter

Z	=	partition function
z	=	spanwise spatial coordinate, mm
δ_L	=	laminar boundary layer thickness, mm
δI	=	fluorescence signal discretization interval
δx	=	spatial discretization interval
δt	=	time discretization interval
Δt	=	time period or duration, ns
Δx	=	displacement, mm
Δv_D	=	Doppler broadening, cm^{-1}
Δv_H	=	homogeneous broadening, cm^{-1}
$\zeta_{\pm}$	=	spanwise displacement resulting from spanwise velocity component, pixels
Φ	=	fluorescence yield
λ	=	wavelength or mean-free-path, nm
μ	=	viscosity, kg/m·s
$\mu_{s,i}$	=	reduced mass of absorbing and collision partner species
η	=	detection efficiency
Ω	=	solid angle, steradian
ρ	=	density, kg/m^3
ρ_{Slot}	=	density at the exit of the seeding slot, kg/m^3
σ	=	standard deviation
$\sigma_{s,i}$	=	collision cross-section, m^2
τ_{LIF}	=	fluorescence lifetime, ns
v	=	frequency, cm^{-1}
χ	=	mole fraction

Subscripts

0	=	stagnation condition
1	=	lower energy state

2	=	excited energy state
AVG	=	average
CM	=	center of mass
D1	=	first exposure delay
D2	=	second exposure delay
Delay	=	time delay
det	=	detection
E1	=	first exposure
E2	=	second exposure
Eff	=	effective
eE1	=	first effective exposure
e	=	condition at edge of velocity boundary layer
est	=	estimated
exp	=	experimental data
k	=	condition at trip height, at trip location, or both
L	=	laminar
Leak	=	conditions at location of gas supply tube leak
m	=	measured
max	=	maximum
min	=	minimum
ND	=	no decay
O	=	origin
P	=	laser pulse
Plenum	=	conditions in model plenum
PROBE	=	probe laser at nominal wavelength of 226 nm
PUMP	=	pump laser at nominal wavelength of 355 nm
rot	=	rotational
Slot	=	conditions at gas seeding slot exit

slip	=	velocity slip
T	=	point from which turbulent boundary layer solution is computed
trans	=	transition-to-turbulence
translation	=	translation temperature
vib	=	vibrational
w, wall	=	condition at model wall
∞	=	infinite or freestream condition

Chapter 1: Introduction

1.1 Statement of Problem

The ability to go farther, faster, and higher than conventional aerospace vehicles has driven hypersonic research efforts. Examples of hypersonic vehicles over a Mach number range of 5-20 include space exploration (Space Shuttle Orbiter, Orion, Apollo, Mercury, etc.), technology demonstrator (X-43), and defense (Falcon HTV-2, X-51, X-37). However, there are numerous problems related to hypersonic flight which must be solved in order to allow for the optimal design and implementation of reliable hypersonic vehicles.

Currently, there no method that can consistently predict hypersonic boundary layer transition from laminar to turbulent flow for an arbitrary aerospace vehicle configuration. Often the skin friction and heat transfer to the vehicle surface resulting from such a transition is of primary concern. In some cases, the heat transfer increases by a factor of four or more above the laminar baseline level.[1] Figure 1.1, taken from Ref. 2 (modified from the original figure in Ref. 3), demonstrates the increased heating trends (denoted by red, green and light blue data points) above the baseline laminar heating rate (denoted by the dark blue data points) generated by an array of discrete roughness elements on the heat shield of an Orion Crew Exploration Vehicle (CEV) model. The roughness elements were of varying height, k, relative to the laminar boundary layer thickness, δ_L, and were located at approximately z/R = -0.4. These data points were obtained along the centerline of the heat shield where hypersonic boundary layer transition-to-turbulence occurs in the wake of the discrete tripping element array. The specific mechanisms

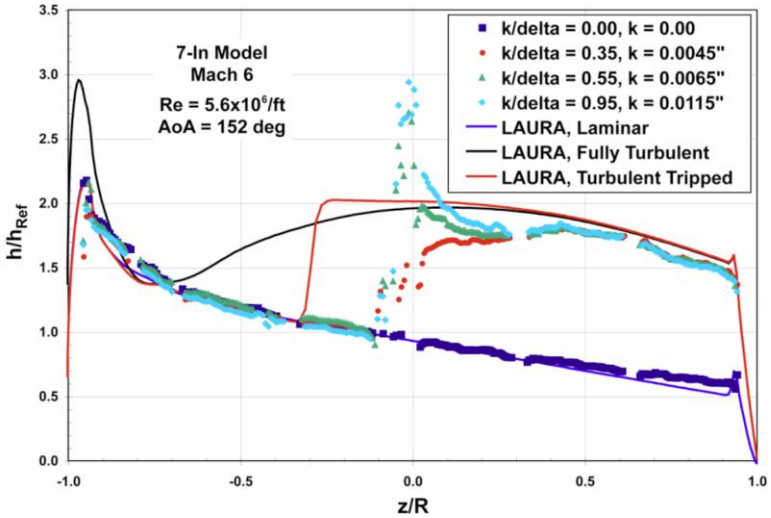

Figure 1.1: Comparison of experimental heating trends resulting from transition-to-turbulence obtained along the centerline of an Orion heat shield model with corresponding CFD simulation. Roughness elements located at z/R = -0.4. Image taken from Ref. 2, modified from original figure presented in Ref. 3, with permission of authors.

responsible for the initiation of this process are poorly understood. This is apparent when looking at the computationally predicted trends denoted by the solid curves in Fig. 1.1. The simulation is incapable of determining (1) the location of transition and (2) the magnitude of the heating spike associated with transition, which depends on the ratio k/δ_L.

What is qualitatively understood about the transition-to-turbulence process for a hypersonic boundary layer can be described schematically for a flat plate configuration with a sharp leading edge in Fig. 1.2, which is based on figures in Refs. 4 and 5. At the leading edge, molecular interactions in the flow result in the formation of an oblique shock emanating from the leading edge.[6] Both the angle and strength of the shock depend upon the freestream Mach number, specific heat ratio of the gas, and angle-of-attack of the plate. Once the freestream gas is processed by the oblique shock, it is turned parallel to the plate surface. At the leading edge, the post-shock gas first encounters the surface of the plate. While the bulk flow travels in the *x*-direction parallel to the plate surface, random molecular motion in the *y*-direction results in an interaction between the molecules and the plate surface. The interaction gives rise to a diffuse reflection of the molecules from the surface and a macroscopic gas velocity of approximately zero at the wall.[7] This difference in velocity between the outer bulk flow and gas at the surface establishes a gradient in the velocity component parallel the plate with respect to the wall-normal direction, $\partial U/\partial y$. The random motion of molecules with lower *x*-momentum near the plate into regions of higher *x*-momentum farther from the plate results in *x*-momentum transfer, which is described on a macroscopic scale by the gas viscosity. An explanation based on kinetic theory can be found in Ref. 8. The propagation or diffusion of this process away from the wall results in the initial establishment of a laminar boundary layer region partially characterized by the velocity profile shown in Fig. 1.2. The flow in the hypersonic laminar

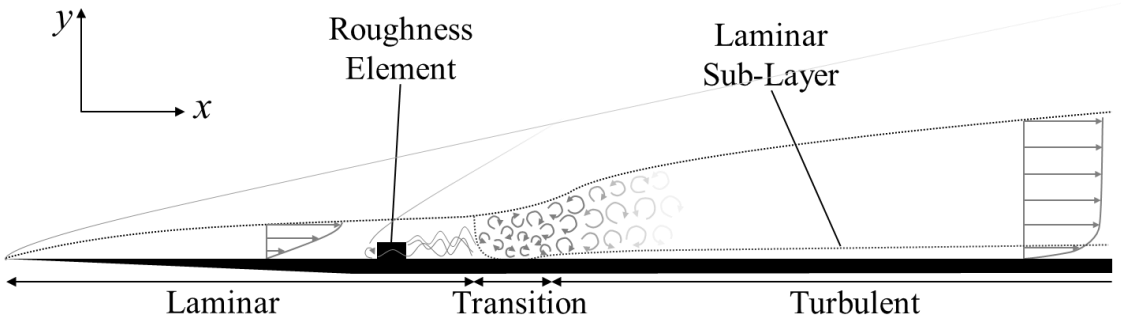

Figure 1.2: Generalized schematic of potential transition-to-turbulence process on a flat plate. After Refs. 4 and 5.

boundary layer is both stable and steady, having a y-direction thickness of $\delta_L(x)$ that grows with x, and where friction and thermal conduction effects dominate.[9] The properties of this region can be computed numerically using compressible similarity solutions of the x-momentum and energy equations as shown in Ref. 9.

At some point, disturbances originating from the freestream flow or from within the boundary layer, such as from the isolated roughness element shown in Fig. 1.2, begin to generate instability waves within the laminar boundary layer. Depending on the conditions within the laminar boundary layer, these instabilities can undergo amplification and begin breakdown of the laminar flow. During breakdown, the boundary layer transitions from being an organized, steady flow to being a chaotic, unsteady flow. In this region of transition-to-turbulence, Van Driest and McCauly noted that a scouring of the surface occurred just prior to the onset of fully turbulent flow.[5] This is depicted schematically in Fig. 1.2.

Once transition-to-turbulence is complete, the fully turbulent flow may be thought of as having three separate layers; a laminar sub-layer, a buffer layer, and a turbulent region.[4] In the turbulent region, turbulent mixing is dominant and enhances momentum and energy transfer and therefore surface friction and convective heat transfer rates.[4] In the buffer layer, diffusion and turbulent mixing rates are comparable, and in the laminar sub-layer, momentum and energy transfer are dominated by laminar diffusion.[4]

For a specific vehicle at specific flight conditions, correlations using flow parameters, such as transition Reynolds number, to predict the location of transition-to-turbulence can be determined through experimentation (for instance see Ref. 10 by Reda). However, such a Reynolds number (e.g. one defined as $\rho_e V_e x_{trans} / \mu_e$) can be a function of 18 or more variables[9] that may have some bearing on the process. Since there are an infinite number of potential vehicle designs, configured for an infinite number of flow parameter combinations, it is impossible to define a single transition Reynolds number that would be applicable to all such combinations. It would also be impractical to perform detailed studies of transition-to-turbulence behavior for all such vehicle configurations and flow parameter combinations. A more practical way forward would be to perform computations and experimental studies that examine the fundamental aspects of transition, with the aim developing predictive capability for an arbitrary configuration.

The hypersonic research community is particularly interested in what effect a discrete protuberance with a height, *k*, on the order of the laminar boundary layer thickness, δ_L, will have on an otherwise laminar hypersonic flow as it passes over a flight vehicle surface. This type of flow/body interaction occurs on several vehicles NASA uses to explore space. Two recent examples include the Space Shuttle Orbiter (BLT-DTO[11] and gap fillers[12,13]) and the Orion Crew Exploration Vehicle (CEV) Module.[14,15]

To gain a fundamental understanding of the interaction between a hypersonic boundary layer and an isolated roughness element (such as the cylindrical tension ties and compression pads associated with the Orion CEV), wind tunnel experiments can be performed in flows over a simple flat, smooth surface model, like that shown in Fig. 1.2. Such experiments can provide data characterizing the transition process for a controlled set of transition parameters. For instance, flow behavior without a roughness element present can be compared against the flow behavior when such elements are present to determine to what extent they alter the flow. Analysis of data from such experiments can be used to characterize the amplitude of instabilities generated by the presence of the isolated roughness as a function of its shape, size, and the aero-thermodynamic parameters that describe the state of the boundary layer flow at and beyond the location of the isolated roughness element. Experiments of this nature should also be conducted in a hypersonic test facility capable of matching as many flight-relevant conditions as possible (such as Mach number and Reynolds number) so that results may be scaled to the actual flight vehicle design. Reference 16 reviews experimental work and flight test data in which hypersonic transition-to-turbulence results from the presence of roughness. While an assortment of data exists in relation to the transition-to-turbulence problem, Ref. 16 notes that there is still no science-based theory capable of predicting this process.

1.1.1 Measurement Needs

Examples of data acquisition techniques used to study hypersonic boundary layer transition include high-frequency model surface pressure measurements,[17] temperature sensitive paints (TSP)[11] and phosphors,[18] hot-wire probes,[19] Pitot probes,[20] focused laser differential interferometry (FLDI),[21] and schlieren imaging.[1] To gain a fundamental understanding of how an otherwise hypersonic boundary layer becomes unstable and transitions to turbulence, a complete quantitative description of the vehicle surface and surrounding flowfield must be provided.

While surface pressure and temperature measurement methods can describe the condition of the model or vehicle surface resulting from interaction with the surrounding flowfield, they cannot describe the state of the flowfield itself. Pitot and hot-wire probes have been demonstrated recently in Mach 3.5 and Mach 6 flows.[19,20] These physical probes have traditionally been used to make aero-thermodynamic measurements and usually provide data at a single point or several points in the flow (by translating the device to different points in the flow). Unfortunately, the presence of such a probe in a hypersonic flow will result in the formation of shocks in front of the measurement device. This alters the aerodynamic and thermodynamic state of the gas being studied. A feedback loop can form, such as through the subsonic portion of the boundary layer, in which perturbations emanating from the probe can propagate upstream and alter the flow property being measured. In higher Mach number test facilities these devices can fail mechanically when subjected to the relatively large mechanical and thermal loads that occur. It is also advantageous to measure multiple points along a line, in a plane, or over a volume simultaneously in order to characterize how the flowfield evolves spatially and/or temporally, which physical probes cannot do. Optical measurements such as schlieren imaging, for the most part, provide only a qualitative, spatially averaged view of the flowfield. Additionally, this measurement is applicable only where there are relatively strong, local variations in density resulting in detectable variations in refractive index. An optical technique such as FLDI can provide a quantitative measure of density fluctuations at MHz acquisition rates; however, the technique is capable of acquiring data only at a point and has a spatial resolution of slightly less than 1 mm.[21]

To characterize the transition-to-turbulence process in a large-scale hypersonic facility, a measurement technique must be capable of resolving both the mean and fluctuating components of a transition parameter of interest in the flow itself with sufficient spatial and temporal resolution while not perturbing the flow. Optically based measurement techniques are an attractive option, as spatial and temporal resolutions can be high, and they are non-intrusive by nature. The following is a list of desired measurement capabilities for hypersonic transition-to-turbulence flows:

1. The technique should be capable of being implemented in a large-scale hypersonic facility. The facility should have sufficient optical access for the measurement to be made and optical ports should have relatively high transmittance at the wavelengths of light associated with the technique.

2. The optical measurement must be made in a hypersonic boundary layer with a spatial resolution much less than the boundary layer thickness. Care should be taken to make measurements as close to the model surface as possible so that comparisons between properties measured using the optical technique can be compared with surface measurements. In large-scale hypersonic facilities such as NASA Langley's 31-inch Mach 10 Air blowdown wind tunnel, boundary layer thicknesses can be on the order of a few millimeters, as was measured and computed in Ref. 22. This requires the optical technique to have sub-millimeter spatial resolution.
3. The measurement time scale should be on the order of the flow time scale. With edge velocities on the order of 1000 m/s, the flow time scales are approximately 1 μs. Therefore the selected measurement technique must be have μs-scale temporal resolution. Measurements occurring over longer timescales may be susceptible to averaging errors that may need to be taken into account in the analysis.
4. The sampling frequency should be as high as possible. Hypersonic boundary layer instabilities with characteristic frequencies on the order of hundreds of kHz have been observed in facilities such as NASA Langley's 31-inch Mach 10 Air Tunnel.[17] To resolve such frequencies, the sampling rate must be more than twice that of the maximum frequency to be resolved.
5. The measurement should acquire as many data points in space as possible simultaneously (e.g. volume better than in a plane, in a plane better along a line, along a line better than at a point).
6. The measurement should be capable of making repeated measurements at each point. This will allow mean and instantaneous measurements to be made along with statistical uncertainty estimates and standard deviations calculated.

From this list, the requirements of item 1 were a necessity, as the experiment for this dissertation could otherwise not be carried out without it. The spatial resolution capability in item 2 is important as many measurement points across the boundary layer allow for a spatial analysis of velocity profile data that can be spatially correlated to geometric features of the flowfield, such as roughness height. Additionally, the

capability to make measurements very near the model surface allows for verification of wall boundary conditions. The temporal resolution requirement in item 3 is driven by the dominant flow velocity. At high velocities (~1 km/s), a shorter measurement time scale reduces the level of spatial averaging occurring during the measurement period. This improves the spatial resolution of the technique with respect to direction of the velocity component being measured. The benefit of a high sampling frequency is of particular importance to transition-to-turbulence, as identification of frequencies and amplitudes associated with various transition-to-turbulence modes is often of interest. Additionally, high sampling frequencies allow for analysis of temporally correlated events, such as the periodic shedding of vortices downstream of a roughness element. However, the laser and camera system used in this experiment was limited to a 10 Hz acquisition rate, which only allows for analysis of amplitude information. Item 5 is of importance because it affects both testing efficiency and cost as well as allowing for spatial correlation of flow parameters. Item 6 is important as it affects the calculation of statistics and uncertainties associated with the flow parameter being measured. This, in turn, is important when the data is then used to validate modeling efforts.

1.2 Importance of Problem

Having a reliable, physics-based transition predictive capability would allow engineers to reduce vehicle development costs and improve vehicle performance. For instance, if heating is a concern, engineers would be able to design flight vehicles that have augmented thermal protection only in the regions where higher heating loads occur. This would be an alternative to covering the entire vehicle with the heavier thermal protection material to compensate for having no specific knowledge of precisely where increased heating will occur. This was the approach used for the Mars Science Laboratory (MSL) spacecraft, which had a total mass of 3,839 kg, and of this, the Entry, Descent and Landing (EDL) system had a mass of 2,401 kg.[*] A significant portion of the EDL mass was contained in the 4.5-m diameter, 3.175-cm thick, spherically-blunted, 70-degree half-angle cone using a Phenolic Impregnated Carbon Ablator (PICA) heat shield.[23] Yet available flight data from thermocouples embedded in the PICA heat shield showed that recession was less than 0.254 cm, or 8% of the total thickness, into the PICA material at the locations of the thermocouples.[23,24] In this case, such over-design required valuable launch resources to

[*] Information accessed on 5/15/2013 from http://mars.jpl.nasa.gov/msl/mission/spacecraft/

be used to transport unneeded heat shield material to Mars rather than, for example, additional scientific instrumentation.

The hypersonic research community has a very specific interest in hypersonic boundary layer transition-to-turbulence in the presence of discrete roughness. As stated previously, roughness-induced transition-to-turbulence is of concern for flight vehicles, such as Orion, being developed by NASA. In the past, engineering correlations from wind tunnel testing have been used extensively for flight vehicle transition predictions, such as those used during the Space Shuttle Orbiter Return to Flight program.[25,18] Unfortunately, these correlations suffer from several uncertainties outlined in Ref. 26, including a correlation's potential inability to relate to true flight conditions. Reference 26 also highlights the limited physical basis and reliability that some correlations have in describing the complexity of hypersonic boundary layer transition.

1.3 Purpose of the Dissertation

One purpose of this dissertation is to provide comprehensive quantitative measurements of hypersonic boundary layer flowfields conducted in a large-scale hypersonic test facility. Another purpose of this dissertation was to determine how accurately and precisely such measurements can be made. Theoretical background considerations, streamwise velocity data, and a detailed analysis are presented for a data set obtained in hypersonic laminar boundary layers and hypersonic boundary layers undergoing transition-to-turbulence, both with and without the presence of an isolated cylindrical roughness element. The streamwise velocity measurements, both mean and instantaneous, are used to describe the nature of the flowfield. This data set can be used for the validation of computational codes simulating transition-to-turbulence behavior within a hypersonic boundary layer.

There are several reasons why this dissertation is centered on making streamwise velocity measurements. All three components of velocity appear in each equation making up the full Navier-Stokes equations (including continuity, momentum, and energy), which govern the gas dynamics under study. In laminar and transitional boundary layer flows across a flat plate, which are the focus of this dissertation, the streamwise velocity component is often the most dominant component. As previously discussed, the state of the boundary layer has a significant impact on heating. For a hypersonic laminar boundary layer, the aerodynamic heating imparted to the wall is directly related to the cube of edge velocity, $q_w \approx \frac{1}{2}\rho_e U_e^3 C_H$,

where q_w is the surface heat transfer, ρ_e the edge density, U_e the edge velocity, and C_H the Stanton number.[9] Additionally, the viscous drag, D_f, is related to the square of the edge velocity, $D_f = \frac{1}{2}\rho_e U_e^2 \Delta x \Delta z C_f$, where $\Delta x \Delta y$ is a reference area, and C_f is the skin friction coefficient.[9] At a basic level, stability analyses of boundary layer flows concern the mean and fluctuating components of the streamwise velocity, with the frequency and magnitude of the fluctuating component of particular interest in instability amplification.

The studies in this dissertation entail the application of two fluorescence-based forms of the Molecular Tagging Velocimetry (MTV) technique. The first is a single-laser excitation technique using fluorescence of nitric oxide (NO). The second is a three-laser technique where nitrogen dioxide (NO_2) is dissociated with a high-intensity beam into NO and oxygen (O), with subsequent probing of NO fluorescence. The measurements presented in this dissertation were obtained using the first application of a quantitative non-intrusive flowfield velocimetry technique in NASA Langley Research Center's 31-Inch Mach 10 Air blowdown wind tunnel. A detailed methodology is presented for analyzing images to compute mean and instantaneous velocities and to compute associated measurement uncertainties.

The selection of fluorescence-based MTV for hypersonic boundary layer measurements, as opposed to other velocity measurement techniques, was motivated by several factors. When compared with point-based techniques, such as hot-wire measurements,[20] MTV can resolve streamwise velocities at multiple points along lines in a plane. This is a particularly attractive feature when considering the high cost, short run time, and long recovery time between runs that are associated with some large-scale hypersonic test facilities. The use of hot-wire probes also does not directly provide velocity data, but rather mass flux information. This is in addition to the drawbacks associated with probe measurements already discussed. Since the fluorescence-based MTV technique uses molecular tracers, it does not suffer as much from the potential drawbacks of particle based methods, such as PIV,[27,28] which include the following: adequate seeding density, seeding uniformity, particle lag in regions with large velocity gradients, and flow perturbations induced by particle seeding. There is also the issue of cleanliness when using a particle technique in a large-scale hypersonic test facility, which is often of great concern to the operators and maintainers of such facilities. The ability of MTV to provide instantaneous velocity measurements makes it attractive when making measurements of flow instabilities. This is in contrast to Doppler-based LIF velocity measurements,[29] which can provide fully planar, two-component velocity measurements (as

opposed to single-component measurements along several lines in a plane with MTV), but are typically only time-averaged in nature. Finally, the lack of quantitative flowfield measurements in boundary layers undergoing roughness-induced transition-to-turbulence presents a unique opportunity to use a non-intrusive, optically-based measurement technique to contribute to the hypersonic research community's understanding of this phenomenon. For these reasons, fluorescence-based MTV was selected for the studies described in this dissertation. This technique is not without its own drawbacks, which include toxicity of the tracer species, reactivity of the tracer species, and introduction of flow perturbations resulting from tracer species injection. These and other issues will be addressed in the dissertation.

1.4 Organization of Dissertation

Chapter 2 discusses the theoretical aspects of the transition-to-turbulence process. This discussion begins by describing the types of disturbances that are relevant to the transition-to-turbulence process and specifically the types of disturbances that are associated with hypersonic wind tunnel facilities (as opposed to true flight conditions). Particular attention is given to the role of an isolated roughness element on promoting transition-to-turbulence. A sample of disturbance magnitudes representative of experimental conditions in hypersonic wind tunnel facilities is also given to establish the measurement precision needed to characterize the transition-to-turbulence phenomenon. Chapter 2 also provides a review of the laser-induced fluorescence process and reviews two fluorescence-based velocimetry methods: Doppler velocimetry and flow-tagging velocimetry (including the MTV technique). Chapter 2 concludes with a discussion of the advantages and limitations of laser-induced fluorescence measurements and the selection of NO and NO_2 as the species used for the MTV measurements.

Chapter 3 describes the experimental setup used to perform the single-laser NO MTV and three-laser NO_2-to-NO photodissociation MTV experiments. First, the 31-Inch Mach 10 Air Tunnel is described, which served as the test facility for all experiments in this dissertation. Second, the optical setup, consisting of the laser system, camera, and optics is discussed, followed by a description of the wind tunnel model used in all experiments. Finally, a listing of the experimental conditions for all experiments is given.

Chapters 4 and 5 describe the development and application of the single-laser NO MTV technique in the 31-Inch Mach 10 Air Tunnel. Chapter 4 focuses on the analysis methods used to measure velocity and determine experimental uncertainties. Chapter 5 focuses on the application of these methods to measure

streamwise velocity in a laminar hypersonic boundary layer both with and without an isolated cylindrical roughness element.

Chapters 6 and 7 describe the development and application of the three-laser NO_2-to-NO MTV technique for the 31-Inch Mach 10 Air Tunnel. As in Chapter 4, Chapter 6 focuses on the analysis methods used to measure velocity and determine experimental uncertainties. Chapter 6 also provides an analysis of the effect of mass injection rate on laminar hypersonic boundary layer behavior. As in Chapter 5, Chapter 7 focuses on the application of these methods to measure streamwise velocity in a hypersonic boundary layer undergoing transition-to-turbulence.

A discussion of lessons learned, conclusions, and recommendations for future work are provided in Chapter 8.

---

[1] Berry, S.A., and Horvath, T.J., "*Discrete Roughness Transition for Hypersonic Flight Vehicles*," 45th AIAA Aerospace Sciences Meeting, AIAA Paper 2007-0307, Reno, NV, January 8 – 11, 2007.

[2] Berry, S.A., Horvath, T.J., Lillard, R.P., Kirk, B.S., and Cassady, A.M., "*Aerothermal Testing for Project Orion Crew Exploration Vehicle*," 41st AIAA Thermophysics Conference, AIAA Paper 2009-3842, San Antonio, TX, June 22 – 25, 2009.

[3] Berger, K.T., "*Aerothermodynamic Testing of the Crew Exploration Vehicle in the LaRC 20-Inch Mach 6 and 31-Inch Mach 10 Tunnels*," 46th AIAA Aerospace Sciences Meeting, AIAA 2008-1225, January 7 – 10, 2008, Reno, NV.

[4] Incropera, F.P., and DeWitt, D.P., *Fundamentals of heat and mass transfer*, 5th ed., John Wiley & Sons, Hoboken, NJ, 2002.

[5] Van Driest, E.R., and McCauley, W.D., "*The Effect of Controlled Three-Dimensional Roughness on Boundary-Layer Transition at Supersonic Speeds*," Journal of Aerospace Sciences, 27(4), pp. 261 – 271, April, 1960.

[6] Anderson, J.D., *Modern Compressible Flow With Historical Perspective*, 3rd ed., McGraw-Hill, New York, 2003, pp. 127 – 153.

[7] White, F.M., *Viscous Fluid Flow*, 2nd ed., McGraw-Hill, New York, 1991, pp. 47 – 48.

[8] Vincenti, W. G., and Kruger Jr., C. H., *Introduction to Physical Gas Dynamics*, Reprint of 1967 ed., Wiley, New York, 1975.

[9] Anderson, J.D., *Hypersonic and High-Temperature Gas Dynamics*, 2nd ed., AIAA, Reston, VA, 2006.

[10] Reda, D.C., "*Review and Synthesis of Roughness-Dominated Transition Correlations for Reentry Applications*," Journal of Spacecraft and Rockets, 39(2), p. 161 – 167, March – April, 2002.

[11] Danehy, P., Ivey, C., Bathel, B., Inman, J., Jones, S., Jiang, N., Webster, M., Lempert, W., Miller, J., and Meyer, T., *"Orbiter BLT Flight Experiment Wind Tunnel Simulations: Nearfield Flowfield Imaging and Surface Thermography,"* 48th AIAA Aerospace Sciences Meeting, AIAA Paper 2010-1571, Orlando, FL, January 4 – 7, 2010.

[12] McGinley, C.B., Berry, S.A., Kinder, G.R., Barnwell, M., Wang, K.C., and Kirk, B.S., "*Review of Orbiter Flight Boundary Layer Transition Data*," 9th AIAA/ASME Joint Thermophysics and Heat Transfer Conference, AIAA Paper 2006-2921, San Francisco, CA, June 5 – 8, 2006.

[13] Campbell, C.H., Driver, D.M., Alter, S.J., Fasanella, E.L., Wood, W.A., and Stone, J.S., "*Orbiter Gap Filler Bending Model for Re-entry*," 45th AIAA Aerospace Sciences Meeting, AIAA Paper 2007 – 413, Reno, NV, January 8 – 11, 2007.

[14] Liechty, D.S., "*Aerothermodynamic Testing of Protuberance and Penetrations on the NASA Crew Exploration Vehicle Heat Shield*," 46th AIAA Aerospace Sciences Meeting, AIAA Paper 2008-1240, Reno, NV, January 7 – 10, 2008.

[15] Danehy, P., Ivey, C., Inman, J., Bathel, B., Jones, S., Jiang, N., Webster, M., Lempert, W., Miller, J., and Meyer, T., *"High-Speed PLIF Imaging of Hypersonic Transition over Discrete Cylindrical Roughness,"* 48th AIAA Aerospace Sciences Meeting, AIAA Paper 2010-0703, Orlando, FL, January 4 – 7, 2010.

[16] Schneider, S.P., "*Effects of Roughness on Hypersonic Boundary-Layer Transition*," Journal of Spacecraft and Rockets, 45(2), pp. 193-209, March –April 2008.

[17] Berridge, D.C., Casper, K.M., Rufer, S.J., Alba, C.R., Lewis, D.R., Beresh, S.J., and Schneider, S.P., "*Measurements and Computations of Second-Mode Instability Waves in Three Hypersonic Wind Tunnels*," 40th Fluid Dynamics Conference, AIAA Paper 2010-5002, Chicago, IL, June 28 – July 1, 2010.

[18] Horvath, T.J., Berry, S.A., Merski, N.R., Berger, K.T., Buck, G.M., Liechty, D.S., and Schneider, S.P., "*Shuttle Damage/Repair from the Perspective of Hypersonic Boundary Layer Transition – Experimental Results*," 9th AIAA/ASME Joint Thermophysics and Heat Transfer Conference, AIAA Paper 2006-2919, San Francisco, CA, June 5 – 8, 2006.

[19] Wheaton, B.M. and Schnieder, S.P., "*Roughness-Induced Instability in a Laminar Boundary Layer at Mach 6*," 48th AIAA Aerospace Sciences Meeting, AIAA Paper 2010-1574, Orlando, FL, January 4 – 7, 2010.

[20] Kegerise, M.A., Owens, L.R., and King, R.A., "*High-Speed Boundary-Layer Transition Induced by an Isolated Roughness Element*," 40th Fluid Dynamics Conference and Exhibit, AIAA Paper 2010-4999, Chicago, IL, June 28 – July 1, 2010.

[21] Parziale, N.J., Shepherd, J.E., and Hornung, H.G., "Differential Interferometric Measurement of Instability in a Hypervelocity Boundary Layer," AIAA Journal, 51(3), pp. 750 – 753, March, 2013.

[22] Danehy, P.M., Bathel. B., Ivey, C., Inman, J.A., and Jones, S.B., "*NO PLIF study of hypersonic transition over a discrete hemispherical roughness element*," 47th AIAA Aerospace Sciences Meeting, AIAA Paper 2009-394, January 5 – 8, 2009, Orlando, FL.

[23] Mahzari, M., Braun, R.D., White, T.R., and Bose, D., "*Preliminary Analysis of the Mars Science Laboratory's Entry, Aerothermodynamic Environment and Thermal Protection System*," 51st AIAA Aerospace Sciences Meeting, AIAA Paper 2013-0185, January 7-10, 2013, Grapevine, TX.

[24] Bose, D., White, T., Santos, J.A., Feldman, J., Mahzari, M., Olsen, M., and Laub, B., "*Initial Assessment of Mars Science Laboratory Heatshield Instrumentation and Flight Data*," 51st AIAA Aerospace Sciences Meeting, AIAA Paper 2013-0908, January 7-10, 2013, Grapevine, TX.

[25] Berry, S.A., King, R.A., Kegerise, M.A., Wood, W.A., McGinley, C.B., Berger, K.T., and Anderson, B.P., "*Orbiter Boundary Layer Transition Prediction Tool Enhancements*," 48th AIAA Aerospace Sciences Meeting, AIAA Paper 2010-246, January 4 – 7, 2010, Orlando, FL.

[26] Reshotko, E., "*Is Re_θ/M_e a Meaningful Transition Criterion?*," AIAA Journal, 45(7), pp. 1441-1443, July 2007.

[27] Sahoo, D., Papgeorge, M., and Smits, A.J., "*Experimental Investigation of a Hypersonic Turbulent Boundary Layer*," 47th AIAA Aerospace Sciences Meeting, AIAA Paper 2009-0780, January 5 – 8, 2009, Orlando, Florida.

[28] Sahoo, D., Papgeorge, M., and Smits, A.J., "*PIV Experiments on a Rough-wall Hypersonic Turbulent Boundary Layer*," 40th AIAA Fluid Dynamics Conference, AIAA Paper 2010-4471, June 28 – July 1, 2010, Chicago, Illinois.

[29] Cecil, E. and McDaniel, J.C., "*Planar Velocity and Temperature Measurements in Rarefied Hypersonic Flow Using Iodine LIF*," 38th AIAA Themophysics Conference, AIAA Paper 2005-4695, June 6 – 9, 2005, Toronto, Ontario, Canada.

Chapter 2: Theoretical Considerations

This chapter begins with a discussion of fluid dynamic disturbances relevant to hypersonic transition-to-turbulence. Specifically, disturbances associated with hypersonic wind tunnel facilities and isolated roughness elements are discussed. This chapter also reviews some fundamental aspects of laser-induced fluorescence and as well as two fluorescence-based velocimetry methods: Doppler velocimetry and flow-tagging velocimetry (including the MTV technique). The chapter concludes with a discussion of the advantages and limitations of laser-induced fluorescence measurements and the selection of NO and NO_2 as the species used for the MTV measurements. The discussions presented in this chapter have, for the most part, been adapted from Ref. 1.

2.1 Transition-to-Turbulence

Hypersonic laminar-to-turbulent transition affects the control of flight vehicles, the heat transfer rate to a flight vehicle's surface, skin friction, the material selected to protect such vehicles from high heating loads, the ultimate weight of a flight vehicle due to the presence of thermal protection systems, the efficiency of fuel-air mixing processes in high-speed combustion applications, etc. Gaining a fundamental understanding the physical mechanisms involved in the transition process will lead to the development of predictive capabilities that can identify transition location and its impact on parameters like surface heating. Currently, there is no general theory that can completely describe the transition-to-turbulence process. However, transition research has led to the identification of the predominant pathways by which this process occurs.

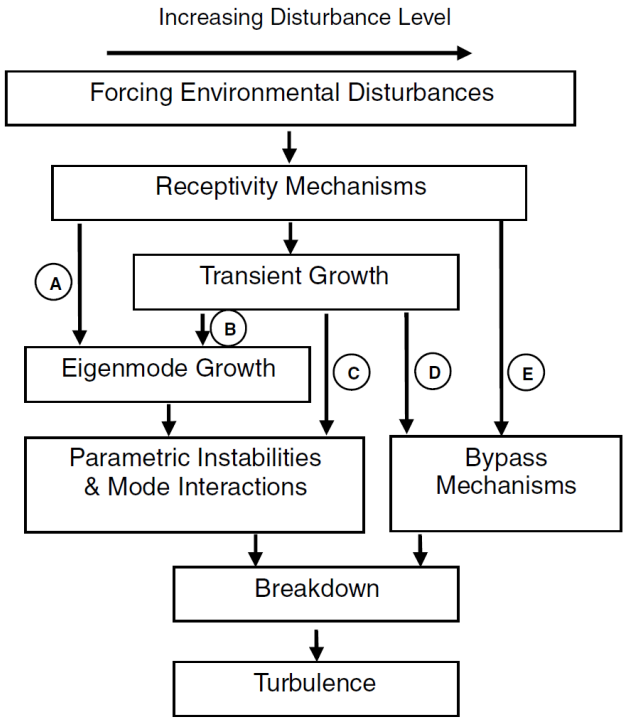

Figure 2.1: Transition pathways from laminar to turbulent flow. Image taken from Ref. 2. (Reprinted with permission of the author and the American Institute of Aeronautics and Astronautics).

Figure 2.1, taken from Ref.2, graphically depicts the known pathways by which an initially stable, laminar boundary layer can become unstable, undergo a process of instability growth, and eventually break down into turbulence. For a truly physics-based model of transition to be developed, the individual stages in the paths leading to the onset of fully turbulent flow must be well understood. This requires that each pathway be computationally modeled and experimentally characterized and validated. This may also lead to the discovery of new physical pathways.

The path to transition in Fig. 2.1 begins with the presence of an initial disturbance, either in the freestream flow or within the boundary layer itself. Disturbances can be classified into one of three types: entropy spots (related to temperature fluctuations), vorticity (curl of the velocity field), and sound (related to pressure waves).[3] Disturbances in the freestream can originate in the settling chamber of a high-speed wind tunnel and pass into the test section. Entropy spots and vorticity originating in the settling chamber can be convected into the test section.[4,5] Sound disturbances can originate in the settling chamber, from the wind tunnel nozzle walls, and along the wind tunnel walls.[4,5] Sound radiating from the nozzle walls is of particular concern as it is the dominant source of noise in high-speed wind tunnels,[6] with its magnitude scaling with Mach number to the fourth power.[7] These disturbances can significantly alter the transition-to-turbulence process.[7-10] Low-disturbance, high-speed wind tunnels have been developed to mitigate these disturbances.[6] These *quiet tunnels* provide a hypersonic freestream flow with disturbance levels similar to those encountered in flight, with freestream pressure fluctuations of less than 0.1%.[7] However, they are limited in extent of Reynolds number, Mach number, and enthalpy operability.[11] Table 2.1 provides velocity (U), temperature (T), mass-flow (m), and pressure (P) fluctuation levels for two conventional hypersonic tunnels[11-13] and one quiet hypersonic tunnel[14,15] as measured with hot-wire (U, T, m) or Pitot (P) probes.

Table 2.1: Measured or computed maximum fluctuation magnitudes in high-speed wind tunnel facilities.

Tunnel Freestream Property	Von Karman Institute Mach 6 Hypersonic Wind Tunnel H3	NASA Langley 20-Inch Mach 6	Purdue Boeing/AFOSR Mach 6 Quiet Tunnel
$U'/\bar{U}$	0.6 %* (Ref. 13)	-	-
$T'/\bar{T}$	0.8 % (Ref. 13)	0.20 % (Ref. 12)	-
$m'/\bar{m}$	5.2 % (Ref. 13)	1.01 % (Ref. 12)	0.2 %** (Ref. 14)
$P'/\bar{P}$	1.0 % (Ref. 13)	1.6 % (Ref. 11)	0.01 % (Ref. 15)

* Derived value

** Measurement made within laminar boundary layer

Disturbances that originate within the boundary layer can be caused by a number of factors, including the presence of discrete two-dimensional and three-dimensional roughness elements, cavities, distributed roughness, and mass injection. Various roughness types, cavity types, and mass injection schemes have been used in transition experiments at NASA Langley.[16-19] Mass-flow fluctuation amplitude and frequency measurements in the wake of a roughness element in a quiet tunnel were performed in Ref. 14, with sample results listed in Table 2.2. Note that the percentage fluctuations are ~2 orders of magnitude larger than the freestream fluctuations in a quiet wind tunnel (Table 2.1).

In the absence of any roughness element, the laminar high-speed flow over a flat plate is susceptible to instability if its velocity profile contains a generalized inflection point, defined as a vertical location $y > y_0$ for which $D(\rho DU) = 0$. Here, D is the differential operator, $D \equiv \partial/\partial y$, and y_0 corresponds to the height in the boundary layer where the velocity relative to the edge velocity has the value $U/U_e = 1 - (M_e)^{-1}$. For an adiabatic wall, there is at least one point within the boundary layer satisfying this condition,[20,35,38] and for a cold wall there can be two points that satisfy this condition.[20,35]

For a typical three-dimensional isolated roughness element, as the height of the roughness, k, relative to the thickness of the laminar velocity boundary layer, δ_L, increases, the transition location moves further upstream. There is a particular height-to-thickness ratio for which the streamwise location of transition-to-turbulence, $x_{trans,k}$, begins to deviate from the distance, x_{trans}, at which transition would occur in the absence of such an element.[23] The roughness size is deemed to be *critical* at the smallest k/δ_L for which $|x_{trans} - x_{trans,k}| > 0$. As k/δ_L is further increased beyond its critical value, $x_{trans,k}$ rapidly moves upstream towards the streamwise location of the roughness element itself, x_k. Low-speed[24] and high-speed[25] examples of this critical and super-critical behavior can be found in the literature. As k/δ_L is increased, there is a point at which further increase to this ratio has no additional effect on $x_{trans,k}$. At this point, the roughness is deemed *fully effective*. Beyond this effective roughness size, increasing k/δ_L may only increase the magnitude of the

Table 2.2: Measured or computed peak fluctuations in hypersonic transition and turbulent flows.

Property	Transition downstream of a large roughness element in a laminar boundary layer	Fully Developed Hypersonic Turbulent Boundary Layer (non-reacting)
$U'/\bar{U}$	25 % (Ref. 21)	15 % (Ref. 22)
$T'/\bar{T}$	33 % (Ref. 21)	47 % (Ref. 22)
$m'/\bar{m}$	43 % (Ref. 14)	52 % (Ref. 22)
$P'/\bar{P}$	5 % (Ref. 14)	7.5 % (Ref. 22)

disturbance imparted to the boundary layer.[23] A common metric used to correlate transition location with roughness size is the roughness Reynolds number, $Re_k = \rho_k U_k k/\mu_k$, where density ($\rho$), streamwise velocity ($U$), and dynamic viscosity (μ) are evaluated at k. For most applications, $Re_k < 25$ represents a bound for which a roughness element has no influence on transition-to-turbulence and is therefore sub-critical.[23,24,26] However, this is a semi-empirical relation, and roughness Reynolds numbers less than 25 have been shown to induce instability.[23] No universal physics-based theory exists that relates roughness Reynolds number and critical roughness for all roughness geometries and flow conditions.[27] The same may be said of the relation between Re_k and effective roughness.

When an isolated roughness element is present, it can introduce instability into the boundary layer through several mechanisms. For isolated roughness elements of $Re_k < 10$, streamwise vorticity may be generated.[23] This can result in disturbance amplification via interaction with a stationary crossflow instability or Görtler vortices,[23] which are associated with eigenmode growth for low disturbance environments[39,40] (path A, Fig. 2.1). Included in this eigenmode instability growth family are the 1st and 2nd modes described by Mack.[35,36] Growth of eigenmode disturbances is exponential, and transition estimates can be performed using methods such as the e^N method.[2] As Re_k is increased, the magnitudes of the disturbances generated by the roughness element increase, and instability growth via the transient growth mechanism occurs.[26] Growth of instabilities occurring via this mechanism is algebraic in nature[39,28] and is greatest for stationary streamwise disturbances[2] such as stationary streamwise vortices.[26] This instability mechanism then provides a higher amplitude disturbance to the eigenmode growth mechanism[39,40] (path B, Fig. 2.1). As Re_k is further increased, the transient growth mechanism continues to play a role, but the eigenmode growth mechanism is bypassed (path C, Fig. 2.1).[2] Up to this value of Re_k, in addition to generating streamwise vorticity, an isolated roughness element will generate a shear layer in its wake. This shear layer may be convectively unstable, such that the instabilities grow as they progress downstream, in which case it may be the dominant instability mechanism leading to transition.[29] However, for higher Mach number flows, a shear layer becomes less unstable, and the convective instability mechanism may be suppressed.[23]

For roughness elements with sufficiently large values of Re_k and with $k \approx \delta_L$, a significant wake region and shear layer is generated along with streamwise vorticity originating from a separation region upstream

of the element. Experiments and computations of a cylindrical roughness element in a $M_e = 6$ boundary layer have shown that for $Re_k > 6x10^4$ and $k/\delta_L > 1$, the wake region is subject to an absolute-like instability resulting from oscillation of horseshoe vortices in the separation region ahead of the roughness element and an unstable shear layer.[29] Computations of a $k/\delta_L = 2.54$ hemispherical roughness element in a $M_e = 3.37$ boundary layer also showed unsteady behavior in the separation region ahead of the element, and the breakdown of streamwise vortices accompanied by the formation of hairpin vortices in the wake of the element, followed by the onset of transition.[30] The formation of hairpin vortices was also affected by the interaction between an unsteady shear layer (emanating from the top of the trip) and the streamwise vortices along the centerline in the wake of the roughness.[31,32]

For a large, isolated roughness element where k/δ_L approaches unity, the applicability of linear stability methods comes into question.[30,33] While some computations and experiments have been performed to gain insight into the transition-to-turbulence mechanism for these elements, it remains unclear as to what conditions lead to an element being sub-critical, critical, or effective and what role convective and absolute instabilities play.[14,23] However, it does appear that the separation region just upstream of the roughness element and the shear layer play important roles in large-roughness-induced transition-to-turbulence, and an improved understanding of these flowfield features is required.

The process by which these disturbances (freestream or otherwise) are coupled into the boundary layer flow ultimately leading to the generation of instability waves is termed receptivity.[34] The magnitude of the imparted disturbance determines which pathway to turbulence they will follow. Reviews of the various instability types encountered along paths A-E in Fig. 2.1 can be found in the literature.[35-40] Both computational and experimental studies have been performed to study the interaction of the disturbances with the various instability mechanisms.[41] The majority of experiments used to conduct these studies involve physical probes, which are either surface mounted or placed in the boundary layer flow itself, to measure disturbance parameters. In low-speed environments, the magnitude of these disturbances varies from a few hundredths of a percent to ~10%.[42] Similar magnitudes can be expected for higher-speed flows.[43] Experiments characterizing normalized amplitude growth of instabilities for supersonic and hypersonic cases have also been conducted.[44]

As stated in the previous chapter, some of the more common measurement devices for flowfield transition-to-turbulence boundary layer measurements include hot-wires and Pitot probes. While hot-wire probes can have a response time and dynamic range appropriate for high-speed measurements, they only provide data at a point, are difficult to calibrate,[42] are fragile, have limited bandwidth,[43] and are intrusive.[11] Pitot probes, while more robust than hot-wires, have similar issues. Since the fluctuation levels associated with the onset of instabilities is an order-of-magnitude less than those associated with turbulence,[43] the intrusive nature of such probes can have an adverse effect on the parameter being measured. Limitations on bandwidth preclude these physical probes from resolving high-speed, high-frequency instability modes, with bandwidths of ~1 MHz being desired.[43] Additionally, the point-wise nature of data acquisition prevents the detailed study of spatial behavior of transition-to-turbulence behavior. A review of some of the available non-intrusive optical diagnostic capabilities with applicability to transition-to-turbulence measurements is available in Ref. 43.

In summary, there are multiple pathways to transition-to-turbulence, and these pathways depend in part on transition parameters such as the roughness Reynolds number (Re_k),[*] ratio of roughness height to boundary layer thickness (k/δ_L), and edge Mach number (M_e), among other parameters. These pathways initiate with small disturbances caused by the roughness that then undergo a receptivity process by the boundary layer and a period of amplitude growth until transition-to-turbulence occurs. Experiments presented in this dissertation involve varying these transition parameters and measuring the resulting streamwise velocity field in order to characterize the transition process. Care will be taken to quantify the measurement precision so that a determination of the applicability of the MTV measurement techniques can be made with respect to the fluctuation levels outlined in Tables 2.1 and 2.2.

The next section will introduce laser-induced fluorescence (LIF) and LIF-based velocimetry techniques. This will aid in ascertaining their applicability to study transition-to-turbulence and to serve as an alternative to physical probe-based techniques.

---

[*] In this dissertation, the roughness Reynolds number is defined as $Re_k = \rho_k U_k k/\mu_w$. The subscript k denotes evaluation of the respective parameter at the roughness height and streamwise location for conditions in a laminar boundary layer without roughness present. The subscript w denotes evaluation of the parameter at the wall temperature. An alternative roughness Reynolds number definition often used in literature is $Re_{kk} = \rho_k U_k k/\mu_k$, however some authors also refer to this definition of roughness Reynolds number as Re_k.

2.2 Laser-Induced Fluorescence

Laser-induced fluorescence (LIF) uses a laser to probe individual species within the flowfield, providing information pertaining to both the thermodynamic (pressure, temperature, mole fraction) and fluid dynamic state (velocity) of the gas. The laser can either be focused to a point for LIF measurements, formed into a thin sheet using a cylindrical and focusing lens in combination for planar LIF measurements (PLIF), or used to illuminate a volume for three-dimensional or stereoscopic imaging. Reviews of the laser-induced fluorescence measurement technique are available from Eckbreth[45] and others.[46,47] The measurement technique works by inducing a transition, usually of an electron, from a lower energy state (E_1) to an excited energy state (E_2) via stimulated absorption of one or more photons in the atomic or molecular species of interest. In a two-level model assumption, the atom or molecule of interest in the E_2 state then returns to the E_1 state by transferring energy via spontaneous emission of a photon (fluorescence), or by transferring energy non-radiatively through a collision with another atom or molecule (collisional quenching).

For an atom, such as N or O, the energy required to induce an absorption transition of an electron to the E_2 state from the ground (E_1) state is equal to the energy difference between the atom with an electron occupying the excited electronic orbital and the atom's ground electronic orbital configuration, respectively. For molecules, such as NO, the energies of the E_2 and E_1 states include the energies associated with the vibrational and rotational motion of the molecule in addition to the energy associated with the molecule's electronic configuration. Figure 2.2 shows a generalized two-level energy model for fluorescence with the stimulated absorption transition induced by a single photon.

In Fig. 2.2, the rate, W_{12}, at which the absorbing medium in the E_1 state transitions to the E_2 state is proportional to the product of the Einstein coefficient for stimulated absorption, B_{12}, and the laser's spectral irradiance (power per unit area per unit frequency), $I_\nu = IL_\nu$, where I is the irradiance (power per unit area) and L_ν is the laser spectral profile or laser line-shape (per unit of frequency).[45] The

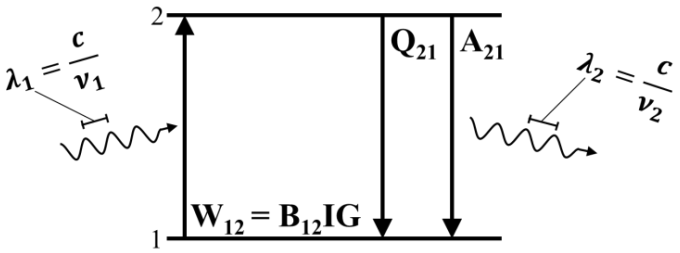

Figure 2.2: Two-level energy model of single-photon fluorescence.

energy of the absorbed photon and emitted photon are their respective frequencies, v_1 and v_2, multiplied by Planck's constant, h. While this two-level model shows upward and downward transitions occurring between the same two states, in reality downward transitions may occur between from different rotational states to lower vibrational or rotational states, resulting in $v_1 \neq v_2$. The Einstein A_{21} and B_{12} coefficients describe the probabilities for emission and absorption,[48] respectively, while Q_{21} is the collisional quenching rate. For absorbing species, the line-shape function, Y_v, describes the spectral width for a particular energy level. This line-shape function combines broadening effects due to Gaussian-shaped Doppler broadening and Lorentzian-shaped homogeneous broadening mechanisms and is represented as:[45]

$$Y_v = \frac{2}{\Delta v_D}\sqrt{\frac{\ln(2)}{\pi}}V(a,\tilde{x}) \tag{2.1}$$

Here, Δv_D is the Doppler-broadened line width due to the thermal motion of the absorbing species and $V(a,\tilde{x})$ is the Voigt integral function describing the convolution of homogeneous and Doppler broadening mechanisms. The line-width resulting from Doppler broadening is given by:[45,48]

$$\Delta v_D = \frac{v_0}{c}\sqrt{\frac{8\ln(2)k_B T}{m}} \tag{2.2}$$

Here, v_0 is the transition center frequency, c is the speed of light, k_B is the Boltzmann constant, T the temperature, and m the species mass. The Voigt integral function is given by:[45]

$$V(a,\tilde{x}) = \frac{a}{\pi}\int_{-\infty}^{\infty}\frac{e^{-\tilde{y}^2}}{a^2+(\tilde{x}-\tilde{y})^2}d\tilde{y} \tag{2.3}$$

where $a = (\Delta v_H/\Delta v_D)\sqrt{\ln(2)}$ accounts for effects of homogeneous broadening (Δv_H) and $\tilde{x} = \{(v-v_0)/\Delta v_D\}\sqrt{4\ln(2)}$. Methods for computing this integral are given in Refs. 49-51.

The integral of the product of the absorption line-shape function, Y_v, and the laser's spectral profile, L_v, is defined by the overlap integral, $G = \int L_v Y_v dv$, and describes what portion of a particular absorption transition is affected by the incident laser radiation. The rate constant for stimulated absorption, W_{12}, which describes the rate at which species in E_1 transition to E_2 via absorption of a single photon[45,47] is given by:

$$W_{12} = B_{12}IG \tag{2.4}$$

As the laser passes through a flowfield, it is absorbed at a rate corresponding to Eq. 2.4, inducing a transition between the E_1 and E_2 states. Consequently, as the laser continues to propagate through the

flowfield, the irradiance is continually diminished as a result of the absorption process. The Beer-Lambert law describes the magnitude of the decrease of the spectral irradiance, and is of the form:[52]

$$-dI_\nu = I_\nu k_s(\nu)dx \tag{2.5}$$

where k_s is the absorption coefficient. The absorption coefficient can be related to B_{12} by the relation $\int k_s(\nu)d\nu = N_S B_{12}\, h\nu_0/c$,[52] where N_S is the number density of the species, h is Plank's constant, and c the speed of light. Integrating Eq. 2.5 results in the relation:[52]

$$I_{\nu,x} = I_{\nu,0}e^{-k_s(\nu)x} \tag{2.6}$$

where $I_{\nu,0}$ is the incident spectral irradiance and $I_{\nu,x}$ the spectral irradiance after the beam travels a distance x.

In both Figures 1 and 2, Q_{21} is the so-called *quenching* rate constant. It describes the rate at which energy is transferred through non-radiative collisions between excited atoms or molecules in the E_2 state and atomic or molecular collision partners of species *i*. This rate constant is computed similarly to that in Ref. 45 as:

$$Q_{21} = N_T \textstyle\sum_i \chi_i \sigma_{s,i} v_{s,i} \tag{2.7}$$

where $N_T = P/k_B T$ is the total population of the excited state, χ_i is the mole fraction of quenching species *i*, $\sigma_{s,i}$ is the collision cross-section between the excited species, *s*, and quenching species, *i*, and $v_{s,i} = \sqrt{8k_B T_{translation}/\pi\mu_{s,i}}$ is the mean relative velocity[53,54] between the excited species and quenching species, with $\mu_{s,i}$ being their reduced mass and $T_{translation}$ their translational temperature. The spontaneous emission coefficient, A_{21}, in Fig. 1 is also known as the Einstein *A* coefficient and describes the probability for spontaneous emission of a photon by an atom or molecule in the excited state.[48]

For the two-level model in Fig. 2.2, the rate of change of the populations N_1 and N_2, in the E_1 and E_2 states, respectively, can be obtained from relations similar to those presented in Ref. 45:

$$\frac{dN_1}{dt} = -\frac{dN_2}{dt} = -N_1 W_{12} + N_2(Q_{21} + A_{21}) \tag{2.8}$$

$$N_1 + N_2 = N_S = \chi_s f_B N_T \tag{2.9}$$

Equation 2.9 is a conservation law saying that the combined populations of the E_1 and E_2 states is equal to the initial population of the excitation species' E_1 state, N_S, which is in turn the product of the species mole fraction, χ_s, the total population, N_T, and the temperature-dependent Boltzmann fraction, f_B. Equation

2.8 assumes that the laser intensity is sufficiently weak such that stimulated emission (W_{21}) can be neglected.

The Boltzmann fraction, f_B, describes the ratio of the number of absorbers initially occupying E_1 relative to all possible energy states at a particular temperature, T, when a system is in thermodynamic equilibrium.[54] This term has a general form given by:[45,54,55]

$$f_B = \frac{g_j e^{-E_j/k_B T}}{\sum_j g_j e^{-E_j/k_B T}} \tag{2.10}$$

where g_j is the degeneracy of state j. Degeneracy refers to the number of quantized states that exist in a given energy level, E_j.[54] The summation in the denominator is termed the *partition function*, Z, and for a diatomic molecule can be represented as the product of the individual partition functions for rotational and vibrational energies, $Z = Z_{rot} Z_{vib}$. The individual partition functions take a form similar to that in Ref. 54:

$$\begin{aligned} Z_{rot} &= \sum_{J=0.5,1.5,2.5,\cdots} (2J+1) \exp\left[-\frac{F_J}{k_B T_{rot}}\right] \\ Z_{vib} &= \sum_{v=0,1,2,\cdots} \exp\left[-\frac{G_v}{k_B T_{vib}}\right] \end{aligned} \tag{2.11}$$

where J is the rotational quantum number, v is the vibrational quantum number, F_J the rotational energy, G_v the vibrational energy, T_{rot} the characteristic rotational temperature, and T_{vib} the characteristic vibrational temperature.

It should be noted that the model presented in Fig. 2.2 neglects transitions from E_1 to E_2 resulting from collisions, with a rate constant of Q_{12}. This is usually a good assumption for large energy separations associated with the visible or UV transitions typically employed for LIF. Transitions from the E_2 state resulting from pre-dissociation (Q_{pre}) and ionization (Q_{ion}), which are described in Refs. 45 and 47, have also been neglected.

2.2.1 Linear, Steady State Solution

If a continuous laser source is used to populate the E_2 state and detection of fluorescence occurs well after this source is turned on, then N_2 can be assumed to have reached its steady-state value. From this assumption, the left-hand-side of Eq. 2.8 is set to zero, resulting in two algebraic equations (Eqs. 2.8 and 2.9) for two unknowns (N_1 and N_2). The same assumption can be made to determine the population, N_2, achieved by a pulsed laser source if the time required to reach steady state is short compared to the duration of the pulse. This population is computed as:

$$N_2 = \frac{\chi_s f_B N_T W_{12}}{W_{12}+Q_{21}+A_{21}} \tag{2.12}$$

The product of this excited state population and the spontaneous emission rate constant is N_2A_{21} and represents the number of transitions per unit time and per unit volume. Integrating this constant value with respect to time gives the total number of transitions per unit volume during the detection period. Substituting Eq. 2.4 for W_{12}, and assuming that it is small compared to A_{21} and Q_{21} (which is valid for low-intensity excitation), a relation for the total number of photons collected via fluorescence by the detection device is:[47]

$$S_{LIF} = \chi_s f_B N_T B_{12} I G \Phi \Delta t_{det} \tilde{V} \frac{\Omega}{4\pi} \eta \tag{2.13}$$

where $\Phi = A_{21}/(Q_{21} + A_{21})$ is the fluorescence yield, Δt_{det} is the period of detection, $\tilde{V}$ is the volume probed by the laser source, Ω is the solid angle over which detection occurs, and η is the detection efficiency. The fluorescence yield, Φ, describes the fraction of de-excitation transitions that occur via spontaneous emission (fluorescence) relative to all de-excitation transitions (i.e. spontaneous emission and collisional quenching, assuming pre-dissociation and ionization are negligible). Neglecting the constants in Eq. 2.13, a generalized form for the fluorescence signal similar to that presented in Refs. 47 and 56, including its thermodynamic (χ,P,T) dependencies and velocity dependence (arising from the Doppler effect), is:

$$S_{LIF} \propto \chi_s f_B(T) B_{12} I G(\chi_s, P, T, U) \Phi(\chi_s, \chi_i, P, T) \Delta t_{det} \tag{2.14}$$

2.2.2 Non-Steady State Solution

For a pulsed laser source, if N_2 is changing during the period of detection, then the entirety of Eq. 2.8 must be solved to obtain the time-dependent population, $N_2(t)$. Similarly, if the duration of the laser pulse is of the same order of magnitude as the time required to reach steady state, then the population at the end of the laser pulse, $N_2(\Delta t_P)$, can be obtained by solving Eq. 2.8. By assuming the laser intensity behaves as a Heaviside step function in time, the population $N_2(t)$, existing during laser excitation can be calculated by substituting the relation for N_1 from Eq. 2.9 into Eq. 2.8 and integrating with respect to time:[47]

$$N_2(t) = \chi_s f_B N_T \frac{W_{12}}{r}(1 - e^{-rt}), \ 0 < t \leq \Delta t_P \tag{2.15}$$

where $r = W_{12} + Q_{21} + A_{21}$. The inverse of this value, r^{-1}, is the characteristic time needed to achieve steady state. This solution assumes an initial condition which typically specifies the initial excited state population to be zero ($N_2(0) = 0$).

When the laser source is turned off, the only pathways to return to the ground state from the excited state are assumed to be through either spontaneous emission or collisional quenching. Therefore, for the period following laser excitation, the first term on the right-hand-side of Eq. 2.8 is zero. This modified version of Eq. 2.8 is then used to determine the excited-state population for the period after laser excitation by integrating with respect to time:[47]

$$N_2(t) = \chi_s f_B N_T \frac{W_{12}}{r} \cdot (1 - e^{-r\Delta t_P}) \cdot e^{-(t-\Delta t_P)/\tau_{LIF}},\ t > \Delta t_P \tag{2.16}$$

This solution assumes that the laser intensity is turned off instantaneously, with an initial condition given by Eq. 2.15, evaluated at $t = \Delta t_P$. This solution shows that the population in the excited state decreases exponentially in time after the laser pulse.

The term $\tau_{LIF} = (Q_{21} + A_{21})^{-1}$ in Eq. 2.16 is referred to as the fluorescence lifetime and describes the rate at which the population in a particular excited state transitions to a lower state. As with the derivation of Eq. 2.13, the total number of photons collected via fluorescence over the detection period is determined by multiplying Eqs. 2.15 and 2.16 by the spontaneous emission rate Einstein coefficient A_{21}, accounting for the collection volume and detection system, and integrating with respect to time:[47]

$$S_{LIF} = \chi_s f_B N_T \Phi B_{12} I G \Delta t_P \left\{\left[1 - \frac{1-e^{-r\Delta t_P}}{r\Delta t_P}\right] + \left[\frac{(1-e^{-r\Delta t_P})}{\Delta t_P/\tau_{LIF}}\right]\right\} \tilde{V} \frac{\Omega}{4\pi} \eta \tag{2.17}$$

Like Eq. 2.13, this solution assumes that W_{12} is small compared to A_{21} and Q_{21}. However, if the laser irradiance, I, is sufficiently large such that W_{12} and W_{21} are of the same order of magnitude as Q_{21} and A_{21}, then both must be included in the solution. This gives $r = W_{12} + W_{21} + Q_{21} + A_{21}$ during laser excitation. By defining the irradiance at which the fluorescence signal saturates as[45,47] $I_{sat} = (Q_{21} + A_{21})/(B_{12} + B_{21})$ and rearranging r such that $r = \tau_{LIF}^{-1}[I/I_{sat} + 1]$, a more detailed formulation for the fluorescence signal, including effects from laser saturation, is given as:[47]

$$S_{LIF} = \chi_s f_B N_T \Phi B_{12} \frac{I}{1+I/I_{sat}} \mathrm{G} \Delta t_P \left\{1 + \frac{1-e^{-r\Delta t_P}}{r\Delta t_P}\left(\frac{I}{I_{sat}}\right)\right\} \tilde{V} \frac{\Omega}{4\pi} \eta \tag{2.18}$$

When $I \ll I_{sat}$, Eq. 2.18 simplifies to a form similar to that of Eq. 2.15.

2.2.3 Multi-Level Fluorescence Modeling

In the preceding discussion, a simplified two-level model of fluorescence was put forth, which provides for an understanding of the most basic physical mechanisms and energy transfer processes involved. This basic description allows for the development of a general analytic relation between the fluorescence signal and these mechanisms and processes. However, such a simple description does not account for rotational or vibrational energy transfer occurring between the absorbing species and the surrounding gas mixture. Since each electronic energy level depicted in Fig. 2.2 can have vibrational and rotational fine structure for molecular species, such energy transfer processes result in a redistribution of the populations to various vibrational and rotational states. To account for these processes, analytical models including multiple energy states and a system of population rate equations are used. Discussion of such modeling aspects can be found in Refs. 45-47.

2.2.4 Doppler-Based Velocimetry

The Doppler Effect can be used to determine flow velocities for atomic and molecular species. The translational motion of the absorbing species in the direction of the excitation laser's propagation, described by a velocity component U, results in a shift of the absorption line-shape function away from its transition center frequency, ν_0, according to:[52]

$$\Delta\nu = \frac{U}{c}\nu_0 \tag{2.19}$$

This velocity-dependent frequency shift of the absorption line-shape function is implicit in the overlap integral, G, and thus, its effect on fluorescence signal can be seen through the dependence of G on the velocity component, U, in Eq. 2.14. When a component of translational motion of the absorbing species opposes the laser's direction of propagation, corresponding to the negative $(-)$ solution of Eq. 2.19, the incident laser radiation appears to be at a higher frequency from the perspective of the gas. Hence, as the laser's frequency is scanned over the absorption transition, Y_v, the measured intensity of fluorescence corresponding to this profile is shifted toward a lower frequency, or red-shifted. The converse is true when motion is in the same direction as the laser's propagation, corresponding to the positive $(+)$ solution of Eq. 2.19, where the absorption profile is shifted toward a higher frequency, or blue-shifted.

In one implementation, velocity component measurements can be made by scanning the laser over an absorption transition in both the measurement volume and a reference cell. In this case, the Doppler shift between the absorption profiles is used to compute an average velocity according to Eq. 2.19. Examples of such measurements include those in an arcjet,[57-60] supersonic underexpanded jets,[61-65] shock tunnel,[66,67] and non-reacting supersonic flow with a rearward-facing step.[68-70] Such measurements require that the flowfield be relatively steady since shot-to-shot fluctuations in fluorescence intensity from thermodynamic and fluid dynamic variations can affect the measured line-shape. The velocity measurements can also be complicated by a frequency shift in the line-shape function resulting from collisional effects (pressure). In compressible flows, the pressure field can vary significantly, and hence the collisional shift in the line-shape function can likewise vary. Absorption of laser energy can also result in an apparent frequency shift in the line-shape function. Recall that the line-shape function must be inferred from the overlap integral, G, which represents the integrated product of the absorption line-shape and laser spectral line-shape. If absorption is significant, then irradiance will vary spatially according to Eq. 2.6, resulting in a spatially varying overlap integral. An analysis of how absorption affects the line-shape frequency shift is presented in Ref. 67. If flow symmetry is assumed, then the frequency shift due to pressure can be estimated.[66] Flow symmetry can also be used in the application of Eq. 2.6 to correct for the frequency shift resulting from absorption.[58] Alternatively, if two counter-propagating laser beams are used, these frequency shift effects can be completely removed. The use of counter-propagating beams results in two excitation peaks, separated in frequency by twice the velocity-induced Doppler shift. The need for a reference cell measurement to ascertain velocity can also be removed, as a counter-propagating beam approach is self-referencing.[63,71,72]

A fluorescence-based Doppler velocimetry approach was used in Ref. 67 to measure two-components of velocity about a heat shield model taken in a hypersonic free-piston shock tunnel. In this experiment, laser sheets were directed in both the radial (vertical) and axial (horizontal) directions so that measurements of the Doppler-shifted absorption profiles for the respective directions could be obtained and compared with measurements from a static reference cell to infer velocities. An estimation of velocity errors incurred from the frequency shifts due to absorption and collisional effects was also performed. In Ref. 67, three separate absorption transitions were probed to measure two different velocity components, with one transition being used for both components. This resulted in a measured axial freestream velocity of

2394±68 m/s and a measured radial velocity of 53±50 m/s, giving respective uncertainties of ~2.8% and ~94.3%.[67]

Another form of the fluorescence-based Doppler velocity measurement is a fixed frequency method, which can allow for an instantaneous velocity component measurement. With the fixed frequency technique, a narrow linewidth laser is tuned off the absorption profile peak to a point where the slope of the profile is maximum and thermodynamic conditions are assumed constant, as described in Refs. 73 and 74. Assuming that the absorption profile is approximately linear in the region of maximum slope, the measured signal intensity can be related to the Doppler shift of the profile. This fixed frequency Doppler velocimetry technique has been applied to a free jet,[75] supersonic underexpanded jet,[76] and reacting supersonic flow.[77] The stated random and systematic errors in Ref. 76, when added in quadrature, gave a total uncertainty of ~12%. In Ref. 77, the stated lowest time-averaged and single-shot uncertainties achieved were ~3% and ~15%, respectively, for a 1600 m/s velocity range.

2.2.5 Flow Tagging Velocimetry

Another technique by which velocity can be measured using fluorescence is flow-tagging velocimetry (also known as molecular tagging velocimetry, MTV). Fluorescence-based flow-tagging velocimetry is a time-of-flight technique that involves laser excitation—or tagging—of the gas along a line, series of lines, or grid pattern. With this form of velocimetry, the species of interest in the gas absorbs the incident radiation from a laser source, which induces either of the following: 1) fluorescence, 2) a reaction that forms a product that then emits a photon via fluorescence, or 3) a reaction that forms a product that can then be probed with another laser source to induce fluorescence. Images of the fluorescence pattern are acquired at two time delays, with velocity computed by measuring the displacement of the tagged molecules between images. Typically, a line or series of lines can be used to measure a single-component of velocity while a crossed grid pattern can be used to measure two-components. Two general fluorescence-based methods of flow-tagging velocimetry are discussed here; one that requires a single laser source and another that requires multiple laser sources. The main advantage of flow-tagging velocimetry, as compared to most Doppler-based methods (which are time averaged), is that it can make instantaneous (single-shot) measurements with fast time resolutions (as short as a few hundred nanoseconds). A disadvantage, however, is that flow-tagging velocimetry cannot provide full velocity field information. A

broader discussion of molecular-tagging velocimetry, which relies on molecular tracers for flow-tagging, is provided in Ref. 78.

2.2.5.1 Single-Laser Methods

The first method involves either direct or indirect excitation of fluorescence with a single laser source. The first application of this method to a gaseous flow involved excitation of phosphorescence of biacetyl molecules, as described in Ref. 79. If this method is used, the fluorescence lifetime of the tagged molecules must be long enough so that advection provides for measurable displacements with tagged regions having signal intensities that are still above the detection limit of the imaging system at the time the second image is acquired. Typical experiments involve capturing a reference image acquired during the tagging process, or a relatively short time thereafter. If a single-framing camera is used, such as in Ref. 80, a single reference image or set of reference images is acquired. The timing of the single-frame camera is then delayed and a subsequent image or set of images is then acquired. If a two-camera system or dual-framing camera is used, the delayed image is acquired in sequence after the reference image. The velocity is computed by measuring the displacement of the tagged molecules that occurs in the time between when the reference and delayed images were acquired. The form of this technique relying on direct excitation of fluorescence for flow tagging has been applied to the study of supersonic jets,[81-87] hypersonic boundary layers,[80,88] and arcjet flowfields.[58]

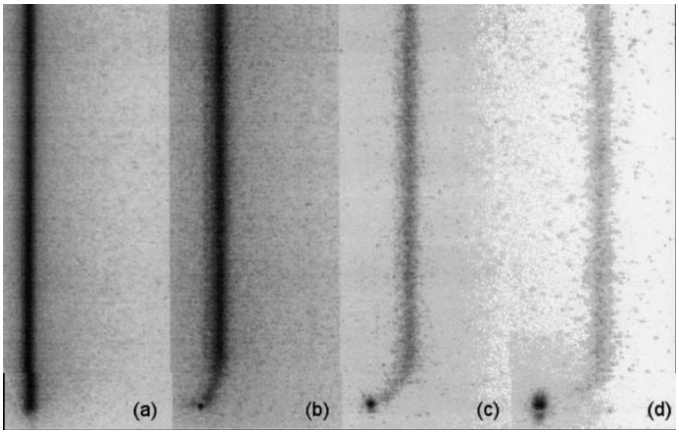

Figure 2.3: Single-line excitation of nitric oxide fluorescence used to study hypersonic boundary layer flow over a flat plate. Images, from left to right, correspond to camera delay settings of 0 ns, 250 ns, 500 ns, and 750 ns. Image taken from Ref. 80 with permission of the authors.

Figure 2.3, taken from Ref. 80, shows images from tagging a single line of nitric oxide using direct excitation of fluorescence within a flat plate hypersonic laminar boundary layer. In this Figure, the left-most image corresponds to the reference image, while the remaining images, from left to right, correspond to delayed images taken at 250 ns, 500 ns, and 750 ns after tagging, respectively. Measurements of freestream velocity, spatially averaged from a point just above the velocity boundary layer (3 mm) to 15

mm above the flat plate, resulted in a mean of 3,035±100 m/s at 90% confidence, giving an uncertainty of 3.3% of the mean.[80] Single-shot uncertainty estimates for a 3,000 m/s freestream flow and for camera delay settings of 250 ns, 500 ns, and 750 ns were 4.6%, 3.5%, and 3.5%, respectively.[80]

An indirect excitation scheme, as described in Refs. 89-91, relies on photodissociation of molecular nitrogen for flow tagging. The technique uses a femtosecond laser pulse to dissociate molecular nitrogen into two nitrogen atoms, which then recombine after a collision, forming molecular nitrogen in an intermediate state. A subsequent collision brings the molecular nitrogen to an excited electronic B state, which then emits a photon via fluorescence upon transitioning to the excited electronic A state. Ref. 82 provides a description of this process. One benefit of this indirect technique, known as Femtosecond Laser Electronic Excitation Tagging (FLEET), is that the recombination rate of dissociated atomic nitrogen allows for a much longer fluorescence lifetime. This would allow displacements to be measured over greater time scales, providing for accurate measurements of velocity in low-speed flow regions, such as in a hypersonic wake flow. Additionally, the technique relies on molecular nitrogen for tagging, which is present in most hypersonic facilities.

2.2.5.2 Multi-Laser Methods

A second method of fluorescence-based flow-tagging velocimetry involves writing a line, series of lines, or grid pattern into the flowfield by one of several laser-based mechanisms. This pattern can then be interrogated, or read, by subsequent laser pulses to induce fluorescence, allowing for the determination of velocity through measurement of the displacement of the pattern. Such techniques usually involve two or three different lasers and are therefore more time consuming to set up and more difficult to execute.

One mechanism by which a pattern can be written into the flowfield is via ionization of the absorbing species, known as Laser Enhanced Ionization (LEI) flow tagging. The tagging process is accomplished by promoting the species (such as sodium in Refs. 92-94) to a higher energy state via laser excitation near the ionization limit. Collisions then result in the ionization of the species, with the tagging pattern corresponding to the ionized regions. Subsequent laser pulses are used to induce fluorescence of the absorbing species in regions that have not been photo-ionized. Supersonic measurements of velocity in a shock tube were performed using LEI flow-tagging in Refs. 92 and 93, and hypersonic velocity measurements in an expansion tube were performed in Ref. 94.

A second mechanism that can be used to write a pattern into the flowfield is by vibrational excitation of molecular oxygen via Raman pumping. This is followed by reading the pattern of the vibrationally-excited oxygen by inducing fluorescence. The technique, known as Raman Excitation and Laser-Induced Electronic Fluorescence (RELIEF),[95] is advantageous as it relies on the flow-tagging of oxygen which is a common working gas of most hypersonic facilities. This technique has been used to characterize turbulence in a free jet[96] and underexpanded jet.[97] The RELIEF technique, however, is limited to temperatures below 750 K. Above this temperature, a significant fraction of oxygen molecules are vibrationally excited, making it difficult to distinguish the tagged molecules from the background.[98]

Yet another mechanism involves using one laser to photo-dissociate a molecular species. This results in the formation of a product species for which a second laser can be used to read the location of the written pattern by exciting laser-induced fluorescence in the product species. The formation of the product species typically occurs through one or more reactions. A list of partner species used in the writing and reading process include: H_2O-OH,[99-105] N_2O-NO,[106] O_2-O_3,[107,108] N_2/O_2-NO,[109-112] and NO_2-NO.[83,113-118]

Figures 2.4a and 2.4b, taken from Ref. 117, show images of vibrationally excited NO fluorescence in a grid pattern formed via photodissociation of NO_2 in a mixture containing 6.3% NO_2 in N_2. The images were taken in a supersonic underexpanded jet 400 ns (Fig. 2.4a) and 800 ns (Fig. 2.4b) after the pattern was written into the flow with a two-dimensional array of 355 nm beams. Two components of velocity were obtained by relating the displacement of the grid in the left image to a grid imaged in a stationary gas. The upper half of Fig. 2.4c, taken from Ref. 117, shows measured streamwise velocities compared with computation, shown in the lower half of Fig. 2.4c. The use of two pulsed dye lasers in this experiment

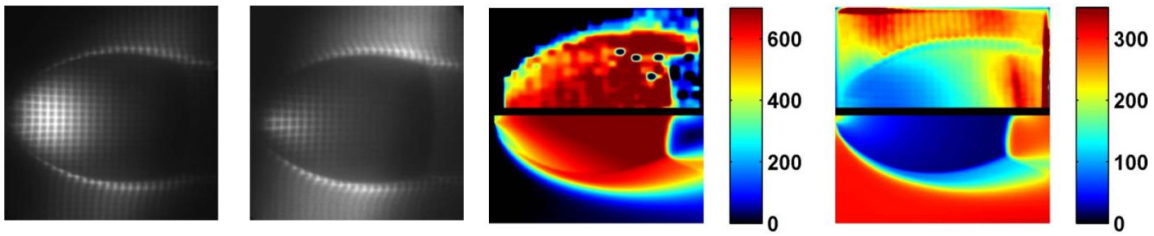

(a) (b) (c) (d)

Figure 2.4: Flow-tagging images of vibrationally excited NO fluorescence obtained (a) 400 ns and (b) 800 ns after photodissociation of NO_2. The two-dimensional grid pattern allows for calculation of two velocity components. Measured (c, top) and computed (c, bottom) streamwise velocity maps. Measured (d, top) and computed (d, bottom) rotational temperature map. Image taken from Ref. 117 with permission of the authors and the publisher.

permitted the excitation of both a low (J = 1.5) and high (J = 8.5) rotational level within the same vibrationally excited (v = 1) NO state. The fluorescence images corresponding to the low-J (Fig. 2.4a) and high-J (Fig. 2.4b) rotational levels also allowed for measurement of the rotational temperature. The top half of Fig. 2.4d, from Ref. 117, shows measured rotational temperature compared with computation, shown in the lower half of Fig. 2.4d. Stated root-mean-square (RMS) uncertainties in the velocity measurement were ~5% with high signal-to-noise.[117] The stated RMS uncertainties in rotational temperature ranged from 9% to 35% prior to the Mach disk.[117]

2.2.6 Advantages and Limitations of Laser-Induced Fluorescence

The time scales associated with inducing fluorescence via laser excitation are typically a few hundred nanoseconds, which is shorter than hypersonic flow time scales, therefore providing sufficient temporal resolution for high-speed transition-to-turbulence measurements. Recently developed kHz- and MHz-rate pulsed laser systems have allowed image sequences consisting of tens to thousands[119] of images to be acquired, providing time-resolved information pertaining to high-speed fluid dynamic behavior. Both fluorescence-based velocimetry[116] and visualization[120,121] experiments in hypersonic flow fields have been performed with these types of laser systems. The spatial resolution of a LIF technique is also sufficient for many applications with laser sheet thicknesses typically in the range of 0.1 to 1 mm and magnifications of tens of pixels per mm, depending on the experimental setup. Fluorescence-based measurements are more sensitive to concentration than other techniques, with sensitivity on the order of parts-per-million or better.[45]

Additionally, a wide range of species including intermediate combustion species can be probed using fluorescence techniques. Reference 46 provides an extensive listing of many species that have been detected using LIF and other methods. Another advantage of LIF is that it is readily extended to planar or volumetric measurement (see Refs. 122 and 123).

Several factors complicate acquisition and interpretation of LIF signals, complicating quantitative measurements. Quenching of the fluorescence prevents easy quantification of signal intensities. Absorption of laser energy as the laser light passes through the flowfield can limit the effectiveness of fluorescence-based measurements, as the energy will decrease in an exponential manner over a given spatial path length according to the Beer-Lambert relations in Eqs. 2.5 and 2.6. This can complicate quantitative

measurements. Absorption can be significant when the concentration of the absorbing ground state population is high, the transition cross-section is relatively large, the Einstein B coefficient for stimulated absorption is relatively large, and/or the path length through which the laser radiation passes is relatively long. To avoid strong absorption, a transition may be selected for which the population is small based on analysis of the Boltzmann fraction, as was done for PLIF visualization measurements in a hypersonic shock tunnel described in Ref. 124. Absorption can also limit measurement capabilities when fluorescence from the probed volume is re-absorbed by the species of interest. This effect, known as *radiative trapping*, occurs when fluorescence emission at frequencies readily absorbed by highly populated states must pass through gas containing these potential absorbers before reaching the imaging system. Measurements in a non-uniform or turbulent mixture are especially susceptible to errors associated with absorption and radiative trapping effects, as the absorption coefficient is a spatially- and temporally-varying property. A discussion of these issues, and some methods used to circumvent them, is provided in Ref. 45.

Consideration must also be given to the optical access of the test facility. Since much of the work described in this discussion requires fluorescence excitation using laser frequencies in the UV portion of the electromagnetic spectrum, the window material used in hypersonic facilities must be capable of transmitting such frequencies with minimal absorption. Also, typically two or three windows are required for LIF or PLIF applications. The laser (beam or sheet) is typically brought in from one window and observed through another window at right angles to the first window. A third window can allow the laser to leave the test section, reducing scattered light, and allowing the quantification of absorption of the laser beam/sheet in some applications.

2.2.7 Selection of Technique for this Dissertation

The relatively high precision, spatial resolution, sensitivity at low concentrations, and non-intrusive nature of the flow tagging techniques described in the preceding sections make the techniques attractive for applications involving hypersonic boundary layer measurements. The flow tagging (or molecular tagging) technique was also identified in Ref. 125 as being the primary technique for making measurements in supersonic and hypersonic flows where planar velocity measurements are needed and for which particle seeding is not possible.

2.2.8 Selection of Working Species for this Dissertation

In this dissertation, nitric oxide (NO) has been selected as the tracer species for the MTV measurements. Several factors, both thermodynamic and spectroscopic, motivate the use of NO over other potential species.

First, NO has a molecular weight (30.01 kg/kmol) very similar to that of air (28.97 kg/kmol). This is beneficial, as the molecular weight of NO mimics that of the working gas of the 31-Inch Mach 10 Air blowdown wind tunnel facility. Second, the diffusion of NO is such that it diffuses completely into the velocity boundary layer within a relatively short streamwise distance. For conditions relevant to this dissertation (edge Mach number of 8.1, static pressure of 201 Pa, edge temperature of 74 K, and plate temperature of 314 K), computations were performed in Ref. 126 to determine the effectiveness of seeding NO at a rate of 3 mg/s into a hypersonic laminar boundary. In those computations, the NO was seeded into the boundary layer 29.4 mm downstream of the leading edge of a flat plate and reached the edge of the boundary layer approximately 26 mm downstream of the seeding location. Flow visualization experiments performed in Ref. 127 using the same model and at conditions similar to those examined in this dissertation also showed that seeded NO, injected 29.4 mm downstream of the leading edge at approximately 6.1 mg/s, reached the edge of the enthalpy boundary layer predicted by a computational fluid dynamic simulation. This ensures that flow visualization measurements and measurements of velocity can be made across the thickness of the boundary layer. NO gas is also relatively stable and can exist in a gaseous form over a wide range of conditions and can purchased in a gas cylinder and easily connected to a gas supply system.

In terms of spectroscopy, the fluorescence behavior of NO has been well documented. Simulation software such as LIFBASE[128] can be used to select specific NO transitions appropriate for conditions of a particular NO PLIF or NO MTV experiment. These transitions are relatively easy to access with a commercially available pulsed dye laser system. The fluorescence lifetime of NO is also long enough lived in low-to-moderate quenching environments to allow for the application of single-laser excitation MTV and a double-framing camera (as will be discussed in Chapter 3). In the absence of quenching species ($Q_{21} = 0$ in Eq. 2.7), the natural lifetime of NO in the $v' = 0$ state is approximately 192 ns.[129] Figure 2.5 shows computed fluorescence lifetimes (red data points) of 1% NO in N_2 (Fig. 2.5a) and in air (Fig. 2.5b) for conditions relevant to this dissertation computed using natural lifetime and quenching data from Ref. 129.

Each red data point is associated with a particular wind tunnel stagnation pressure and model plate angle, which are described in Chapter 3. The appropriate static pressure and temperature were computed with the Virginia Tech Compressible Aerodynamics Calculator[130] using conditions typical of the wind tunnel freestream. The blue curves in Fig. 2.5 represent the fluorescence lifetimes of NO at constant pressure as a function of temperature. Apparent in these figures is the role of both increasing pressure and O_2 on decreasing fluorescence lifetime. This fluorescence can be captured with commercially available cameras that provide adequate signal-to-noise ratios for both flow visualization and velocity measurement purposes.

Unfortunately, to achieve higher Reynolds numbers necessary for hypersonic transition-to-turbulence to occur for the specific model configuration examined in this dissertation, as will be described in later chapters, the wind tunnel stagnation pressure, model plate angle, or both must be increased. Either of these changes results in a reduced the fluorescence lifetime as can be seen in Fig. 2.5. This, in turn, drastically decreases the fluorescence signal captured in the second exposure by a dual frame camera. Figure 2.6 shows an estimate of the ratio of signals collected in the second exposure relative to the first exposure for a camera having a 5 ns first exposure duration and 100 ns second exposure duration corresponding to the wind tunnel conditions shown in Fig. 2.5. For measurements made with 1% NO in air, as the fluorescence lifetime is decreased, a dramatic decrease in

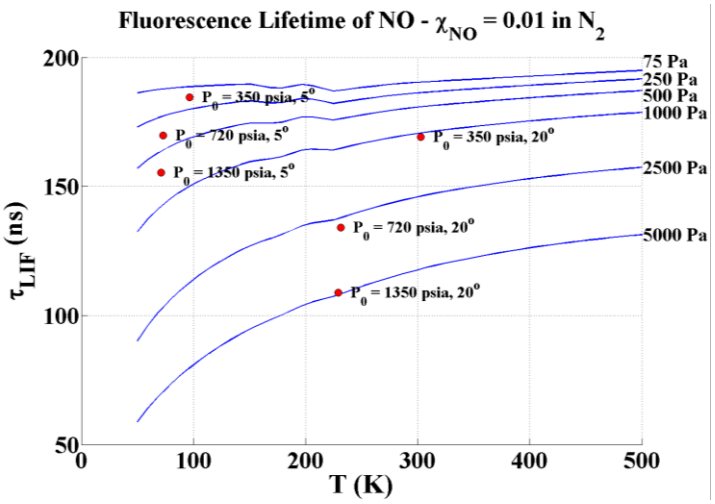

(a)

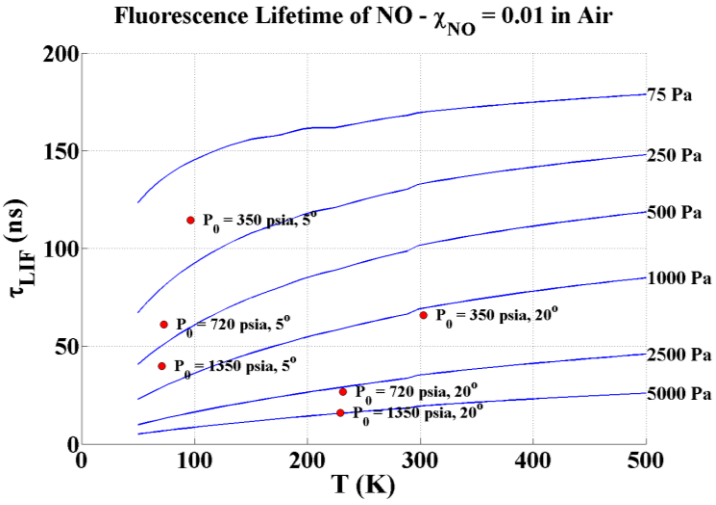

(b)

Figure 2.5: Fluorescence lifetime for 1% NO in (a) N_2 and (b) air. Values computed using Virginia Tech oblique shock calculator (Ref. 130) and constants from Ref. 129.

signal in the second exposure relative to the first exposure occurs. At such conditions, a single-laser NO MTV technique simply will not work.

The results in Fig. 2.6 motivate the use of the three-laser NO_2-to-NO photodissociation technique described in section 2.2.5. Such a technique would allow for a velocity measurement that was independent of fluorescence lifetime. While NO_2 has a larger molecular weight (46.01 kg/kmol) than that of air and NO, and therefore does not diffuse as readily as NO, the ability to use the same laser systems as used as for single-laser NO MTV experiments makes selection of the three-laser NO_2-to-NO photodissociation MTV technique attractive. As will be discussed in Chapter 3, the 355 nm output from the laser system used for the work in this dissertation results in photodissociation of NO_2. In this process, NO is created via the reaction $NO_2 + h\nu_{355\,nm} \rightarrow NO_{v''=0,1} + O$,[115] with an initial distribution of 62±3% $NO_{v''=0}$ and 38∓3% $NO_{v''=1}$.[131] After photodissociation occurs, the initial vibrational temperature of NO is approximately 6700 K, and decays to an equilibrium vibrational temperature within approximately 5-10 μs, although the decay is dependent upon pressure.[115] The initial rotational temperature of NO is also in non-equilibrium, with the $NO_{v''=0}$ rotational temperature initially higher than that of $NO_{v''=1}$, and rotational equilibrium occurring within 1-1.5 μs,[118] depending on the conditions. The photodissociation process also results in the product NO fragments having an initially high velocity for 100 ns after they are created, which can result in a broadening of the MTV profiles.[118]

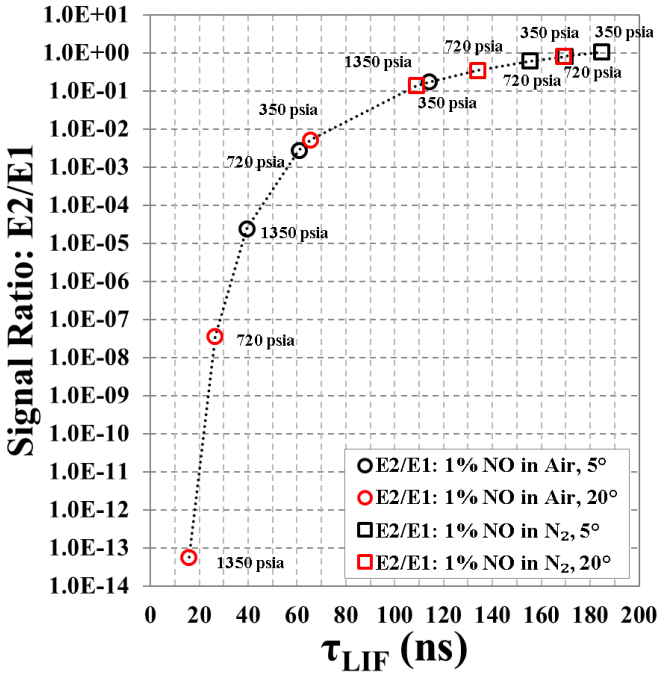

Figure 2.6: Ratio of fluorescence signals captured in second exposure (E2) relative to first exposure (E1) as a function of fluorescence lifetime for 5° (black) and 20° (red) plate angles. Calculations for 1% NO in air (circles) and N_2 (squares).

A drawback of using NO and NO_2 is the potential safety hazard and reaction potential each gas presents. When NO is exposed to air, it will eventually form NO_2, which is highly toxic, and when exposed to water, forms nitrous acid (HNO_2) and nitric acid (HNO_3), which are both corrosive.[132] The reaction of

gaseous NO with O_2 to form NO_2 is also exothermic and could potentially result in heat addition to the boundary layer. Any heat addition would then alter the thermal boundary layer profile and, because of the coupled relation of energy and momentum within the boundary layer, alter the velocity boundary layer profile. This reaction was studied in Ref. 133 over the temperature range of 226 K to 758 K and pressure range of approximately 27 Pa to 4 kPa. In that study the reaction rate, which is a function of temperature, was shown to increase with decreasing temperature below approximately 600 K. An analysis in Ref. 134 of low-temperature reaction rates at the conditions examined in this dissertation showed that the NO/O_2 reaction has a negligible influence on the hypersonic boundary layer flowfield. This analysis, however, relied on extrapolation of the reaction rate below 226 K to compute NO_2 production rates at the colder boundary layer edge temperatures. Further study is needed to confirm this low-temperature behavior, which is beyond the scope of this dissertation.

2.3 Conclusions

This chapter provided a review of the process of roughness-induced transition-to-turbulence and of the laser-induced fluorescence process. A discussion of laser-induced fluorescence-based velocimetry methods was also presented. A discussion of the advantages of using a fluorescence-based measurement technique and selection of NO and NO_2 as tracer species for the MTV measurements detailed in this dissertation were also presented. The following chapter will describe the experimental setup used for both the single-laser NO MTV and three-laser NO_2-to-NO photolysis MTV techniques used for measurements described in this dissertation. Details regarding the specific conditions of the wind tunnel experiments will also be provided.

---

[1] Bathel, B.F., Danehy, P.M., and Cutler, A.D., *Molecular-based optical measurement techniques for transition and turbulence in high-speed flow*, Von Karman Institute Lecture Series Manuscript, Brussels, Belgium, May 27 – 31, 2013.

[2] Reshotko, E., "*Transition Issues for Atmospheric Entry*," Journal of Spacecraft and Rockets, 45(2), pp. 161-164, March-April, 2008.

[3] Kovasznay, L.S.G., "*Turbulence in Supersonic Flow*," Journal of the Aeronautical Sciences, 20(10), pp. 657-682, October, 1953.

[4] Morkovin, M.V., "*On Transition Experiments at Moderate Supersonic Speeds*," Journal of the Aeronautical Sciences, 24(7), pp. 480-486, July, 1957.

[5] Morkovin, M.V., "*On Supersonic Wind Tunnels With Low Free-Stream Disturbances*," Journal of Applied Mechanics, 26(3), pp. 319-324, September, 1959.

[6] Schneider, S.P., "*Development of Hypersonic Quiet Tunnels*," Journal of Spacecraft and Rockets, 45(4), pp. 641-664, July-August, 2008.

[7] Schneider, S.P., "*Effects of High-Speed Tunnel Noise on Laminar-Turbulent Transition*," Journal of Spacecraft and Rockets, 38(3), pp. 323-333, May-June, 2001.

[8] Beckwith, I.E., and Miller III, C.G., "*Aerothermodynamics and transition in high-speed wind tunnels at NASA Langley*," Annual Review of Fluid Mechanics, 22, pp. 419-439, 1990.

[9] Pate, S.R., and Schueler, C.J., "*Radiated Aerodynamic Noise Effects on Boundary-Layer Transition in Supersonic and Hypersonic Wind Tunnels*," AIAA Journal, 7(3), pp. 450-457, March, 1969.

[10] Pate, S.R., "*Measurements and Correlations of Transition Reynolds Numbers on Sharp Slender Cones at High Speeds*," AIAA Journal, 9(6), pp. 1082-1090, June, 1971.

[11] Rufer, S.J., and Berridge, D.C., "*Pressure Fluctuation Measurements in the NASA Langley 20-Inch Mach 6 Wind Tunnel*," 42nd AIAA Fluid Dynamics Conference, AIAA 2012-3262, New Orleans, LA., June 25-28, 2012.

[12] Chokani, N., Shiplyuk, A.N., Sidorenko, A.A., and McGinley, C.B. "*Comparison between a hybrid constant-temperature anemometer and constant-voltage anemometer in hypersonic flow*," 34th AIAA Fluid Dynamics Conference, AIAA 2004-2248, Portland, OR. June 28 – July 1, 2004.

[13] Masutti, D., Spinosa, E., Chazot, O., and Carbonaro, M., "*Disturbance Level Characterization of a Hypersonic Blowdown Facility*," AIAA Journal, 50(12), pp. 2720-2730, December, 2012.

[14] Wheaton, B.M., and Schneider, S.P., "*Roughness-Induced Instability in a Hypersonic Laminar Boundary Layer*," AIAA Journal, 50(6), pp. 1245-1256, June, 2012.

[15] Steen, L.E., *Characterization and Development of Nozzles for a Hypersonic Quiet Wind Tunnel*, Master's Thesis, Purdue University, December, 2010.

[16] Berry, S.A. and Horvath T.J., "*Discrete Roughness Transition for Hypersonic Flight Vehicles*," 45th AIAA Aerospace Sciences Meeting, AIAA 2007-307, Reno, NV, January 8-11, 2007.

[17] Berry, S.A., Horvath, T.J., Lillard, R.P., Kirk, B.S., and Cassady, A.M., "*Aerothermal Testing for Project Orion Crew Exploration Vehicle*," 41st AIAA Thermophysics Conference, AIAA 2009-3842, San Antonio, TX., June 22-25, 2009.

[18] Everhart, J.L., "*Supersonic/Hypersonic Laminar Heating Correlations for Rectangular and Impact-Induced Open and Closed Cavities*," Journal of Spacecraft and Rockets, 46(3), pp. 545-560, May-June, 2009.

[19] Liechty, D.S., "*Aerothermodynamic Testing of Protuberances and Penetrations on the NASA Crew Exploration Vehicle Heat Shield*," 46th AIAA Aerospace Sciences Meeting, AIAA 2008-1240, Reno, NV, January 7-10, 2008.

[20] Malik, M.R., "*Prediction and Control of Transition in Supersonic and Hypersonic Boundary Layers*," AIAA Journal, 27(11), pp. 1487-1493, November, 1989.

[21] Chang, C-L., Choudhari, M.M., and Li, F., "Numerical Computations of Hypersonic Boundary-Layer over Surface Irregularities," 48th AIAA Aerospace Sciences Meeting, AIAA 2010-1572, Orlando, FL., January 4-7, 2010.

[22] Duan, L., Beekman, I., and Martín, M.P., "*Direct numerical simulation of hypersonic turbulent boundary layers. Part 3. Effect of Mach number*," Journal of Fluid Mechanics, 672, pp. 245-267, 2011.

[23] Schneider, S.P., "*Effects of Roughness on Hypersonic Boundary-Layer Transition*," Journal of Spacecraft and Rockets, 45(2), pp. 193-209, March –April 2008.

[24] Smith, A.M.O., and Clutter, D.W., "*The Smallest Height of Roughness Capable of Affecting Boundary-Layer Transition*," Journal of Aerospace Sciences, 26(4), pp. 229-245, April, 1959.

[25] Van Driest, E.R., and McCauley, W.D., "*The Effect of Controlled Three-Dimensional Roughness on Boundary-Layer Transition at Supersonic Speeds*," Journal of Aerospace Sciences, 27(4), pp. 261-271, April, 1960.

[26] Reshotko, E., "*Roughness-Induced Transition, Experiment and Modeling*," 38th AIAA Fluid Dynamics Conference, AIAA 2008-4294, Seattle, WA, June 23-26, 2008.

[27] Reda, D.C., "*Review and Synthesis of Roughness-Dominated Transition Correlations for Reentry Applications*," Journal of Spacecraft and Rockets, 39(2), p. 161-167, March-April, 2002.

[28] Reshotko, E., and Tumin, A., "*Role of Transient Growth in Roughness-Induced Transition*," AIAA Journal, 42(4), pp. 766-770, April, 2004.

[29] Wheaton, B.M., Bartkowicz, M.D., Subbareddy, P.K., Schneider, S.P., and Candler, G.V., "*Roughness-Induced Instabilities at Mach 6: A Combined Numerical and Experimental Study*," 41st AIAA Fluid Dynamics Conference, AIAA 2011-3248, June 27-30, 2011, Honolulu, HI.

[30] Iyer, P.S., Muppidi, S., and Mahesh, K., "*Roughness-induced transition in high speed flows*," 49th AIAA Aerospace Sciences Meeting, AIAA 2011-566, January 4-7, 2011, Orlando, FL.

[31] Iyer, P.S., Muppidi, S., and Mahesh, K., "*Transition of hypersonic flow past flat plate with roughness elements*," 40th AIAA Fluid Dynamics Conference, AIAA 2010-5015, June 28 – July 1, 2010, Chicago, IL.

[32] Iyer, P.S., Muppidi, S., and Mahesh, K., "*Boundary layer transition in high-speed flows due to roughness*," 50th AIAA Aerospace Sciences Meeting, AIAA 2012-1106, January 9-12, 2012, Nashville, TN.

[33] Tirtey, S.C., Chazot, O., and Walpot, L., "*Characterization of hypersonic roughness-induced transition*," Experiments in Fluids, 50, pp. 407-418, 2011.

[34] Heinrich, R.A., Choudhari, M., and Kerschen, E.J., "*A comparison of boundary layer receptivity mechanisms*," AIAA, SIAM, and APS, National Fluid Dynamics Congress, 1, pp. 1273-1280, 1988.

[35] Mack, L.M., "*Linear Stability Theory and the Problem of Supersonic Boundary-Layer Transition*," AIAA Journal, 13(3), pp. 278-289, March, 1975.

[36] Mack, L.M., "*Boundary-Layer Linear Instability Theory*," AGARD Report 709, pp. 3-1 – 3-81, 1984.

[37] Reshotko, E., "*Boundary Layer Instability, Transition, and Control*," 32nd AIAA Aerospace Sciences Meeting, AIAA 1994-1, Reno, NV., January 10-13, 1994.

[38] Reed, H.L., and Saric, W.S., "*Linear Stability Theory Applied to Boundary Layers*," Annual Review of Fluid Mechanics, 28(1), pp. 389-428, 1996.

[39] Reshotko, E., "*Transient growth: A factor in bypass transition*," Physics of Fluids, 13(5), pp. 1067-1075, May, 2001.

[40] Federov, A., "*Transition and Stability of High-Speed Boundary Layers*," Annual Review of Fluid Mechanics, 43, pp. 79-95, 2011.

[41] Saric, W.S., Reed, H.L., and Kerschen, E.J., "*Boundary-Layer Receptivity to Freestream Disturbances*," Annual Review of Fluid Mechanics, 34(1), pp. 291-319, 2002.

[42] Kendall, J.M., "*Experiments on Boundary-Layer Receptivity to Freestream Turbulence*," 36th AIAA Aerospace Sciences Meeting, AIAA 1998-530, 1998.

[43] Collicott, S.H., Schneider, S.P., and Messersmith, N.L., "*Review of Optical Diagnostic Methods for Hypersonic Low-Noise Facilities*," 34th AIAA Aerospace Sciences Meeting, AIAA 1996-0851, Reno, NV., January 15-18, 1996.

[44] Kendall, J.M., "*Wind Tunnel Experiments Relating to Supersonic and Hypersonic Boundary-Layer Transition*," AIAA Journal, 13(3), pp. 290-299, March, 1975.

[45] Eckbreth, A.C., *Laser Diagnostics for Combustion Temperature and Species 2nd Ed*., Combustion Science & Technology Book Series, Volume 3, Taylor & Francis, New York, 1996.

[46] Kohse-Höinghaus, K., and Jeffries, J.B., eds., *Applied Combustion Diagnostics*, Combustion: An International Series, Taylor & Francis, New York, 2002.

[47] Palma, P.C., *Laser-Induced Fluorescence Imaging in Free-Piston Shock Tunnels*, PhD Thesis, Australian National University, submitted May 1998, revised February 1999.

[48] Saleh, B.A.E., and Teich, M.C., *Fundamentals of Photonics 2nd Ed*., John Wiley & Sons, Inc., Hoboken, New Jersey, 2007.

[49] Humlíček, J., "*An efficient method for the evaluation of the complex probability function: The Voigt function and its derivatives*," Journal of Quantitative Spectroscopy and Radiative Transfer, 21, pp. 309-313, 1979.

[50] Kuntz, M., "*A new implementation of the Humlicek algorithm for the calculation of the Voigt profile function*," Journal of Quantitative Spectroscopy and Radiative Transfer, 57(6), pp. 819-824, 1997.

[51] Ruyten, W., "*Comment on "A new implementation of the Humlicek algorithm for the calculation of the Voigt profile function" by M. Kuntz [JQSRT 57(6) (1997) 819-824]*," Journal of Quantitative Spectroscopy and Radiative Transfer, 86, pp. 231-233, 2004.

[52] Thorne, A., Litzén, U., and Johansson, S., *Spectrophysics: Principles and Applications*, Berlin Heidelberg, 1999.

[53] Crosley, D.R., "*Rotational and Translational Effects in Collisions of Electronically Excited Diatomic Hydrides*," Journal of Physical Chemistry, 1989, 93, 6273 – 6282.

[54] Anderson Jr., J.D., *Hypersonic and High-Temperature Gas Dynamics 2nd ed.*, AIAA Education Series, AIAA, Reston, VA, 2006.

[55] Vincenti, W.G., and Kruger Jr., C.H., *Introduction to Physical Gas Dynamics*, Reprint of 1967 ed., Wiley, New York, 1975.

[56] Paul, P.H., Gray, J.A., Durant, J.L., and Thoman, J.W., "*Collisional Quenching Corrections for Laser-Induced Fluorescence Measurements of NO $A^2\Sigma^+$*," AIAA Journal, 32(8), August 1994.

[57] Liebeskind, J.G., Hanson, R.K., and Cappelli, M.A., "*Laser-induced fluorescence diagnostic for temperature and velocity measurements in a hydrogen arcjet plume*," Applied Optics, 32(30), pp. 6117-6127, October 20, 1993.

[58] Inman, J.A., Bathel, B.F., Johansen, C.T., Danehy, P.M., Jones, S.B., Gragg, J.G., and Splinter, S.C., "*Nitric Oxide PLIF Measurements in the Hypersonic Materials Environmental Test System (HYMETS)*," 49th AIAA Aerospace Sciences Meeting, AIAA Paper 2011-1090, Orlando, FL, January 4-7, 2011.

[59] Storm, P.V., and Cappelli, M.A., "*LIF Characterization of Arcjet Nozzle Flows*," AIAA, ASME, SAE, and ASEE, Joint Propulsion Conference, AIAA Paper 1996-2987, Lake Buena Vista, FL, July 1 – 3, 1996.

[60] Marinelli, W.J., Kessler, W.J., Allen, M.G., Davis, S.J., Arepalli, S., and Scott, C.D., "*Copper atom based measurements of velocity and turbulence in arc jet flows*," 29th Aerospace Sciences Meeting, AIAA 1991-358, Reno, NV., January 7-10, 1991.

[61] McDaniel, J.C., Hiller, B., and Hanson, R.K., "*Simultaneous multiple-point velocity measurements using laser-induced iodine fluorescence*," Optics Letters, 8(1), pp. 51-53, January 1983.

[62] Chang, A.Y., Battles, B.E., and Hanson, R.K., "*Simultaneous measurements of velocity, temperature, and pressure using rapid cw wavelength-modulation laser-induced fluorescence of OH*," Optics Letters, 15(12), June 15, 1990.

[63] Klavuhn, K.G., Gauba, G., and McDaniel, J.C., "*OH Laser-Induced Fluorescence Velocimetry Technique for Steady, High-Speed, Reacting Flows*," Journal of Propulsion and Power, 10(6), 1994.

[64] Kulatilaka, W.D., Naik, S.V., and Lucht, R.P., "*Development of High-Spectral-Resolution Planar Laser-Induced Fluorescence Imaging Diagnostics for High-Speed Gas Flows*," AIAA Journal, 46(1), January 2008.

[65] Naik, S.V., Kulatilaka, W.D., Venkatesan, K.K., and Lucht, R.P., "*Pressure, Temperature, and Velocity Measurements in Underexpanded Jets Using Laser-Induced Fluorescence Imaging*," AIAA Journal, 47(4), April 2009.

[66] Danehy, P.M., Mere, P., Gaston, M.J., O'Bryne, S., Palma, P. C., and Houwing, A.F.P., "*Fluorescence velocimetry of the hypersonic, separated flow over a cone*," AIAA Journal, 39(7), pp. 1320-1328, 2001.

[67] Hruschka, R., O'Byrne, S., and Kleine, H., "*Two-component Doppler-shift fluorescence velocimetry applied to a generic planetary entry probe model*," Experiments in Fluids, 48, pp. 1109-1120, 2010.

[68] Fletcher, D.G., and McDaniel, J.C., "*Laser-Induced Iodine Fluorescence Technique for Quantitative Measurement in a Nonreacting Supersonic Combustor*," AIAA Journal, 27(5), May 1989.

[69] Hartfield, R.J., Hollo, S.D., and McDaniel, J.C., "*Planar Measurement Technique for Compressible Flows Using Laser-Induced Iodine Fluorescence*," AIAA Journal, 31(3), March 1993.

[70] Donohue, J.M., and McDaniel, J.C., "*Computer-Controlled Multiparameter Flowfield Measurements Using Planar Laser-Induced Iodine Fluorescence*," AIAA Journal, 34(8), August 1996.

[71] Zimmerman, M., and Miles, R.B., "*Hypersonic-helium-flow-field measurements with the resonant Doppler velocimeter*," Applied Physics Letters, 37(10), November 15, 1980.

[72] Bathel, B.F., Johansen, C., Inman, J.A., Jones, S.B., and Danehy, P.M., "*Review of Fluorescence-Based Velocimetry Techniques to Study High-Speed Compressible Flows*," AIAA 2013-0339, 51st AIAA Aerospace Sciences Meeting, Grapevine, TX, January 7-10, 2013.

[73] Hiller, B., and Hanson, R.K., "*Two-frequency laser-induced fluorescence technique for rapid velocity-field measurements in gas flows*," Optics Letters, 10(5), May, 1985.

[74] Hiller, B., and Hanson, R.K., "*Simultaneous planar measurements of velocity and pressure fields in gas flows using laser-induced fluorescence*," Applied Optics, 27(1), January 1, 1988.

[75] Westblom, U., and Aldėn, M., "*Spatially resolved flow velocity measurements using laser-induced fluorescence from a pulsed laser*," Optics Letters, 14(1), January 1, 1989.

[76] Paul, P.H., Lee, M.P., and Hanson, R.K., "*Molecular velocity imaging of supersonic flows using pulsed planar laser-induced fluorescence of NO*," Optics Letters, 14(9), May 1, 1989.

[77] Allen, M., Davis, S., Kessler, W., Legner, H., McManus, K., Mulhall, P., Parker, T., and Sonnenfroh, D., "*Velocity Field Imaging in Supersonic Reacting Flows near Atmospheric Pressure*," AIAA Journal, 32(8), August 1994.

[78] Koochesfahani, M.M., and Nocera, D.G., *"Molecular Tagging Velocimetry*," *Handbook of Experimental Fluid Dynamics*, Chap. 5.4, edited by J. Foss, C. Tropea, and A. Yarin, Springer-Verlag, Berlin, 2007.

[79] Hiller, B., Booman, R.A., Hassa, C., and Hanson, R.K., "*Velocity Visualization in Gas Flows Using Laser-Induced Phosphorescence of Biacetyle*," Review of Scientific Instruments, 55(12), pp. 1964-1967, December, 1984.

[80] Danehy, P.M., O'Byrne, S., Houwing, A.F.P., Fox, J.S., and Smith, D.R., "*Flow-Tagging Velocimetry for Hypersonic Flows Using Fluorescence of Nitric Oxide*," AIAA Journal, 41(2), February 2003.

[81] Lempert, W.R., Jiang, N., Sethuram, S., and Samimy, M., "*Molecular Tagging Velocimetry Measurements in Supersonic Microjets*," AIAA Journal, 40(6), June, 2002.

[82] Lempert, W.R., Boehm, M., Jiang, N., Gimelshein, S., and Levin, D., "*Comparison of molecular tagging velocimetry data and direct simulation Monte Carlo simulations in supersonic micro jet flows*," Experiments in Fluids, 34, pp. 403-411, 2003.

[83] Hsu, A.G., Srinivasan, R., Bowersox, R.D.W., and North, S.W., "*Two-component molecular tagging velocimetry utilizing NO fluorescence lifetime and NO_2 photodissociation techniques in an underexpanded jet flowfield*," Applied Optics, 48(22), August 1, 2009.

[84] Inman, J.A., Danehy, P.M., Bathel, B.F., Alderfer, D.W., and Nowak, R.J., "*Laser-Induced Fluorescence Velocity Measurements in Supersonic Underexpanded Impinging Jets*," 48th AIAA Aerospace Sciences Meeting, AIAA 2010-1438, Orlando, FL., January 4-7, 2010.

[85] Johansen, C.T., Danehy, P.M., Ashcraft, S.W., Bathel, B.F., Inman, J.A., and Jones, S.B., "*PLIF study of Mars Science Laboratory capsule reaction control system jets*," 41st AIAA Fluid Dynamics Conference, AIAA Paper 2011-3890, Honolulu, HI., June 27-30, 2011.

[86] Johansen, C.T., Novak, J., Bathel, B., Ashcraft, S.W., and Danehy, P.M., "*Comparison of MSL RCS jet computations with flow visualization and velocimetry*," 50th AIAA Aerospace Sciences Meeting, AIAA Paper 2012-0594, Nashville, TN., January 4-7, 2012.

[87] Balla, R.J., "*Iodine Tagging Velocimetry in a Mach 10 Wake*", AIAA Journal, 51(7), pp. 1783 – 1785, July, 2013.

[88] Houwing, A.F.P., Smith, D.R., Fox, J.S., Danehy, P.M., and Mudford, N.R., "*Laminar boundary layer separation at a fin-body junction in a hypersonic flow*," Shock Waves, 11, pp. 31-42, 2001.

[89] Michael, J.B., Edwards, M.R., Dogariu, A., and Miles, R.B., "*Femtosecond laser electronic excitation tagging for quantitative velocity imaging in air*," Applied Optics, 50(26), pp. 5158-5162, September 10, 2011.

[90] Michael, J.B., Edwards, M.R., Dogariu, A., and Miles, R.B., "*Velocimetry by femtosecond laser electronic excitation tagging (FLEET) of air and nitrogen*," 50th AIAA Aerospace Sciences Meeting, AIAA 2012-1053, Nashville, TN., January 9-12, 2012.

[91] Edwards, M.R., Dogariu, A., and Miles, R.B., "*Simultaneous Temperature and Velocity Measurement in Unseeded Air Flows with FLEET*," 51st AIAA Aerospace Sciences Meeting, AIAA 2013-0043, Grapevine, TX., January 7-10, 2013.

[92] Barker, P., Bishop, A., and Rubinsztein-Dunlop, H., "*Supersonic velocimetry in a shock tube using laser enhanced ionization and planar laser induced fluorescence*," Appl. Phys. B, 64 (3), pp. 369-376, 1997.

[93] Barker, P.F., Thomas, A.M., McIntyre, T.J., and Dunlop-Rubinsztein, H., "*Velocimetry and Thermometry of Supersonic Flow Around a Cylindrical Body*," AIAA Journal, 36 (6), pp. 1055-1060, June 1998.

[94] Littleton, B.N., Bishop, A.I., McIntyre, T.J., Barker, P.F., and Dunlop-Rubinsztein, H., "*Flow tagging velocimetry in a superorbital expansion tube*," Shock Waves, 10, pp. 225-228, 2000.

[95] Miles, R., Cohen, C., Connors, J., Howard, P., Huang, S., Markovitz, E., and Russell, G., "*Velocity measurements by vibrational tagging and fluorescent probing of oxygen*," Optics Letters, 12 (11), pp. 861-863, November, 1987.

[96] Miles, R.B., Zhou, D., Zhang, B., Lempert, W.R., and She, Z-S., "*Fundamental Turbulence Measurements by Relief Flow Tagging*," AIAA Journal, 31(3), March, 1993.

[97] Miles, R.B., Conners, J., Markovitz, E., Howard, P., and Roth, G., "*Instantaneous supersonic velocity profiles in an underexpanded sonic air jet by oxygen flow tagging*," Physics of Fluids A, 1(2), pp. 389-393, February, 1989.

[98] Miles, R.B., Grinstead, J., Kohl, R.H., and Diskin, G., "*The RELIEF flow tagging technique and its application in engine testing facilities and for helium-air mixing studies*," Measurement Science and Technology, 11(9), pp. 1272-1281, September, 2000.

[99] Boedeker, L.R., "*Velocity measurement by H2O photolysis and laser-induced fluorescence of OH*," Optics Letters, 14 (10), pp. 473-475, May 15, 1989.

[100] Wehrmeyer, J.A., Ribarov, L.A., Oguss, D.A., Batliwala, F., Pitz, R.W., and DeBarber, P.A., "*Flow tagging velocimetry for low and high temperature flowfields*," *37th AIAA Aerospace Sciences Meeting*, Reno, NV, 1999.

[101] Wehrmeyer, J.A., Ribarov, L.A., Oguss, D.A., and Pitz, R.W., "*Flame flow tagging velocimetry with 193-nm H2O photodissociation*," Applied Optics, 38 (33), pp. 6912-6917, November, 20, 1999.

[102] Ribarov, L.A., Wehrmeyer, J.A., Hu, S., and Pitz, R.W., "*Multiline hydroxyl tagging velocimetry measurements in reacting and nonreacting experimental flows*," Experiments in Fluids, 37, pp. 65-74, 2004.

[103] Ribarov, L.A., Hu, S., Wehrmeyer, J.A., and Pitz, R.W., "*Hydroxyl tagging velocimetry method optimization: signal intensity and spectroscopy*," Applied Optics, 44 (31), pp. 6616-6626, November, 1, 2005.

[104] Pitz, R.W., Lahr, M.D., Douglas, Z.W., Wehrmeyer, J.A., Hu, S., Carter, C.D., Hsu, K-Y., Lum, C., and Koochesfahani, M.M., "*Hydroxyl tagging velocimetry in a supersonic flow over a cavity*," Applied Optics, 44(31), pp. 6692-6700, November 1, 2005.

[105] Lahr, M.D., Pitz, R.W., Douglas, Z.W., and Carter, C.D., "*Hydroxyl-Tagging-Velocimetry Measurements of a Supersonic Flow over a Cavity*," Journal of Propulsion and Power, 26 (4), pp. 790-797, July – August 2010.

[106] ElBaz, A.M., and Pitz, R.W., "*N_2O molecular tagging velocimetry*," Applied Physics B, 106, pp. 961-969, 2012.

[107] Pitz, R.W., Brown, T.M., Nandula, S.P., Skaggs, P.A., DeBarber, P.A., Brown, M.S., and Segall, J., "*Unseeded velocity measurement by ozone tagging velocimetry*," Optics Letters, 21 (10), pp. 755-757, 1996.

[108] Ribarov, L.A., Wehrmeyer, J.A., Batliwala, F., Pitz, R.W., DeBarber, P.A., "*Ozone Tagging Velocimetry Using Narrowband Excimer Lasers*," AIAA Journal, 37(6), June 1999.

[109] Dam, N.J., Klein-Douwel, R.J.H., Sijtsema, N.M., and ter Meulen, J.J., "*Nitric oxide flow tagging in unseeded air*," Optics Letters, 26 (1), pp. 36-38, January 1, 2001.

[110] Sijtsema, N.M., Dam, N.J., Klein-Douwel, R.J.H., and ter Meulen, J.J., "*Air Photolysis and Recombination Tracking: A New Molecular Tagging Velocimetry Scheme*," AIAA Journal, 40 (6), pp. 1061-1064, June 2002.

[111] Van der Lann, W.P.N., Tolboom, R.A.L., Dam, N.J., and ter Meulen, J.J., "*Molecular tagging velocimetry in the wake of an object in supersonic flow*," Experiments in Fluids, 34, pp. 531-534, 2003.

[112] Bominaar, J., Pashtrapanska, M., Elenbaas, T., Dam, N., ter Meulen, H., and van de Water, W., "*Writing in turbulent air*," Physical Review E, 77, 2008.

[113] Orlemann, C., Schulz, C., and Wolfrum, J., "*NO-flow tagging by photodissociation of NO_2. A new approach for measuring small-scale flow structures*," Chem. Phys. Lett., 307, pp. 15-20, 1999.

[114] Shinji, N., Kasahara, M., Tsue, M., and Kono, M., "*Velocity Measurements of Reactive and Non-reactive Flows by NO-LIF Method Using NO_2 Photodissociation*," Heat Transfer – Asian Research, 34 (1), pp. 40-52, 2005.

[115] Hsu, A.G., Srinivasan, R., Bowersox, R.D.W., and North, S.W., "*Molecular Tagging Using Vibrationally Excited Nitric Oxide in an Underexpanded Jet Flowfield*," AIAA Journal, 47 (11), pp. 2597-2604, November, 2009.

[116] Jiang, N., Nishihara, M., and Lempert, W.R., "*500 kHz NO_2 Molecular Tagging Velocimetry in a Mach 5 Wind Tunnel*," 27th AIAA Aerodynamic Measurement Technology and Ground Testing Conference, AIAA 2010-4348, Chicago, IL., Jun 28-July 1, 2010.

[117] Sánchez-González, R., Srinivasan, R., Bowersox, R.D.W., and North, S.W., "*Simultaneous velocity and temperature measurements in gaseous flow fields using the VENOM technique*," Optics Letters, 36(2), pp. 196-198, January 15, 2011.

[118] Sánchez-González, R., Srinivasan, R., Bowersox, R.D.W., and North, S.W., "*Simultaneous velocity and temperature measurements in gaseous flowfields using the vibrationally excited nitric oxide monitoring technique: a comprehensive study*," Applied Optics, 51(9), pp. 1216-1228, March 20, 2012.

[119] Boxx, I., Stöhr, M., Carter, C., and Meier, W., "*Sustained multi-kHz flamefront and 3-component velocity-field measurements for the study of turbulent flames*, Applied Physics B, 95(1), pp. 23-29, April, 2009.

[120] Jiang, N., Webster, M., Lempert, W.R., Miller, J.D., Meyer, T.R., Ivey, C.B., and Danehy, P.M., "*MHz-rate nitric oxide planar laser-induced fluorescence imaging in a Mach 10 hypersonic wind tunnel*," Applied Optics, 50(4), February 1, 2011.

[121] Jiang, N., Bruzzese, J., Patton, R., Sutton, J., Yentsch, R., Gaitonde, D.V., Lempert, W.R., Miller, K.D., Meyer, T.R., Parker, R., Wadham, T., Holden, M., and Danehy, P.M., "*NO PLIF imaging in the CUBRC 48-inch shock tunnel*," Experiments in Fluids, 53, pp. 1637-1646, 2012.

[122] Yip, B., Schmitt, R.L., and Long, M.B., "*Instantaneous three-dimensional concentration measurements in turbulent jets and flames*," Optics Letters, 13(2), pp. 96-98, February, 1988.

[123] Danehy, P.M., Bathel, B.F., Inman, J.A., Alderfer, D.W., and Jones, S.B., "*Stereoscopic Imaging in Hypersonic Boundary Layers using Planar Laser-Induced Fluorescence*," 26th AIAA Aerodynamic Measurement Technology and Ground Testing Conference, AIAA 2008-4267, Seattle, WA., June 23-26, 2008.

[124] Combs, C.S., Clemens, N.T., Danehy, P.M., Bathel, B.F., Parker, R., Wadhams, T., Holden, M., and Kirk, B., "*NO PLIF Visualizations of the Orion Capsule in LENS-I*," 51st AIAA Aerospace Sciences Meeting, AIAA 2013-0033, Grapevine, TX., January 7-10, 2013.

[125] Estruch, D., Lawson, N.J., and Garry, K.P., "*Application of Optical Measurement Techniques to Supersonic and Hypersonic Aerospace Flows*," Journal of Aerospace Engineering, 22(4), pp. 383 – 395, October, 2009.

[126] Johansen, C.T., Danehy, P.M., "*Numerical investigation of PLIF gas seeding for hypersonic boundary layer flows*," 50th AIAA Aerospace Sciences Meeting, AIAA 2012-1057, January 9-12, 2012, Nashville, TN.

[127] Danehy, P.M., Bathel, B., Ivey, C., Inman, J.A., and Jones, S.B., "*NO PLIF study of hypersonic transition over a discrete hemispherical roughness element*," 47th AIAA Aerospace Sciences Meeting, AIAA 2009-394, January 5-8, 2009, Orlando, FL.

[128] Luque, J., and Crowley, D.R., "*LIFBASE: Database and Spectral Simulation Program (Version 1.5)*," SRI International Report MP 99-009, 1999.

[129] Settersten, T.B., Patterson, B.D., and Carter, C.D., "*Collisional quenching of NO $A^2\Sigma^+(v' = 0)$ between 125 and 294 K*," The Journal of Chemical Physics, 130(20), May 28, 2009.

[130] Devenport, W.J., *Compressible Aerodynamics Calculator 2.0*, http://www.dept.aoe.vt.edu/~devenpor/aoe3114/calc.html [last accessed May 18, 2013].

[131] Harrison, J.A., Yang, X., Rösslein, M., Felder, P., and Huber, J.R., "*Photodissociation of NO_2 at 355 and 351 nm Investigated by Photofragment Translational Spectroscopy*," The Journal of Physical Chemistry, 98(47), pp. 12260-12269, November, 1994.

[132] Chang, R., *Chemistry, Seventh Edition*, McGraw-Hill, New York, 2002.

[133] Olbregts, J., "*Termolecular Reaction of Nitrogen Monoxide and Oxygen: A Still Unsolved Problem*," International Journal of Chemical Kinetics, 17(8), pp. 835 – 848, 1985.

[134] Arisman, C.J., Johansen, C.T., Galuppo, W.C., and McPhail, A., "*Nitric Oxide Chemistry Effects in Hypersonic Boundary Layers*," 43rd AIAA Fluid Dynamics Conference, AIAA Paper 2013-3104, June 24 – 27, 2013, San Diego, CA.

Chapter 3: Experimental Setup

This chapter provides details of the wind tunnel test facility, laser and camera systems, wind tunnel model, and test conditions used in this dissertation.

3.1 Wind Tunnel Facility

The experiments described in this dissertation were performed in the 31-inch Mach 10 Air blowdown wind tunnel facility at NASA Langley Research Center. Figure 3.1 shows a virtual rendering of this facility. The facility is described in Ref. 1 and a brief description is provided here. Air for the facility is supplied from a centralized bottle field to a pressurized chamber containing a 12.5 MW electrical resistance heater. For the experiments to be described in this paper, the nominal stagnation pressures inside the chamber ranged from 2.41 MPa to 9.31 MPa (350 psia to 1350 psia) and stagnation temperature remained fixed at 1000 K (1800 °R). The air passes through a settling chamber and filter prior to passing through a converging-diverging contoured nozzle with a 2.72 cm (1.07 inch) square throat. The flow is accelerated to a nominal Mach number of 10 as it expands through the nozzle into a 31-inch square test section. The stated pressure fluctuations within the inviscid core flow are ±1.0%.[1] Three large UV-transmitting windows are mounted flush to the top, side, and bottom interior walls of the test section. These windows are capable of transmitting light down to a wavelength of 190 nm. The fourth sidewall contains a sliding door that separates the wind tunnel test section from the housing for the model injection system (called the *model housing box*). Once the Mach 10 flow is established within the test section, this door is opened, and the

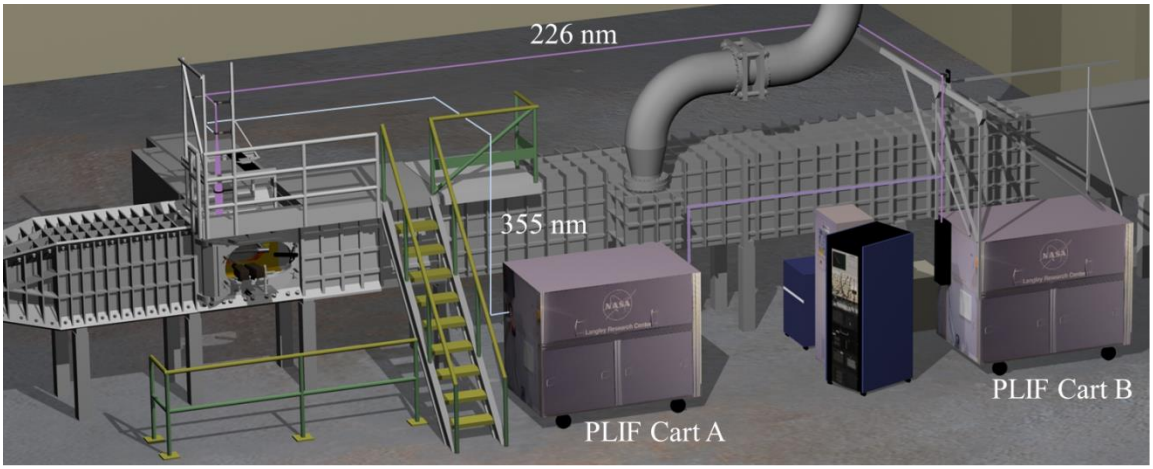

Figure 3.1: Rendering of 31-Inch Mach 10 Air blowdown wind tunnel facility at NASA Langley Research Center. Rendering courtesy of Andrew McCrea and Rich Schwartz, AMA, Inc.

wind tunnel model is injected into the flow via a hydraulic injection system. The sting used to support the wind tunnel model is mounted to an aerodynamic strut, which is capable of providing automated angle-of-attack control and manually adjusted yaw control.

3.2 Laser and Imaging Systems

3.2.1 Single-Laser NO MTV Experiments

Portions of this description have been taken or adapted from text presented in Refs. 2-5. A pulsed Spectra Physics Pro-230 Nd:YAG laser was used to generate 1064 nm light. This 1064 nm output was then frequency doubled to produce 532 nm, which subsequently pumped a Sirah Cobra Stretch dye laser to achieve a 622 nm output beam. This output was sum frequency mixed with 355 nm light from the Nd:YAG, obtained by frequency tripling the fundamental 1064 nm output, in a Sirah Frequency Conversion Unit (FCU) to produce a 226 nm beam. This 226 nm beam had a spectral width of approximately 0.07 cm^{-1}. The duration of the pulse at 226 nm was approximately 10 ns at a 10 Hz repetition rate. This 226 nm beam, which was produced by PLIF Cart B shown in Fig. 3.1, was directed above the wind tunnel test section following the delay path shown in Fig. 3.1. Once above the wind tunnel test section, the 226 nm beam was then passed through a series of sheet-forming optics mounted above the tunnel test section.

To form a laser sheet, the collimated 226 nm beam passed through a 36 mm focal length cylindrical lens, which focused and then diverged the beam along one axis while leaving it collimated in the other. A 1 m focal length spherical lens then collimated the diverging axis of the beam and focused the other axis into a thin sheet approximately 75-mm-wide × 0.5-mm-thick. To tag multiple lines of NO in the test section for the velocimetry measurement, a 50-mm-long, LaserOptik GmbH diffusion-welded lens array of 25, 1 m focal length cylindrical lenses focused the laser sheet into 25 lines. The lens array had an anti-reflection coating.

To image the MTV profiles, a Cooke DiCAM-PRO camera, utilizing an intensified 1280×1024 (horizontal width × vertical height) pixel array interline progressive scan CCD, was used. A smaller vertical pixel region was used to image the flow so that an image read-out rate of 10 Hz, corresponding to the laser repetition rate, could be achieved. The camera was fitted with a 100 mm focal length, F/2.0 Bernhard Halle

Nachfolger GmbH lens. A spectral filter was placed in front of this lens (Layertec GmbH: <1% transmission at 226 nm; >80% from 235 nm – 280 nm) to block any scattered laser light. When used in double shutter mode, the camera is capable of acquiring an image pair with a minimum Δt_{D2} = 500 ns delay between the end of the first exposure and the beginning of the second. Each exposure has a minimum duration of 20 ns, with delay settings and durations set in increments of 20 ns. The delay between camera trigger signal the opening of the first exposure, Δt_{D1}, is variable, although the camera hardware requires an internal 185 ns delay followed by a variable user delay prior to the opening of the first exposure.

Once the NO gas in the boundary layer is excited by the laser pulse the fluorescence intensity decays exponentially in time. The rate of this decay depends upon the local pressure, temperature, and gas composition influencing the tagged molecules as described in Chapter 2. Unfortunately, the camera used in these experiments did not allow for independent gain settings for the first and second exposures so that comparable signals could be obtained in the respective exposures. To ensure a measurable signal during the second exposure, it was necessary to use the minimum exposure delay setting of Δt_{D2} = 500 ns and keep the second exposure open long enough to collect an adequate number of photons. Additionally, to maintain comparable signal intensities in both the first and second CCD exposures, the signal in the first exposure had to be attenuated. This was partly achieved by using the shortest exposure possible (Δt_{E1} = 20 ns). Additionally, the timing of the first exposure was such that it opened prior to the laser pulse and then collected fluorescence only during the first several nanoseconds of the laser pulse. This overlap of the first exposure and laser pulse is achieved by simultaneously triggering the camera and laser with a LabSmith LC880. The camera software then allowed coarse adjustment of the relative timing of the laser and first camera exposure, in 20 ns increments. Fine adjustments on the order of 1 ns were then made by adding varying lengths of coaxial cable between the LC880 and the camera trigger input, resulting in a total delay between the

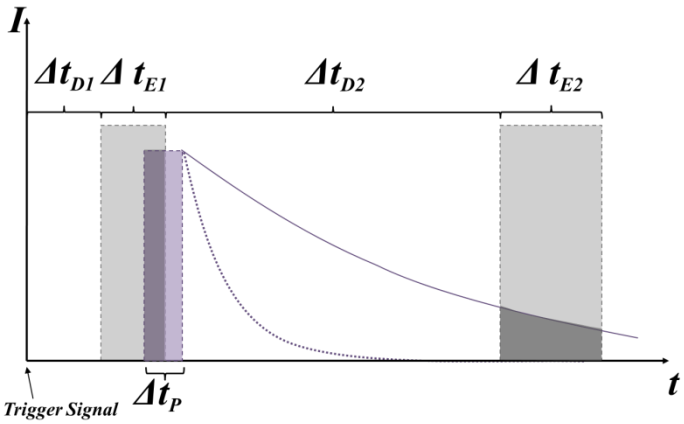

Figure 3.2: Camera and laser timing sequence for single-laser, NO MTV technique. Adapted from Ref. 5.

initial trigger signal from the LC880 and the first exposure of Δt_{D1}. The resulting overlap of the first camera exposure and the laser pulse is referred to as the *effective first exposure*, having a duration of Δt_{eE1}. During experimentation, care was taken to avoid saturation of the CCD.

Figure 3.2 shows a generalized timing sequence adopted for these experiments and represents an idealization of the excitation, decay, and image acquisition process. The vertical axis represents signal intensity. The solid violet line shows the exponential decay behavior of fluorescence with time for low-to-moderate quenching environments. The dotted violet line shows the exponential decay behavior of fluorescence with time for relatively high quenching environments. The darkly shaded regions represent the signal intensity captured during the effective first exposure and second exposure. The lightly shaded regions are indicative of the first and second exposure durations, Δt_{E1} and Δt_{E2}, respectively, while the violet region with the dashed violet border indicates the laser pulse duration, Δt_p.

3.2.2 Three-Laser NO_2-to-NO Photolysis MTV Experiments

Portions of this description have been taken or adapted from text presented in Refs. 5-8. For the NO_2-to-NO photolysis MTV experiments, two different laser systems were used. The first laser system, shown as PLIF Cart A in Fig. 3.1, used a Spectra Physics Pro-250 Nd:YAG laser to pump a Sirah Cobra Stretch dye at 532 nm. The 622 nm laser light from the dye laser was then sum frequency mixed with a portion of the 355 nm from the Nd:YAG in the Sirah FCU unit to produce a 226 nm beam. This beam is referred to hereafter as the first probe beam and had a spectral width of approximately 0.07 cm^{-1}. The remaining portion of the 355 nm beam, referred to hereafter as the pump beam, was diverted by a pick-off window to the wind tunnel test section. The second laser system was the same as that used in the single-laser NO MTV experiments (PLIF Cart B, Fig. 3.1). A LabSmith LC880 was used to generate a variable-delay between the output of the PLIF Cart A and output of PLIF Cart B. The 226 nm beam from PLIF Cart B, referred to hereafter as the second probe beam, had an energy similar to the first probe beam. The duration of each probe beam pulse at 226 nm was approximately 10 ns. The repetition rate of each laser system was 10 Hz.

Both the first and second probe beams were aligned near the output of PLIF Cart B to be collinear. These beams then followed the same delay path as that used in the single-laser NO MTV experiment to a point above test section. These beams were then directed to the sheet-forming optics and were aligned to be

both adjacent and parallel to the pump beam prior to passing through the sheet-forming optics. The 355 nm pump beam followed a shorter delay path than that used for the probe beams, which is shown in Fig. 3.1. The pump beam delay path was such that the time interval, Δt_{PUMP}, between the arrival of the pump beam and arrival of the subsequent first probe beam was approximately 35 ns. Figure 3.3 presents timing schematics showing the relative positions and intensities of the pump and probe beams used for the experiments described in Chapters 6 and 7 of this dissertation. In Fig. 3.3a, the two camera exposures with exposure durations of Δt_{E1} and Δt_{E2} were initially timed such that they completely enveloped the first and second probe beams, respectively. This was initially done to maximize the signal in both of the exposures; there was no longer the problem of having unequal intensities between the exposures resulting from fluorescence decay, as was a problem with the single-laser NO MTV technique. Unfortunately, scatter from the pump and probe beams off the bottom metallic surface of the wind tunnel model, observed on and through a quartz window insert (described in the 3.3.2), diminished the signal-to-noise ratio in both exposures.

Initially, two filters were used to block this scatter, one for the 355 nm light (Semrock HG01 254 nm filter: <1% transmission below 236 nm and above 263 nm; >65% from 244 nm – 256 nm) and one for the 226 nm light (Layertec GmbH: <1% transmission at 226 nm; >80% from 235 nm – 280 nm). However, it was determined that the 355 nm filter blocked approximately 75% of the NO fluorescence, thus drastically reducing signal levels. Therefore, a second approach was adopted using only the 226 nm filter. It consisted of delaying both camera exposures by approximately $\Delta t_{PROBE_{Delay}}$= 28 ns after the start of the respective probe laser pulses. This delay setting corresponded to a combined delay of approximately Δt_{PUMP} + $\Delta t_{PROBE_{Delay}}$ = 35 ns + 28 ns = 63 ns beyond the start of the pump laser so that the camera's intensifier (closed during the pump pulse) would block the pump pulse. This timing methodology is shown in Fig. 3.3b. While the collisional quenching at the conditions of interest resulted in a relatively short NO fluorescence lifetime, the amount of fluorescence signal collected was still adequate such that sufficient signal-to-noise levels were achieved throughout the remaining experiments. An additional benefit of using the timing arrangement in Fig. 3.3b was that the measurement was less sensitive to timing jitter associated with the laser (though sensitivity to timing jitter associated with the camera exposures was retained).

In order to generate multiple lines of NO via photo-dissociation of NO_2, the pump beam was first passed through a 300 mm cylindrical lens and then collimated by a 1 m spherical lens to form a 355 nm light sheet. The spherical focusing lens was approximately 1 m from the wind tunnel test model. The 355 nm light sheet was then passed through a portion of the same 50-mm-long, LaserOptik diffusion-welded lens array used for the single-laser NO MTV experiments. Only a portion of this lens array (15 cylindrical lens elements) was filled in order to ensure that the photo-dissociation of NO_2 (and subsequent generation of NO) along 15 spatial lines. The lens array focused the light sheet into 15 lines aligned in the streamwise direction. The lines in the initial set of experiments formed a nominal 75° angle of incidence with respect to the model surface. The angle of incidence was then modified to be between approximately 90° with respect to the model surface. This modification coincided with the timing change described above.

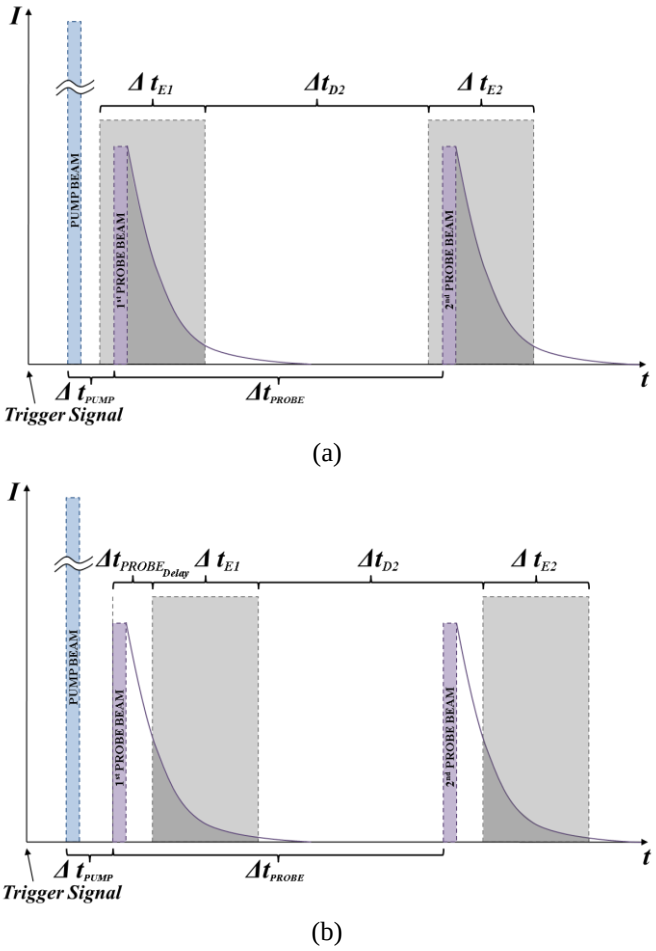

Figure 3.3: Timing schematic for three-laser NO_2-to-NO photolysis MTV experiments using (a) overlapping exposures with the probe beams and (b) using delayed exposures. Adapted from Ref. 5.

To excite the NO generated by the pump beam, the probe beams were passed through a 150 mm cylindrical lens and collimated with the same 1 m spherical lens used to collimate the 355 nm light from the pump beam. The 226 nm laser sheets were offset a few mm from the 355 nm laser sheet so that the 226 nm laser sheets did not pass through the lens array. The 355 nm sheet was also rotated slightly (a few degrees) with respect to the 226 nm sheets to ensure that the beams would be in alignment even if vibrations caused the sheets to move relative to each other during the run.

3.3 Wind Tunnel Model

A 10° half-angle wedge model with a sharp leading edge was used in this experiment. The leading edge radius is less than 0.024±0.005 mm. The upper surface of the wedge model, over which the MTV measurements and PLIF flow visualizations were made, was a stainless steel flat surface that was 127.0 mm (5 inches) wide and 162.5 mm (6.4 inches) long. The top surface was painted with a flat black high temperature paint to minimize laser scatter. In experiments with an isolated roughness element, the element was positioned along the streamwise symmetry plane and centered at 75.4 mm downstream of the leading edge. The isolated roughness element consisted of a 4 mm diameter stainless steel cylinder. Three different cylinder heights were used in the experiments: k = 0.5 mm, k = 1.0 mm, and k = 2.0 mm. The tracer gas (either NO or NO_2) was seeded into the hypersonic laminar boundary layer from an 11-mm-wide, 0.81-mm-long slot centered on the streamwise symmetry plane and 29.4 mm downstream of the leading edge. The surface pressure was monitored by a Druck pressure gauge, model PDCR 4060, 0.04% accuracy to 34.5 kPa (5 psia). A thermocouple was attached to the underside of the model's 1/5-inch-thick stainless steel surface with Kapton® tape to measure the plate temperature. The placement of the thermocouple provided only an estimate of the true plate temperature. The temperature measurement did not account for heat transfer effects occurring through the thickness of the plate.

3.3.1 Model Configuration for Single-Laser NO MTV Experiments

A representation of the wedge model used in the single-laser NO MTV experiments described in Chapters 4 and 5 is shown in Fig. 3.4. The seeded gas was 100% NO supplied at approximately 150 SCCM, 300 SCCM, or 350 SCCM (standard cubic centimeters per minute) depending on the experiment. This corresponds to mass flow rates of 3.04 mg/s, 6.09 mg/s, and 7.11 mg/s, respectively. The mass flowrate supplied through this slot was assumed to have a negligible impact on the boundary layer flow. This assumption is based in part upon surface heat transfer measurements performed by Berry et al. in Ref. 9 using a similar gas supply configuration. Analysis of those heat transfer measurements and the degree of boundary layer perturbation associated with different gas-injection flow rates for the present wedge model are discussed by Danehy et al. in Ref. 10. A computational study has also been conducted at

the 3 mg/s flowrate for NO and showed that relatively small deviations occur in the streamwise velocity and thermal boundary layers when compared to a case with no gas injection.[11]

Two different model orientations were used to obtain the single-laser NO MTV images. In both cases, the camera was perpendicular to the plane containing the laser lines. The model was first oriented such that axial velocity measurements were performed along a series of lines perpendicular to the top surface and aligned with the centerline. This view is hereafter referred to as the *side-view* orientation and is shown in Fig. 3.4a. The second orientation was with the laser lines running parallel to the model surface in the spanwise direction. This view is hereafter referred to as the *plan-view* orientation and is shown in Fig. 3.4b. For the side-view and plan-view orientations, the top surface of the model formed an angle of 5° relative to the freestream flow direction. This angle is herein referred to as the *plate angle*. The MTV profiles formed for the side-view and plan-view model orientations had widths of approximately 1.45±0.19 mm and 0.82±0.11 mm at FWHM, respectively. The approximate separation distance between each line in was 3.28±0.24 mm and 2.16±0.10 mm, respectively.

3.3.2 Model Configuration for Three-Laser NO_2-to-NO MTV Experiments

For all three-laser NO_2-to-NO photolysis MTV experiments, the model was oriented with a 20° plate angle and imaging was performed exclusively with a side-view orientation. For the initial three-laser NO_2-to-NO photolysis MTV experiments, a 50.8 mm outer diameter, 6.4 mm thick quartz window centered

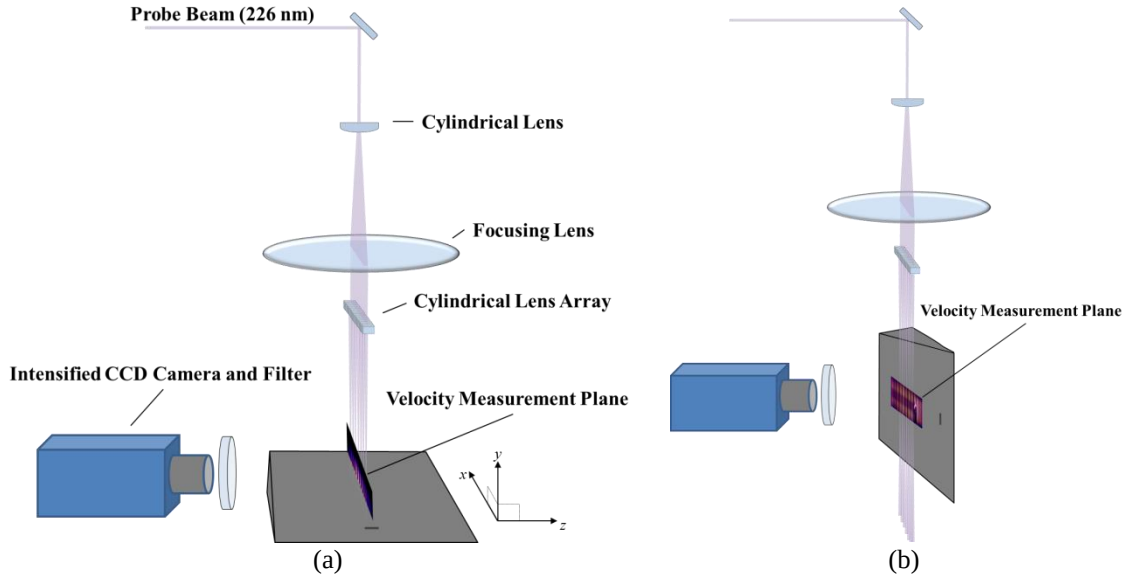

Figure 3.4: Schematic of model *side-view* (a) and *plan-view* (b) orientations for single laser NO MTV experiments. The *plate angle* for the single-laser NO MTV experiments was 5° for both orientations. Adapted from Ref. 2.

114.3 mm downstream of the leading edge and about the spanwise axis of symmetry was mounted flush to the model surface. The window had a 2.8 mm chamfer, resulting in a 46.8 mm inner diameter portion of the window that was exposed at the surface. Figure 3.5a shows an image of the model with the mounted window. Figure 3.5b shows a schematic of the model in the side-view orientation and the alignment of the pump and probe beams and optics. The use of the UV-transparent window prevented damage to the model's otherwise black painted surface and helped to reduce the laser scatter generated by the focused 355 nm pump beam.

After completing the initial series of experiments with this model, scatter from the pump and probe beams off the bottom metallic surface within the model was still observed on and through the quartz window insert. This scatter limited the signal-to-noise ratio in the raw images. To reduce this scatter a second window was installed on the bottom surface of the model. This modification was in addition to the timing, spectral filter, and laser line angle-of-incidence modifications described in section 3.2.2. The leading edge of this window was positioned 95.4 mm downstream of the leading edge of the model. The location of this window on the lower surface of the model allowed nearly all of the laser light from both the pump and probe beams to pass completely through the model so that laser scatter off of internal model surfaces was minimized. This in turn contributed to lowering the noise levels imaged over the measurement surface. However, a small portion of the incident light was still observed in the experimental images reflecting off the lower surface window and being redirected through the window on the measurement surface.

The 100% NO_2 gas was seeded into the boundary layer from the same 11-mm-long, 0.81-mm-wide spanwise seeding slot insert used in the single-laser NO MTV experiments, located 29.4 mm downstream of the leading edge. The gas flowrate was metered by both a 1 standard liter per minute (SLPM) and a 10 SLPM mass flow controller configured in parallel with one another. These controllers supplied the NO_2 gas to a plenum inside the model through a stainless steel tube, with the top of the plenum being covered by the seeding slot insert. After the completion of the modified experiments, it was discovered that the pressure reading for the NO_2 supply plenum inside the model during the boundary layer measurements was consistently lower than that of the measured plate static pressure. Since NO_2 was observed to be flowing into the boundary layer during normal operation with tunnel gases flowing, the true plenum pressure had to

be greater than that of the measured static plate pressure. Thus, it was determined that a leak had formed somewhere between the NO_2 plenum and the associated pressure gauge. The following paragraphs detail how the plumbing setup was designed to operate normally, how it was checked for leaks post-test, and how this uncertainty was quantified.

The L_{Line} = 1.37 m long, D_{Line} = 1.1 mm inner-diameter stainless steel supply tube that connected to the plenum was fed through the model sting, the aerodynamic strut, and into the model housing box. Inside the model housing box, a T-junction split the line, with one end being connected to the Druck pressure gauge and the other end being capped off. A post-test examination of the 1.37 m supply tube revealed no leak, and it was therefore assumed that the leak most likely occurred between the end of this pressure line and the Druck gauge. It also appeared that the leak was relatively small, as the measured plenum pressure, P_{Leak}, was no less than 252 Pa of the measured static plate pressure, P_w, but was, on average, 2600 Pa above that of the measured model housing box pressure where the Druck gauge was located. However, it was unclear as to what percentage of the supplied mass flow rate was actually being fed through the seeding slot as opposed to the leak site, so an analysis was performed to quantify this error.

For the analysis, the supplied NO_2 mass flow rate ($\dot{m}_{NO_2}$), static plate or wall pressure (P_w), area of the seeding slot ($A_{Slot} = L_{Slot} \times W_{Slot}$), pressure line inner diameter (D_{Line}), and measured plenum pressure

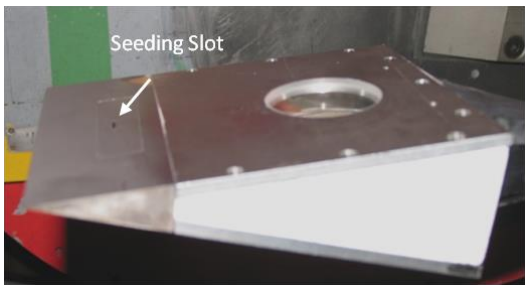

(a)

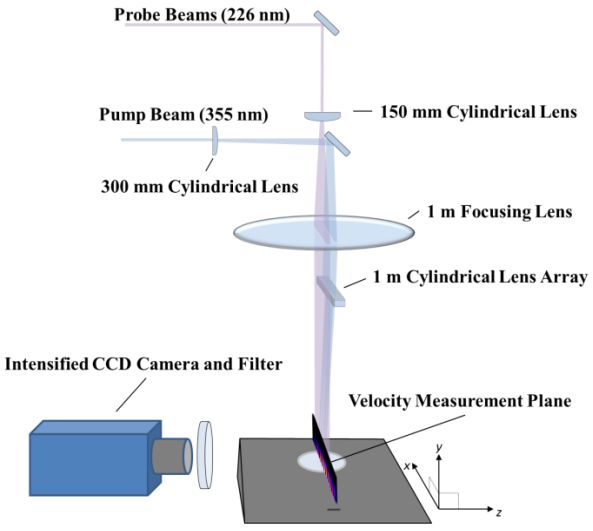

(b)

Figure 3.5: Photograph of wind tunnel model with quartz insert on upper (measurement) surface (a) and schematic of *side-view* orientation for three-laser NO_2-to-NO photolysis MTV experiments. Adapted from Ref. 5.

(P_{Leak}) were all known. The unknowns were the true plenum pressure (P_{Plenum}), NO_2 mass flow rate through the slot ($\dot{m}_{Slot}$), and mass flow rate through the leak site ($\dot{m}_{Leak}$). A pipe flow analysis, using equations similar to those in fluid dynamics textbooks such as Ref. 12, can be applied to provide three equations for the three unknowns. For the simple analysis, it was assumed that the leak site was located at the end of the plenum pressure line. The mass flow rate through the slot, $\dot{m}_{Slot}$, can be determined using the relation for orifice flow:

$$\dot{m}_{Slot} = A_{Slot}\sqrt{\frac{2\cdot\rho_{Slot}(P_{Plenum}-P_w)}{C_{loss}}} \tag{3.1}$$

The mass flow rate of the leak, $\dot{m}_{Leak}$, assuming laminar flow through the supply line (laminar pipe flow), can be determined using:

$$\dot{m}_{Leak} = \frac{P_{Plenum}(P_{Plenum}-P_{Leak})\pi D_{Line}^2}{128\cdot R_{NO_2}\cdot T_{Plenum}\cdot\mu_{Plenum}\cdot L_{Line}} \tag{3.2}$$

Mass conservation gives the third equation:

$$\dot{m}_{Slot} + \dot{m}_{Leak} = \dot{m}_{NO_2} \tag{3.3}$$

Based upon analysis of previous experimental data in which no leak was present, a loss coefficient of C_{loss} = 1.75 was estimated for the seeding slot. In Eq. 3.1, ρ_{Slot} is the density at the exit of the slot. In Eq. 3.2, R_{NO_2} is the gas constant for NO_2, T_{Plenum} is the temperature of the plenum gas (assumed to be 300 K), μ_{Plenum} is the viscosity of the plenum gas evaluated at T_{Plenum} using a Sutherland viscosity model. The assumption of laminar pipe flow in Eq. 3.2 was based upon an estimate of the Reynolds number at the entrance of the pressure line, $Re_{Line} = \rho_{Plenum}U_{Line}D_{Line}/\mu_{Plenum}$. Upon obtaining a solution to Eqs. 3.1 – 3.2, the plenum density, ρ_{Plenum}, was computed along with the average velocity through the pipe for laminar flow which is:

$$U_{Line} = \frac{(P_{Plenum}-P_{Leak})D_{Line}^2}{32\cdot\mu_{Plenum}\cdot L_{Line}} \tag{3.4}$$

This gave a Reynolds number that was less than 2300.

From this analysis, it was determined that the flow rate through the leak was, at worst, 1% of the supplied mass flow rate, $\dot{m}_{NO_2}$. Therefore, it was assumed that the mass flow rate supplied to the plenum was essentially the same as that issued from the seeding slot for all measurements.

3.4 Experimental Conditions

Chapter 4 discusses the development of the single-laser NO MTV technique for use in NASA Langley Research Center's 31-inch Mach 10 Air blowdown tunnel and describes the analysis methodology for computing velocities and corresponding uncertainties through a detailed propagation of error approach. Measurements of streamwise mean velocities in the presence of a 2 mm cylindrical isolated roughness element are presented. Velocities are reported in a plane spanning the spanwise direction above the wedge model surface within a hypersonic boundary layer are used to demonstrate the application of the technique. The experimental conditions for these two velocity measurement demonstrations are given in Table 3.1. The unique test and run number in Table 3.1 are given to each test performed in 31-inch Mach 10 Air blowdown wind tunnel. Also listed in Table 3.1 are the model views (side-view or plan-view), ratio of roughness height to laminar boundary layer thickness at the roughness (k/δ_L), freestream Reynolds number (Re_∞), edge Mach number (M_e), edge temperature (T_e), edge pressure (P_e), wall temperature (T_w), measured wall pressure (P_w), roughness Reynolds number (Re_k), mass flow rate of NO ($\dot{m}_{NO}$), and the test objective. The exposure delay for this experiment was Δt_{D2} = 500 ns. The second exposure was Δt_{E2} = 100 ns.

The measured wall temperatures, pressures, and mass flow rates presented in Table 3.1 and following tables represent estimates of the true values. For the wall temperatures, these estimates are complicated by the fact that the thermocouple measurement occurred on the underside of the plate. The temperature values reported were computed by either averaging the thermocouple data or fitting a polynomial to the data and subsequently computing an average based on the fit. For the wall pressures, the average reported wall pressures are computed using only data that had appeared to stabilize based on observation of plotted pressure gauge data. The stated mass flow rates for NO represent the set point of the mass flow controller. Flow rates for NO_2 represent averages obtained from the wind tunnel data acquisition system. For data in which the wind tunnel was operating, the stated NO_2 mass flow rates are estimates that account for the leak in the supply line and any lag observed between the moment the mass flow controllers were set and when that gas was observed to exit from the seeding slot. Edge conditions are computed using freestream data

Table 3.1: Estimated experimental conditions for NO MTV demonstration in Chapter 4.

Test-Run	View	Roughness	k/δ_L	Re_∞ (m^{-1})	M_e	T_e (K)	P_e (Pa)	T_w (K)	P_w (Pa)	Re_k	$\dot{m}_{NO}$ (mg/s)	Test Objective
462-25	Plan	Cylinder	0.69	1.7×10^6	8.07	73.7	200.7	304.1	255.3	282	3.05	NO MTV

provided by the wind tunnel data acquisition system and oblique shock calculations performed using the Virginia Tech Compressible Aerodynamics Calculator.[13] Estimates for k/δ_L and Re_k were made by solving for the compressible laminar boundary layer velocity and temperature profiles using the method outlined in Ref. 14, with the estimated edge and wall conditions used as boundary conditions. Upon obtaining a numerical solution for the compressible laminar boundary layer profiles, the appropriate properties at the location of the isolated roughness element were then computed and used to calculate k/δ_L and Re_k.

Chapter 5 presents data for the study of hypersonic laminar boundary layers with and without an isolated cylindrical roughness element using the single-laser NO MTV technique. The experiments were conducted for an edge Mach number of approximately 8.1. The purpose of the measurements are to determine streamwise velocity in a hypersonic laminar boundary layer at conditions for which the boundary layer remains laminar, even in the presence of an isolated roughness element with a height on the order of the boundary layer thickness. This chapter will also provide a comparison with temperature sensitive paint (TSP) measurements of the convective heat transfer coefficient relative to the Fay and Riddell heat transfer coefficient for stagnation point heating on a hemisphere.[15] Table 3.2 gives the experimental conditions for

Table 3.2: Estimated experimental conditions for NO MTV measurements in Chapter 5.

Test-Run	View	Roughness	k/δ_L	Re_∞ (m^{-1})	M_e	T_e (K)	P_e (Pa)	T_w (K)	P_w (Pa)	Re_k	$\dot{m}_{NO}$ (mg/s)	Test Objective
462-15	Side	-	-	1.7×10^6	8.07	73.5	200.8	325.8	265.6	-	7.11	Velocity
462-27	Plan	-	-	1.7×10^6	8.07	74.1	200.5	304.0 317.1 313.0 309.3	261.0	-	3.05	Velocity
462-30	Plan	-	-	1.7×10^6	8.07	73.6	200.0	-	-	-	-	TSP
462-17	Side	-	-	3.5×10^6	8.16	72.0	386.5	295.4	435.7	-	3.05	Velocity
462-18	Side	Cylinder	0.69	1.7×10^6	8.07	73.4	200.5	301.8	262.4	287	3.05	Velocity
462-25	Plan	Cylinder	0.69	1.7×10^6	8.07	73.7	200.7	295.7 304.1 300.5	255.3	282	3.05	Velocity
462-29	Plan	Cylinder	-	1.7×10^6	8.07	73.4	199.8	-	-	-	-	TSP
462-26	Plan	Cylinder	0.94 0.92 0.93 0.93	3.3×10^6	8.16	73.5	386.4	312.4 331.2 325.3 319.8	479.4 459.0 463.8 469.2	1527 1295 1363 1430	3.05	Velocity
462-31	Plan	Cylinder	-	3.4×10^6	8.16	73.3	386.0	-	-	-	-	TSP
462-33	Plan	Cylinder	-	3.4×10^6	8.16	73.2	386.0	-	-	-	5.69[†]	TSP

[†] *Flowrate for N_2 gas*

the laminar study. Conditions are first grouped according to roughness height, then by freestream Reynolds number (low to high), then by view (side-view or plan-view), and then by test objective (NO MTV or TSP). For conditions in which multiple wall temperatures are listed, the laser sheet was scanned to different locations within the boundary layer. For Run 27, the estimated laser sheet was position was 0 mm, 0.8 mm, 2.1 mm, and 3.3 mm, respectively. For Run 25, the estimated laser sheet was position was 0 mm, 2.2 mm, and 3.4 mm, respectively. For Run 26, the estimated laser sheet was position was 0 mm, 0.8 mm, 2.1 mm, and 3.3 mm, respectively. The exposure delay for this experiment was Δt_{D2} = 500 ns. Runs 15, 17, and 18 used a second exposure setting of Δt_{E2} = 300 ns. Runs 25, 26, and 27 used a second exposure setting of Δt_{E2} = 100 ns.

Chapter 6 discusses the development of the NO_2-to-NO photodissociation MTV technique for measurement of mean and instantaneous velocity profiles in a hypersonic boundary layer undergoing transition-to-turbulence. Table 3.3 provides the conditions examined in that chapter.

Chapter 7 will provides experimental hypersonic velocity boundary layer data in the wake of an isolated cylindrical roughness element by measuring the streamwise velocity component using the three-laser NO_2-to-NO photolysis MTV technique. A comparison with flow visualization images obtained at

Table 3.3: Estimated experimental conditions for NO_2-to-NO photolysis MTV demonstration in Chapter 6.

Test-Run	Re_∞ (m^{-1})	M_e	T_e (K)	P_e (Pa)	T_w (K)	P_w (Pa)	$\dot{m}_{NO_2}$ (mg/s)	Δt_{PROBE} (μs)	Test Objective
481-18			-	-	297.0	2891.8	30.2	1	
481-17			-	-	297.0	2893.6	30.5	2	Spatial uncertainty, data
481-19	0	0	-	-	296.9	2893.5	30.0	5	yield, accuracy, signal-to-
481-20			-	-	296.5	2890.1	30.5	10	noise
481-21			-	-	296.2	2890.9	30.6	25	
481-26			-	-	295.9	414.4	30.8	2	
481-25			-	-	296.0	592.6	30.8	2	
481-24			-	-	296.0	1288.2	30.6	2	Spatial uncertainty, data
481-23	0	0	-	-	296.0	2587.2	30.3	2	yield, accuracy, signal-to-
481-27			-	-	296.4	6807.3	30.8	2	noise
481-28			-	-	296.9	13693.7	31.0	2	
481-29			-	-	298.1	27525.7	30.8	2	
					315.9	2874.0	15.6	1	
481-5	3.3×10^6	4.2	236.7	2765.2	372.8	2909.3	15.6	2	Velocity measurement repeatability, uncertainty
					416.1	2968.5	8.8	5	
					316.8	2883.0	15.3		
					320.8	2864.0	22.7		
					326.2	2861.8	31.7		Velocity perturbation,
481-12	3.3×10^6	4.2	236.4	2766.1	336.3	2866.1	62.6	1	instability, optimal
					392.0	2928.6	97.4		blowing rate
					348.6	2874.8	141.0		
					402.7	2940.7	161.3		

similar flow conditions is also made. Table 3.4 provides details of the experimental conditions for the isolated roughness study. Details of the flow visualization experiments reported by Danehy et al. can be found in Ref. 16. Conditions are first grouped according to roughness height, then by freestream Reynolds number (low to high), and then by laser sheet position. For all MTV runs, a side-view model orientation was used. As in

Table 3.2 and 3.3, for conditions in which multiple wall temperatures are listed, the laser sheet was scanned to different locations away from the centerline. For Run 30, the estimated laser sheet was position was 0 mm, 4.5 mm, and 6.0 mm, respectively. For Run 16, the estimated laser sheet was position was 0 mm and -4.5 mm, respectively. For Run 14, the estimated laser sheet was position was 0 mm, -4.5 mm, -6.0 mm, and -7.5 mm, respectively. For Run 13, the estimated laser sheet was position was -3.5 mm, -4.5 mm, -5.5 mm, -6.5 mm, and -7.5 mm, respectively.

Figure 3.6 shows curves of computed mole fraction for NO ($\bar{\chi}_{NO}$) and NO_2 ($\bar{\chi}_{NO_2}$) as a function of streamwise position, x. These computations assume that the seeded species, s = NO or NO_2, have diffused uniformly across the thickness of the velocity boundary layer such that:

$$\bar{\chi}_s = \frac{(\dot{m}_s/L_{Slot})}{\left(\int_0^{\delta_L} \rho \bar{u} dy\right)\Big|_x} \cdot \frac{MW_{Air}}{MW_s} \tag{3.5}$$

The computed mole fractions in Fig. 3.6 decrease with increasing streamwise distance due to the increasing

Table 3.4: Estimated experimental conditions for NO_2-to-NO photolysis MTV measurements in Chapter 7.

Test-Run	Re_∞ (m^{-1})	k (mm)	k/δ_L	M_e	T_e (K)	P_e (Pa)	T_w (K)	P_w (Pa)	$\dot{m}_{NO_2}$ (mg/s)	Re_k	Δt_{PROBE} (μs)	Test Objective
481-12	3.3×10^6	-	-	4.2	236.4	2766.1	326.2	2861.8	31.7	-	1	Velocity, Instability
481-30	2.4×10^6	0.53	0.41	4.2	233.8	1971.1	378.6 364.9 350.0	2078.5 2069.9 2062.2	22.8 22.5 22.7	293 265 284	2	Velocity, Instability
481-16	3.3×10^6	0.53	0.47	4.2	236.9	2763.7	394.8 378.9	2908.2 2892.1	30.5 30.4	393 420	2	Velocity, Instability
481-14	3.3×10^6	1.00	0.86 0.87 0.88 0.90	4.2	238.8	2765.9	418.8 401.4 386.2 369.3	2936.4 2916.8 2899.6 2885.1	46.6 46.8 46.7 46.7	1698 1798 1891 1999	1	Velocity, Instability
481-13	3.3×10^6	2.00	1.89 1.86 1.83 1.80 1.76	4.2	237.4	2764.9	310.2 328.7 348.4 367.1 390.6	2868.9 2864.0 2744.6 2886.9 2909.0	30.0 30.3 30.6 30.6 30.6	5535 5296 5072 4881 4665	1	Velocity, Instability

boundary layer thickness, δ_L.

The conditions selected for these computations are representative of conditions in the boundary layers to be examined in this dissertation. The black curves in Fig. 3.6 were computed using the respective values from Tables 3.2 and 3.3. The red curve (denoted in the legend as *NO: T462 – Run 15**) corresponds to conditions in Run 15 in Test 462 (Table 3.2), however a mass flow rate of $\dot{m}_{NO} = 3.05$ mg/s was assumed. The mole fraction estimates in Fig. 3.6

Figure 3.6 shows that for the single-laser NO MTV experiments described in Chapters 4 and 5 (corresponding to conditions listed in Tables 3.1 and 3.2), the mole fraction within the boundary layer is, on average, approximately 1% within the measurement region. Recall that this value of $\bar{\chi}_{NO}$ was used in Fig. 2.5 of Chapter 2 to estimate the fluorescence lifetime of NO. The exception to the estimate of $\bar{\chi}_{NO}$ = 0.01 is Run 15 of Test 462 (Table 3.2), where a larger $\dot{m}_{NO}$ was used, resulting in a higher $\bar{\chi}_{NO}$ over the measurement region. The computations for $\bar{\chi}_{NO}$ also qualitatively agree with the magnitudes obtained from CFD in Ref. 11.

For the three-laser NO_2-to-NO photolysis MTV experiments described in Chapters 6 and 7 (corresponding to conditions listed in Tables 3.3 and 3.4), the minimum mole fraction in the boundary layer varies, on average, between approximately 2% and 4%. For the higher blowing rates listed in Tables 3.3 and 3.4, the curve of $\bar{\chi}_{NO_2}$ plotted in Fig. 3.6 scales with the ratio of $\dot{m}_{NO_2}$ relative to $\dot{m}_{NO_2} = 15.6$ mg/s for Run 5 of Test 481.

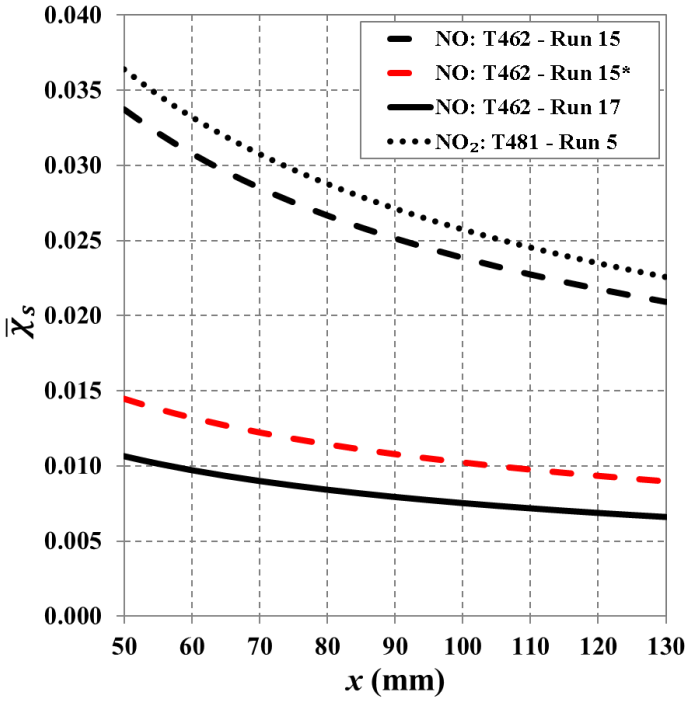

Figure 3.6: Computed mole fraction, $\bar{\chi}_s$, for $s = $ NO or $s = NO_2$ as a function of streamwise location, x. Computations assume uniform diffusion of the tracer species across the velocity boundary layer thickness, δ_L.

3.5 Conclusions

Details of the wind tunnel test facility, laser and camera system, wind tunnel model, and test conditions used

for hypersonic boundary layer measurements in the following chapters were provided. Sample calculations to determine the magnitude of leaks within the NO_2 gas supply system were performed and showed that such leaks were negligible. Sample calculations were also performed to estimate the average mole fractions of NO and NO_2 present within the boundary layers for several test conditions where the single-laser NO MTV and three-laser NO_2-to-NO photolysis MTV techniques were applied, respectively.

---

[1] Micol, J.R., "*Langley Aerothermodynamic Facilities Complex: Enhancements and Testing Capabilities*," 38th AIAA Aerospace Sciences Meeting, AIAA 1998-147, 1998.

[2] Bathel, B.F., Danehy, P.M., Inman, J.A., Jones, S.B., Ivey, C.B., and Goyne, C.P., "*Multiple Velocity Profile Measurements in Hypersonic Flows Using Sequentially-Imaged Fluorescence Tagging*," 48th AIAA Aerospace Sciences Meeting, AIAA Paper 2010-1404, January 4 – 7, 2010, Orlando, FL.

[3] Bathel, B.F., Danehy, P.M., Inman, J.A., Jones, S.B., Ivey, C.B., and Goyne, C.P., "*Velocity Profile Measurements in Hypersonic Flows Using Sequentially-Imaged Fluorescence-Based Molecular Tagging Velocimetry*," AIAA Journal, 49(9), pp. 1183-1896, September, 2011.

[4] Bathel, B.F., Danehy, P.M., Inman, J.A., Watkins, A.N., Jones, S.B., Lipford, W.E., Goodman, K.Z., Ivey, C.B., and Goyne, C.P., "*Hypersonic Laminar Boundary Layer Velocimetry with Discrete Roughness on a Flat Plate*," AIAA Paper 2010-4998, 40th Fluid Dynamics Conference and Exhibit, June 28 – July 1, 2010, Chicago, IL.

[5] Bathel, B.F., Johansen, C.T., Inman, J.A., Jones, S.B., and Danehy, P.M., "*Review of Fluorescence-Based Velocimetry Techniques to Study High-Speed Compressible Flows*," 51st AIAA Aerospace Sciences Meeting, AIAA Paper 2013-0339, Grapevine, TX, January 4 – 7, 2013.

[6] Bathel, B.F., Johansen, C.T., Danehy, P.M., Inman, J.A., Jones, S.B., and Goyne, C.P., "*Hypersonic Boundary Layer Transition Measurements Using $NO_2 \rightarrow NO$ Photo-dissociation Tagging Velocimetry*," AIAA Paper 2011-3246, 41st AIAA Fluid Dynamics Conference and Exhibit, June 27 – 30, 2011, Honolulu, HI.

[7] Bathel, B.F., Danehy, P.M., Johansen, C.T., Jones, S.B., and Goyne, C.P., "*Hypersonic Boundary Layer Measurements with Variable Blowing Rates Using Molecular Tagging Velocimetry*," AIAA Paper 2012-2886, 28th AIAA Aerodynamic Measurement Technology, Ground Testing, and Flight Testing Conference, June 25 – 28, 2012, New Orleans, LA.

[8] Bathel, B.F., Johansen, C.T., Jones, S.B., Danehy, P.M., and Goyne, C.P., "*Trip-induced Transition Measurements in a Hypersonic Boundary Layer Using Molecular Tagging Velocimetry*," 51st AIAA Aerospace Sciences Meeting, AIAA Paper 2013-0042, January 7 – 10, 2013, Grapevine, TX.

[9] Berry, S.A., Nowak, R.J., and Horvath, T.J., "*Boundary Layer Control for Hypersonic Airbreathing Vehicles*," AIAA 2004-2246, 34th AIAA Fluid Dynamics Conference and Exhibit, June 28 – July 1, 2004, Portland, Oregon, 2004.

[10] Danehy, P.M., Bathel, B.F., Ivey, C., Inman, J.A., and Jones, S.B., "*NO PLIF study of hypersonic transition over a discrete hemispherical roughness element*," 47th AIAA Aerospace Sciences Meeting, AIAA Paper 2009-394, January 5 – 8, 2009, Orlando, FL.

[11] Johansen, C.T., Danehy, P.M., "*Numerical investigation of PLIF gas seeding for hypersonic boundary layer flows*," 50th AIAA Aerospace Sciences Meeting, AIAA Paper 2012-1057, January 9 – 12, 2012, Nashville, TN.

[12] Çengel, Y.A., and Cimbala, J.M., *Fluid Mechanics, Fundamentals and Applications*, 1st ed., McGraw-Hill, New York, 2006, pp. 321-385.

[13] Devenport, W.J., *Compressible Aerodynamics Calculator 2.0*, http://www.dept.aoe.vt.edu/~devenpor/aoe3114/calc.html [last accessed May 18, 2013].

[14] Anderson Jr., J. D., *Hypersonic and High-Temperature Gas Dynamics 2nd ed.*, AIAA Education Series, AIAA, Reston, VA, 2006.

[15] Fay, J.A. and Riddell, F.R., "*Theory of Stagnation Point Heat Transfer in Dissociated Air*," Journal of the Aeronautical Sciences, 25(2), pp. 73-85, 1958.

[16] Danehy, P.M., Ivey, C.B., Inman, J.A., Bathel, B.F., Jones, S.B., McCrea, A.C., Jiang, N., Webster, M., Lempert, W., Miller, J., and Meyer, T., "*High-Speed PLIF Imaging of Hypersonic Transition over Discrete Cylindrical Roughness*," AIAA Paper 2010-703, 48th AIAA Aerospace Sciences Meeting, January 4 – 7, 2010, Orlando, FL.

Chapter 4: Development of Single-Laser, Sequentially Imaged NO Molecular Tagging Velocimetry

The purpose of this chapter is to report both the demonstration of the MTV technique as applied to a hypersonic flow in a large-scale wind tunnel facility and to describe the analysis technique used to determine the velocity profiles and the associated measurement uncertainties. Prior work using similar MTV techniques has been performed by a number of authors using various techniques to analyze the fluorescence profiles. One particular analysis method described in Ref. 1, involving the cross-correlation of image pairs to calculate 2-dimensional velocity profiles with sub-pixel accuracy, is loosely followed in this chapter. However, this correlation approach has been adapted for a one-component velocity measurement. The work reported in this chapter makes use of an intensified, double-framing camera with sequential frame spacing of 500 ns. This removes measurement sensitivity to facility vibration, which is a potential problem for single-shutter operations. The facility also contributes to the vibration of the optical setup and therefore imparts small vibrations to the tagged profiles. This can result in increased velocity uncertainty if a single-framing camera is used for measurement of velocity since the 'reference' profiles would have been taken at a slightly different position. The camera used in this work also eliminates errors that are otherwise associated with a two-camera velocimetry measurement, namely, scaling and shifting the two separately acquired images. A method to compensate for fluorescence decay and its effect on the spatial displacement of MTV profiles obtained via cross-correlation is presented. A description of how scalar velocity values are obtained, how the spectroscopic behavior of the gas changes the measurement, and how such behavior is corrected through geometric considerations is provided. A description of the associated uncertainty calculations is also given. Finally, a demonstration of the technique as applied to the wind tunnel model is provided. The discussion and results in this chapter have been adapted from Refs. 2 and 3.

4.1 Velocity Analysis Method for Single-Laser NO MTV

Determination of the axial velocity is based upon a time-of-flight calculation using the measured displacement between the center of mass of the profile observed in the reference (first) and delayed (second) images. The displacement, Δx_{ND}, is divided by the time separating their acquisition, Δt_{ND}, where

the subscript *ND* means "no decay" and refers to the respective parameter determined in the absence of any fluorescence decay. The velocity relation is therefore:

$$U = \frac{\Delta x_{ND}}{\Delta t_{ND}} \tag{4.1}$$

Determination of values for Δx_{ND} and Δt_{ND} is described in sections 4.1.2 and 4.1.3, respectively.

4.1.1 Image Pre-Processing

The magnification was measured by acquiring an image of a matrix of square marks separated at equal spatial intervals, known as a *dotcard* and described in Ref. 4. This dotcard image was created with Adobe® Acrobat® software. When these spatial calibration images were acquired, the dotcard was placed in the plane of the laser sheet, later used to interrogate the seeded NO gas.

To correct for optical and perspective distortion of the images, the image of the dotcard in the test section was acquired with the camera. An image registration algorithm, *UnwarpJ* (Ref. 5), was then used to correct the distortion by mapping the distorted image acquired with the camera to the undistorted template image created with the Adobe® Acrobat® software. The *UwarpJ* software is a plug-in created for the image processing software, *ImageJ*, a freeware image-processing program available from the National Institutes of Health.[6]

To improve the signal-to-noise ratio in the images, MATLAB® was used to apply a 4-pixel radius averaging disk filter to the reference and delayed fluorescence images. The images were then binned by 4 pixels in the vertical direction. These two steps improved the signal-to-noise by smoothing camera noise and consolidating the signal in regions tagged by the laser. This provided approximate streamwise and spanwise spatial resolutions of 0.5 mm and 0.7 mm, respectively.

Prior to processing each image for velocity information, a background offset level was subtracted from the reference and delayed images. The background level was obtained from images taken with the laser blocked. The minimum exposure delay of Δt_{D2} = 500 ns used between the reference and delayed images and the relatively long decay time of the P46 phosphor in the intensifier resulted in some *ghosting* of the reference image in the delayed image. Ghosting refers to an image artifact in which a residual fraction of the first exposure image remains in the second exposure. For the 500 ns gate delay, this level was experimentally determined to be approximately 1/126th of the reference image. Therefore, this fraction of the reference image was also subtracted from the delayed image in addition to the background offset level.

4.1.2 Spatial Analysis

To obtain the relative shift between individual lines in the reference and delayed image, a W = 45-pixel-wide window was selected that encompassed each vertical tagged line in the reference image. For each row of pixels in this window, a reference fluorescence profile was obtained. This window was re-positioned to encompass the same pixel region in the delayed image, with the delayed fluorescence profiles again acquired for each row in the window. The center of this window was positioned approximately 5 pixels to the right of the of the line center in the reference image. This was done to minimize clipping either side of the reference or delayed profile. A user-defined threshold, as a function of the maximum pixel intensity for each row in the reference image, was used to reject low signal intensity profiles which might otherwise provide poor quality velocity information. In these cases, no velocity information is reported.

For each remaining profile pair, each of length W = 45 pixels, a cross-correlation was performed using the MATLAB® *xcorr* function. The maximum value resulting from the array (of length $2W - 1 = 89$ pixels) of cross-correlation coefficient values was then found. A 7^{th}-order polynomial fit centered about the maximum was then obtained. This method is similar to the method used in Ref. 1. For this analysis, 11 points (centered about the maximum) were used to compute the polynomial fit. Setting the first derivative of this polynomial equal to zero and using a root-finding algorithm to determine the maxima of the polynomial fit, the resolved maximum of the coefficient values was obtained. The resulting difference between this resolved maximum and the length of the input profile vector corresponds to the total shift, in pixels, of each profile pair.

To obtain the mean spatial displacement, in time, at a particular location along a tagged profile in the flowfield, the mean spatial shift for a set of N resolved single-shot image streamwise velocity measurements was calculated.

4.1.3 Timing Simulation and Analysis

4.1.3.1 *Phenomenological Derivation of Displacement (Neglecting Fluorescence Decay)*

In the absence of fluorescence decay, a phenomenological geometric argument can be made, based upon the camera and laser timing parameters selected, to describe the elapsed time between the reference and delayed images. This approach is a refinement of that of Danehy et al. in Ref. 7. Figures 4.1 and 4.2 shows idealized space-time-intensity diagrams describing an infinitesimal spatial width laser beam exciting

fluorescence at a rate of 1 block of molecules per unit of time. The axes are x for space, t for time, and I for PLIF signal intensity. Items along the axes (such as x_i or t_i) refer to a point or time, respectively, at which a particular event is initiated. Items along the axes with the symbol prefix Δ (such as Δt_i) refer to the duration of a particular event, such as the duration of a camera exposure. Items with the symbol prefix δ (such as δx or δt) refer to a spatial step or time discretization interval, respectively, used to idealize the fluorescence tagging process. The vertical plane along the time axis in Figs. 4.1a and 4.2a shows the relative timing of the first exposure and laser pulse, which are represented by the shaded areas with dashed borders, and are similar to those shown in Fig. 3.2 of Chapter 3. The vertical plane along the time axis in Figs. 4.1b and 4.2b shows the relative timing of the second exposure with respect to the first exposure and laser pulse. The idealizations in Figs. 4.1 and 4.2 assume that the MTV process involves gas moving from left-to-right at constant velocity within the time required to make a single MTV measurement.

Figure 4.1 corresponds to a case where the first exposure is timed such that only a portion of it overlaps the laser pulse, which allows for an independent control of signal buildup in the first exposure (as described in Chapter 3, section 3.2.1). Even though the camera exposure begins before to the laser pulse, the exposure does not *effectively* begin until the laser turns on. In this case, the first camera exposure starts before the first *effective* exposure ($t_{E1} \leq t_{eE1}$) and the duration of the first *effective* exposure is less than the

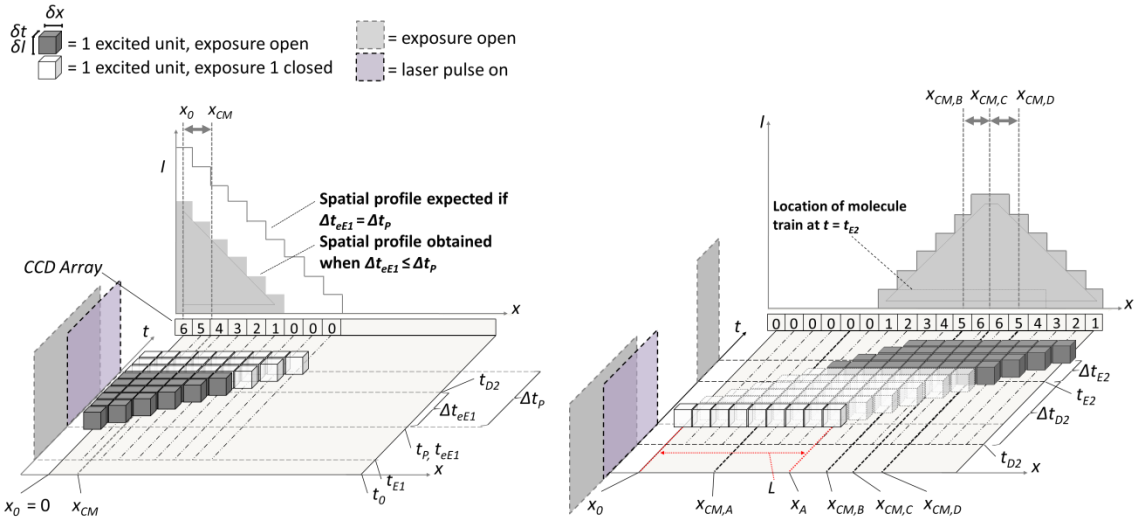

Figure 4.1: Space-time-signal diagram of idealized (not to scale) CCD signal and acquisition of fluorescence with (a) effective first exposure duration shorter than or equal to laser pulse duration and (b) subsequent CCD signal in second exposure. The laser and exposures are assumed to have top-hat temporal profiles.

first exposure ($\Delta t_{eE1} \leq \Delta t_{E1}$). The start of the first effective exposure corresponds to the start of the laser pulse ($t_{eE1} = t_P$) and its duration is less than or equal to the duration of the laser pulse ($\Delta t_{eE1} \leq \Delta t_P$). Additionally, the start of the second exposure can be related to events prior to the start of the second exposure via the relation ($t_{E2} = t_{eE1} + \Delta t_{eE1} + \Delta t_{D2}$).

Figure 4.2 corresponds to a case similar to that in Fig. 4.1, however the duration of both the first exposure and first effective exposure are both greater than that of the laser pulse duration ($\Delta t_P < \Delta t_{eE1} \leq \Delta t_{E1}$) such that the first exposure completely envelops the laser pulse.

The blocks in Figs. 4.1 and 4.2, which represent a 1-dimensional region of NO gas in air moving left-to-right, are shaded according to the means by which they emit fluorescence photons. The gray blocks in Figs. 4.1a and 4.2a on the space-time plane are excited by the laser pulse (width of δx = 1 with uniform irradiance δI = 1) and emit photons captured by the CCD camera during the overlap period of the first exposure and the laser pulse. In Fig. 4.1a, the transparent white blocks continue to be excited by the laser pulse and emit fluorescence while the laser pulse continues, but after the first camera exposure has been closed (that is, they are not captured by the first camera exposure). In Fig. 4.2a, the transparent white blocks remain excited and emit fluorescence after the laser pulse has ceased, but before the first camera exposure has been closed.

In Fig. 4.1b, the transparent white blocks on the space-time plane represent the train of excited

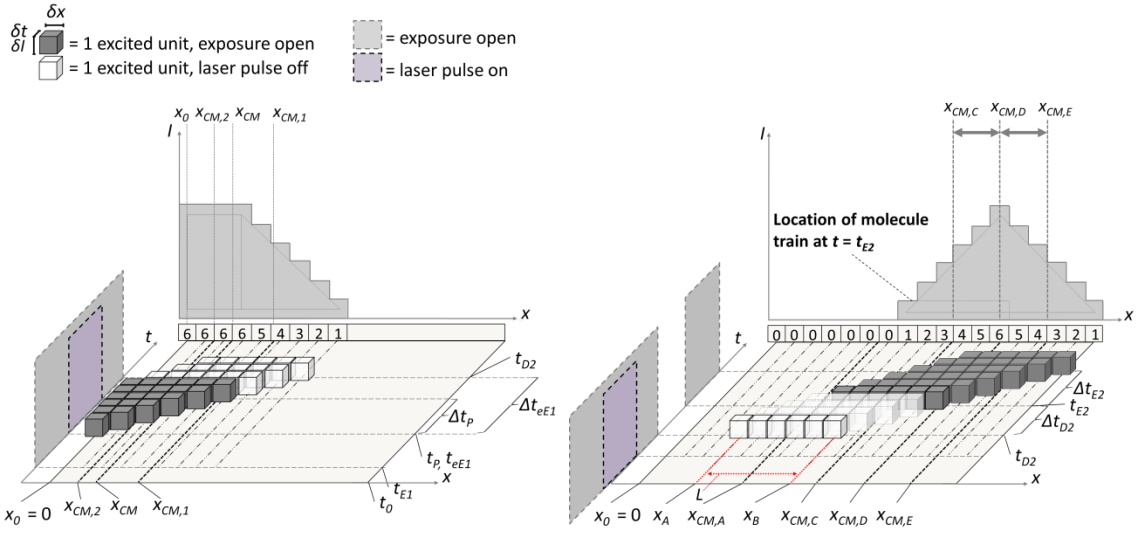

(a) (b)

Figure 4.2: Space-time-signal diagram of idealized (not to scale) CCD signal and acquisition of fluorescence with (a) effective first exposure duration greater than laser pulse duration and (b) subsequent CCD signal in second exposure.

molecules of length L at the instant the laser pulse ceases. The clear blocks in this figure represent this train as it is advected downstream between the end of the laser pulse and the beginning of the second exposure. The gray blocks in Fig. 4.1b represent the molecule train during the second camera exposure while it continues to move from left-to-right. In Fig. 4.2b, the transparent white blocks on the space-time plane represent the train of excited molecules of length L at the instant the first exposure closes. The clear blocks in Fig. 4.2b again represent the train as it is advected downstream between the end of the first camera exposure and the beginning of the second exposure. The gray blocks in Fig. 4.2b again represent the molecule train during the second camera exposure while it continues to move from left-to-right.

During the laser pulse, and in the absence of fluorescence decay, laser excitation of each block of NO gas is assumed to be instantaneous and with constant intensity. Each block is advected one spatial unit, δx, downstream per unit of time, δt, with the ratio corresponding to a constant velocity, $U = \delta x/\delta t$. At each time step in this process, and while the first exposure is open, the fluorescence from each block is captured by CCD array pixels (denoted by the rectangular region below the *I*-*x* plane). The numbers in this region are segmented into pixels along an array of the CCD and represent the total charge accumulated (in arbitrary units) during the two exposures. In Figs. 4.1 and 4.2, the accumulated charge is also represented by the gray shaded area on the *I*-*x* plane.

If the effective first exposure is shorter than or equal to the laser pulse duration ($\Delta t_{eE1} \leq \Delta t_P$), as in Fig. 4.1a, the resulting fluorescence intensity distribution is that of a right triangle on the CCD. If the effective first exposure is greater than the laser pulse duration ($\Delta t_{eE1} > \Delta t_P$), as in Fig. 4.2a, the resulting fluorescence intensity distribution is that of a rectangle with a right triangle of equal height appended to its right-hand-side on the CCD. A small error is introduced in this analysis because the temporal evolution of the laser pulse is more like a Gaussian rather than a square top-hat profile, which is assumed in this analysis. The use of a Gaussian would slightly shift the observed intensity distribution on the CCD, though it does not affect the second exposure. By modeling the laser pulse with both Gaussian and square top-hat temporal behavior, it was determined that the discrepancy is less than 0.3% of the velocity magnitude for the conditions of the experiment.

In Fig. 4.1a, after the first camera exposure has closed, six blocks of NO gas have been excited by the laser pulse. As the laser pulse continues for three time units, three additional blocks of NO gas are excited,

resulting in a train of excited NO gas that is L = 9 blocks long. The location of the center, x_{CM}, of the signal intensity distribution in the *I*-*x* plane with respect to the origin is:

$$x_{CM} - x_0 = U \cdot \frac{1}{3}\Delta t_{eE1} \tag{4.2}$$

At the end of the first exposure, the NO gas train continues to grow in length until the end of the laser pulse. At the end of the laser pulse, the center, $x_{CM,A}$, of the NO gas train (now of length $L = x_A - x_0 = U \cdot \Delta t_P$) relative to the origin, as shown in Fig. 4.1b, is given by:

$$x_{CM,A} - x_0 = x_A - x_{CM,A} = \frac{x_A - x_0}{2} = \frac{L_2}{2} = U \cdot \frac{1}{2}\Delta t_P \tag{4.3}$$

At the end of the laser pulse, the full length of the gas train is advected downstream. This occurs during the interframe delay period, Δt_{D2}, occurring between the end of the laser pulse and beginning of the second exposure. When the second exposure is opened, the gas train has been displaced from $x_{CM,A}$ by a distance:

$$x_{CM,B} - x_{CM,A} = U \cdot [\Delta t_{D2} - (\Delta t_P - \Delta t_{eE1})] \tag{4.4}$$

The train then continues to be advected downstream while fluorescence is captured by the CCD. The charge distribution across the pixels takes on a trapezoidal shape, as shown by the shaded area of the signal-spatial axis in Fig. 4.1b. The displacement of the center of this object relative to $x_{CM,B}$ is given by:

$$x_{CM,C} - x_{CM,B} = x_{CM,D} - x_{CM,C} = \frac{x_{CM,D} - x_{CM,B}}{2} = U \cdot \frac{1}{2}\Delta t_{E2} \tag{4.5}$$

Combining Eqs. 4.2 through 4.5, the displacement observed between the centers of the intensity distributions in the first and second exposures in the absence of fluorescence decay is:

$$\begin{gathered}\Delta x_{ND} = x_{CM,C} - x_{CM} = \begin{bmatrix}(x_{CM,C} - x_{CM,B}) + (x_{CM,B} - x_{CM,A}) + \cdots \\ (x_{CM,A} - x_0)\end{bmatrix} - (x_{CM} - x_0) \\ \Delta x_{ND} = U \cdot \left[\frac{2}{3}\Delta t_{eE1} + \Delta t_{D2} + \frac{1}{2}(\Delta t_{E2} - \Delta t_P)\right] \equiv U \cdot \Delta t_{ND}\end{gathered} \tag{4.6}$$

A slightly different approach is required when analyzing the situation shown in Fig. 4.2a. In this figure, after the laser pulse has ceased, the $L = 6 \cdot \delta x$ blocks of NO tagged by the laser remain excited. For the remaining three time units of the effective first exposure, this train of excited NO gas is advected three additional spatial steps downstream, with its fluorescence captured by the CCD. The composite intensity distribution observed on the CCD can be separated into the rectangular and triangular shapes shown in the

I-x plane in Fig. 4.2a. The center of the rectangular portion of the intensity distribution with respect to the origin is given by:

$$x_{CM,2} - x_0 = U \cdot \frac{1}{2}(\Delta t_{eE1} - \Delta t_P) \tag{4.7}$$

The center of the triangular portion of the intensity distribution with respect to the origin is:

$$x_{CM,1} - x_0 = U \cdot \left[(\Delta t_{eE1} - \Delta t_P) + \frac{1}{3}\Delta t_P\right] \tag{4.8}$$

To obtain the center of the composite intensity distribution, a center-of-mass calculation of the form $x_{CM} - x_0 = \sum(\Delta x_{CM,i} \cdot A_i)/\sum A_i$ can be used, where Δx_i is obtained from Eqs. 4.7 and 4.8 and A_i corresponds to the spatial-intensity area of each composite shape in the *I-x* plane in Fig. 4.2a. For the rectangular intensity distribution, the area is:

$$A_2 = [U \cdot (\Delta t_{eE1} - \Delta t_P)] \cdot \Delta t_P \tag{4.9}$$

and for the triangular intensity distribution, the area is:

$$A_1 = \frac{1}{2}[U \cdot \Delta t_P] \cdot \Delta t_P \tag{4.10}$$

This gives a composite intensity distribution center of:

$$x_{CM} - x_0 = \frac{\left[U\cdot\left(\{\Delta t_{eE1}-\Delta t_P\}+\frac{1}{3}\Delta t_P\right)\cdot\frac{1}{2}(U\cdot\Delta t_P)\cdot\Delta t_P\right]+\left[U\cdot\frac{1}{2}(\Delta t_{eE1}-\Delta t_P)\cdot(U\cdot\{\Delta t_{eE1}-\Delta t_P\})\cdot\Delta t_P\right]}{\left[\frac{1}{2}(U\cdot\Delta t_P)\cdot\Delta t_P\right]+[(U\cdot\{\Delta t_{eE1}-\Delta t_P\}\cdot\Delta t_P)]}$$
$$x_{CM} - x_0 = U \cdot \frac{(\Delta t_{eE1})^2-\Delta t_{eE1}\cdot\Delta t_P+\frac{(\Delta t_P)^2}{3}}{2\cdot\Delta t_{eE1}-\Delta t_P} \tag{4.11}$$

At the end of the first exposure the left-hand-edge of the NO gas train of length $L = x_B - x_A = U \cdot \Delta t_P$, relative to the origin as shown in Fig. 4.2b, is given by:

$$x_A - x_0 = U \cdot (\Delta t_{eE1} - \Delta t_P) \tag{4.12}$$

with its center relative to x_A being:

$$x_{CM,A} - x_A = x_B - x_{CM,A} = \frac{x_B - x_A}{2} = \frac{L}{2} = U \cdot \frac{1}{2}\Delta t_P \tag{4.13}$$

The gas train is then advected downstream during the period, Δt_{D2}, between the end of the first exposure and beginning of the second exposure. When the second exposure is opened, the gas train has been displaced relative to $x_{CM,A}$ by:

$$x_{CM,C} - x_{CM,A} = U \cdot \Delta t_{D2} \tag{4.14}$$

As in Eq. 4.5, the displacement of the center of the signal intensity distribution from $x_{CM,C}$ at the end of the second exposure is given by:

$$x_{CM,D} - x_{CM,C} = x_{CM,E} - x_{CM,D} = \frac{x_{CM,E} - x_{CM,C}}{2} = U \cdot \frac{1}{2}\Delta t_{E2} \tag{4.15}$$

Combining Eqs. 4.11 through 4.15, the displacement observed between the centers of the intensity distributions in the first and second exposures in the absence of fluorescence decay is:

$$\begin{gathered} \Delta x_{ND} = \begin{bmatrix} \left(x_{CM,D} - x_{CM,C}\right) + \left(x_{CM,C} - x_{CM,A}\right) + \cdots \\ \left(x_{CM,A} - x_A\right) + \left(x_A - x_0\right) \end{bmatrix} - \left(x_{CM} - x_0\right) \\ \Delta x_{ND} = U \cdot \left[\frac{6\cdot(\Delta t_{eE1})^2 + 6\cdot\Delta t_{eE1}\cdot(\Delta t_{E2} - \Delta t_P) + \Delta t_P\cdot(\Delta t_P - 3\cdot\Delta t_{E2})}{6\cdot(2\cdot\Delta t_{eE1} - \Delta t_P)} + \Delta t_{D2}\right] \equiv U \cdot \Delta t_{ND} \end{gathered} \tag{4.16}$$

Based on the preceding analysis, and in the absence of fluorescence decay, the time separating the profiles imaged in the reference and delayed exposures is:

$$\Delta t_{ND} = \begin{cases} \frac{2}{3}\Delta t_{eE1} + \Delta t_{D2} + \frac{1}{2}(\Delta t_{E2} - \Delta t_P) & \Delta t_{eE1} \le \Delta t_P \\ \frac{6\cdot(\Delta t_{eE1})^2 + 6\cdot\Delta t_{eE1}\cdot(\Delta t_{E2} - \Delta t_P) + \Delta t_P\cdot(\Delta t_P - 3\cdot\Delta t_{E2})}{6\cdot(2\cdot\Delta t_{eE1} - \Delta t_P)} + \Delta t_{D2} & \Delta t_{eE1} > \Delta t_P \end{cases} \tag{4.17}$$

This formulation differs slightly from that presented in Ref. 3, which was given as:

$$\Delta t_{ND} = \frac{2}{3}\Delta t_{eE1} + \Delta t_{D2} + \frac{1}{2}\Delta t_{E2} + \frac{1}{2}(\Delta t_{eE1} - \Delta t_P) \tag{4.18}$$

While the formulation in Eq. 4.18 is simple compared to Eq. 4.17, it consistently over-estimates the time separation, Δt_{ND}. However, for the timing parameters used in this dissertation, this over-prediction results in an error of less than 0.9% relative to the more precise relation in Eq. 4.17.

4.1.3.2 *Simulation and Validation of the Effect of Fluorescence Decay*

If relatively uniform thermodynamic conditions exist over the imaged region of a flow moving from left-to-right, fluorescence decay causes the perceived center of the intensity profile observed in both the

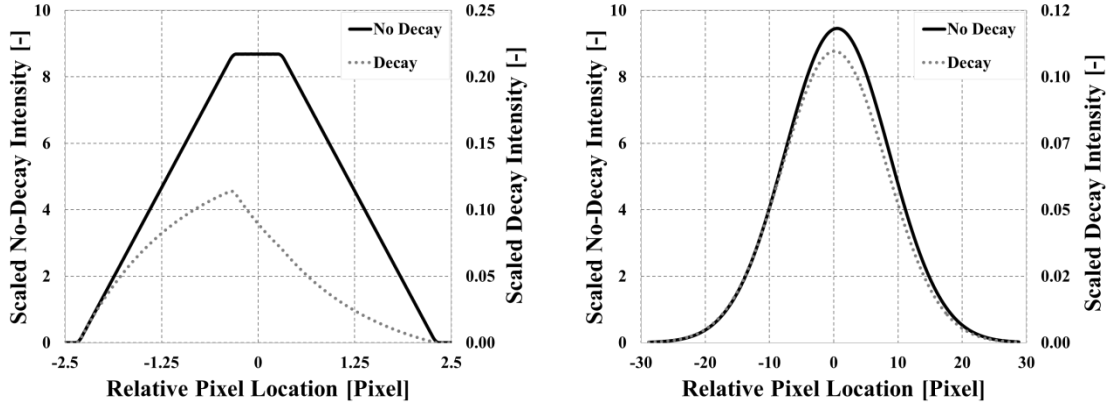

(a) (b)

Figure 4.3: Simulated second CCD exposure with Δt_{E2} = 300 ns, τ_{LIF} = 150 ns, U = 500 m/s using (a) a narrow 2-pixel-wide top-hat spatial laser profile and (b) a Gaussian 19-pixel FWHM spatial laser profile. Images originally presented in Ref. 3.

first and second exposure to become slightly left-weighted, with the effect being much more apparent in the second exposure. This is because the fluorescence intensity of the tagged gas region decays exponentially in time, so as the gas is advected downstream, the upstream pixels receive more photons than the downstream pixels. It should be noted that while the fluorescence decay rate depends on the composition, pressure, and temperature of the tagged gas, the observed profile on the CCD is spatially dependent on both the fluorescence decay rate and velocity. Figure 4.3a shows a simulated CCD second exposure in which a spatially narrow top-hat beam, 2 pixels in width, is used to excite NO molecules being advected from left-to-right. This simulated second exposure, lasting 300 ns and beginning 500 ns after the end of the first exposure, shows the resulting fluorescence profiles observed with (solid black) and without (dotted gray) the effect of decay. The simulation results in Fig. 4.3a emphasizes that an error can result if care is not taken to compensate for the effect of fluorescence decay. Figure 4.3b shows a simulation involving a more realistic 19-pixel wide (FWHM) Gaussian beam profile with (solid black) and without (dotted gray) fluorescence decay, using the same exposure conditions. The effect is more subtle than in Fig. 4.3a, but important to correct for in order to provide accurate results (correction described in Section 4.1.3.3).

Prior to simulating the first exposure, a zero-valued matrix consisting of $\mathcal{R} = \Delta t_{eE1}/\delta t$ rows and *K* columns was initialized. For each time step, the intensity distribution was added to the r^{th} row of a *profile matrix*, initially a matrix of zeros, and then progressed as a wave traveling a distance $\Delta x = U \cdot (r - 1)\delta t$ for each time step. The process was repeated for the duration of the effective first exposure from r = 1 to $\mathcal{R}$. At each row, a cumulative summation including all subsequent rows was then performed. This summation represented the contribution of a single blurred profile instantaneously created at the r^{th} time step. Using this summation matrix, a final summation was performed from rows $r = 1$ through $r = \Delta t_P/\delta t$ to create the first *exposure array*.

For the second exposure, a profile matrix was again generated consisting of $\mathcal{R} = (\Delta t_{E2} + \Delta t_P)/\delta t$ rows and *K* columns. For each time step, the intensity distribution was added to the r^{th} row and then progressed spatially by $\Delta x = U \cdot [\Delta t_{D2} + (\Delta t_{eE1} - \Delta t_P) + (r - 1)\delta t]$. An array was then calculated by performing a summation over a total of $\Delta t_{E2}/\delta t$ rows, and repeating this summation beginning at the first row and proceeding to the $r = \Delta t_P/\delta t$ row, adding each summation to the previous array, ultimately resulting in the second exposure array.

For both the first and second profile array, the intensity distribution at each time step was multiplied by the exponential decay factor:

$$exp\left(-\frac{(r-1)\cdot\delta t}{\tau_{LIF}}\right) \tag{4.19}$$

where r is the current time step of the simulation and τ_{LIF} the fluorescence lifetime, as described in Chapter 2. Values for Q_{21} and A_{21}, used to compute τ_{LIF}, can be obtained from Refs. 8 and 9.

For these simulations, Δt_P and Δt_{D2} were fixed at 9.5 ns and 500 ns, respectively. A temporal spacing of δt = 0.05 ns was used with a grid spacing of δx = 0.01 pixels, corresponding to 0.6 μm experimentally. For the particular velocity used in the simulation, care was taken to satisfy the Courant-Friedrichs-Lewy (CFL) condition and a discretization density study was performed to ensure grid independence. The simulated laser excitation source had an intensity distribution approximated by a Gaussian spatial profile with a FWHM of 19 pixels located -2 pixels from the center of the correlation window.

To estimate the effective first exposure duration for the simulation corresponding to the experiment, experimental signal ratios were obtained over a range of pressures at 298 K from a near-zero velocity field. While absolute signal intensity depends on spectral properties of the laser (spectral line width, intensity, wavelength), collection optics, kinetic properties of the gas being probed (rate constants, saturation intensity, absorption lineshape, population fraction, fluorescence lifetime, etc.), and gas velocity, taking the ratio of both signals removes nearly all of these dependencies. The one term which does not cancel in the ratio is the time-integrated distribution of signal during both exposures due to different integration intervals. Using the appropriate integration limits, this term is $\int_0^{\Delta t_{eE1}} S(x-Ut)\cdot exp(-t/\tau_{LIF})\cdot\ dt$ for the effective first exposure and for the second exposure is $\int_{\Delta t_{eE1}+\Delta t_{D2}}^{\Delta t_{eE1}+\Delta t_{D2}+\Delta t_{E2}} S(x-Ut)\cdot exp(-t/\tau_{LIF})\cdot\ dt$. Here, $S(x-Ut)$ represents the instantaneous intensity distribution of the tagged gas at t = 0 and $exp(-t/\ \tau_{LIF})$ is the decay rate of this intensity with respect to fluorescence lifetime and is similar to terms described in Eq. 4.19.

These experimental signal ratios were calculated by dividing the peak of the time-integrated signal occurring in each W = 45-pixel-wide correlation window in the first effective exposure by the peak of the time-integrated signal in each W = 45-pixel-wide correlation window in the second exposure. The experimental ratios were then compared with simulated signal ratios, which considered only the ratio of

time-integrated distribution of signal, over the same pressure range and temperature, but for multiple values of Δt_{eE1}. From this, it was determined that the effective first exposure duration for the experiment was Δt_{eE1} = 10.25 ns. Figure 4.4 shows the result of this validation.

4.1.3.3 *Use of Signal Ratio to Correct for Effects of Fluorescence Decay*

If the composition, pressure, and temperature are known, the apparent shift in the center of the fluorescence profile can be estimated by simulating the fluorescence acquired by both camera exposures, as described in section 4.1.3.2. By performing such a simulation, which accounts for blurring due to a finite (non-infinitesimal) exposure duration, a relation between the ratio of the maximum signal intensities of the reference and delayed exposures and the fluorescence lifetime can be formulated. However, if the experimental fluorescence lifetime is not known, as is commonly the case, a simulation using the experimental camera timing parameters can be used to estimate the profile shape and signal intensity ratio for several different lifetimes. Using this approach, an experimentally obtained signal ratio can be used in conjunction with the simulation results to infer the fluorescence lifetime. With inferred fluorescence lifetime, the simulation can then provide an estimate for the level of compensation needed to correct for the perceived profile shift relative to the displacement that would otherwise occur in the absence of fluorescence decay, as described in Eq. 4.17. The results in this chapter and Chapter 5 use this simulation approach to estimate the true profile shifts based upon the camera timing parameters and observed experimental signal ratios. It should be noted that for the results presented in this chapter and Chapter 5, the simpler formulation in Eq. 4.18 has been used to calculate the profile displacements. A range of fluorescence lifetimes corresponding to conditions encountered during typical wind tunnel tests were simulated for three different second exposure durations: 100 ns, 200 ns, and 300 ns.

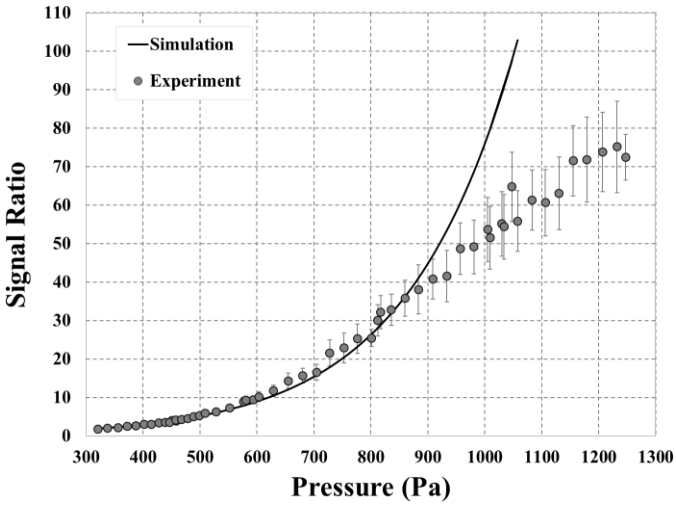

Figure 4.4: Comparison of simulated and experimental signal ratio (first gate intensity divided by second gate intensity) as a function of air pressure. Temperature is a constant 298 K, Δt_{D2} = 500 ns, and Δt_{E2} = 500 ns. Image originally presented in Ref. 3.

Figure 4.4 shows that above pressures of approximately 900 Pa, a significant deviation from the simulated signal ratio trend occurs. This corresponds to $\tau_{LIF} < 74$ ns. For the test conditions reported in this chapter, τ_{LIF} remained above this lower limit. The primary trend, however, is that as pressure increases, the signal observed during the second exposure decreases, causing the ratio to increase.

Once the first and second simulated exposures were obtained, both with and without fluorescence decay, a cross-correlation algorithm was applied to the simulated profiles in the first and second exposures to determine the relative displacement. For an arbitrarily simulated velocity magnitude, U, the time separation in the absence of fluorescence decay is known (Δt_{ND}), and the ratio of relative spatial displacement obtained from the simulated exposures with (Δx) and without (Δx_{ND}) fluorescence decay, along with the result of Eq. 4.17 or 4.18, provides the following relationship:

$$U = \frac{\Delta x}{CF \cdot \Delta t_{ND}} = \frac{\Delta x_{ND}}{\Delta t_{ND}} \tag{4.20}$$

where the fluorescence decay correction factor, CF, is used in the analysis to correct the time separation between exposures. Thus, the relation in Eq. 4.20 simplifies to:

$$CF = \frac{\Delta x}{\Delta x_{ND}} \tag{4.21}$$

The coefficient, CF, is determined from the simulation by analyzing the ratio of maximum signal intensities in the reference, $S_{1,max}$, and delayed, $S_{2,max}$, profiles and relating it to the profile displacements, Δx and Δx_{ND}. Based upon analysis of the experimental profiles, the ratio of intensity values, $S_{1,max}/S_{2,max}$, can be used in conjunction with the simulation results to measure the NO fluorescence lifetime, τ_{LIF}, and then infer the magnitude of apparent displacement due to fluorescence decay. Using this methodology, the following relation between signal intensity ratio and correction factor was obtained using TableCurve 2D®:

$$CF = a_{CF} + b_{CF}\left(\frac{S_{1,max}}{S_{2,max}}\right)^{1/2} + c_{CF}\, ln\left(\frac{S_{1,max}}{S_{2,max}}\right) \tag{4.22}$$

where the coefficient values for a_{CF}, b_{CF}, and c_{CF}, for a particular Δt_{eE1} and Δt_P, vary with the second exposure duration, Δt_{E2}. Table 4.1 provides the coefficient values used to compute the correction factor for

Table 4.1: Correction factor, *CF*, coefficients for $\Delta t_{eE1} = 10.25$ ns and $\Delta t_{E2} = 100$ ns.

Coefficient	Value
a_{CF}	9.92×10^{-1}
b_{CF}	4.25×10^{-5}
c_{CF}	-2.73×10^{-3}

the experiment using the relation in Eq. 4.18 for Δt_{ND}. Figure 4.5 shows the behavior of this correction factor as a function of fluorescence lifetime. Curves for an effective first exposure of 8.25 ns and second exposure durations of 100 ns, 200 ns, and 300 ns are shown. Figure 4.5, with plots obtained from Eq. 4.22, shows that the effect of fluorescence decay, and thus of the correction factor, is most pronounced for short fluorescence lifetimes and long exposure times.

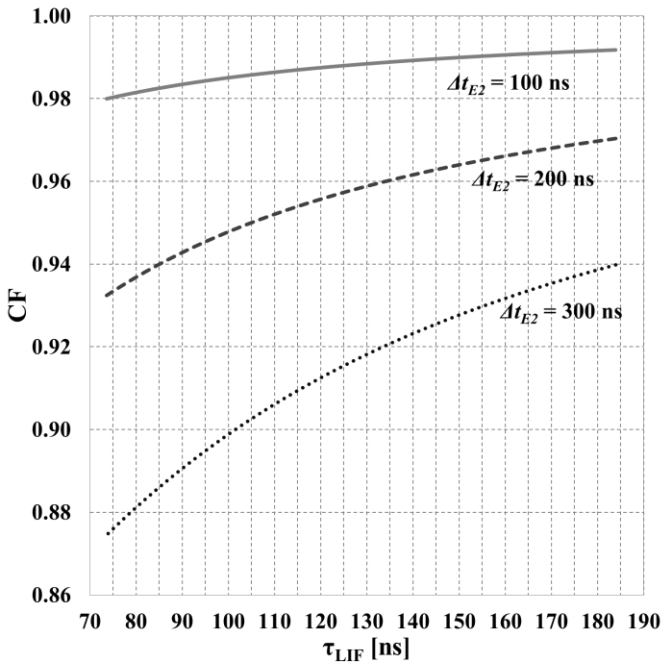

Figure 4.5: Variation of timing correction factor as a function of fluorescence lifetime for $\Delta t_{eE1} = 8.25$ ns. Image originally presented in Ref. 3.

4.2 Uncertainty Analysis

The velocity uncertainty was based upon the contributions of spatial ($u_{\overline{U},\overline{\Delta x}}$) uncertainty, timing uncertainty ($u_{\overline{U},\overline{\Delta t}}$), magnification uncertainty ($u_{\overline{U},\overline{M}}$), accuracy ($u_{\overline{U},\text{Accuracy}}$), and errors associated with spanwise velocity components ($u_{\overline{U},\text{Spanwise}}$). Calculation of the uncertainty involves propagation of empirically observed elemental errors and is similar to the approach outlined in Ref. 10. The general form of the uncertainty in the mean streamwise velocity, $\overline{U}$, is:

$$u_{\overline{U}} = \sqrt{\left(u_{\overline{U},\overline{\Delta x}}\right)^2 + \left(u_{\overline{U},\overline{\Delta t}}\right)^2 + \left(u_{\overline{U},\overline{M}}\right)^2 + \left(u_{\overline{U},\text{Accuracy}}\right)^2 + \left(u_{\overline{U},\text{Spanwise}}\right)^2} \tag{4.23}$$

In Eq. 4.23, the term $u_{\overline{U},\overline{\Delta x}}$ concerns the precision at which $\overline{U}$ can be measured because of uncertainty in determining the displacement of MTV profiles in the experiment. The term $u_{\overline{U},\overline{\Delta t}}$ concerns the precision that $\overline{U}$ can be measured because of random timing errors and jitter in the laser and camera systems. The term $u_{\overline{U},\overline{M}}$ concerns how precisely $\overline{U}$ can be measured because of uncertainty in determining the magnification from dotcard images. The term $u_{\overline{U},\text{Accuracy}}$ describes how accurately $\overline{U}$ can be measured. See Section 4.2.4 for a description of the term $u_{\overline{U},\text{Spanwise}}$.

4.2.1 Spatial Uncertainty

The uncertainty in velocity due to spatial uncertainties, $u_{U,\Delta x}$, was obtained by first determining the experimentally measured spatial shift, Δx_i, along each fluorescence profile for each single shot image. The spatial uncertainty in the mean at 95% confidence for a particular location was determined by analyzing the sensitivity of the measured velocity to variations in spatial shift:

$$u_{\overline{U},\overline{\Delta x}} = \frac{\partial \overline{U}}{\partial(\overline{\Delta x})} u_{\overline{\Delta x}} = \frac{1}{\overline{CF}\cdot\Delta t_{ND}} \frac{t_{N-1,95\%}\cdot\sigma_{\overline{\Delta x}}}{\sqrt{N}} \tag{4.24}$$

where the product of the standard deviation of the mean of Δx, $\sigma_{\overline{\Delta x}}$, and the student t-distribution value at 95% confidence, $t_{N-1,95\%}$, represents the spatial uncertainty. In this equation N represents the number of resolved single-shot velocity measurements at a particular point in the flow field, which can vary from point to point, and is less than or equal to the number of single shot images being analyzed. The term $\overline{CF}$ is the mean of the correction factors obtained using Eq. 4.22.

4.2.2 Timing Uncertainty

The uncertainty in velocity due to uncertainties in the time separation, Δt, includes systematic uncertainties resulting from empirically determined camera and laser timing jitters and duration uncertainties. Experimentally observed variations in signal intensities, which are used to infer the lifetime and calculate the correction factor, CF, also contribute to this uncertainty. The definition of the uncertainty in velocity due the timing separation is:

$$u_{\overline{U},\overline{\Delta t}} = \frac{\partial \overline{U}}{\partial(\overline{\Delta t})} \cdot u_{\overline{\Delta t}} \tag{4.25}$$

The net uncertainty in the mean due to timing, $u_{\overline{\Delta t}}$, based upon the formulation for Δt_{ND} in Eq. 4.17, is:

$$u_{\overline{\Delta t}} = \sqrt{u^2_{\overline{\Delta t},\overline{CF}} + \overline{CF}^2\left[\left(\frac{2u_{\Delta t_{eE1}}}{3}\right)^2 + u^2_{\Delta t_{D2}} + \left(\frac{u_{\Delta t_{E2}}}{2}\right)^2 + \left(\frac{u_{\Delta t_P}}{2}\right)^2\right]} \tag{4.26}$$

in the instance where $\Delta t_{eE1} \leq \Delta t_P$ and:

$$u_{\overline{\Delta t}} = \sqrt{u^2_{\overline{\Delta t},\overline{CF}} + \overline{CF}^2\left[\left(\frac{u_{\Delta t_{E2}}}{2}\right)^2 + \frac{u^2_{\Delta t_P}\left(6\Delta t^2_{eE1} - 4\Delta t_{eE1}\Delta t_P + \Delta t^2_P\right)^2 + 16u^2_{\Delta t_{eE1}}\left(3\Delta t^2_{eE1} - 3\Delta t_{eE1}\Delta t_P + \Delta t^2_P\right)^2}{6^2\left(\Delta t_P - 2\Delta t_{eE1}\right)^4} + u^2_{\Delta t_{D2}}\right]} \tag{4.27}$$

in the instance where $\Delta t_{eE1} > \Delta t_P$. The original form of the timing uncertainty in Ref. 3, corresponding to the formulation for Δt_{ND} in Eq. 4.18, is:

$$u_{\overline{\Delta t}} = \sqrt{u^2_{\overline{\Delta t},\overline{CF}} + u^2_{\Delta t_{D1}} + \overline{CF}^2\left[\left(\frac{2u_{\Delta t_{eE1}}}{3}\right)^2 + u^2_{\Delta t_{D2}} + \left(\frac{u_{\Delta t_{E2}}}{2}\right)^2 + \left(\frac{u_{\Delta t_{eE1}}}{2}\right)^2 + \left(\frac{u_{\Delta t_P}}{2}\right)^2\right]} \tag{4.28}$$

The root-sum-squared of the individual temporal uncertainties in these equations is applied to calculate the net temporal uncertainties because of the random nature of the individual uncertainties encountered during acquisition of the data.

The term $u_{\overline{\Delta t},\overline{CF}}$ in Eqs. 4.26, 4.27, and 4.28 is the timing uncertainty associated with the mean of the correction factor, CF, from Eqs. 4.21 and 4.22. On a shot-to-shot basis, variation in the signal intensity between the reference image and delayed image at a point in the tagged profiles results in a variation in the correction factor. This results in apparent variations to the elapsed time between images. To minimize the magnitude of this variation, the second exposure duration can be decreased. In Fig. 4.5, as the second gate duration is decreased, the variation in correction factor as a function of fluorescence lifetime decreases. The uncertainty in the mean velocity associated with the influence of the correction factor, $u_{\overline{\Delta t},\overline{CF}}$, at a point is:

$$u_{\overline{\Delta t},\overline{CF}} = \frac{\partial(\overline{\Delta t})}{\partial \overline{CF}} \cdot u_{\overline{CF}} = \Delta t_{ND} \cdot \frac{\partial \overline{CF}}{\partial(\overline{S_{1,max}}/\overline{S_{2,max}})} \cdot u_{(\overline{S_{1,max}}/\overline{S_{2,max}})} \tag{4.29}$$

where $u_{(\overline{S_{1,max}}/\overline{S_{2,max}})}$ is given by:

$$u_{(\overline{S_{1,max}}/\overline{S_{2,max}})} = \sqrt{\left(\frac{\partial(\overline{S_{1,max}}/\overline{S_{2,max}})}{\partial \overline{S_{1,max}}} \frac{t_{N-1,95\%} \cdot \sigma_{\overline{S_{1,max}}}}{\sqrt{N}}\right)^2 + \left(\frac{\partial(\overline{S_{1,max}}/\overline{S_{2,max}})}{\partial \overline{S_{2,max}}} \frac{t_{N-1,95\%} \cdot \sigma_{\overline{S_{2,max}}}}{\sqrt{N}}\right)^2} \tag{4.30}$$

and $\overline{CF}$ and its derivative are based on the functional form of the correction factor in Eq. 4.22.

The variation in the camera and laser timing also contributed to the timing uncertainty. The largest contribution to the timing uncertainty was from the jitter in the delay of the first exposure, Δt_{D1}. This jitter affected the overlap of the first gate and the laser pulse, as shown in Fig. 3.2. In Eqs. 4.26 and 4.27, the uncertainty associated with the first effective gate, $u_{\Delta t_{eE1}}$, incorporates this jitter, as from Figs. 4.1a and 4.2a:

$$\begin{gathered} t_{eE1} = t_P = t_{E1} + \Delta t_{E1} - \Delta t_{eE1} \\ \Delta t_{eE1} = t_{E1} + \Delta t_{E1} - t_P \end{gathered} \tag{4.31}$$

In Eq. 4.31, the time at which the laser starts, t_P, is delayed from the initial trigger of the LC880, t_0, by $\Delta t_{\mathrm{Q-Switch}}$, or $t_P = t_0 + \Delta t_{\mathrm{Q-Switch}}$. The time at which the first exposure opens, t_{E1}, is delayed from t_0 by Δt_{D1}. Rearranging Eq. 4.31 and including the relation describing the start of the laser pulse and first exposure gives:

$$u_{\Delta t_{eE1}} = \sqrt{\left(\frac{\partial(\Delta t_{eE1})}{\partial(t_{E1})} u_{t_{E1}}\right)^2 + \left(\frac{\partial(\Delta t_{eE1})}{\partial(\Delta t_{E1})} u_{\Delta t_{E1}}\right)^2 + \left(\frac{\partial(\Delta t_{eE1})}{\partial(t_P)} u_{t_P}\right)^2} \tag{4.32}$$

Table 4.2: Laser and camera timing uncertainties.

Parameter	Value, ns (Eq. 4.28, Also Ref. 3)	Value, ns (Eqs. 4.26 and 4.27)
Trigger Signal, u_{t_0}	-	0.2[e]
First Exposure Delay, $u_{\Delta t_{D1}}$	2.0[a]	1.9[f]
Q-Switch, $u_{\mathrm{Q-Switch}}$	-	1.0[g]
First Exposure, $u_{\Delta t_{E1}}$	1.0[b]	0.2[f]
Laser Pulse, $u_{\Delta t_P}$	0.1[c]	0.5[g]
Second Exposure Delay, $u_{\Delta t_{D2}}$	0.5[d]	0.2[f]
Second Exposure, $u_{\Delta t_{E2}}$	1.0[b]	0.2[f]

[a] DiCAM PRO Manual, http://www.pco.de/fileadmin/user_upload/db/download/MA_DPOPIE_0411.pdf, [retrieved May 29, 2013]
[b] PCO Document via private communication, 2/21/2008
[c] Estimated
[d] Product Sheet,http://www.pco.de/fileadmin/user_upload/db/products/datasheet/dicam_pro_20110531.pdf, [retrieved May 29, 2013]
[e] LabSmith® LC880 Specifications, http://www.labsmith.com/products/LabSmith_LC880_Brochure.pdf, [retrieved May 29, 2013]
[f] Estimate based on analysis of output trigger signal from DiCAM PRO
[g] Quanta-Ray® Pro Series Specification Sheet, http://assets.newport.com/webDocuments-EN/images/Quanta-Ray_Pulsed_YAG_SP.pdf, [retrieved May 29, 2013]

where $u_{t_{E1}} = \sqrt{u_{t_0}^2 + u_{\Delta t_{D1}}^2}$ and $u_{t_P} = \sqrt{u_{t_0}^2 + u_{\Delta t_{\mathrm{Q-Switch}}}^2}$. The timing uncertainty associated with the first effective exposure is then:

$$u_{\Delta t_{eE1}} = \sqrt{2u_{t_0}^2 + u_{\Delta t_{D1}}^2 + u_{\Delta t_{E1}}^2 + u_{\Delta t_{\mathrm{Q-Switch}}}^2} \tag{4.33}$$

This relation should be applied to Eqs. 4.26 and 4.27. It was not applied in Ref. 3 to Eq. 4.28. Instead, $u_{\Delta t_{eE1}}$ was assumed equal to $u_{\Delta t_{E1}}$, and $u_{\Delta t_{D1}}$ was treated independently of this term.

The timing uncertainties in Eqs. 4.26, 4.27, and 4.28 have been obtained from manufacturer-provided specifications, measurement, or estimate. Table 4.2 gives the magnitude of camera and laser timing uncertainties used in this uncertainty analysis and those used in Ref. 3.

4.2.3 Magnification and Accuracy

To determine the uncertainty due to magnification, several measurements were taken at different locations on the dotcard image. The mean of the magnification, $\bar{M}$, and its standard deviation, $\sigma_{\bar{M}}$, for the experiment in this chapter is given in Table 4.3. The general form of the magnification uncertainty using N measurements at 95% confidence is:

$$u_{\bar{U},\bar{M}} = \frac{\partial \bar{U}}{\partial \bar{M}} u_{\bar{M}} = \frac{(\overline{\Delta x})_{PIXEL}}{CF \cdot \Delta t_{ND}} \cdot \sigma_{\bar{M}} \cdot t_{N-1,95\%} \tag{4.34}$$

Table 4.3: Magnification and accuracy values.

Parameter	Value
Mean Magnification, $\overline{M}$	5.70×10^{-2} mm/pixel
Uncertainty in the Mean Magnification, $u_{\overline{M}}$	$\pm8.46\times10^{-5}$ mm/pixel
Maximum Uncertainty in the $\overline{U}$ caused by Magnification Uncertainty, $u_{\overline{U},\overline{M}}$	±1.49 m/s
Velocity Accuracy, $u_{\overline{U},\text{Accuracy}}$	±10 m/s

where $(\overline{\Delta x})_{PIXEL} = \overline{\Delta x}/\overline{M}$ is the displacement, in pixels, between profiles in the reference and delayed images of the processed images. This uncertainty scales linearly with the measured displacement between the reference and delayed images. Table 4.3 provides an upper-bound estimation of the uncertainty in the mean velocity due to magnification error considering a maximum velocity of 1260 m/s for the wedge experiment.

To estimate the accuracy of the cross-correlation technique as applied to the wedge experiment, velocity images were obtained while the wind tunnel was not operating, resulting in (nearly) static gas. While these images were collected, the tunnel pressure was allowed to slowly increase from approximately 320 Pa to 1250 Pa to study the effects of pressure (mainly collisional quenching) on the measurement accuracy and precision. Pressure was increased via leaks present in the tunnel when the pressure was reduced to near vacuum, and created the potential for small velocities within the test section. The images were then analyzed with the cross-correlation software to determine the velocity and uncertainty, as well as the signal ratio data provided in Fig. 4.5. Figure 4.6 shows the results of this zero-velocity analysis over the range of pressures tested. Based upon the mean velocity analysis, the accuracy was estimated to be ±10 m/s for the conditions of the experiment, shown by the accuracy bounds in Fig. 4.6. Table 4.3 also lists this accuracy value.

Both the accuracy and magnification uncertainty terms for a particular set of experiments (for which the optical arrangement is not altered) have absolute magnitudes, are invariant on a shot-to-shot basis, and do not vary between individual runs. In Ref. 3 they were originally added

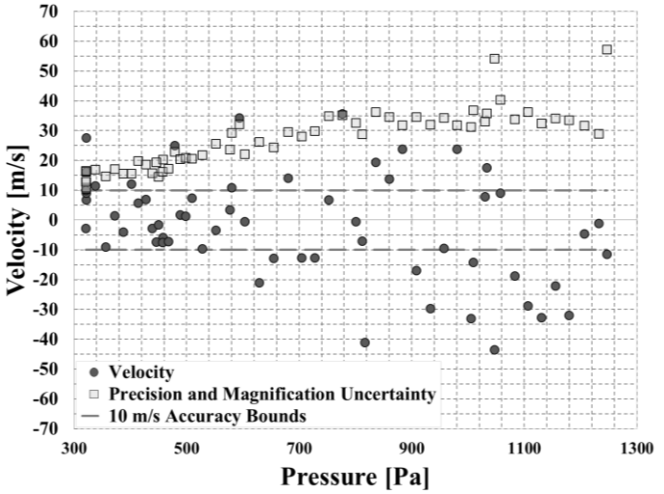

Figure 4.6: Velocity accuracy data obtained from low pressure, no-flow wind tunnel test. Image originally presented in Ref. 3.

separately to the root-sum-squared precision errors of Eqs. 4.24 and 4.25 such that:

$$u_{\bar{U}} = u_{\bar{U},\bar{M}} + u_{\bar{U},\text{Accuracy}} + u_{\bar{U},\text{Spanwise}} + \sqrt{\left(u_{\bar{U},\overline{\Delta x}}\right)^2 + \left(u_{\bar{U},\overline{\Delta t}}\right)^2} \tag{4.35}$$

However, in this analysis, the form in Eq. 4.23 is used as it is assumed that each of these uncertainty terms are random and independent of each other.

4.2.4 Spanwise Velocity Uncertainty

In estimating the streamwise velocity uncertainty, uncertainty due to a possible velocity component, V, parallel to the laser beam must also be included. After the first exposure has closed, a point (x_0, z_0) along the profile will transit to a new point at $(x_0 + \Delta x,\ z_0 + \Delta z)$, at which time the second exposure opens. The cross-correlation is then performed between the profiles centered at (x_0, z_0) in the first exposure and $(x_0 + \Delta x_m, z_0)$ in the second exposure, where the subscript *m* refers to the measured displacement.

This situation is shown schematically in Fig. 4.7, and is similar to that in Fig. 7 of Ref. 11 and Fig. 2 of Ref. 12. In this figure, the straight, vertical violet line corresponds to the profile imaged in the first effective exposure and the curved violet profile corresponds to the profile imaged in the second exposure. A spanwise velocity component, V, results in a measured streamwise velocity of $U_m = \Delta x_m/\Delta t$ while the true streamwise velocity is $U = \Delta x/\Delta t$.

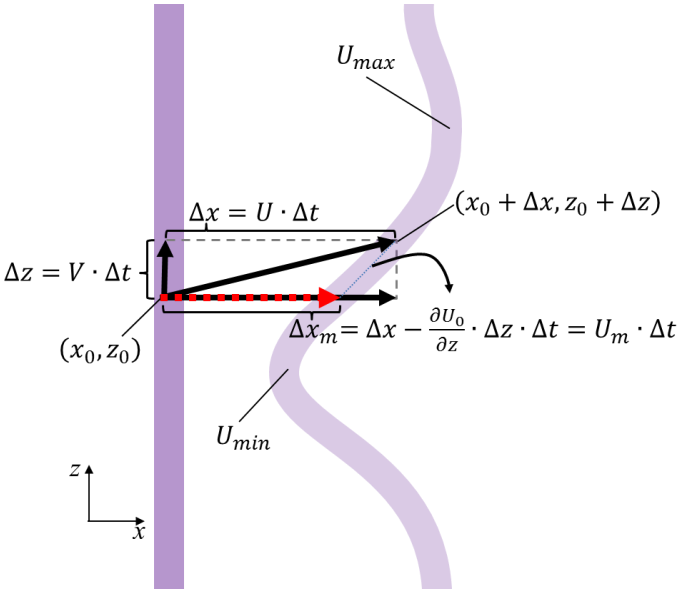

Figure 4.7: Velocity uncertainty resulting from velocity component parallel to tagged profile. After Fig. 7 of Ref. 11 and Fig. 2 in Ref. 12.

The error in the streamwise displacement measurement incurred from the presence of the V component of velocity, similar to the derivation in Ref. 11, is:

$$\Delta x - \Delta x_m = \frac{\partial U_0}{\partial z} \cdot \Delta z \cdot \Delta t \tag{4.36}$$

Using the relations in Fig. 4.7 of $\Delta x = U \cdot \Delta t$ and $\Delta z = V \cdot \Delta t$, and relating the measured streamwise displacement (denoted by the dashed red arrow in Fig. 4.7) to the measured streamwise velocity through $\Delta x_m = U_m \cdot \Delta t$, Eq. 4.36 can be rearranged in a form similar to that in Ref. 11 as:

$$(U - U_m)\Delta t = \frac{\partial U_0}{\partial z} \cdot (V \cdot \Delta t) \cdot \Delta t \tag{4.37}$$

Dividing Eq. 4.37 through by Δt gives the streamwise velocity uncertainty resulting from a z-component of velocity as:[11]

$$u_{\bar{U},\text{Spanwise}} = U - U_m = \frac{\partial U_0}{\partial z} \cdot V \cdot \Delta t \tag{4.38}$$

This error will be most notable in regions of the flow with a relatively large streamwise velocity gradient ($\partial U_0/\partial z$), a relatively large z-component of velocity (V), or a long time delay (Δt). While $\partial U_0/\partial z$ can be obtained through analysis of the delayed image at the point $(x_0 + \Delta x_m, z_0)$ and Δt can be obtained through the relation in Eq. 4.17, no knowledge of the magnitude or direction of V is available.

An alternative method to Eq. 4.38 to obtain an estimate of this uncertainty is to assume that the only significant velocity components existed in the streamwise direction (x-direction) and spanwise direction (z-direction). Initially, the squared difference between the global maximum ($\bar{U}_{max}$) and local measured ($\bar{U}_m$) velocity magnitude at a point, as shown in Fig. 4.7, is assumed to be the upper bound of the spanwise velocity at that point such that $V_{est}^2 \leq \bar{U}_{max}^2 - \bar{U}_m^2$.

Using the V_{est} value at a point, the delayed image is then shifted both up and down (in the z-direction) and the streamwise velocity recalculated corresponding to shift magnitudes of $\zeta_\pm = \pm V_{est} \cdot \Delta t/\bar{M}$, respectively. These recalculated streamwise velocities, corresponding to shift positions ζ_+ and ζ_-, are U_{ζ_+} and U_{ζ_-}, respectively.

A schematic of this process is shown in Fig. 4.8. In this figure, the vertical violet line corresponds to the tagged profile imaged in the first exposure. The

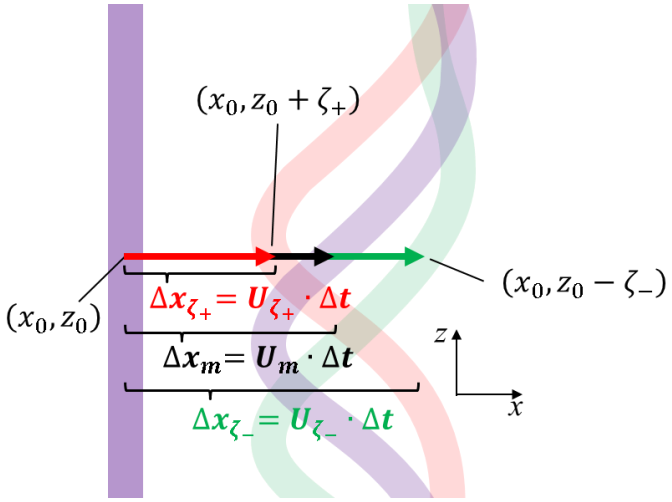

Figure 4.8: Schematic of method for estimating uncertainty in velocity resulting from a spanwise velocity component.

lighter violet curved profile corresponds to the profile imaged in the second exposure, with the black arrow representing the measured streamwise displacement. The light red curved profile corresponds to the profile imaged in the second exposure, which has been shifted by ζ_+, and with a measured streamwise displacement denoted by the red arrow. The light green curved profile corresponds to the profile imaged in the second exposure, which has been shifted by ζ_-, and with a measured streamwise displacement denoted by the green arrow.

The streamwise velocities, U_{ζ_+} and U_{ζ_-}, obtained from this process are then used to compute the streamwise velocity uncertainty at each point along a tagged profile resulting from a spanwise component of velocity:

$$u_{\overline{U},\text{Spanwise}} = \sqrt{\left(\overline{U}_m - \overline{U}_{\zeta_+}\right)^2 + \left(\overline{U}_m - \overline{U}_{\zeta_-}\right)^2} \tag{4.39}$$

As an example, a measured streamwise velocity of $\overline{U}_m = 700$ m/s along a profile having a maximum velocity of $\overline{U}_{max} = 1100$ m/s gives $V_{est} = \pm 849$ m/s. If the spanwise velocity gradient at the measurement location is $\partial\overline{U}/\partial z =$ 340000 s^{-1}, and assuming Δt = 550 ns, then $(\overline{U}_m - \overline{U}_{\zeta_+})^2 = (\overline{U}_m - \overline{U}_{\zeta_-})^2 \approx$ (159 m/s)^2. This gives $u_{\overline{U},\text{Spanwise}} \approx$ 225 m/s.

4.3 Results

Table 3.1 in Chapter 3 provides the conditions for the experiment described here. Figure 4.9 shows the wedge model with the 2-mm-tall × 4-mm-diameter isolated cylindrical roughness element and the corresponding field of view imaged by the camera. Figure 4.10a shows an averaged PLIF flow visualization image approximately 1.7±0.3-mm off the model surface. Figures 4.10b and 4.10c show the 38-shot averaged tagged profiles for the reference and delayed images, respectively. Figure 4.10d shows the measured mean velocity profiles obtained with the cross-correlation algorithm. The width of the bars represents the uncertainty in the mean streamwise velocity. Profile numbers are provided below the velocity axes.

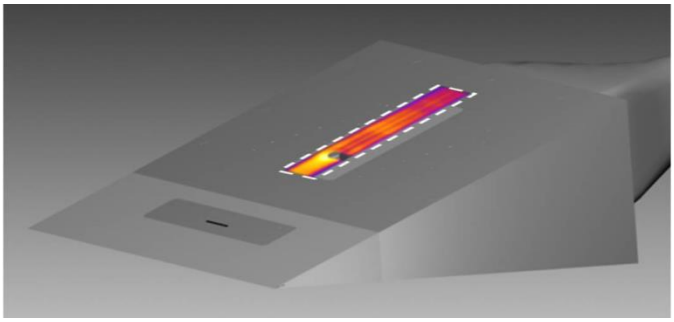

Figure 4.9: Perspective view of wedge model, cylindrical roughness, and corresponding field of view. Image originally presented in Ref. 3.

In Fig. 4.10a, prior to passing around the cylindrical boundary layer roughness element, the boundary layer flow is completely laminar. After the flow passes the cylinder, the region directly behind the roughness shows that some level of disturbance is occurring based upon the variation of signal intensity in this image.

The streamwise velocity measurement, shown in Fig. 4.10d, was taken approximately 2.1±0.2-mm above the model surface. The velocity scale for this image is 0 to 1438 m/s. In the first two profiles upstream of the cylinder, the flow indeed appears to be nearly uniform and laminar. For the 1st profile, the mean velocity along the line is 915 m/s with an average uncertainty of 41 m/s. For the 2nd profile, the mean

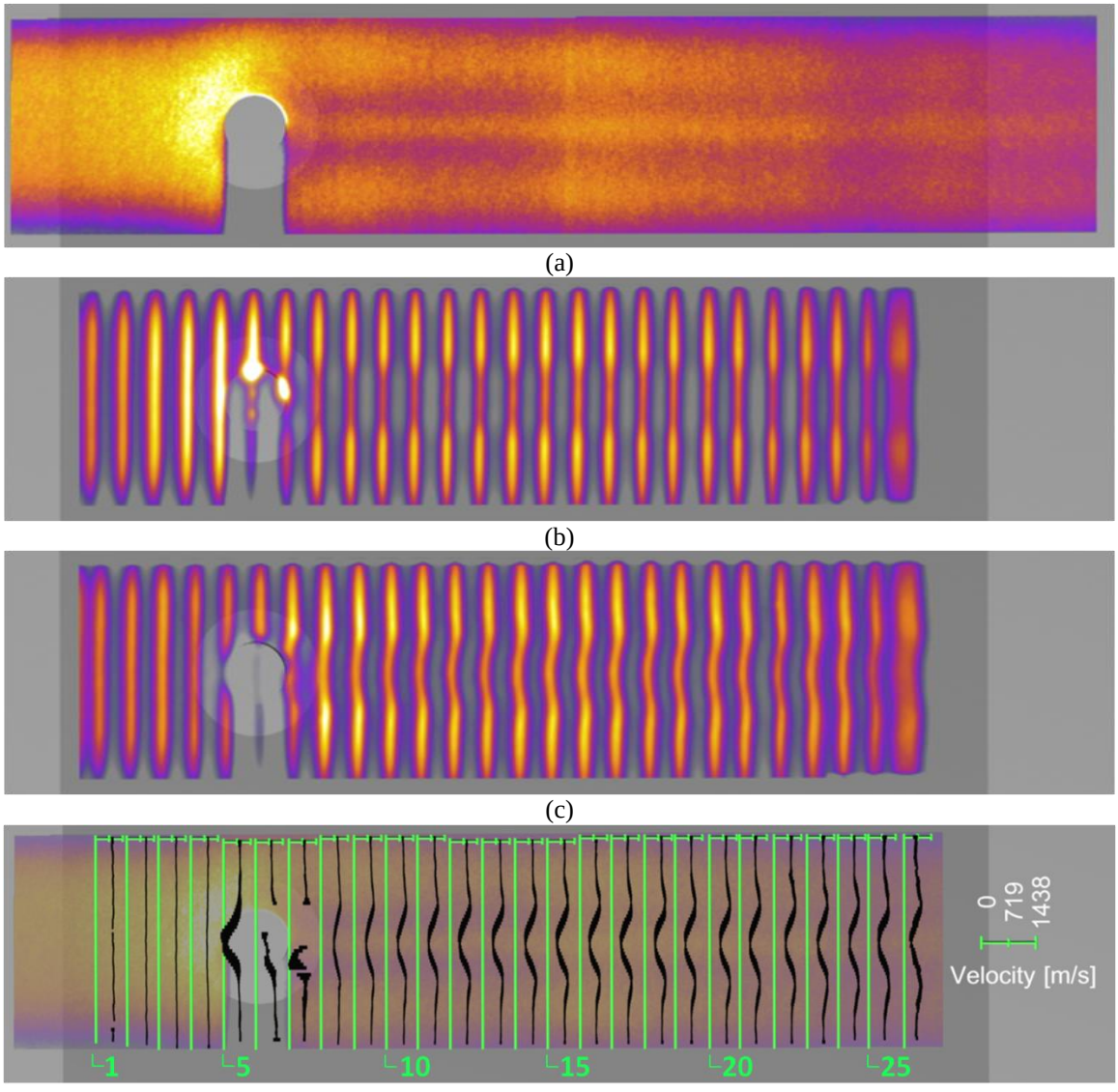

Figure 4.10: Wedge model: (a) flow visualization image, (b) reference image, (c) delayed image, and (d) mean velocity and uncertainty in the mean results. Images originally presented in Ref. 3.

velocity along the line is 1008 m/s with an average uncertainty of 32 m/s. Close examination of the 3rd and 4th profiles in the region directly upstream of the cylinder shows a small level of bowing away from the cylinder. This could signify some level of interaction with the roughness element. Along the 3rd line, the velocity drops to 905 m/s, along the 4th line it drops to 830 m/s at the point of intersection with the centerline, and the flow is nearly brought to rest in front of the cylinder.

As the flow progresses around the roughness element, the measured velocity profiles appear undisturbed with the exception of the velocity values in the immediate wake of the cylinder. As the flow passes around the cylinder, a deficit of velocity extends downstream along the centerline, which is visible even in the raw delayed image shown in Figure 4.10c. In contrast, the flow downstream of the upper and lower edges of the roughness element in these images is accelerated beyond the baseline streamwise velocity. Downstream of the cylinder, the streamwise velocity observed along the centerline drops to a measured low of 344 m/s on the last (26th) line. In the accelerated flow region directly downstream of the top and bottom edges of the cylinder, the maximum velocity encountered is 1093 m/s on the 22nd line.

Figure 4.11 shows, from left to right, the magnified views of the 2nd, 4th, 10th, and 24th streamwise velocity profiles, respectively. The 2nd profile (Fig. 4.11a) with a mean streamwise velocity of approximately 1008 m/s has uncertainties ranging from 27 m/s to 43 m/s. The decreased streamwise velocity feature, a left-bowing profile, in the 4th velocity profile (Fig. 4.11b) gives uncertainty-in-the-mean magnitudes ranging from 30 m/s to 43 m/s. The 10th profile (Fig. 4.11c) shows a drop in velocity along the centerline to approximately 612 m/s. The increased velocities occurring above and below the low-velocity region are approximately 1040 m/s and 1021 m/s, respectively. In regions of steep velocity gradients, the maximum uncertainties encountered along this profile are on the order of 116 m/s to 125 m/s. The largest uncertainty is 125 m/s, and is due to the inclusion of the spanwise velocity component uncertainty. The 24th profile (in Fig. 4.11d) shows a similar trend to that of the 10th profile. The flow above and below the low velocity region, which has a minimum velocity of 593 m/s, has maximum velocities of 1058 m/s and1050 m/s, respectively.

4.4 Discussion

The double-shutter camera used in this experiment served to reduce measurement sensitivity to vibration that would otherwise be encountered when using a single-framing camera, such as in Ref. 7,

where delayed images are compared with a reference image that is separately acquired and uncorrelated in time. To estimate the improvement in uncertainty achieved by using the single camera in double-shutter mode, rather than a single-framing camera, an averaged image from the set of effective first exposure images was paired with the set of second exposure images, and analyzed using the cross-correlation method described in the previous sections. This was done to replicate an experiment in which a single-framing camera obtains an initial set of images with no delay, and the average of those images is correlated with another set subsequently taken with a time delay. The resulting spatial uncertainty $u_{\overline{U},\overline{\Delta x}}$, which is the largest contributor to the total uncertainty, was, on average, 41% greater than that obtained when correlating single sequential image pairs. Similarly, a 40% increase in uncertainty is obtained when correlating a single image from the effective first exposure set paired with the set of second exposure images. Stated another way, the use of the single double-shutter camera technique improves uncertainty in the mean streamwise velocity by 28%. In experiments having larger vibration levels, the single double-shutter camera technique could provide further reduction in uncertainty compared to single-shutter camera techniques.

The double-shutter camera streamwise velocity measurement was also free of additional errors that would otherwise be encountered if a two-camera or single-framing camera velocimetry system, which can be sensitive to vibration, beam pointing, and alignment issues, were used. The disadvantage of the double-shutter camera, in comparison to a two-camera or single-framing camera system, is the hardware-

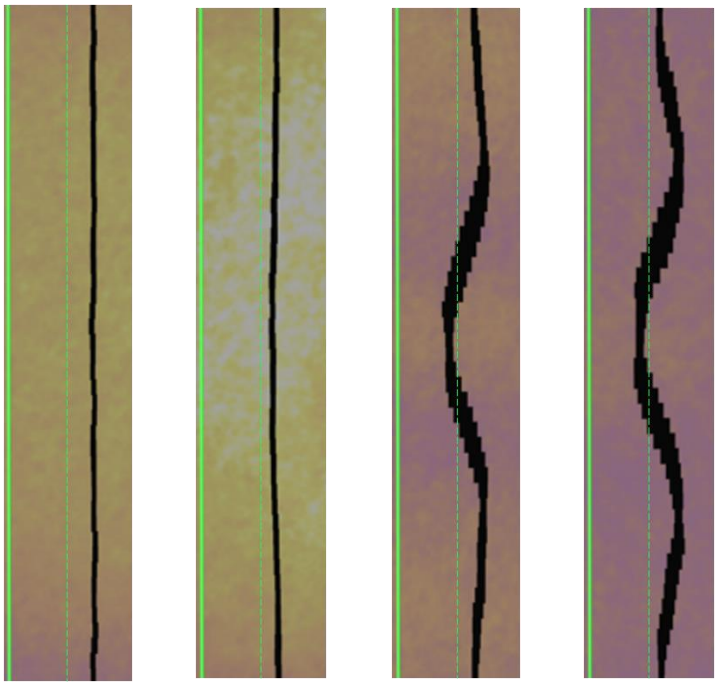

(a) (b) (c) (d)

Figure 4.11: Magnified view of the midportion of the (a) 2nd, (b) 4th, (c) 10th, and (d) 24th mean streamwise velocity profiles and their corresponding uncertainties. The dashed green line represents the mid-scale velocity of 719 m/s. Images originally presented in Ref. 3.

limited Δt_{D2} = 500 ns exposure delay between the reference and delayed images and the limitation of a single gain setting (i.e. the gain cannot be controlled independently for the two exposures). These limitations result in delayed images with reduced signal, which can be avoided with a two-camera or single-framing camera by increasing gain or using a shorter delay. However, since the total uncertainty is inversely proportional to the exposure delay, if the signal in both exposures is held constant, reductions in gate delay (which is possible with a two-camera or single-framing camera system) result in increased uncertainty. Therefore, although increased signal levels can be achieved through independent gain adjustments using a two-camera system, reduction of the gate delay to increase signal levels with such a system mainly results in a tradeoff with increased uncertainty.

To compensate for the decreased signal level associated with the double-shutter camera, a timing methodology was developed in which the first exposure was partially overlapped with the laser pulse (as depicted in Fig. 4.1). This allowed only a small fraction of the fluorescence from the tagged velocity profiles to be captured in the first exposure, resulting in comparable signal levels in the reference and delayed image. Additionally, by varying the length of the second exposure, the amount of fluorescence acquired in the second exposure could be controlled to some level. However, by increasing the second exposure duration, the level of blurring and asymmetry of the tagged profile also increased. To account for this, a correction (described in Section 4.1.3.3) was applied that depended upon the ratio of signal intensities in the reference and delayed profiles (and implicitly on the fluorescence lifetime), the overlap between the laser pulse and effective first exposure, as well as the duration of the second exposure. This correction was independent of the streamwise velocity, and hence the extent of blurring introduced by the velocity. The methodology can be extended to 2-dimensional MTV measurements.

In relatively good signal-to-noise regions with uniform streamwise velocity components along the length of the tagged profile, the measured uncertainty in the mean streamwise velocity is on the order of 3% (30 m/s for a 1000 m/s flow). In regions where the signal-to-noise ratio remains relatively high but large spanwise velocity gradients exist, the measured velocity uncertainty is on the order of 20%. Table 4.4 provides a listing of the typical constituent uncertainty in the mean magnitudes for the experiment using Eq. 4.35 of Ref. 3. The left column of Table 4.4 provides these values for the 2nd profile (see Figs. 4.10d and 4.11b). The right column contains the constituent uncertainty in the mean magnitudes at two points on

opposite sides of the centerline for profiles 11 through 25 where the maximum spanwise velocity uncertainty is encountered. These points correspond to the location of maximum spanwise velocity gradients. The total uncertainties, as a percentage of the mean velocity, represent the extremes of the uncertainty magnitudes encountered in this experiment.

Based upon the measurements observed in this experiment and the simulations performed to determine the correction factor, it was determined that using a shorter second exposure will limit the variability (and therefore timing uncertainty in Eqs. 4.26 and 4.27) in the correction factor compared to using a longer second exposure. This was detailed in Fig. 4.5. An alternative way to avoid the variability due to the correction factor and its associated uncertainty is by using a three-laser MTV technique such as the NO_2-to-NO photolysis technique described in Chapter 2. The tagged profiles would be optically excited with a laser source prior to both the first and second exposures, which would be of equal durations. This method would result in similarly shaped fluorescence profiles, would generally not require any correction for profile asymmetry, and would remove any uncertainties associated with the overlap of the first exposure and the excitation laser. Another benefit of such a scheme would be the removal of the limitation on the maximum time separation between exposures that is imposed as a result of the finite fluorescence lifetime. This would allow for increased temporal separation between the reference and delayed images, resulting in decreased uncertainties proportional to the increased separation time. This would also provide the capability to work in higher-pressure conditions where fluorescence quenching would otherwise limit the signal in the second exposure. Difficulties with this three-laser technique include increased experimental complexity (3 lasers are used), seeding NO_2 safely into the flow (it is toxic), the need for higher laser energies in order to dissociate the NO_2, and the heavier molecular weight of NO_2 with respect to air. This approach is explored in Chapters 6 and 7.

Table 4.4: Constituent uncertainty term analysis for wedge experiment for an average of N = 38 single-shot measurements.

	2nd Profile: $\overline{U}_{AVG}$ = 1008 m/s Mean % of $\overline{U}_{AVG}$	$(\partial \overline{U}_{AVG}/\partial y)\|_{max}$ = 787 m/s Mean % of $\overline{U}_{AVG}$
$u_{\overline{U},\overline{M}}$	0.15	0.15
$u_{\overline{U},\text{Accuracy}}$	0.99	1.27
$u_{\overline{U},\text{Spanwise}}$	0.13	15.45
$\sqrt{u_{\overline{U},\overline{\Delta x}}^2 + u_{\overline{U},\overline{\Delta t}}^2}\begin{cases}u_{\overline{U},\overline{\Delta x}}\\u_{\overline{U},\overline{\Delta t}}\end{cases}$	$1.93\begin{cases}1.88\\0.41\end{cases}$	$4.10\begin{cases}4.08\\0.41\end{cases}$
$u_{\overline{U}}$	2.18	16.04

A significant contribution to the uncertainty in the mean streamwise velocity measurement was the measured accuracy. After the experiment was performed, it was learned that there was the potential for small velocities within the test section when it was reduced to near vacuum. This was a result of leaks in the facility test section. If a non-zero gas velocity field did indeed exist within the test section during acquisition of the zero-velocity images, the resulting accuracy value would be skewed from a true zero value, leading to an underestimation of the true accuracy of the measurement (overestimation of the error). Measurements along individual lines from these images seem to confirm this hypothesis, as non-zero velocities were observed with trends that appear to have a functional relationship with the tunnel pressure. Correction of this may result in lower velocity uncertainties with improved accuracy estimation. A possible solution is to have a static cell at the tunnel pressure that can be imaged separately to obtain a measure of velocity accuracy. Such a measurement could potentially improve the determination of the experimental accuracy.

The next two sections detail two additional error sources that were identified after performing the experiment, but were not included in the uncertainty analysis outlined in Section 4.2.

4.4.1 Measurement Error Resulting from Collisional Quenching Gradients

One issue encountered when making streamwise velocity measurements in a Reaction Control System (RCS) jet in Ref. 3 was the asymmetric error of streamwise velocity in the immediate vicinity of the jet nozzle exit. As the gas exits the nozzle in this region, a rapid drop in pressure occurs, resulting in a negative collisional quenching gradient, meaning that the quenching rate is decreasing rapidly (see Eq. 2.7 in Chapter 2). The result of this gradient is an apparent shift in the tagged profile much greater than that expected. Therefore, in the presence of a negative collisional quenching gradient, the measured velocities will appear to be higher than those measured if no gradient were present. Figure 4.12 shows the results of a simulation performed to analyze the effects of such a gradient. For this simulation, Δt_{eE1}= 8.25 ns, Δt_P= 9.5 ns, and Δt_{E2}= 100 ns.

In the simulation, a 19-pixel FWHM excitation source located 2 pixels to the left of a 55-pixel wide correlation window was used. At the center of the correlation window, the pressure (and hence quenching rate), was set to a particular value, noted in the legend of Fig. 4.12. Additionally, for each pressure condition, an axial velocity magnitude ranging from 100 m/s to 1200 m/s was simulated to see what, if any,

effect gas velocity had on skewing of the velocity measurement in the presence of a quenching gradient. In Fig. 4.12, the horizontal axis corresponds to the magnitude of the quenching gradient simulated. The vertical axis in this figure corresponds to the difference between the profile shift measured, in pixels, for the case with ($\Delta x_{Gradient}$) and without ($\Delta x_{No\ Gradient}$) a quenching gradient present. For relatively weak gradient values (> -3 (ns·mm)$^{-1}$), $\Delta x_{Gradient}$ scales linearly with $\Delta x_{No\ Gradient}$ as the magnitude of the gradient increases, as shown in Fig. 4.12. Over this range of gradient magnitudes, the effect of the gradient is approximately independent of velocity, and can be defined by the relation:

$$\Delta x_{Gradient} \approx -112 \cdot \left(\frac{dQ_{21}}{dx}\right) + \Delta x_{No\ Gradient},\ -3 < \frac{dQ_{21}}{dx} < 0 \tag{4.39}$$

This influence manifests itself most strongly during the second exposure, when the quenching field determines the spatial shape of the fluorescence profile. For stronger gradients, the velocity of the tagged profile begins to affect $\Delta x_{Gradient}$. As the magnitude of the quenching gradient increases, increases in the gas velocity have the effect of decreasing the influence of the gradient on the measured displacement of the profiles, $\Delta x_{Gradient}$.

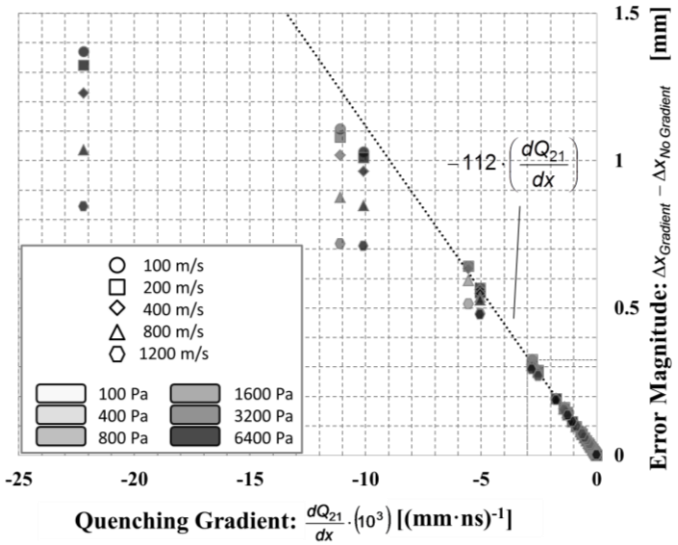

Figure 4.12: Non-zero quenching gradient influence on perceived profile shift. Image originally presented in Ref. 3.

This is because the increased velocity places the profile into a region where the quenching is much less than that at the center of the correlation window where the profile was initially tagged, resulting in a right-weighting of the apparent profile. As the quenching gradient magnitude exceeds 6 (ns·mm)$^{-1}$, increases in collisional quenching at the center of the correlation window will begin to further left-weight the profile observed in the second exposure as the combined effect of fluorescence decay and blurring affect the apparent profile. This in turn counteracts the right-weighting occurring due to the presence of the gradient.

4.4.2 Measurement Error Resulting from Velocity Gradients

The presence of a pressure gradient, such as that ahead of the isolated cylindrical roughness element, may result in a significant error in the measured streamwise velocity obtained from a MTV measurement.

Figure 4.13a shows an idealized representation of the influence of a local adverse pressure gradient on the MTV measurement. In this figure, the molecules are initially tagged and imaged at a location x_1 having a local velocity profile corresponding to U_1. During Δt (Eqs. 4.17 or 4.18), a tagged molecule proceeds downstream in the presence of the adverse pressure gradient and experiences a deceleration. After Δt, a given tagged molecule, now at a location x_2, is subject to the local velocity profile corresponding to U_2. Since the velocity at x_1 is inferred from the displacement, Δx, of the tagged molecules observed over Δt, the velocity measurement error is potentially as great as $\Delta U = (U_2 + U_1)/2$. Qualitatively, this error will be lower at positions near the wall, where the low-speed conditions minimize profile displacement, and at positions with minimal pressure gradients, where ΔU is small.

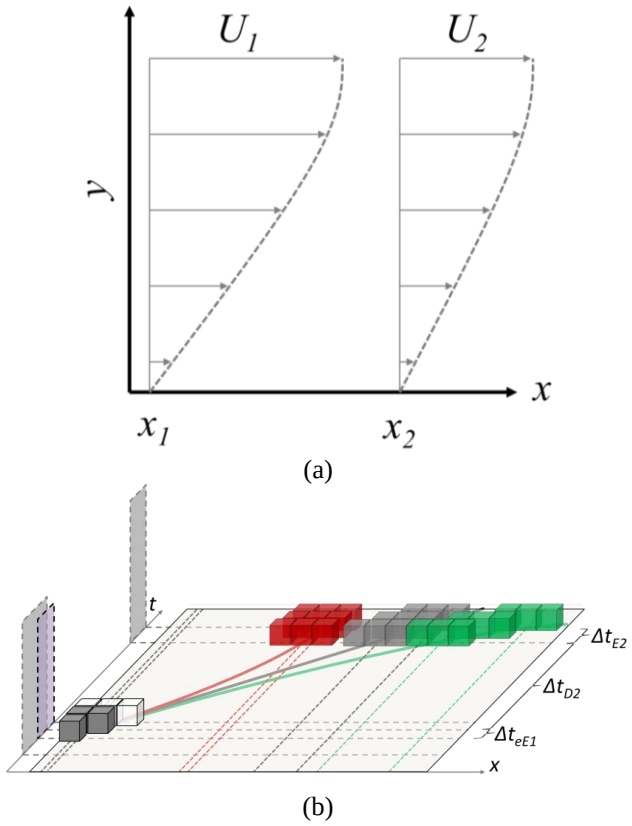

Figure 4.13: Graph of (a) influence of an adverse pressure gradient on streamwise velocity and (b) space-time diagram of single-laser MTV process with adverse (red), zero (gray), and favorable (green) acceleration.

Figure 4.13b provides a space-time diagram of the single-laser MTV process in the presence of adverse (red), zero (gray), and favorable (green) pressure gradients. This figure is similar to Figs. 4.1 and 4.2. It shows that a constant acceleration or deceleration can potentially result in a dramatically different intensity distribution captured in the second exposure. This measurement error can be accounted for by directly comparing experimental displacements with CFD. This is discussed in the Future Work in Chapter 8.

4.5 Conclusions

This chapter describes a velocimetry technique using a single, double-frame camera to obtain spatially and temporally correlated images. To overcome the camera hardware restriction of a single gain setting, a

new timing methodology was developed to acquire the reference and delayed images so that comparable signal intensities would be obtained in both exposures. An analysis comparing uncertainty levels achieved with a single-shutter camera technique versus the double-shutter technique described in this paper show a 28% decrease in uncertainty using the double-shutter camera. A correction technique was introduced which estimated the apparent profile shift that would be observed in the delayed image due to fluorescence decay and blurring of tagged profiles over the duration of second exposure. This correction technique used a geometric representation of the time-dependent signal intensity to relate the spatial CCD signal distribution to the measured velocity component. A detailed derivation of the total uncertainty in the mean streamwise velocity was presented which accounted for all major sources of spatial, temporal, and signal error. Errors associated with velocity components orthogonal to the measured component (parallel to the laser sheet) were also quantified. Mean streamwise velocities and uncertainties were calculated for the 10-degree half-angle wedge in a Mach 10 perfect gas air flow. Average uncertainties in the mean below 30 m/s (2.7% of the measured average velocity) have been obtained in regions with optimal signal intensities using this technique. A discussion of the biasing effect of collisional quenching gradients and pressure gradients on these types of velocity measurements was also provided. Chapter 5 details the application of this technique to measure streamwise velocity in a hypersonic laminar boundary layer both with and without an isolated roughness element.

---

[1] Gendrich, C.P, and Koochesfahani, M.M., "*A spatial correlation technique for estimating velocity fields using molecular tagging velocimetry (MTV)*," Experiments in Fluids, Vol. 22, pp. 67-77, 1996.

[2] Bathel, B.F., Danehy, P.M., Inman, J.A., Jones, S.B., Ivey, C.B., and Goyne, C.P., "*Multiple Velocity Profile Measurements in Hypersonic Flows Using Sequentially-Imaged Fluorescence Tagging*," 48th AIAA Aerospace Sciences Meeting, AIAA Paper 2010-1404, January 4-7, 2010, Orlando, FL.

[3] Bathel, B.F., Danehy, P.M., Inman, J.A., Jones, S.B., Ivey, C.B., and Goyne, C.P., "*Velocity Profile Measurements in Hypersonic Flows Using Sequentially-Imaged Fluorescence-Based Molecular Tagging Velocimetry*," AIAA Journal, 49(9), pp. 1183-1896, September, 2011.

[4] Alderfer, D.W., Danehy, P.M., Wilkes Inman, J.A., Berger, K.T., Buck, G.M., and Schwartz, R.J., "*Fluorescence Visualization of Hypersonic Flow Over Rapid Prototype Wind-Tunnel Models*," AIAA 2007-1063, 45th Aerospace Sciences Meeting and Exhibit, Reno, NV, January 8-11, 2007.

[5] Sanchez Sorzano, C.O., Thevenaz, P., and Unser, M., "*Elastic Registration of Biological Images Using Vector-Spline Regularization*," IEEE Transactions on Biomedical Engineering, 52(4), pp. 652-663, April, 2005.

[6] Rasband, W.S., ImageJ, U.S. National Institutes of Health, Bethesda, MD, USA, http://rsb.info.nih.gov/ij, 1997-2009.

[7] Danehy, P.M., O'Byrne, S., Houwing, A.F.P, Fox, J.S., and Smith, D.R., "*Flow-Tagging Velocimetry for Hypersonic Flows Using Fluorescence of Nitric Oxide*," AIAA Journal, 41 (2), pp. 263-271, February 2003.

[8] Settersten, T.B., Patterson, B.D., and Carter, C.D., "*Collisional quenching of NO A2Σ+(v'=0) between 125 and 294 K*," Journal of Chemical Physics, Vol. 130, 2009.

[9] Settersten, T.B., Patterson, B.D., and Humphries IV, W.H., "*Radiative lifetimes of NO A2Σ+(v'=0,1,2) and the electronic transition moment of the A2Σ+-X2Π system*," Journal of Chemical Physics, Vol. 131, 2009.

[10] Figliola, R.S. and Beasley D.E., *Theory and Design for Mechanical Measurements*, 3rd ed., Wiley, Hoboken, NJ, 2000, Chap. 5.

[11] Hill, R.B., and Klewicki, J.C., "*Data reduction methods for flow tagging velocity measurements*," Experiments in Fluids, 20(3), pp. 142 – 152, January, 1996.

[12] Koochesfahani, M.M., Cohn, R.K., Gendrich, C.P., and Nocera, D.G., "*Molecular Tagging Diagnostics for the Study of Kinematics and Mixing in Liquid-Phase Flows*," 8th International Symposium on Applications of Laser Techniques to Fluid Mechanics, pp. 1.2.1 – 1.2.12, Lisbon, Portugal, July 8-11, 1996.

Chapter 5: Application of Single-Laser, Sequentially Imaged NO Molecular Tagging Velocimetry

The purpose of this chapter is to provide quantitative mean streamwise velocity and uncertainty data in laminar hypersonic boundary layer flows, with and without an isolated cylindrical roughness element. The data can be used for validation and improvement of existing computational codes, in addition to providing additional insight into the physics of laminar hypersonic boundary layers with and without an isolated roughness element. A portion of the data in this chapter has recently been used to validate DNS computations with a cylindrical roughness element in a hypersonic boundary layer.[1] The data in this chapter presents the first application of the NO MTV technique in NASA Langley's 31-Inch Mach 10 Air Tunnel, and in fact, the first measurement of gas velocity in that facility. Multiple streamwise velocity datasets using both a side-view and a plan-view model orientation were obtained. Multiple streamwise velocity datasets using both a side-view and a plan-view model orientation were obtained. The streamwise velocity measurements are compared to heat transfer data obtained from temperature sensitive paint (TSP) measurements. These measurements were performed with the 2-mm-tall × 4-mm-diameter cylindrical roughness element at two unit Reynolds number conditions. The TSP measurements are meant to complement the velocity data and provide an enhanced understanding of the flowfield in the immediate vicinity of the roughness element. A 1-dimensional cross-correlation method, similar to that discussed in Chapter 4, was used to calculate mean streamwise velocity and uncertainty values. The discussion and results in this chapter have been adapted from Ref. 2.

5.1 Image Analysis

5.1.1 Initial Image Processing

Table 3.2 in Chapter 3 provides the conditions for the experiments described in this chapter. Table 5.1 lists the magnification and magnification uncertainty values used in this experiment. The approximate streamwise and wall-normal spatial resolutions of the velocity measurement for Runs 15 and 18 of Test 462 were 1.45 mm and 0.07 mm, respectively. For Run 17 of Test 462, the images were binned by 8 pixels in the vertical direction during acquisition of the images, with no other subsequent filtering applied. This reduced the vertical imaging system spatial resolution to approximately 0.56 mm.

5.1.2 Velocity Analysis

As discussed in Chapter 4, the correlation window in the delayed images was shifted by 5 pixels in the streamwise direction. This was done so that the fluorescence intensity profile of the tagged molecules in the delayed *plan-view* images would be captured by the correlation window, allowing for a reliable measure of Δx (Eq. 4.20). In this chapter, the *side-view* measurements of streamwise velocity complicate this approach, as a relatively large range of streamwise velocity magnitudes exist over the extent of the boundary layer thickness. As an alternative to the uniform 5-pixel-shift approach used in Chapter 4, an iterative shift procedure was adopted for the correlation window used in the delayed image. This was accomplished by first performing the 1-dimensional cross-correlation for a 45-pixel-wide window centered about a tagged profile at a particular vertical pixel location in both the reference and delayed images. The correlation window in the delayed image was then shifted by an integral number of pixels corresponding to the initial estimate obtained in the cross-correlation. The cross-correlation was then repeated with the unshifted and shifted window in the reference and delayed frames, respectively, and a final value for Δx was obtained. For image sets with relatively high signal-to-noise ratios (SNR), the average resulting change in measured velocity due to this procedure is on the order of 5%.

Table 5.1: Magnification values.

Parameter	Value
Run 15, 17, and 18: Mean Magnification, $\bar{M}$	6.36×10^{-2} mm/pixel
Run 15, 17, and 18: Uncertainty in the Mean Magnification, $u_{\bar{M}}$	16.01×10^{-5} mm/pixel
Run 25, 26, and 27: Mean Magnification, $\bar{M}$	5.70×10^{-2} mm/pixel
Run 25, 26, and 27: Uncertainty in the Mean Magnification, $u_{\bar{M}}$	8.30×10^{-5} mm/pixel

5.2 Results

5.2.1 Centerline Side-View Streamwise Velocity Measurements

Figure 5.1 shows the measured centerline mean streamwise velocity profiles ($\bar{U}$). Figures 5.1a and 5.1b show results for a hypersonic laminar boundary layer at two different unit Reynolds numbers, 1.7×10^{6} m^{-1} and 3.5×10^{6} m^{-1}, respectively, and similar edge Mach numbers, 8.07 and 8.16, respectively. Figure 5.1c shows a boundary layer flow with an isolated cylindrical roughness element (denoted by the gray shaded rectangle) at Re_{∞} = 1.7×10^{6} m^{-1}, $M_e = 8.07$, $k/\delta_L = 0.69$, and $Re_k = 287$. The cylinder is 2-mm-tall × 4-mm-diameter.

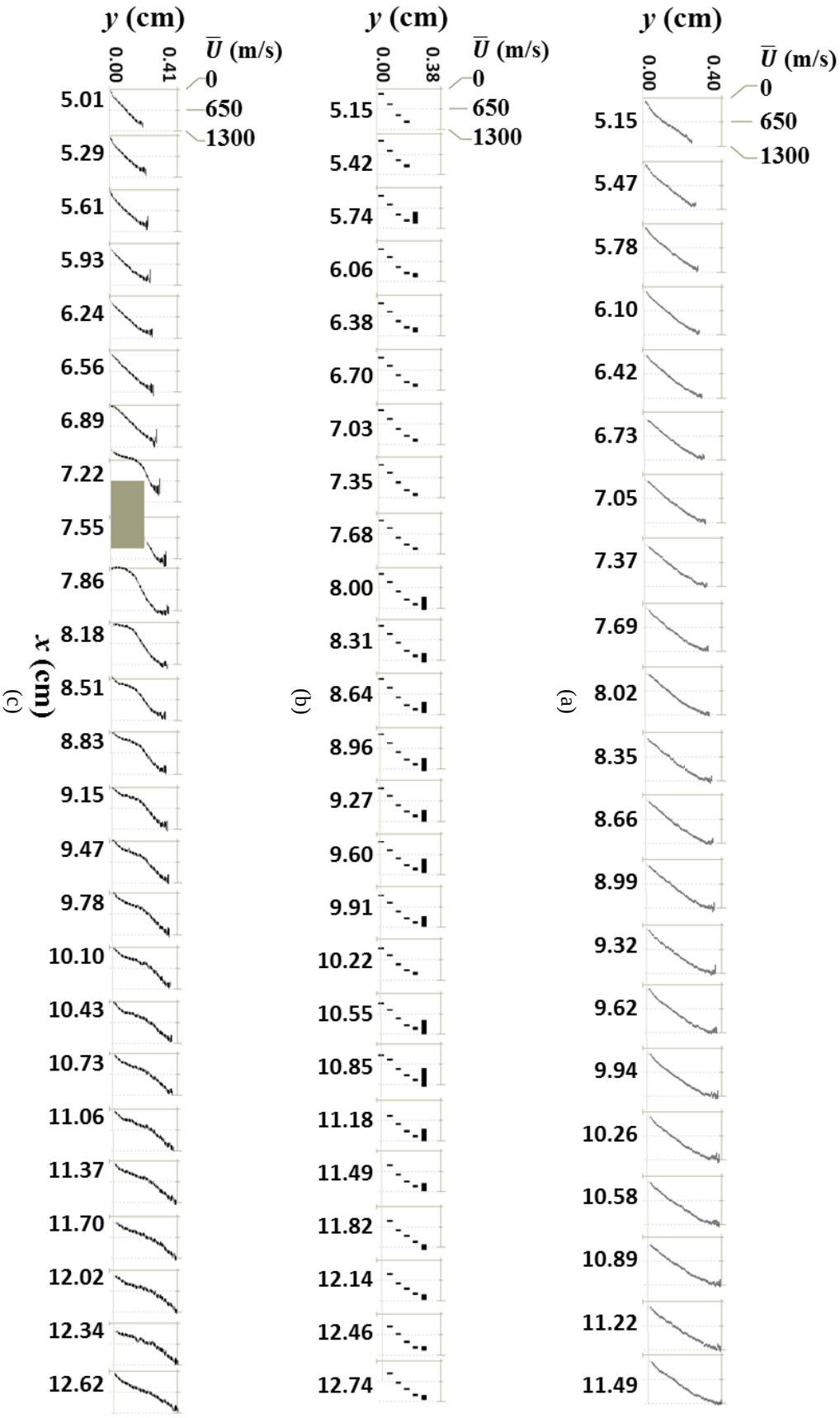

Figure 5.1: (a) and (b) Centerline mean streamwise velocity ($\overline{U}$) with no roughness for Re_∞ = 1.7×10^6 m^{-1} and 3.5×10^6 m^{-1}, respectively. (c) Centerline velocity with cylindrical roughness element for Re_∞ = 1.7×10^6 m^{-1}. The cylindrical roughness in (c) represented by a gray shaded area. Estimated uncertainty in laser sheet position is ±0.5 mm. Images (a), (b), and (c) correspond to Runs 15, 17, and 18 of Test 462, respectively. Images originally presented in Ref. 2.

The figures show an axis that represents a linear velocity scale, ranging from 0 to 1300 m/s, which is the same for each measurement. The streamwise measurement location with respect to the leading edge is denoted along the bottom of the figures. The direction of flow is in the direction of increasing streamwise distance. The continuous light gray line just above the lower axis represents the location of the model surface. This line is not precisely parallel to the data's domain because the camera and model were not perfectly aligned with respect to the horizontal in the experiment. The streamwise velocity points themselves are represented by black rectangles whose center position and width, in relation to the velocity axis, represent the mean streamwise velocity and uncertainty in the mean, respectively, at that point.

In all of the $\bar{U}$ profiles shown in Fig. 5.1a, with the exception of the profiles at 5.15 cm and 5.47 cm from the leading edge, a parabolic-like velocity distribution is observed, as expected. The minimum uncertainty encountered among all of the profiles is 22.6 m/s. These profiles terminate near the boundary layer edge, attaining a velocity of approximately 1300 m/s. An inviscid oblique shock calculation places the edge velocity at 1389 m/s, which may be an overestimate, as any viscous interaction has been ignored. The injection of low-speed NO gas from the seeding slot may contribute to a slight reduction in streamwise velocity. The computational study performed by Johansen and Danehy in Ref. 3 at the conditions corresponding to Fig. 5.1a showed that a 3 mg/s injection of NO gas from the seeding slot resulted in a small streamwise velocity deficit of approximately 50 m/s across a portion the thickness of the boundary layer when compared to a case with no injection. The computations in Ref. 3 also showed that the seeded NO gas does not reach the edge of the velocity boundary layer until approximately 8.0 cm from the leading edge.

The measurement points nearest to the edge of the boundary layer exhibit relatively larger uncertainties due in part to reduced and/or intermittent signal levels near the edge of the boundary layer. This is thought to be a result of either unsteadiness in the seeding and entrainment of NO gas into the boundary layer from the seeding slot, small facility-based acoustic disturbances, or some combination of the two. Another possible explanation for the unsteadiness at the boundary layer edge is that the existence of a generalized inflection point (see Chapter 2, Section 1) near the edge of the boundary layer may result in an instability that affects the streamwise velocity measurement. An unpublished analysis (not shown)[*] of CFD data from

[*] Johansen, C.T., University of Calgary, May 2013 (private communication).

computations performed in Ref. 3 showed that just downstream of the seeding slot, such inflection points exist for simulations both with and without NO seeding near the edge of the boundary layer. A generalized inflection point also exists near the edge of the boundary layer when considering the similarity solution, as shown by the red dotted line in Fig. 5.2 for a cold wall at T_{wall} = 314 K. The green line in Fig. 5.2 corresponds to the location, y_0, above which a generalized inflection point may exist. However, further analysis is needed to determine the stability of such a point.

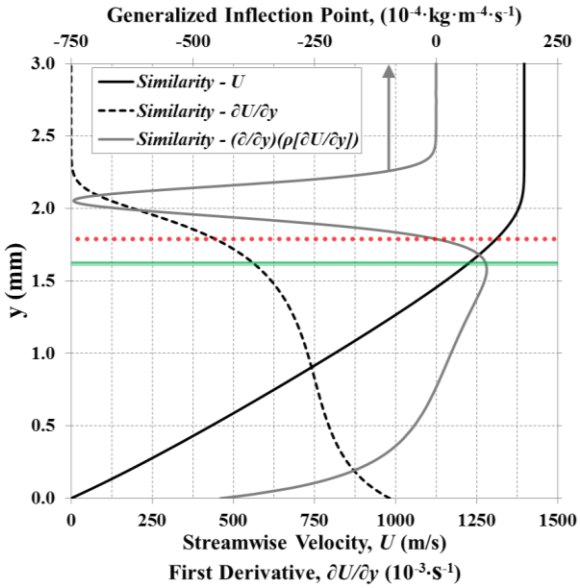

Figure 5.2: Similarity solution at x = 3.54 cm for conditions similar to those in Fig. 5.1a. Solid black line is streamwise velocity (lower axis), dashed black line is derivative of velocity (lower axis), gray line is generalized inflection point relation (upper axis). Red dotted line corresponds to generalized inflection point.

Figure 5.1b shows a $\overline{U}$ measurement with no roughness element at a unit Reynolds number of 3.5×10^6 m^{-1}. The reduced number of data points seen here is a consequence of the 8-pixel camera binning in the vertical direction. For this data set, it appears that each of the data profiles, although sparse, take on a laminar parabolic-like profile, as expected. As with the lower unit Reynolds number case in Fig. 5.1a, some of the data points farthest from the wall exhibit relatively larger uncertainties with respect to the other data points. It should be noted that the data points farthest from the wall are not necessarily located at the velocity boundary layer edge. They are either near the NO concentration boundary layer edge or, in some instances near the edge of the boundary layer, data points have been removed due to relatively large uncertainties, some exceeding ±500 m/s.

Figure 5.1c shows the resulting $\overline{U}$ profiles at a unit Reynolds number of 1.7×10^6 m^{-1} with the 2-mm-tall × 4-mm-diameter cylindrical roughness element. In this figure, profiles 2 through 6 (5.29 cm through 6.56 cm, respectively) have the expected parabolic-like velocity distribution. Along the 7th profile (6.89 cm), as the flow approaches the cylindrical trip, the streamwise velocity gradient near the wall is approximately zero. The mean velocity along this profile appears to have uniformly decreased when compared to the 6th profile (6.56 cm) at the same vertical station. These features indicate the presence of an adverse pressure

gradient. The $\bar{U}$ profile immediately in front of the trip at x = 7.22 cm has a flow reversal extending nearly to the height of the roughness element. Above the height of the roughness element, this same profile exhibits a strong velocity gradient. As the boundary layer gas passes over the tripping element, the flow is accelerated while maintaining a steep velocity gradient. The $\bar{U}$ profile immediately downstream of the cylindrical roughness element exhibits a near-zero velocity gradient extending from the wall up to approximately 1 mm. Above 1 mm, the velocity along this profile increases in a parabolic-like fashion up to approximately 3 mm.

The presence of a shear layer is apparent in Fig. 5.1c, with an inflection point at the approximate height of the roughness element. This profile is also shown in Fig. 5.3. A 7-pixel-average filter has been applied to the data (circles) in order to obtain a smooth $\bar{U}$ profile (black curve). The first (dashed black curve) and second (gray curve) derivatives of $\bar{U}$ are also shown. These derivatives were computed using a 1st-order central difference method applied to the 7-pixel-average-filter $\bar{U}$ and the 7-pixel-average-filter $\partial\bar{U}/\partial y$ profiles, respectively. The derivatives themselves were then smoothed with a 7-pixel-average filter. Figure 5.3 shows the location of the inflection point (point at which $\partial^2\bar{U}/\partial y^2 = 0$) at approximately y = 2.0 mm, corresponding to height of the cylinder. The existence of such points can result in an inviscid instability.[4]

This shear layer and velocity deficit appear to persist along several subsequent profiles downstream of the roughness element. However, the $\bar{U}$ profiles appear to return to a laminar similarity state several roughness diameters downstream of the roughness element and both the velocity deficit near the wall and shear layer gradually disappear. The minimum uncertainty encountered among the

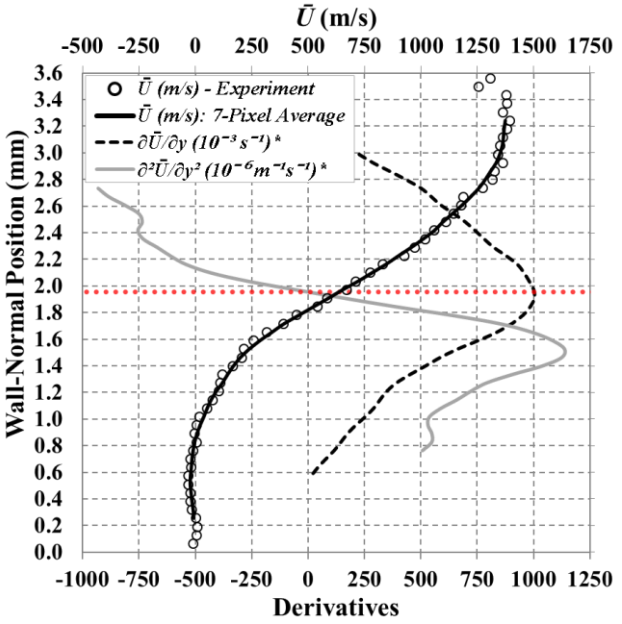

Figure 5.3: Experimental $\bar{U}$ profile data (circles) at x = 78.6 mm from Fig. 5.1c. Profile of $\bar{U}$ after applying 7-pixel average filter (black curve). Profile of $\partial\bar{U}/\partial y$ computed from smoothed $\bar{U}$ profile after applying additional 7-pixel average filter (dashed black curve). Profile of $\partial^2\bar{U}/\partial y^2$ from smoothed $\partial\bar{U}/\partial y$ profile after applying additional 7-pixel average filter (gray curve). Location of inflection point denoted by dotted red line.

mean profiles for this run was approximately 24 m/s. The DNS computations performed in Ref. 1 showed relatively good agreement with MTV measurements in Fig. 5.1c in regions away from the isolated cylindrical roughness element.

As the profiles approach the wall boundary, they appear to trend towards zero and satisfy the no-slip wall boundary condition. However, close inspection of each of the profile's data points nearest to the wall reveals that, in most cases, a finite velocity component has been measured. These data points have been shaded light gray in Fig. 5.1. They were originally assumed to represent an unphysical measurement of $\overline{U}$. However, an estimate of the potential slip velocity, U_{slip}, has shown that a non-zero wall velocity may, in fact, exist. An estimate for the slip velocity can be obtained through the relation:[5]

$$U_{slip} = \lambda \frac{\partial \overline{U}}{\partial y} \tag{5.1}$$

where λ is the mean-free-path given by:[6]

$$\lambda = \frac{1}{\sqrt{2}\sigma_{s,i} N_T} \tag{5.2}$$

Here, $\sigma_{s,i}$ is the collision cross-section of species s with species i and N_T the total population, both originally presented in Eq. 2.7. Referring to Table 3.2 and using the conditions at the wall, the minimum population corresponds to Run 15 where N_T = (200.8 Pa)/(1.38 × 10^{-23} $\frac{\text{J}}{\text{K·molecule}}$ 325.8 K) = 4.47 × 10^{22} $\frac{\text{molecules}}{\text{m}^3}$. For 1% NO in air, the effective collisional cross-section can be estimated using the relation:[7]

$$\sigma_{\text{NO,Eff}} = \sum_i \chi_i \sigma_{\text{NO},i} \left(1 + \frac{m_{NO}}{m_i}\right)^{1/2} \tag{5.3}$$

Using the collisional cross-section relations in Ref. 8 in Eq. 5.3 yields an effective collisional cross-section of $\sigma_{\text{NO,Eff}}$ = 8.22 × 10^{-20} m^2. Using this in Eq. 5.2 gives λ = 1.93 × 10^{-4} m. A similarity solution at x = 5.0 cm, comparable to that shown by the dashed curve in Fig. 5.2, gives $\partial\overline{U}/\partial y$ = 7.94 × 10^5 s^{-1} and δ_L = 2.43 mm. These results give a Knudsen number ($Kn = \lambda/\delta_L$), of Kn = 0.08 and a slip velocity of approximately U_{slip} = 153 m/s. This represents only an estimate of the slip velocity, and more analysis is needed to resolve the behavior at the wall.

A portion of the non-zero wall velocity may also be attributed to scatter of the laser light off the model surface in the reference image. In the delayed image, near the location of this scatter, it appears that a depletion of available signal in the camera's phosphor screen has occurred. The result is a false right-

weighting of the delayed profile at the wall, and consequently a non-zero velocity measurement at that location. Figure 5.4 shows an averaged reference (Fig. 5.4a) and averaged delayed (Fig. 5.4b) raw image from Run 18 of Test 462 where the phosphor-depleting effect of laser scatter can be observed. The estimated maximum extent of this phenomenon off the surface of the model is 0.38 mm.

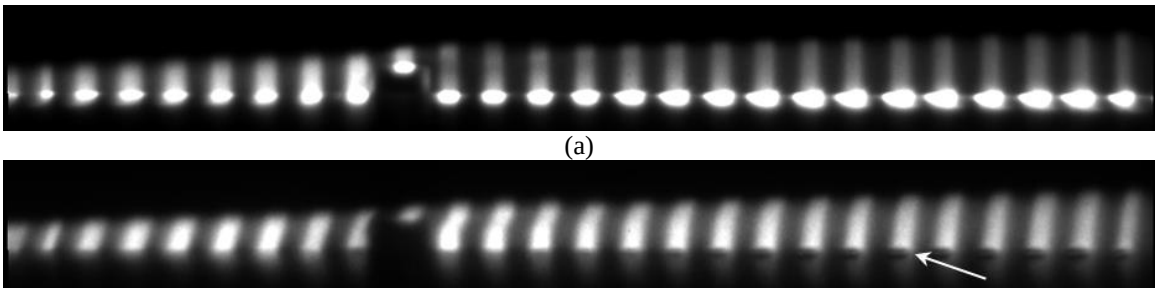

(a)

(b)

Figure 5.4: Averaged centerline (a) reference and (b) delayed raw velocity images corresponding to Fig. 5.1c. The phosphor depletion effect is especially noticeable in the bottom right of (b) where an arrow shows a depleted region corresponding to a very bright region in (a). Images originally presented in Ref. 2.

5.2.2 Plan-View Streamwise Velocity Measurements

Figures 5.5a through 5.5d represent the plan-view laminar boundary layer velocity measurements for the $Re_\infty = 1.7\times10^6$ m^{-1} case. These streamwise velocity maps correspond to the same conditions as those for the side-view $\bar{U}$ measurement shown in Fig. 5.1a. The respective wall-normal positions of the measurements are 0.0 mm, 0.8 mm, 2.1 mm, and 3.3 mm with an estimated position uncertainty of ±0.5 mm. In Fig. 5.5a (the measurement closest to the wall), the mean streamwise velocities are on the order of 100 m/s to 400 m/s. Due to the close proximity of the measurement plane to the model surface, the relatively large uncertainties encountered are attributed in part to mechanical vibrations affecting the laser sheet position. In some instances, this resulted in a portion of the laser sheet being blocked by the model. The model was also deflected upward over the course of the run in a linear manner, which resulted in a portion of the laser sheet being blocked by the model. The relatively large uncertainties in velocity are also attributed to scatter from the laser across the surface, which affects the image processing technique. The minimum uncertainty in the mean observed at this position is 34 m/s, with the average uncertainty in the mean being 86 m/s. In general, these profiles appear to be uniformly linear (within the confines of the experimental uncertainty), which is the expected behavior for this unperturbed laminar flow.

In Fig. 5.5b, the measurement plane has been positioned farther (0.8 mm) from the model surface, resulting in reduced experimental velocity uncertainty across all of the velocity profiles. The minimum

uncertainty in the mean encountered at this position is 20 m/s, with an average uncertainty in the mean of 28 m/s. The profiles are again uniformly linear, as expected. Figure 5.5c shows the velocity profiles for a measurement plane positioned even farther (2.1 mm) from the model surface. Mean streamwise velocities across this plane are on the order of 800 m/s. The profiles again exhibit a uniformly linear velocity behavior, with relatively small uncertainties in the mean, indicating that very little flow unsteadiness exists within the boundary layer at this position. The minimum uncertainty in the mean observed at this position is 27 m/s, with an average uncertainty in the mean of 36 m/s. Figure 5.5d shows the velocity profiles measured at 3.3 mm off the model surface. The profiles located beyond 7.5 cm downstream of the model leading edge exhibit similar uniform linear streamwise velocity behavior with relatively low uncertainty in the mean. However, profiles upstream of this location exhibit increased uncertainties in the mean. This increased uncertainty in the mean results from the measurement plane intersecting near, at, or above the edge of the concentration boundary layer containing NO, resulting in intermittent fluorescence signal. Computations performed in Ref. 3 show that the x = 7.5 cm streamwise location approximately corresponds to the location where the NO concentration boundary layer overtakes the velocity boundary layer.

Figures 5.6a through 5.6c show the plan-view $\bar{U}$ boundary layer measurements for the $Re_\infty = 1.7\times10^6$ m^{-1} case with the cylindrical roughness element (same conditions as in Fig. 5.1c). The 2-mm-tall × 4-mm-diameter isolated cylindrical roughness element is represented by the lightly shaded gray circle. The respective off-wall positions of the measurements are 0.0 mm, 2.2 mm, and 3.4 mm with an estimated position uncertainty of ±0.5 mm.

In Fig. 5.6a, the first three profiles exhibit uniform $\bar{U}$ behavior. Again, a slight increase in uncertainty along all profiles is observed due to model interference with the laser sheet and surface scatter. The profiles at 7.09 cm and 7.31 cm show a slight bowing of the velocity, indicating that the roughness element is beginning to influence the boundary layer. The centerline velocities are 127 m/s and -272 m/s along the respective profiles. Downstream of the roughness element and along the centerline of the model, a streamwise velocity deficit persists downstream to the end of the measurement region. To either side of this deficit, and downstream of the spanwise edges of the roughness element, each profile exhibits a region of increased $\bar{U}$, which also persists downstream to the end of the measurement region. The prominence of these post-roughness profile curvature features gradually diminishes with increasing downstream distance.

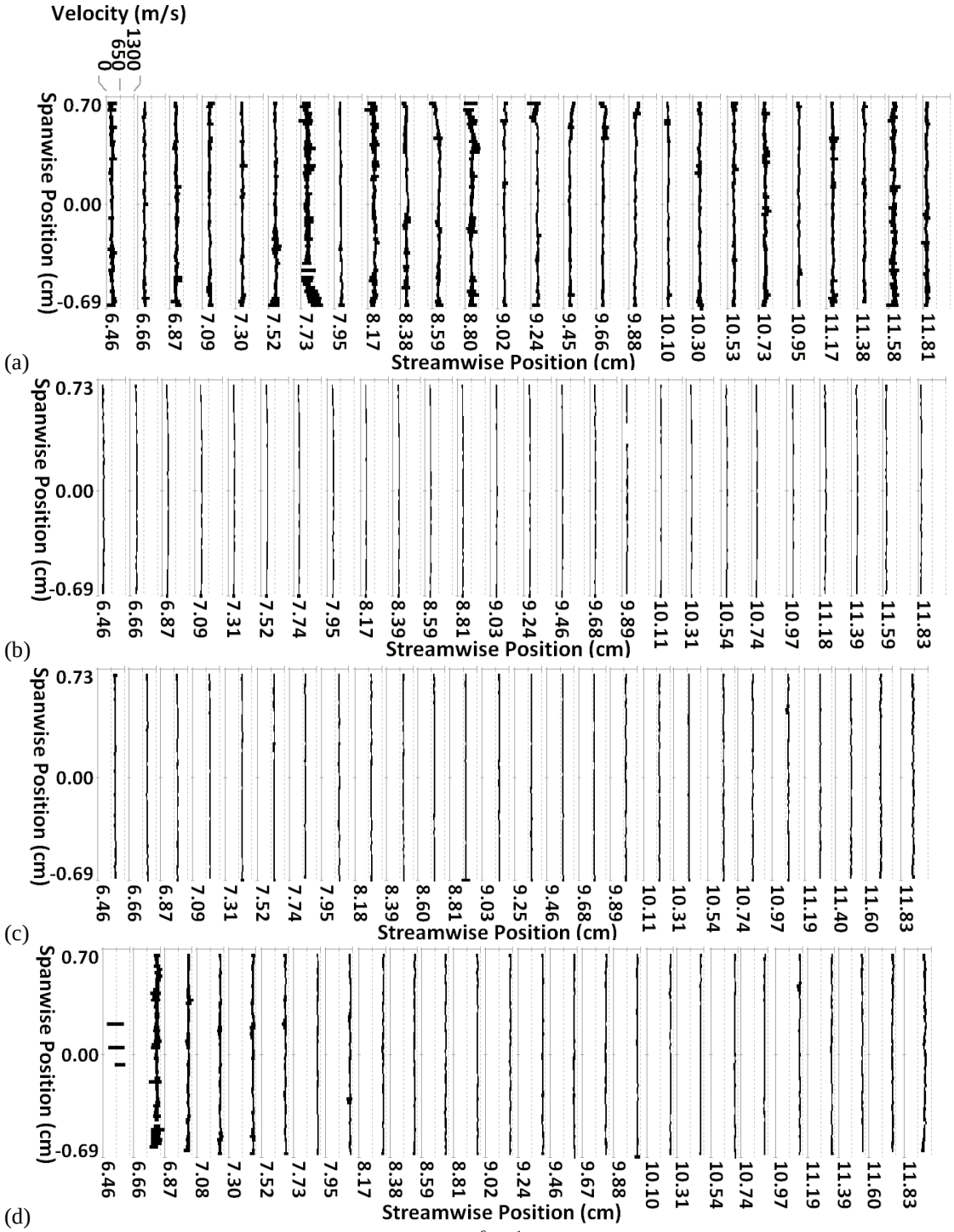

Figure 5.5: Plan-view $\overline{U}$ profiles for Re_∞ = 1.7×10^6 m^{-1} with no roughness element. Measurements at off-body positions of (a) 0.0 mm, (b) 0.8 mm, (c) 2.1 mm, and (d) 3.3 mm. Estimated uncertainty in laser sheet position is ±0.5 mm. Images from Run 27 of Test 462. Images originally presented in Ref. 2.

In Fig. 5.6b, the same general behavior is observed farther off the model surface. However, the curvature in the first several profiles downstream of the roughness element increases slightly until x = 8.82

cm. Beyond this location, subsequent profiles exhibit nearly similar $\overline{U}$ behavior. This is unlike Fig. 5.6a, where the wake disturbance diminishes with distance downstream. As with the side-view measurements in Fig. 5.1c, DNS computations in Ref. 1 were also performed at the conditions of Fig. 5.6b and showed relatively good agreement with the plan-view streamwise velocity measurements.

In Fig. 5.6c, the laser sheet position is either at or above the edge of the boundary layer along the first six velocity profiles (x = 6.46 cm to x = 7.52 cm). This results in relatively low signal intensities and relatively large measurement uncertainties. The profiles upstream of the x = 9.25 cm station appear to be

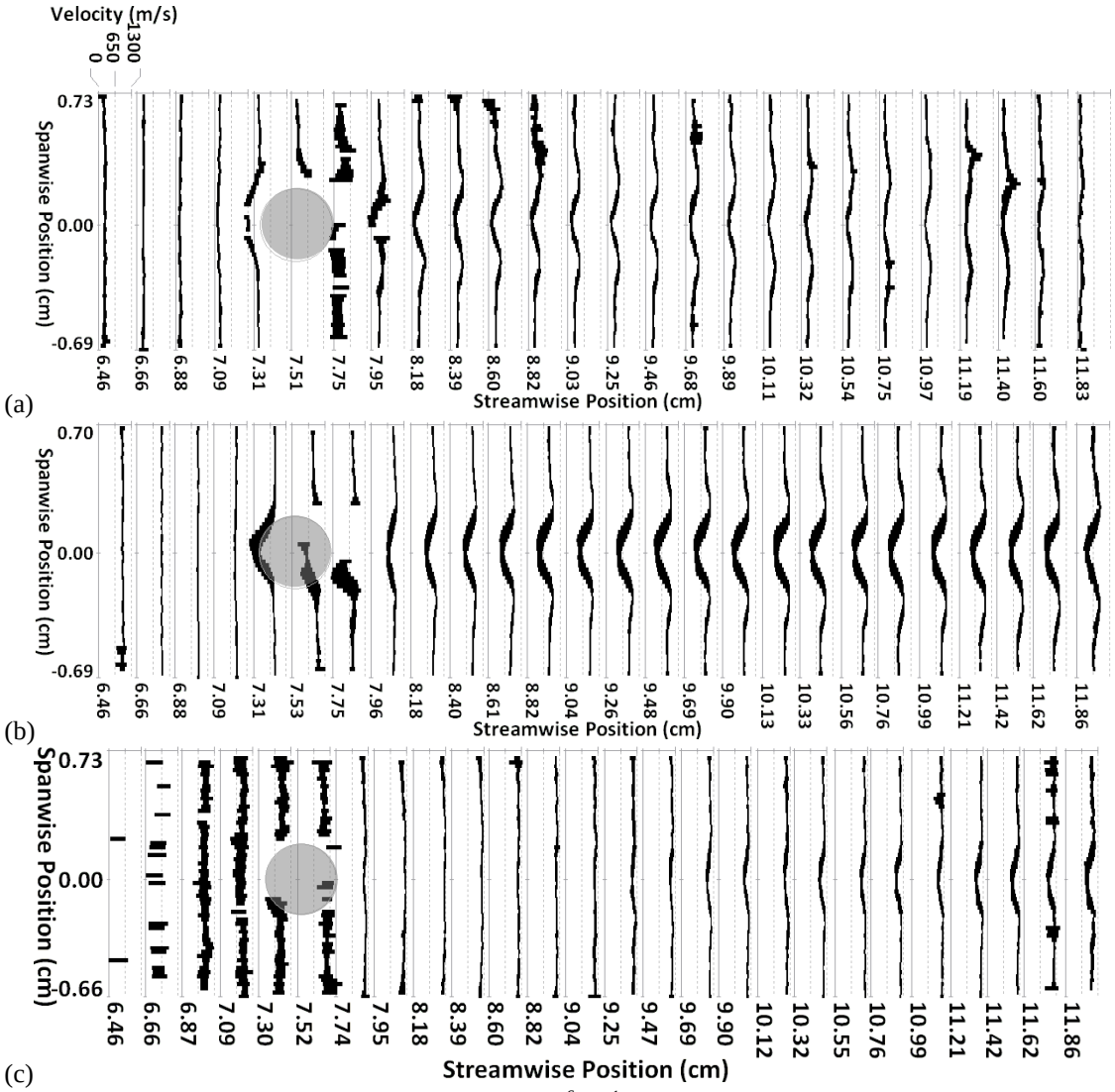

Figure 5.6: Plan-view $\overline{U}$ profiles at Re_∞ = 1.7×10^6 m^{-1} with 2-mm-tall × 4-mm-diameter cylindrical roughness element. Laser sheet at off-body positions of (a) 0.0 mm, (b) 2.2 mm, and (c) 3.4 mm. Estimated uncertainty in laser sheet position is ±0.5 mm. Images from Run 25 of Test 462. Images originally presented in Ref. 2.

unaffected by the presence of the roughness element. Downstream of this location, a velocity deficit begins to appear and strengthen with downstream distance. This indicates that the disturbance created by the cylindrical roughness element is growing in height as it propagates downstream.

In general, one of the more interesting aspects of Figs. 5.6a through 5.6c are the relatively large velocity gradients that exist downstream from the spanwise edges of the roughness element, very near the model surface. Observation of the $\overline{U}$ profiles along the centerline of the model downstream of the roughness indicates relatively small velocity gradients existing in the wall-normal direction. Thus, if only centerline side-view $\overline{U}$ profiles had been obtained, these features would not have been observed.

Figures 5.7a through 5.7d show similar streamwise velocity measurements at the higher Re_∞ = 3.3×10^6 m^{-1} condition at $M_e = 8.16$, $k/\delta_L = 0.92$ - 0.94, and $Re_k = 1295$ - 1527 and with an isolated cylindrical roughness element. The 2-mm-tall × 4-mm-diameter isolated cylindrical roughness element is again represented by the lightly shaded gray circle. This case, which also remained laminar, was tested primarily to probe the limits of the single-laser NO MTV measurement technique. The respective off-wall positions of the measurements are 0.0 mm, 0.8 mm, 2.1 mm, and 3.3 mm with an estimated position uncertainty of ±0.5 mm. In Figs. 5.7a and 5.7b, the increased uncertainty in the mean along all profiles is thought to be a result of the model interference with the laser sheet and laser scatter. In Fig. 5.7a, the profiles downstream of the roughness element exhibit a similar curvature as observed in Fig. 5.6a. In Figs. 5.7b and 5.7c, as in 5.6b, the profile curvature trend downstream of the roughness element is again observed. In Fig. 5.7d, the profiles in the near-wake region of the roughness element exhibit the gradual development of a $\overline{U}$ deficit with downstream distance, like that in Fig. 5.6c. As in Fig. 5.6a, a relatively strong velocity gradient exists near the model surface, extending downstream from the spanwise edges of the roughness element. Additionally, as with the lower Re_∞ case in Fig. 5.6, a $\overline{U}$ deficit persists downstream of the roughness element along the model centerline.

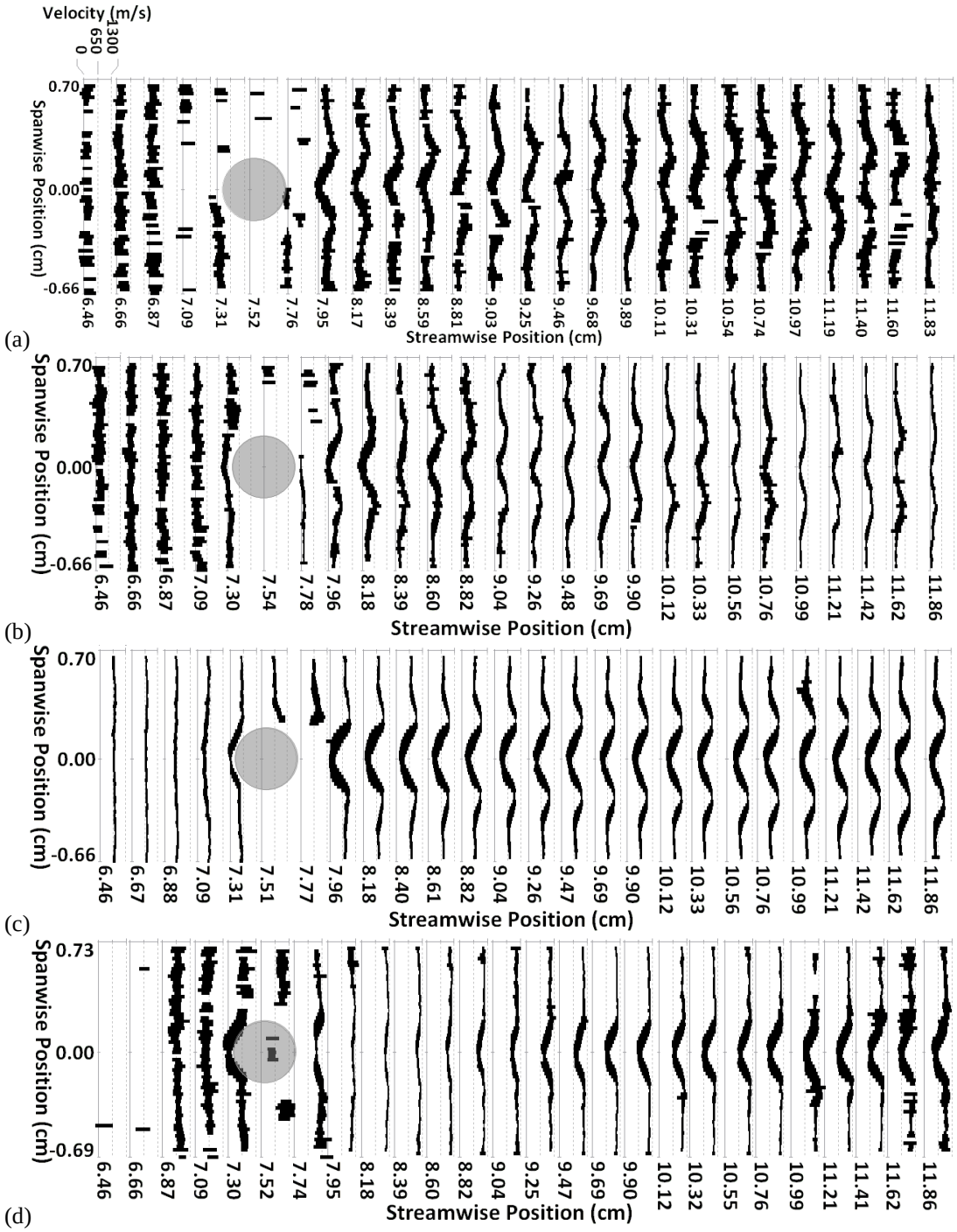

Figure 5.7: Plan-view $\overline{U}$ profiles with 2-mm-tall × 4-mm-diameter isolated cylindrical roughness element at Re_∞ = 3.3×10^6 m^{-1}. Laser sheet positions of (a) 0.0 mm, (b) 0.8 mm, (c) 2.1 mm, and (d) 3.3 mm. Estimated uncertainty in laser sheet position is ±0.5 mm. Images from Run 26 of Test 462. Images originally presented in Ref. 2.

5.2.3 Comparison of Streamwise Velocity Measurements with TSP

Figures 5.8a through 5.8d show temperature sensitive paint measurements originally presented in Ref. 2. The measurements were performed on a rectangular insert in the surface of the model by Dr. Neal

Watkins, Mr. William Lipford, and Mr. Kyle Goodman of the Advanced Sensing and Optical Measurement Branch at NASA Langley Research Center. They are presented here again in order to compare streamwise velocity features obtained with the single-laser NO MTV technique to surface heating patterns obtained with the TSP measurement. Details pertaining to the TSP measurement technique can be found in Ref. 9 and, with respect to this particular set of experiments, in Ref. 2.

In Fig. 5.8, note that the white circles indicate regions where no TSP data were acquired. These regions correspond to the 8 mm outer diameter of the roughness element insert onto which the 4-mm diameter cylindrical roughness element was machined. The roughness element was centered on the insert, as indicated by the smaller inner circles. The color map associated with the TSP measurements approximately corresponds to the ratio of the convective heat transfer coefficient, C_h, to the convective heat transfer coefficient that would occur at the stagnation point on a hemisphere at the same conditions based on the method outlined in Ref. 10, C_{hFR}.

For the no-roughness case at Re_∞ = 1.7×10^6 m^{-1} in Fig. 5.8a, a relatively uniform heat transfer distribution exists across the insert surface. This TSP image corresponds to the NO MTV measurements in Figs. 5.1a and 5.5. Figure 5.8b shows the heat transfer pattern at Re_∞ = 1.7×10^6 m^{-1} for M_e = 8.07,

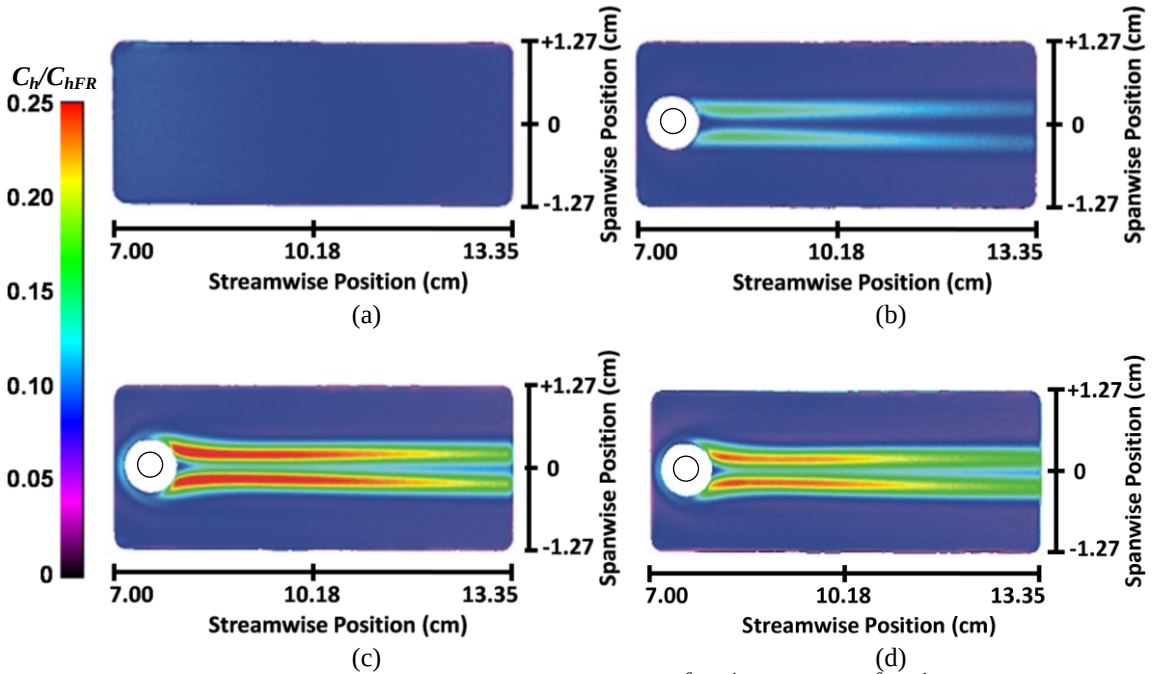

Figure 5.8: TSP heat transfer images for Re_∞ = (a) 1.7×10^6 m^{-1}, (b) 1.7×10^6 m^{-1} with roughness, (c) 3.4×10^6 m^{-1} with roughness, and (d) 3.4×10^6 m^{-1} with roughness and 5.69 mg/s N_2 gas supplied from seeding slot. Images originally presented in Ref. 2.

corresponding to the streamwise velocity measurements shown in Figs. 5.1c and 5.6. Immediately downstream of the spanwise edges of the roughness element, a double-streak pattern of increased heat transfer develops. These streaks are broadest approximately 2 roughness diameters downstream of the element, each being approximately 2/3 the width of the cylinder at this location. Beyond this point, the streaks slowly narrow and the heat transfer to the surface decreases with downstream distance. The outer boundary of this heat transfer pattern (farthest from the model centerline) maintains a relatively sharp edge downstream of the roughness element. Along the centerline in Fig. 5.8b, no noticeable increase in heat transfer above the baseline is observed. This coincides with the streamwise velocity deficit region observed in the streamwise velocity measurements. As expected, the region over which increased heat transfer is observed corresponds to the regions of relatively large velocity gradients with respect to the wall-normal direction. This also corresponds to where the streamwise velocity is highest downstream of the spanwise edges of the roughness element.

Figure 5.8c shows the heat transfer pattern at the $Re_\infty = 3.4\times10^6$ m^{-1} condition for $M_e = 8.16$ with the cylindrical roughness element, corresponding to velocity measurements provided in Fig. 5.7. Unlike the $Re_\infty = 1.7\times10^6$ m^{-1} heat transfer image in Fig. 5.8b, a region of increased heat transfer can be seen wrapping around the front edge of the roughness element. This extends well beyond the spanwise edges of the roughness (and beyond the base of the roughness insert), decreasing in intensity to the level of the ambient heat transfer values at approximately 2 roughness diameters above and below the center axis of the cylinder. At this point, a heat transfer pattern emerges that is similar, but not identical, to the heating pattern observed in Fig. 5.8b. A key difference at the $Re_\infty = 3.4\times10^6$ m^{-1} condition is the markedly higher heat transfer and the associated broadening of the dual streak pattern behind the roughness, with the increased heating pattern now penetrating all the way to the centerline. As with the heat transfer image in Fig. 5.8b, the increased heat transfer occurs in regions having relatively large streamwise velocity gradients with respect to the wall-normal direction.

Figure 5.8d shows a heat transfer pattern obtained for the same $Re_\infty = 3.4\times10^6$ m^{-1} condition as in Fig. 5.8c, but with 5.69 mg/s of N_2 gas seeded through the upstream slot. This was meant to replicate the effect of injecting relatively cold gas into the boundary layer (as is done with seeding NO). These images show a

very slight difference in heat transfer pattern, and therefore the injection of cold gas at this flow rate or below is assumed to have a minimal effect on the heat transfer associated with the boundary layer flow.

The heat transfer patterns in Figs. 5.8c and 5.8d are qualitatively similar to the temperature gradient maps computed in Ref. 11 and shown in Fig. 5.9a. In the computation in Ref. 11, $Re_\infty = 3.84\times10^6$ m^{-1}, $M_e = 6.52$, $k/\delta_L = 0.82$, and $Re_{kk} = 5940$. Figure 5.9b shows vorticity magnitude contours, also from Ref. 11, at the same conditions. These figures are shown in order to provide a qualitative description of boundary layer characteristics in the presence of the cylindrical roughness.

When the cylindrical roughness element is present, a separation region ahead of the roughness element forms and a system of counter-rotating vortices is produced. These vortices then wrap around the roughness element, resulting in streamwise vortex tubes that persist downstream and scour the model surface.[12] This behavior was detailed with surface oil-flow measurements in Ref. 13. Fig. 5.9b shows this system of vortices forming ahead of the trip, with the vortex closest to the leading edge of the roughness element wrapping around the roughness and resulting in a pair of streamwise vortices that persist downstream. Examination of Fig. 5.9a shows that two of the vortices ahead of the cylinder are associated with increased surface heating. However, only the vortex closest to the roughness continues to induce relatively high surface heating after wrapping around the cylinder. Returning to Figs. 5.8c and 5.8d, the patterns of increased heating just ahead of the roughness insert (white circle) are qualitatively similar to the pattern observed in Fig. 5.9b. The similarity is both in terms of position and in terms of the location where the pattern begins to fade, specifically above and below the spanwise edges of the roughness element. Similar patterns are also observed for the horseshoe vortex, which forms immediately in front of the roughness element.

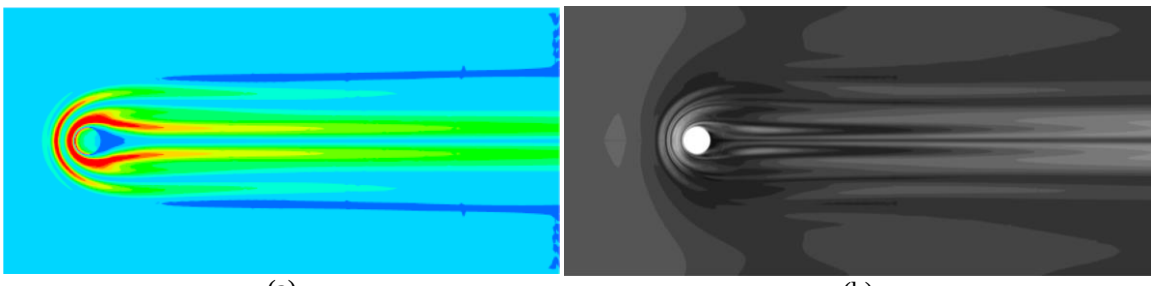

(a) (b)

Figure 5.9: Contour maps of computed (a) normalized surface temperature gradient and (b) vorticity magnitude at y = 0.5 mm. Images taken from Ref. 11 with permission of the author.

As noted in Ref. 11, the conditions associated with Fig. 5.9 result in a steady system of vortices, and the flow remains laminar. This is consistent with both the MTV and TSP measurements. Additionally, the laminar behavior observed at a lower M_e condition in Ref. 11 suggests that the higher M_e flows examined in this chapter will be laminar, as the higher edge Mach number tends to have a stabilizing influence, as discussed in Chapter 2 and Ref. 12.

Figure 5.10 shows the combined TSP and MTV data superimposed on a virtual rendering of a portion of the model. Figures 5.10a and 5.10b show the TSP images at the $Re_\infty = 1.7\times10^6$ m^{-1} (Fig. 5.8b) and $Re_\infty = 3.4\times10^6$ m^{-1} (Fig. 5.8d) conditions, respectively. The plan-view velocity maps in Figs. 5.10a and 5.10b correspond to the velocity maps at the $Re_\infty = 1.7\times10^6$ m^{-1} (Fig. 5.6b) and $Re_\infty = 3.4\times10^6$ m^{-1} (Fig. 5.7c) conditions, respectively. Note that the TSP color scale provided in these images varies slightly from that in Fig. 5.8. The black borders around the edges of the TSP images correspond to regions on the edge of the TSP-coated insert that provided no heat transfer signal. The regions of increased heat transfer on the TSP maps can be seen to correspond to the regions of increased velocity downstream of the spanwise edges of the cylindrical roughness element. In Fig. 5.10b, it is interesting to note that along the path of increased heat transfer and higher velocity, and between 0 to 2 roughness diameters behind the cylinder, it appears that a relatively significant spanwise velocity component most likely exists in the direction of the centerline. To a smaller extent, this appears to occur in Fig. 5.10a as well. In Figs. 5.10a and 5.10b, the approximate wall-normal position of the velocity measurements are at 2.2 mm and 2.1 mm, respectively.

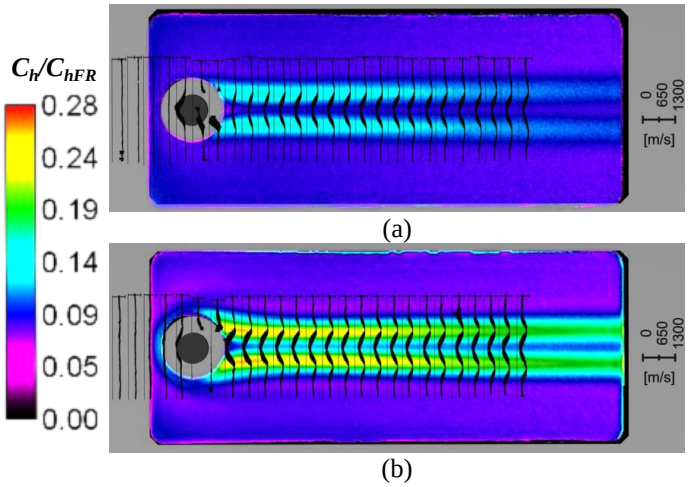

Figure 5.10: TSP heat transfer images with superimposed plan-view $\bar{U}$ maps for Re_∞ of (a) 1.7×10^6 m^{-1} and (b) 3.4×10^6 m^{-1}. Velocity scale is from 0 to 1300 m/s. Images originally presented in Ref. 2.

5.3 Discussion

In retrospect, some observations can be made about the various measurement strategies employed in the experiment. Two different model orientations, side-view and plan-view, were used. In order to make the highest resolution

measurements with the smallest uncertainty in the measurement location, side-views are preferable to plan-views. This preference stems from the relatively large uncertainty in the position of the laser sheet, u_y, over the course of a single tunnel run, which can be affected by facility vibrations, uncertainty in the scanning system, and model displacement because of thermal loads. Additionally, the scatter observed when a plan-view orientation is used tends to affect the entire velocity measurement, whereas scatter in the side-view orientation only affects the measurement at the model surface.

In regions of the flow having relatively large variations in streamwise velocity, it is particularly undesirable to have large uncertainties in laser sheet position. First, with the plan-view orientation, out-of-plane velocity gradients ($\partial\bar{U}/\partial y \neq 0$) can result in relatively a large uncertainty in the mean streamwise velocity, as the uncertainty in the mean streamwise velocity resulting from uncertainty in the mean of the laser sheet position, $u_{\bar{y}}$, and the thickness of the laser sheet, $\Delta y_{\mathrm{Laser}}$, can be approximated by:

$$u_{\bar{U},\bar{y}} = \sqrt{\left(\frac{\partial \bar{U}}{\partial \bar{y}} u_{\bar{y}}\right)^2 + \left(\frac{\partial \bar{U}}{\partial \bar{y}} \Delta y_{\mathrm{Laser}}\right)^2} \tag{5.4}$$

This error has not been taken into account in this analysis, because a measure of the streamwise velocity gradient with respect to y is needed to quantify the uncertainty. Second, the estimated spanwise velocity components in this experiment cause relatively large uncertainties along the profiles where $\partial\bar{U}/\partial z \neq 0$ and is relatively large. It is then better to position the laser sheet along regions with relatively small out-of-plane velocity gradients and relatively small in-plane velocity components parallel to the MTV profiles. As noted in Eq. 5.4, the thickness of the laser sheet results in spatial averaging over the flow structures, as does the width of each tagged line, $\Delta x_{\mathrm{Laser}}$. These dimensions should also be oriented along the smallest gradients in the flow. To minimize errors associated with the laser sheet position and profile thickness, a side-view model orientation is preferred. However, several interesting streamwise velocity patterns were observed with the plan-view model orientations that were not observed in the side-view orientation. Therefore, it is recommended that measurements with both orientations be used, and for each orientation the laser sheet should be scanned to several locations to acquire several off-wall (when in plan-view orientation) and off-centerline (when in side-view orientation) streamwise velocity measurements.

Another observation is that there was a factor-of-two difference in the width of the profiles when using a plan-view (0.8 mm) versus side-view (1.5 mm) orientation. This was primarily caused by the placement

of the cylindrical lens array. Generally, narrower lines result in more accurate and more precise velocity measurements. In future experiments, care should be taken to move the cylindrical lens array to minimize the width of these lines in the flow, thereby increasing both measurement accuracy and spatial precision.

As mentioned previously, the measurements near the wall were often corrupted by intense laser scatter, which in some cases depleted the phosphor, resulting in erroneous streamwise velocity measurements. Precautions must be taken to reduce scatter from the surface, which would also allow for measurements of velocity closer to the wall. This issue is addressed in Chapters 6 and 7.

Finally, one goal of this dissertation is to characterize the transition-to-turbulence process in the presence of an isolated roughness element. Unfortunately, the conditions necessary for transition-to-turbulence to occur within the measurement region were never achieved in this MTV experiment. One reason for this was that a large enough Reynolds number (at the fixed 5° plate angle of this experiment) could not be achieved while simultaneously maintaining an adequate SNR in the second exposure. Since the Reynolds number at a given plate angle is a function of the facility stagnation pressure, and a larger Reynolds number requires a larger stagnation pressure, the fluorescence lifetime is significantly reduced at high Reynolds numbers. Recall from Fig. 4.4 in Chapter 4 that the upper static pressure limit for adequate SNR in the second exposure was estimated to be 900 Pa. A static pressure calculation at the 5° plate angle condition (as depicted in Fig. 2.5b) shows that the P_0 = 720 psia (~ 5 MPa) stagnation pressure condition (corresponding to $Re_\infty = 3.4\times10^6$ m^{-1}) is approximately at this upper 900 Pa static pressure limit. Above this limit, the fluorescence lifetime is reduced such that the fluorescence intensity in the second exposure is inadequate for an MTV measurement. A calculation of the signal in the second exposure relative to that in the first exposure is quantified in Fig. 2.6 in Chapter 2, and qualitatively shown in Fig. 3.2 in Chapter 3.

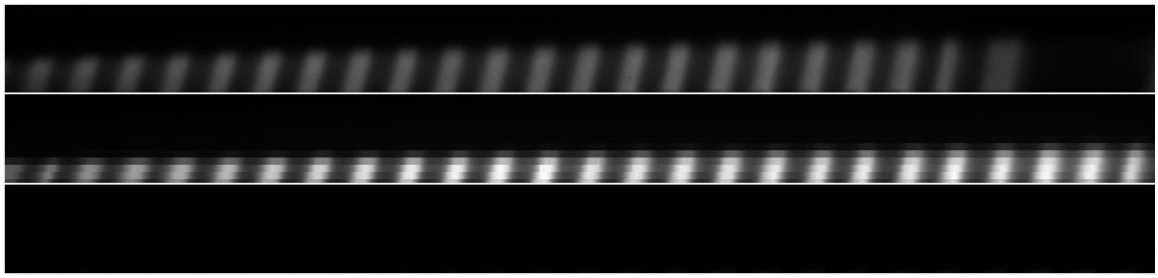

Figure 5.11: Comparison of fluorescence signal intensity in an averaged second exposure at nominal facility stagnation pressure of (top) 350 psia, (middle) 720 psia, and (bottom) 1350 psia. These pressures approximately correspond to $Re_\infty = 1.7\times10^6$ m^{-1}, 3.4×10^6 m^{-1}, and 6.2×10^6 m^{-1}, respectively.

This is also shown in the averaged second exposure images in Fig. 5.11. In Fig. 5.11, averaged second exposure images for three different nominal facility stagnation pressure conditions, 350 psia, 720 psia, and 1350 psia, are shown from top to bottom, which correspond to Re_∞ = 1.7×10^6 m^{-1}, 3.4×10^6 m^{-1}, and 6.2×10^6 m^{-1}, respectively. The NO flow rates in Fig. 5.11 were approximately 7.11 mg/s, 6.09 mg/s, and 6.09 mg/s, respectively. The camera gain settings were 60%, 60%, and 70%, respectively. Camera binning by 8 pixels in the vertical direction was employed in the acquisition of the middle image of Fig. 5.11. For the highest stagnation pressure, P_0 = 1350 psia, the SNR was inadequate for a streamwise velocity measurement using the single-laser NO MTV technique. This condition is also close to the highest operational stagnation pressure (P_0 = 1450 psia) of the 31-inch Mach 10 Air Tunnel.[14] The higher intensity observed in the middle image in Fig. 5.11 is partially a result of the hardware binning (8 vertical pixels) and changes in laser irradiance, I, occurring between the runs.

Even if SNR were adequate for a velocity measurement at P_0 = 1350 psia, the flow visualization study performed in Ref. 15 showed that at the 5° plate angle, transition-to-turbulence appeared to not occur downstream of the 2-mm-tall × 4-mm-diameter cylindrical roughness element. Figure 5.12, taken from Ref. 15, shows side-view single-shot NO PLIF flow visualization images with the laser sheet aligned to the model centerline with a 2-mm-tall × 4-mm-diameter cylindrical roughness element. Figures 5.12a through 5.12d were taken at plate angles of 5°, 7.5°, 10°, and 12.5°, respectively. In Fig. 5.12a, the flow appears to be relatively laminar downstream of the roughness element. As the plate angle is increased to 7.5° in Fig. 5.12b, unsteadiness is observed downstream of the roughness. As the plate angle is further increased in Figs. 5.12c and 5.12d, the unsteadiness quickly moves forward. Computations of the post-oblique shock conditions

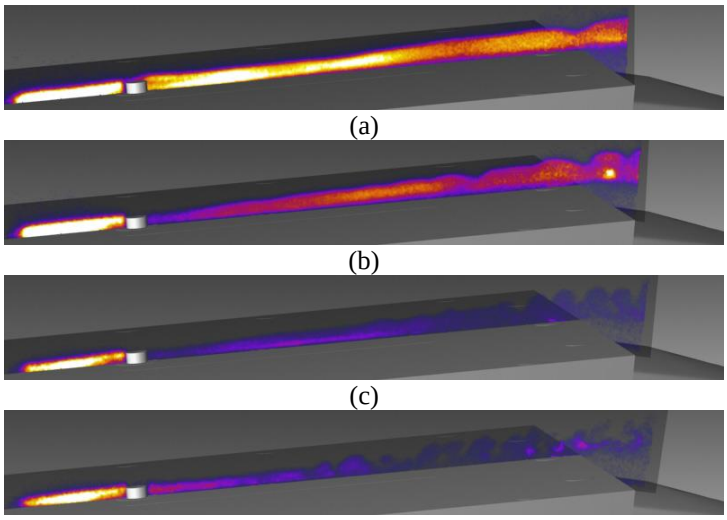

Figure 5.12: Side-view NO PLIF flow visualization images with 2-mm-tall × 4-mm-diameter cylindrical roughness at P_0 = 1350 psia and plate angles of (a) 5°, (b) 7.5°, (c) 10°, and (d) 12.5°. Mass flow rate of NO is approximately 6.09 mg/s. Images taken from Ref. 15.

performed using the Virginia Tech Compressible Aerodynamics Calculator[16] show that as the plate angle *increases* from 5° to 12.5°, the unit Reynolds number based upon the conditions at the edge of the boundary layer, Re_e, *decreases* by approximately 6%. This is in contrast to the increase of more than 250% in Re_e encountered at the fixed plate angle of 5° as P_0 is increased from 350 psia to 1350 psia.

At the roughness location, the boundary layer thickness, δ_L, decreases by approximately 38% and k/δ_L increases by approximately 61% when the plate angle is increased from 5° to 12.5°. At the 5° plate angle, as P_0 is increased from 350 psia to 1350 psia, δ_L decreases by approximately 48% and therefore k/δ_L increases by approximately 95%. While the edge Mach number, M_e, is relatively unaffected by changes in P_0, it decreases by approximately 28% with the increase in plate angle from 5° to 12.5°. Therefore, the primary difference from Fig. 5.12a to 5.12d is *not* the increase in Re_e, which increases only marginally. Rather, it is the increase in the relative height of the roughness element to the boundary layer thickness (i.e. k/δ_L) and the decrease in M_e that promote transition.

The destabilizing effect of decreasing M_e and the simultaneous increase in k/δ_L, both with increasing plate angle and at a relatively high Re_e, appear to promote transition-to-turbulence. Unfortunately, this requires that the plate angle be increased, which consequently significantly increases the static pressure and decreases the fluorescence lifetime, as detailed in Fig. 2.5b. This eliminates the single-laser NO MTV technique for consideration as a measurement method at such conditions. Therefore, a three-laser NO_2-to-NO MTV technique will be described in Chapter 6 which can potentially provide reliable velocity measurements regardless of the fluorescence lifetime.

5.4 Conclusions

This chapter provided fundamental experimental laminar boundary layer velocity and uncertainty data for comparison with hypersonic boundary layer CFD solutions. This work represents the first application of the single-laser NO MTV technique in NASA Langley's 31-Inch Mach 10 Air Tunnel with the objective of obtaining hypersonic boundary layer flowfield velocity data. Data for two model orientations (side-view and plan-view) and two unit Reynolds number conditions, both with and without a cylindrical roughness element, were provided. Side-view velocity data with a k = 2.0 mm cylindrical roughness element showed that a shear layer and wake region were generated by the roughness element, however these features did not

persist downstream for the conditions of this experiment. Plan-view velocity results were compared with TSP heat transfer measurements and CFD computations in order to identify streamwise velocity features that resulted in increased heating patterns. These features were attributed to streamwise vortices that initiated from a horseshoe vortex system generated by the roughness element. While the experiments showed that the cylindrical roughness element influenced the laminar boundary and surface heat transfer, the conditions of the experiment were not sufficient to induce transition-to-turbulence behavior. An analysis of experimental images showed that at the 5° plate angle, transition will not occur even for the highest freestream unit Reynolds number tested. Additionally, at the highest freestream unit Reynolds number condition tested, the fluorescence lifetime was significantly reduced, precluding the use of single-laser NO MTV at that condition.

---

[1] Iyer, P.S., Muppidi, S., and Mahesh, K., "*Roughness-induced transition in high speed flows*," 49th AIAA Aerospace Sciences Meeting, AIAA 2011-566, January 4-7, 2011, Orlando, FL.

[2] Bathel, B.F., Danehy, P.M., Inman, J.A., Watkins, A.N., Jones, S.B., Lipford, W.E., Goodman, K.Z., Ivey, C.B., and Goyne, C.P., "*Hypersonic Laminar Boundary Layer Velocimetry with Discrete Roughness on a Flat Plate*," 40th Fluid Dynamics Conference and Exhibit, AIAA Paper 2010-4998, June 28 – July 1, 2010, Chicago, IL.

[3] Johansen, C.T., Danehy, P.M., "*Numerical investigation of PLIF gas seeding for hypersonic boundary layer flows*," 50th AIAA Aerospace Sciences Meeting, AIAA 2012-1057, January 9-12, 2012, Nashville, TN.

[4] White, F.M., *Viscous Fluid Flow*, 2nd ed., McGraw-Hill, New York, NY, 1991, pp. 345-348.

[5] Vincenti, W.G. and Kruger Jr., C.H., *Introduction to Physical Gas Dynamics*, 2nd ed., John Wiley & Sons, 1967, New York, NY, p. 428.

[6] Anderson, J.D., *Hypersonic and High-Temperature Gas Dynamics*, 2nd ed., AIAA, Reston, VA, 2006, pp. 559-573.

[7] Paul, P.H., Gray, J.A., Durant, J.L., Thoman, J.W., "*Collisional Quenching Corrections for Laser-Induced Fluorescence Measurements of NO $A^2\Sigma^+$*," AIAA Journal, 32(8), August 1994.

[8] Settersten, T.B., Patterson, B.D., and Carter, C.D., "*Collisional quenching of NO $A^2\Sigma^+(v' = 0)$ between 125 and 294 K*," The Journal of Chemical Physics, 130(20), May 28, 2009.

[9] Watkins, A.N., Buck, G.M., Leighty, B.D., Lipford, W.E., and Oglesby, D.M., "*Using Pressure- and Temperature-Sensitive Paint on the Aftbody of a Capsule Vehicle*," AIAA Journal, 47(4), pp. 821-829, 2009.

[10] Fay, J.A., and Riddell, F.R., "*Theory of Stagnation Point Heat Transfer in Dissociated Air*," Journal of the Aeronautical Sciences, 25(2), pp. 73-85, February, 1958.

[11] Chang, C-L., Choudhari, M.M., and Li, F., "*Numerical Computations of Hypersonic Boundary-Layer over Surface Irregularities*," 48th AIAA Aerospace Sciences Meeting, AIAA Paper 2010-1572, January 4-7, 2010, Orlando, FL.

[12] Schneider, S.P., "*Effects of Roughness on Hypersonic Boundary-Layer Transition*," Journal of Spacecraft and Rockets, 45(2), pp. 193-209, March – April, 2008.

[13] Whitehead Jr., A.H., "*Flowfield and Drag Characteristics of Several Boundary-Layer Tripping Elements in Hypersonic Flow*," NASA TN D-5454, October, 1969.

[14] Micol, J.R., "*Langley Aerothermodynamic Facilities Complex: Enhancements and Testing Capabilities*," 38th AIAA Aerospace Sciences Meeting, AIAA 1998-147, 1998.

[15] Danehy, P.M., Ivey, C.B., Inman, J.A., Bathel, B.F., Jones, S.B., McCrea, A.C., Jiang, N., Webster, M., Lempert, W., Miller, J., and Meyer, T., "*High-Speed PLIF Imaging of Hypersonic Transition over Discrete Cylindrical Roughness*," AIAA Paper 2010-703, 48th AIAA Aerospace Sciences Meeting, January 4 – 7, 2010, Orlando, FL.

[16] Devenport, W.J., *Compressible Aerodynamics Calculator 2.0*, http://www.dept.aoe.vt.edu/~devenpor/aoe3114/calc.html [last accessed June 8, 2013].

Chapter 6: Development of Three-Laser, Sequentially Imaged NO_2-to-NO Molecular Tagging Velocimetry

While laser-based optical measurement techniques have the potential to provide quantitative, off-body flowfield information, care must be taken to select a technique appropriate for the flow conditions of interest in order to ensure adequate signal-to-noise levels. For velocity measurements in a hypersonic boundary layer flow undergoing laminar-to-turbulent transition, molecular tagging velocimetry (MTV) is a particularly attractive technique, as it allows for instantaneous measurement of one or two components of velocity at multiple locations simultaneously (multiple velocity profiles) within the boundary layer.

One MTV method in particular, which uses fluorescence tagging of nitric oxide (NO) and described in Chapters 4 and 5, has been applied in both the 31-Inch Mach 10 Air blowdown wind tunnel[1-5] and the Hypersonic Materials Environmental Test System (HyMETS)[6] at NASA Langley Research Center. The development and application of the single-laser NO MTV technique for streamwise velocity measurements in a hypersonic laminar boundary layer in the 31-inch Mach 10 Air Tunnel were described in Chapters 4 and 5, respectively. For the conditions in those experiments, the fluorescence lifetime was long enough to allow for measurable signal intensity in both reference and 500-ns-delayed exposures with uncertainty in the mean velocities of less than 30 m/s. However, for the same facility and model, obtaining measurements in a hypersonic boundary layer undergoing transition-to-turbulence required a flow at higher unit Reynolds number (Re_e), lower edge Mach number (M_e), and increased k/δ_L. To achieve these conditions, the facility stagnation pressure, P_0, and model plate angle had to be increased. These changes resulted in a higher static pressure across the model surface and a dramatically reduced fluorescence lifetime, which in turn reduced the signal in the delayed images to unacceptably low levels. Therefore, to measure streamwise velocity profiles within a hypersonic boundary layer undergoing transition-to-turbulence, an alternative to the single laser MTV technique was needed.

The purpose of this chapter is to detail the development of a three-laser NO_2-to-NO photolysis MTV technique for use in NASA Langley's 31-Inch Mach 10 Air Tunnel to measure instantaneous and mean streamwise velocity profiles in a hypersonic boundary layer undergoing transition-to-turbulence. As noted in Chapter 2, this technique has been both developed and demonstrated by several researchers.[7-11] This technique consists of a *write step*, in which a spatial pattern is written onto the gas flowfield, followed by

two *read steps*, which cause the spatial pattern to fluoresce. See Fig. 3.5 for a schematic of the experimental setup and Section 3.3.2 for more details on the implementation of the technique. The results presented in this chapter represent the first application of the three-laser NO_2-to-NO photolysis MTV technique in a hypersonic boundary layer. This chapter also provides a description of the behavior of the hypersonic boundary layer as a function of mass injection (blowing) rate, $\dot{m}_{NO_2}$, of the NO_2 gas. This description includes an analysis of the mean and fluctuating behavior of streamwise velocity profiles as well as a characterization of data yield, all as functions of $\dot{m}_{NO_2}$. The discussion and results in this chapter have been adapted from Refs. 12 and 13.

6.1 Velocity Analysis Method for Three-Laser NO_2→NO MTV

In initial NO_2-to-NO experiments (Ref. 13), the duration of both the first and second exposures was the kept the same and the temporal overlap of each exposure with the respective probe beam was kept constant. This timing method allowed the velocity measurement to be relatively unaffected by distortions which might otherwise occur as a combined result of fluorescence decay and the time-integrated nature of each exposure, as was the case with the single-laser method (for instance see Fig. 4.3 of Chapter 4). This somewhat simplifies the velocity analysis, as velocity can be defined as the product of the measured mean magnification, $\bar{M}$, and the displacement of the profiles (in pixels), Δx, between the first and second exposures, divided by the time separation between the first and second exposures, Δt, or:

$$U = \bar{M}\frac{\Delta x}{\Delta t} \tag{6.1}$$

This form of the streamwise velocity relation does not (and need not) contain a correction factor for either fluorescence decay or blurring, as was necessary in the single-laser NO MTV technique covered in Chapters 4 and 5.

6.1.1 Initial Image Processing

The image magnification and spatial resolution were measured by acquiring an image of a dotcard with square markings separated at 0.25-inch spatial intervals, similar to that described in Chapter 4. Additional data sets acquired with varying exposure time delays, Δt, for the purpose of estimating the uncertainty in determining the spatial shift of the tagged lines between two exposures. Hereafter, this is referred to as the spatial velocity uncertainty and is a function of the signal-to-noise ratio.

To correct for optical and perspective distortion of the images, the image of the dotcard in the test section was acquired with the camera and compared to a corresponding undistorted digital image of the same dotcard. The image registration algorithm, *UnwarpJ*,[14] was again used to correct the distortion. This software is a plug-in created for the image processing software, *ImageJ*, a freeware image processing program available from the National Institutes of Health.[15]

Prior to processing each image for velocity information, a background image was subtracted from the first and second exposure images. The background images were created by separately averaging a series of images from the first and second exposures while the laser was blocked. Due to the shortness of the delay, Δt_{D2}, between the end of the first exposure and the beginning of the second exposure images and the relatively long decay time of the P46 phosphor in the camera's intensifier, some ghosting from the first exposure was observed in the delayed image. The ghosting level was assumed to be approximately 1.2% of the signal intensity in the first exposure. This fraction of the first exposure image was also subtracted from the second exposure image. A bleaching effect was observed to occur when the signal intensity in the first exposure approached the maximum dynamic range of the camera, resulting in an absence of signal in the second exposure. To avoid biasing the measurement as a result of this bleaching effect, any data profiles having maximum counts of 3000 or higher were discarded.

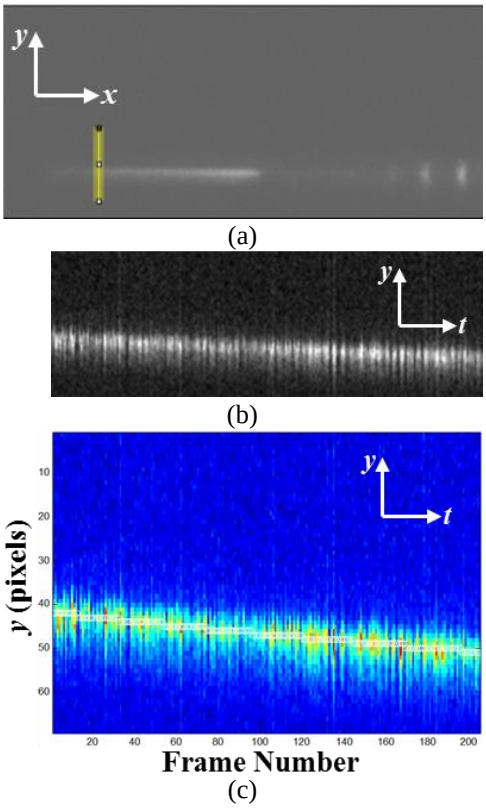

Figure 6.1: Method to correct for model displacement. Laser scatter observed on model surface in (a) was used to generate an image (b) that characterized model displacement as a function of frame number. MATLAB® was then used to fit a function to the laser scatter image as in (c).

For these measurements, the wedge model moved slightly during acquisition of the experimental images. This was assumed to be an effect of thermal loading on the model body and sting. In Run 12 of Test 481 (see Chapter 3, Table 3.3), for instance, the model surface temperature, measured using a thermocouple on the underside of the top surface of the model, increased from approximately 316 K to 400 K over the course of more than 120 seconds of

image acquisition time. This was accompanied by an observed model displacement of approximately 1.5 mm. This displacement was determined by tracking the path of scattered light at the leading and trailing edges of the quartz window insert. Figure 6.1a shows this scatter forward of the quartz window insert. The yellow line in Fig. 6.1a corresponds to a 10-pixel-wide line that was positioned to encompass the laser scatter in each image in a 205 image set. The *Reslice* function in *ImageJ* was then used to produce the image in Fig. 6.1b, which characterized the location of the scatter observed on the model surface and along the yellow line in Fig. 6.1a as a function of the camera frame number (horizontal axis). The image in Fig. 6.1b was then read into MATLAB®. A function (either linear or polynomial) was then fit to the laser scatter, with the independent variable being the camera frame number and the dependent variable being the model's relative position. In Fig. 6.1c, the white circles correspond to a 2^{nd}-order polynomial fit to the peak of the intensity in each frame. The experimental images were then translated vertically in whole-pixel increments so that the scatter appeared in the same approximate location in each image. This allowed for a more accurate measurement of the location of boundary layer streamwise velocity measurements.

6.1.2 Timing Analysis

6.1.2.1 *Phenomenological Derivation of Displacement (Probe Laser within Exposure)*

When both exposures completely encompass the respective probe laser pulses, the time between initial intensity generation by the probe laser and the end of the exposure serves as the *effective* exposure time. During this period, the probe laser first populates the excited electronic state of the NO gas train created via the NO_2-to-NO photolysis process. Photons are emitted from this excited state and collected by the CCD array. When the probe laser ceases, the NO gas train continues to emit photons, which continue to be captured by the CCD array until the end of the respective exposure. During both effective exposures, the excited NO molecules are advected over the entirety of the respective effective exposure time, resulting in spatial blurring. As discussed in Chapter 4, the amount of blurring depends on the velocity of the NO gas. If the decay of the fluorescence intensity is taken into account, the spatial intensity distribution in each exposure will be affected, with the perceived intensity distribution being weighted opposite the direction of travel of the NO gas. Nonetheless, as will be described in detail below, if the gas velocity and fluorescence lifetime are the same in both effective exposures, then this does not result in a systematic error in measurement. Conversely, in suddenly expanded (accelerated) or compressed (decelerated) flows, a

significant error in computed velocity can occur because the velocity is not constant during the measurement interval. Such an error was described in Section 4.4.2 of Chapter 4, and that description is applicable to the current results as well. Figure 6.2 provides an idealized representation of the NO_2-to-NO photolysis process, subsequent probe laser excitations, and CCD exposures. In this idealization, the laser excites only a single spatial unit of gas and both the first and second camera exposures completely encompass the respective probe laser pulses. In Fig. 6.2a, it is assumed that the fluorescence intensity following probe laser excitation in the first and second exposures is constant over the duration of the respective exposures, whereas in Fig. 6.2b, the fluorescence intensity decays exponentially in time.

Near the time origin of the intensity-time (*I*-*t*) axis, the pump beam is turned on for $\delta t = 2$ time units, generating a $\delta x = 3$ unit wide train of NO molecules from the NO_2 gas. The light blue blocks are created at time steps t = 0, 1, and 2. These blocks (or molecules) in the space-time (*x*-*t*) plane move from left to right with a velocity U. Approximately $\delta t = 1$ time unit later, the first exposure is opened at $t_{E1} = t_0 + \Delta t_{D1}$ (not shown). Another $\delta t = 1.5$ time units after this, the first probe beam is turned on ($t_{PROBE_1} = t_0 + \Delta t_{PROBE_1}$) and excites the $\delta x = 3$ unit wide NO gas train, which is centered at $x_{CM,A}$ (the subscript *CM* indicates the center of mass). This excitation is represented by the light violet blocks closest to the origin on the space-time (*x*-*t*) plane. This excitation lasts for $\delta t = 1$ time unit and the photons generated by this excitation are simultaneously captured by the CCD array. After the first probe laser is turned off, the excited NO molecule train, now represented by the gray blocks on the space-time (*x*-*t*) plane, continue to emit photons at a constant intensity as they travel with velocity U in the *x*-direction. Photons from these

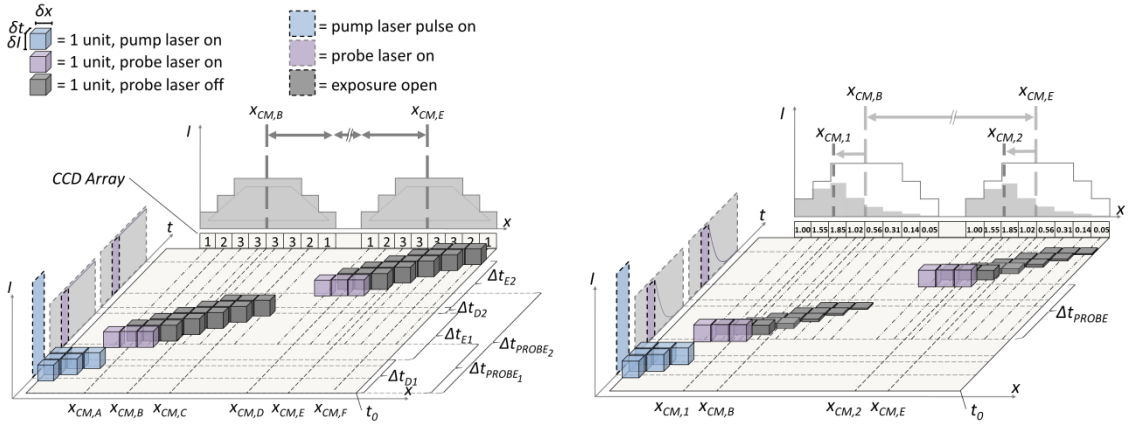

Figure 6.2: Idealized space-time-intensity diagram (not to scale) of NO_2-to-NO photolysis and subsequent NO fluorescence (a) without and (b) with fluorescence decay. Exposures overlap probe laser pulses. Image adapted from Ref. 13.

molecules are continually captured by the CCD array until the end of the first exposure, which occurs $\delta t = 5$ time units after the first probe laser is turned on. At the moment the first exposure is closed, the $\delta x = 3$ unit wide train of NO molecules is centered at $x_{CM,C}$.

The left-most gray shaded area on the intensity-space (*I*-*x*) plane represents the intensity profile captured by the first effective exposure. The intensity at each spatial location on this profile is the time-integrated fluorescence. At the first spatial location in Fig. 6.2a, for example, only $\delta I = 1$ unit is registered by the CCD. This intensity unit originated from the left-most violet block. At the second spatial location, which is also $x_{CM,A}$, $\delta I = 2$ units are registered by the CCD, with the first originating from the middle violet block and the second from the left-most gray block. This time-integrated intensity at each spatial location continues for the duration of the exposure and the final intensity distribution takes the approximate form of a symmetric trapezoid with its center at $x_{CM,B}$. After a period of time corresponding to the interframe delay (Δt_{D2}) the second exposure begins at $t_{E2} = t_0 + \Delta t_{D1} + \Delta t_{E1} + \Delta t_{D2}$ (not shown). This is followed by the re-excitation of the NO gas train by the second probe laser at $t_{PROBE_2} = t_0 + \Delta t_{PROBE_2}$, now centered at $x_{CM,D}$. The intensity distribution captured by the CCD in the second exposure is the same as that obtained in the first exposure, although it has been shifted as a result of advection. The measured displacement between the two intensity profiles captured in the first and second exposures is the difference $\Delta x = x_{CM,E} - x_{CM,B}$, as shown in Fig. 6.2a. Note that the sequence shown in the (*I*-*t*) plane in Fig. 6.2a is similar to the schematic shown in Fig. 3.3a in Chapter 3.

If the effect of fluorescence decay is included in this idealization, as shown in Fig. 6.2b, the measured displacement, $\Delta x = x_{CM,2} - x_{CM,1}$, occurring between the first and second exposures remains the same. However, the captured intensity distribution in each exposure in the (*I*-*x*) plane appears to be shifted away from the direction of travel of the NO gas train as is shown in Fig. 6.2b. The decay process displayed in the intensity-time (*I*-*t*) plane in Fig. 6.2b is similar to the schematic shown in Fig. 3.3b in Chapter 3.

As shown in Fig. 6.2a, the displacement observed between the center of initially marked NO gas train at $x_{CM,A}$ and the center of the intensity distribution captured by the first exposure, $x_{CM,B}$, is:

$$x_{CM,B} - x_{CM,A} = x_{CM,C} - x_{CM,B} = \frac{x_{CM,C} - x_{CM,A}}{2} = U \cdot \frac{\Delta t_{eE1}}{2} \tag{6.2}$$

Recall that the effective first exposure, Δt_{eE1}, is the time between the initial excitation of the first probe laser and the end of the first exposure, or:

$$\Delta t_{eE1} = (t_0 + \Delta t_{D1} + \Delta t_{E1}) - \left(t_0 + \Delta t_{PROBE_1}\right) = \Delta t_{E1} - \left(\Delta t_{PROBE_1} - \Delta t_{D1}\right) \tag{6.3}$$

In Eq. 6.3, the term in the right-most parenthesis is defined as the first probe delay, $\Delta t_{PROBE_{1,Delay}}$, as it represents the delay between the opening of the first exposure and the firing of the first probe laser. Prior to this period, no signal is collected by the CCD. Substituting Eq. 6.3 into Eq. 6.2 gives:

$$x_{CM,B} - x_{CM,A} = U \cdot \frac{\Delta t_{E1} - \Delta t_{PROBE_{1,Delay}}}{2} \tag{6.4}$$

When the first exposure is closed, the NO gas train continues to travel downstream during the interframe delay, Δt_{D2}. As in the first exposure, the firing of the second probe laser is delayed from the opening of the second exposure. When the second probe laser is turned on, the second effective exposure, Δt_{eE2}, begins.

$$\Delta t_{eE2} = \Delta t_{E2} - \left(\Delta t_{PROBE_2} - \Delta t_{D2} - \Delta t_{E1} - \Delta t_{D1}\right) \tag{6.5}$$

The term in parenthesis in Eq. 6.5 is defined as the second probe delay, $\Delta t_{PROBE_{2,Delay}}$. After the second probe delay, the NO gas train is centered at $x_{CM,D}$. The displacement measured between the location of the NO gas train at the end of the first effective exposure and the beginning of the second effective exposure is then:

$$x_{CM,D} - x_{CM,C} = U \cdot \left(\Delta t_{D2} + \Delta t_{PROBE_{2,Delay}}\right) \tag{6.6}$$

As in Eq. 6.2, the displacement observed between the center of initially marked NO gas train at $x_{CM,D}$ and the center of the intensity distribution captured by the second exposure, $x_{CM,E}$, is:

$$x_{CM,E} - x_{CM,D} = x_{CM,F} - x_{CM,E} = \frac{x_{CM,F} - x_{CM,D}}{2} = U \cdot \frac{\Delta t_{eE2}}{2} \tag{6.7}$$

Substituting Eq. 6.5 into 6.7 gives:

$$x_{CM,E} - x_{CM,D} = U \cdot \frac{\Delta t_{E2} - \Delta t_{PROBE_{2,Delay}}}{2} \tag{6.8}$$

Combining the results of Eqs. 6.2, 6.4, 6.6, and 6.8 gives the total displacement between the profiles imaged in the first and second effective exposures:

$$\Delta x = \begin{bmatrix} \left(x_{CM,E} - x_{CM,D}\right) + \left(x_{CM,D} - x_{CM,C}\right) + \cdots \\ \left(x_{CM,C} - x_{CM,B}\right) + \left(x_{CM,B} - x_{CM,A}\right) \end{bmatrix} - \left(x_{CM,B} - x_{CM,A}\right)$$

$$\Delta x = U \cdot \left[\frac{\Delta t_{E2} - \Delta t_{PROBE_{2,Delay}}}{2} + \Delta t_{D2} + \Delta t_{PROBE_{2,Delay}} + \frac{\Delta t_{E1} - \Delta t_{PROBE_{1,Delay}}}{2}\right] \equiv U \cdot \Delta t \tag{6.9}$$

In the experiment, settings of $\Delta t_{PROBE_{1,Delay}} = \Delta t_{PROBE_{2,Delay}}$ and $\Delta t_{E2} = \Delta t_{E1}$ were used to ensure a symmetric intensity distribution would be captured in the first and second camera exposures. Using these settings, the definitions for probe delay in Eqs. 6.3 and 6.5, respectively, and the result of Eq. 6.9, an alternative, but equivalent, relation for Δt (as implied by Fig. 3.3a in Chapter 3 and Fig. 6.2b) is:

$$\Delta x = U \cdot \Delta t = U \cdot \Delta t_{PROBE} \equiv U \cdot \left(\Delta t_{PROBE_2} - \Delta t_{PROBE_1}\right) \tag{6.10}$$

6.1.2.2 *Phenomenological Derivation of Displacement (Probe Laser Prior to Exposure)*

Figure 6.3 provides an idealized representation of the same process as shown in Fig. 6.2; however, in this idealization, the first and second exposures open *after* the respective probe laser pulses. In Fig. 6.3a, as in Fig. 6.2a, it is assumed that the fluorescence intensity following probe laser excitation in the first and second exposures is constant during the respective exposures.

In Fig. 6.3a, the distance traveled by the NO gas train after initial excitation by the first probe laser, but before the first exposure opens, is:

$$x_{CM,A} - x_{CM,a} = U \cdot \left[\Delta t_{D1} - \left(\Delta t_{PROBE_1} + \Delta t_P\right)\right] \tag{6.11}$$

Similar to the case shown in Fig. 6.3a and described by Eq. 6.2, the displacement observed between the center of the NO gas train at the beginning of the first exposure and the center of the intensity

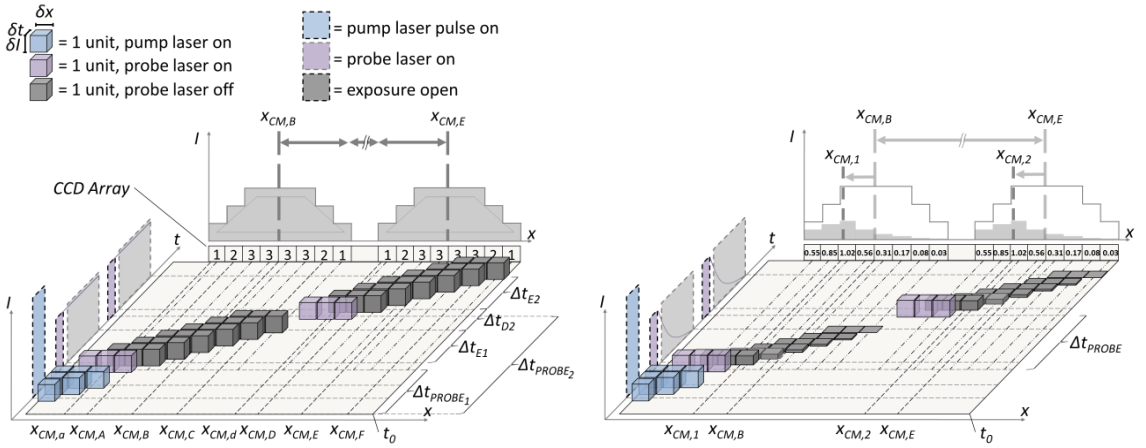

Figure 6.3: Idealized space-time-intensity diagram (not to scale) of NO_2-to-NO photolysis and subsequent NO fluorescence (a) without and (b) with fluorescence decay. Exposures after probe laser pulses. Image adapted from Ref. 12.

distribution captured by the first exposure is:

$$x_{CM,B} - x_{CM,A} = x_{CM,C} - x_{CM,B} = \frac{x_{CM,C} - x_{CM,A}}{2} = U \cdot \frac{\Delta t_{E1}}{2} \tag{6.12}$$

Once the first exposure is closed, the NO gas train continues downstream at a constant velocity U. The second probe laser then re-excites the NO. The displacement occurring between the end of the first exposure and the end of this re-excitation is:

$$x_{CM,d} - x_{CM,C} = U \cdot \left[\left(\Delta t_{PROBE_2} + \Delta t_P\right) - \left(\Delta t_{D1} + \Delta t_{E1}\right)\right] \tag{6.13}$$

The distance traveled by the NO gas train after the re-excitation by the second probe laser, but before the second exposure opens, is:

$$x_{CM,D} - x_{CM,d} = U \cdot \left[\left(\Delta t_{D1} + \Delta t_{E1} + \Delta t_{D2}\right) - \left(\Delta t_{PROBE_2} + \Delta t_P\right)\right] \tag{6.14}$$

As in Eq. 6.7, the displacement observed between the center of the NO gas train at beginning of the second exposure and the center of the intensity distribution captured by the second exposure is:

$$x_{CM,E} - x_{CM,D} = x_{CM,F} - x_{CM,E} = \frac{x_{CM,F} - x_{CM,D}}{2} = U \cdot \frac{\Delta t_{E2}}{2} \tag{6.15}$$

Combining Eqs. 6.11, 6.12, 6.13, 6.14, and 6.15 gives the total displacement between the profiles imaged in the first and second exposures:

$$\begin{gathered}\Delta x = \begin{bmatrix} \left(x_{CM,E} - x_{CM,D}\right) + \left(x_{CM,D} - x_{CM,d}\right) + \cdots \\ \cdots \\ \left(x_{CM,B} - x_{CM,A}\right) + \left(x_{CM,A} - x_{CM,a}\right) \end{bmatrix} - \begin{bmatrix} \left(x_{CM,B} - x_{CM,A}\right) + \cdots \\ \left(x_{CM,A} - x_{CM,a}\right) \end{bmatrix} \\ \Delta x = x_{CM,E} - x_{CM,B} = U \cdot \left(\frac{\Delta t_{E2}}{2} + \Delta t_{D2} + \frac{\Delta t_{E1}}{2}\right) \equiv U \cdot \Delta t\end{gathered} \tag{6.16}$$

Note that in Eq. 6.9, if $\Delta t_{PROBE_{1,Delay}} = \Delta t_{PROBE_{2,Delay}}$, the relation for Δx is identical to the result obtained in Eq. 6.16.

With this timing configuration, Δt_{PROBE} was set such that the final expression in Eq. 6.16 is equivalent to:

$$\Delta x = U \cdot \Delta t = U \cdot \Delta t_{PROBE} \tag{6.17}$$

6.2 Uncertainty Analysis

The general form of the uncertainty in the mean streamwise velocity and single-shot streamwise velocity uncertainty is similar to that presented in Eq. 4.23 of Chapter 4. In this chapter, the uncertainty in the mean streamwise velocity is represented as:

$$u_{\bar{U}} = \sqrt{\left(u_{\bar{U},\overline{\Delta x}}\right)^2 + \left(u_{\bar{U},\Delta t}\right)^2 + \left(u_{\bar{U},\bar{M}}\right)^2 + \left(u_{\bar{U},\text{Accuracy}}\right)^2} \tag{6.18}$$

and the single-shot streamwise velocity uncertainty is represented as:

$$u_U = \sqrt{\left(u_{U,\Delta x}\right)^2 + \left(u_{U,\Delta t}\right)^2 + \left(u_{U,\bar{M}}\right)^2 + \left(u_{U,\text{Accuracy}}\right)^2} \tag{6.19}$$

6.2.1 Spatial Uncertainty

6.2.1.1 *Uncertainty in the Mean*

For a sample of instantaneous measurements, the uncertainty in the mean streamwise velocity resulting from uncertainty in measured displacement (spatial uncertainty) is $u_{\bar{U},\overline{\Delta x}}$. This uncertainty term is composed of uncertainty in $\overline{\Delta x}$ resulting from (1) flow unsteadiness, resulting in measured fluctuations in Δx and (2) reduced signal-to-noise levels, resulting in errors in determining the precise value of Δx due to poorly conditioned cross-correlation results. Using Eq. 6.1, this term is:

$$u_{\bar{U},\overline{\Delta x}} = \frac{\partial \bar{U}}{\partial(\overline{\Delta x})} \cdot u_{\overline{\Delta x}} = \frac{1}{\Delta t} \cdot \frac{t_{N-1,95\%} \cdot \sigma_{\overline{\Delta x}}}{\sqrt{N}} \tag{6.20}$$

where $t_{N-1,95\%}$, is the student t-statistic at 95% confidence, N is the number of data points used to compute velocity at a particular point in the images, and $\sigma_{\overline{\Delta x}}$ is the measured standard deviation of $\overline{\Delta x}$.

6.2.1.2 *Single-Shot Uncertainty*

Measurement of displacement, Δx, on a shot-to-shot basis is affected by the signal-to-noise ratio and true flow unsteadiness. For single-shot MTV measurements, especially those made in a flow undergoing transition-to-turbulence, one of the primary parameters of interest is the fluctuating component of streamwise velocity, U'. Therefore, a method to isolate the contribution of systematic measurement error resulting from signal-to-noise ratio effects from the contribution of U' to variance in the measured Δx is needed. This will allow for an estimate of the single-shot spatial measurement uncertainty, $u_{U,\Delta x}$, and a separate estimate of U'.

To estimate the signal-to-noise ratio, correlation windows of width $W_i = 45$ pixels (described in Chapter 4) were centered along a series of MTV profiles. The subscript *i* refers to either the first or second exposure. For each window and for each single-shot image pair, the displacement, Δx, maximum signal (or *peak*), P_i, and minimum signal (or *valley*), V_i, were measured while the wind tunnel was not operating. This allowed for measurement of these parameters in a (nearly) static gas where both the mean and fluctuating

component of streamwise velocity were assumed to be zero. Figure 6.4 shows representative intensity profiles from a reference (first exposure) and delayed (second exposure) image where the peak, valley, and displacement are identified. It should be noted that the measurement of V_i was limited to the 21 pixels centered about P_i. This was done to ensure that signal information from neighboring profiles was not included in the measurement. Additionally, the standard deviation of the signal within a 5×5-pixel-square window, centered about P_i, was used to estimate the noise, N_i. For each single-shot image, the signal-to-noise ratio, SNR_i, was computed by dividing the difference between the peak and valley signal by the noise, $SNR_i = (P_i - V_i)/N_i$. For each measurement of Δx, the signal-to-noise ratio for each sequential image pair of was computed by multiplying the individual signal-to-noise ratios of the first and second exposures and then computing the square root of this product:

$$SNR = \sqrt{SNR_{E1} \cdot SNR_{E2}} \tag{6.21}$$

This method of calculating SNR was chosen because it accounts for the quality of the data in both the first and second exposures.

Using the SNR in Eq. 6.21 and measured Δx for each sequential image pair, an analysis of the standard deviation in Δx as a function of SNR can be performed to determine a relation for $u_{U,\Delta x}$. To do this, SNR data points were grouped together in bins in increments of 0.25. For this analysis, if fewer than 100 single-shot measurements were used to compute a particular $u_{U,\Delta x}$ value for a given SNR bin, the point was rejected. The measurement was repeated for Δt settings of 1, 2, 5, 10, and 25 μs.

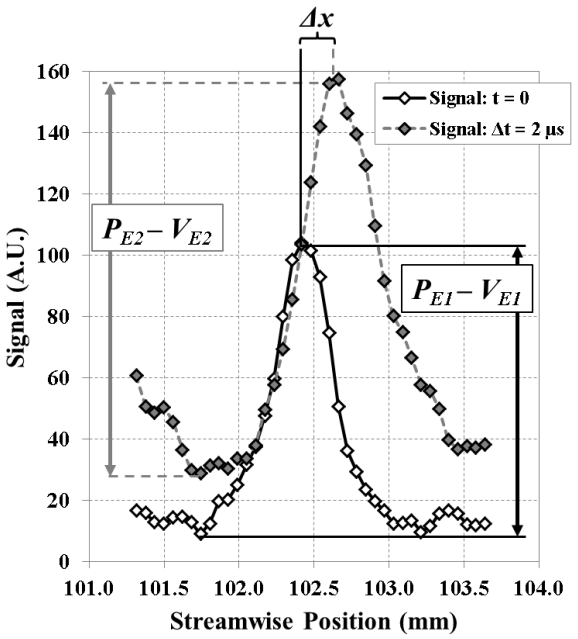

Figure 6.4: Fluorescence intensity profiles in first (white) and second (gray) exposures. Parameters used for computing signal-to-noise ratio are also shown. Image adapted from Ref. 12.

Figure 6.5 shows the spatial single-shot velocity uncertainty, or spatial uncertainty, $u_{U,\Delta x}$, defined as:

$$u_{U,\Delta x} = t_{N-1,95\%} \cdot \sigma_{U,\Delta x_{SNR}} \tag{6.22}$$

where $\sigma_{U,\Delta x_{SNR}}$ is the standard deviation in N single-shot streamwise velocity measurements assuming $U = 0$, and $t_{N-1,95\%}$ is the student t-statistic at 95% confidence. This value is plotted as a function of SNR. The behavior of spatial uncertainty as a function of signal-to-noise ratio in Fig. 6.5 is similar to that of the right-hand-side of a Gaussian-like distribution. A similar behavior occurs for $\sigma_{U,\Delta x_{SNR}}$ (not shown) as a function of SNR. A fit to the data at the any of the Δt delay settings will then be of the form:

$$\sigma_{U,\Delta x_{SNR}} = \frac{A+Bexp\left[-(C\cdot\{SNR-D\})^2\right]}{\Delta t} \tag{6.23}$$

where the coefficients *B*, *C*, and *D* are all functions of Δt. The spatial uncertainty shown in Fig. 6.5 can be obtained using Eq. 6.22. Since at least 100 measurements per SNR increment were used to generate the relation in Eq. 6.23, $t_{N-1,95\%}$ can be approximated as $t_{N\geq100,95\%} \approx t_{\infty,95\%} = 1.960$. For the streamwise velocity measurements presented in this chapter, only measurements with $SNR \geq 5$ are accepted for processing, with those falling below this threshold being rejected.

The inset plot in Fig. 6.5 represents the spatial uncertainty at 95% confidence in terms of measured displacement of the velocity profiles in units of pixels. Examination of the inset plot in Fig. 6.5 shows two important trends. First, considering the data at the highest signal-to-noise levels, the current image analysis method can measure velocity to within 0.5 pixels at 95% confidence. This limit appears to be nearly independent of Δt for the conditions of this experiment. This could be the result of a systematic error in the image analysis algorithm, a true velocity fluctuation in the flowfield, or both. Second, as Δt is increased, the uncertainties at lower signal-to-noise levels increase. This behavior may be a result of mass diffusion, which increases

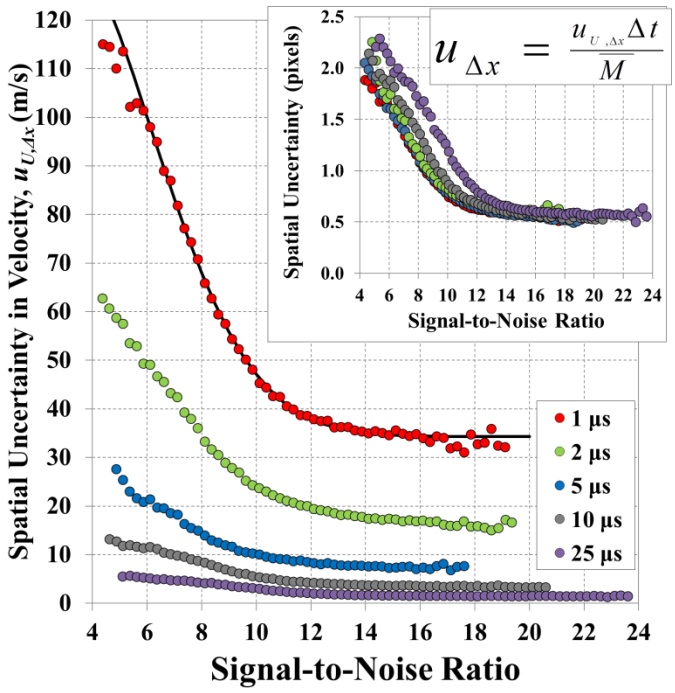

Figure 6.5: Measured spatial uncertainty in m/s (velocity, larger plot) and pixels (inset plot) as a function of signal-to-noise ratio for several Δt settings. P_{static} = 2.9 kPa. Measurements performed in a nominally quiescent flow. Image adapted from Ref. 12.

the width of the profiles, and broadens the correlation peak, making it more difficult to identify the center of the peak.

Figure 6.6 shows the data yield as a function of SNR for the five Δt settings examined in Fig. 6.5. Here, the data yield is the percent of measurement points that result in an acceptable streamwise velocity measurement after applying the rejection threshold of $SNR < 5$. At the lowest SNR, the data yield trend is nearly the same for each Δt. At the highest SNR levels ($SNR > 14$), the data yield is nearly 100% for each Δt.

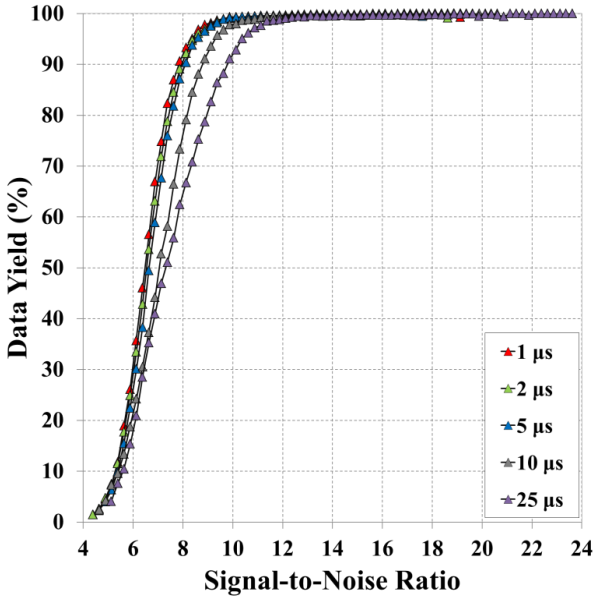

Figure 6.6: Data yield as a function of SNR for several Δt settings. Measurements performed in a nominally quiescent flow. Image adapted from Ref. 12.

For $5 < SNR < 14$, the slope of the intermediate region (the region in which the data yield increases from less than 10% to nearly 100%) decreases with increasing probe delay. Again, this may be a result of gas diffusion adversely affecting data yield in this region.

Figure 6.7 shows the average of spatial uncertainty (circles) as a function of Δt setting, rather than signal-to-noise ratio as in Fig. 6.5. The average is first computed for all data with a yield between 10% – 90% (solid circles), corresponding to both the intermediate region shown in Fig. 6.6 and the quasi-linear portion of the Gaussian-like distribution in Fig. 6.5. The average is also computed for all data with a yield above 98% (empty circles), corresponding to the wing of the Gaussian-like distribution in Fig. 6.5. These points represent the "best case" spatial uncertainty for this experiment. In both instances, the average spatial uncertainty decreases monotonically with Δt and follows the power fit relations provided in the figure.

6.2.2 Timing Uncertainty

Initial experiments in Ref. 13 used a timing sequence similar to that in Fig. 6.2b where the fluorescence lifetime is small relative to the exposures. With this assumption, and because the NO gas train is excited independently in both the first and second exposures by the respective probe lasers, the

measurement uncertainty in streamwise velocity resulting from timing uncertainties have been assumed to be a function of systematic errors associated with the laser system and the triggering device (Labsmith LC880 timing generator). This timing uncertainty in this analysis is assumed to be insensitive to uncertainties associated with the camera timing. Using Eq. 6.17, the timing uncertainty is:

$$u_{\Delta t} = \sqrt{\left(\frac{\partial(\Delta t)}{\partial\left(\Delta t_{PROBE_2}\right)} \cdot u_{\Delta t_{PROBE_2}}\right)^2 + \left(\frac{\partial(\Delta t)}{\partial\left(\Delta t_{PROBE_1}\right)} \cdot u_{\Delta t_{PROBE_1}}\right)^2} \tag{6.24}$$

In Eq. 6.24, $u_{\Delta t_{PROBE_1}}$ and $u_{\Delta t_{PROBE_2}}$ are a result of systematic errors caused by the timing circuits of the laser system and triggering device. Recall from Section 6.1.2.1 that the moment the first probe laser is turned on corresponds to $t_{PROBE_1} = t_0 + \Delta t_{PROBE_1}$, and for the second probe laser, $t_{PROBE_2} = t_0 + \Delta t_{PROBE_2}$. From Table 4.2 in Chapter 4, the uncertainty associated with the triggering device is $u_{t_0} = 0.2$ ns. In this analysis, the uncertainties associated with t_{PROBE_1} and t_{PROBE_2} are assumed equivalent to that associated with the probe laser Q-switch: $u_{t_{PROBE_1}} = u_{t_{PROBE_2}} = u_{\text{Q-Switch}} = 1.0$ ns. The timing uncertainty of either probe laser is then:

$$u_{\Delta t_{PROBE_i}} = \sqrt{\left(\frac{\partial\left(\Delta t_{PROBE_i}\right)}{\partial(t_0)} \cdot u_{t_0}\right)^2 + \left(\frac{\partial\left(\Delta t_{PROBE_i}\right)}{\partial\left(t_{PROBE_i}\right)} \cdot u_{\text{Q-Switch}}\right)^2} \tag{6.25}$$

where i = 1 or 2. Combining Eq. 6.25 with Eq. 6.24 gives the total timing uncertainty as:

$$u_{\Delta t} = \sqrt{2 \cdot \left(u_{t_0}^2 + u_{\text{Q-Switch}}^2\right)} \tag{6.26}$$

Using Eq. 6.26 and the appropriate values from Table 4.2 in Chapter 4, $u_{\Delta t} = u_{\overline{\Delta t}} = 1.44$ ns.

In this experiment, the experimental conditions are assumed to result in a process similar to that presented in Fig. 6.3b. This results in a different expression for timing uncertainty using the result of Eq. 6.16:

$$u_{\Delta t} = \sqrt{\left(u_{\Delta t_{E2}}/2\right)^2 + \left(u_{\Delta t_{D2}}\right)^2 + \left(u_{\Delta t_{E1}}/2\right)^2} \tag{6.27}$$

Using Eq. 6.27 and the appropriate values from Table 4.2 in Chapter 4, $u_{\Delta t} = u_{\overline{\Delta t}} = 0.25$ ns.

Using Eq. 6.1, the uncertainty in the mean streamwise velocity is:

$$u_{\overline{U},\Delta t} = \frac{\partial \overline{U}}{\partial \Delta t} \cdot u_{\Delta t} \tag{6.28}$$

and the single-shot uncertainty resulting from timing uncertainties is:

$$u_{U,\Delta t} = \frac{\partial U}{\partial \Delta t} \cdot u_{\Delta t} \tag{6.29}$$

For the analysis presented in the chapter and Chapter 7, the timing uncertainty of the form in Eq. 6.26 has been used.

6.2.3 Magnification and Accuracy

The uncertainty in the mean streamwise velocity resulting from uncertainty in magnification, $u_{\bar{U},\bar{M}}$, and the single-shot streamwise velocity uncertainty resulting from uncertainty in magnification, $u_{U,\bar{M}}$, were computed using the same method outlined in Section 4.2.3 of Chapter 4. Table 6.1 provides the mean magnification and uncertainty in the mean magnification for this experiment.

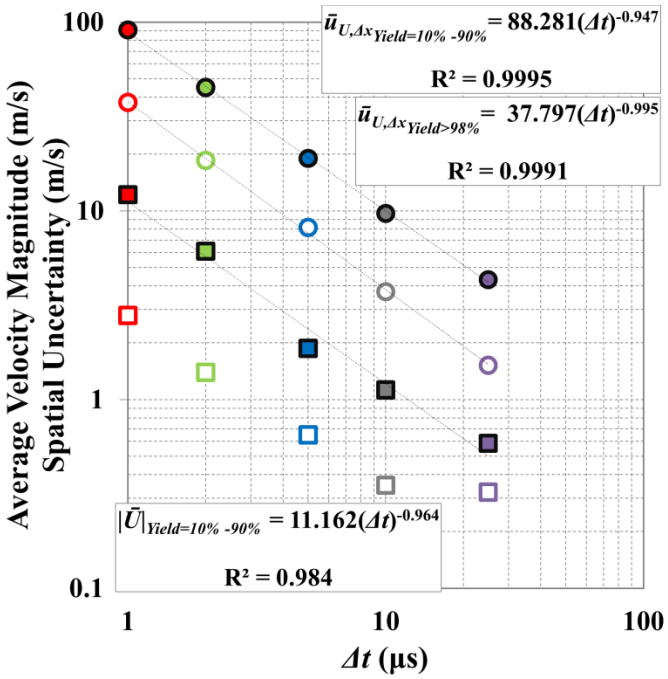

Figure 6.7: Average measured streamwise velocity magnitude ($\bar{U}$, squares) and the associated average spatial uncertainty ($\overline{u_{U,\Delta x}}$, circles) for higher (>98%, open) and lower (10% - 90%, filled) data yields as functions of several Δt settings. Measurements performed in a nominally quiescent flow. Image adapted from Ref. 12.

Figure 6.7 also shows measured average streamwise velocity magnitude, $\bar{U}$, as a function of Δt represented by the square data points. For the velocity data with a yield between 10% – 90% (solid squares), the same monotonic decreasing pattern observed with spatial uncertainty occurs. This data set follows the power fit relation shown in the lower left-hand corner. The average streamwise velocity data with a yield greater than 98% (empty squares) exhibit a similar trend up to Δt = 10 µs. However, for Δt = 25 µs, no further reduction in measured velocity occurs. This suggests that the nearly quiescent flow actually had small streamwise velocity components or streamwise velocity fluctuations of approximately 0.3 m/s. Any measured

Table 6.1: Magnification values.

Parameter	Value
Mean Magnification, $\bar{M}$	6.12×10^{-2} mm/pixel
Uncertainty in the Mean Magnification, $u_{\bar{M}}$	$\pm10.96\times10^{-5}$ mm/pixel

velocities above 0.3 m/s are assumed to be a result of systematic errors in the measurement system. The filled squares in Fig. 6.7 represent the accuracy terms, $u_{\bar{U},Accuracy}$ and $u_{U,Accuracy}$, used in the calculation of both uncertainty in mean streamwise velocity and single-shot streamwise velocity, respectively.

The average streamwise velocity magnitude trend shown in Fig. 6.7 has a dependence on Δt that is similar to the simple relation:

$$|\bar{U}| = \frac{\Delta x_{true} + \Delta x_{systematic\ error}}{\Delta t} \tag{6.30}$$

where Δx_{true} is the measured displacement of the profile in an amount of time, Δt, and $\Delta x_{systematic\ error}$ is a systematic error of constant magnitude associated with the analysis method. For relatively short Δt settings, the magnitude of $\Delta x_{systematic\ error}$ may be significant compared to Δx_{true} and therefore have a significant effect on measured velocity. As Δt is increased, the influence of $\Delta x_{systematic\ error}$ on measured streamwise velocity is diminished. The trends in Fig. 6.7 therefore provide a quantitative description of the contribution of the spatial uncertainty to the systematic error present in the measurement.

6.3 Results

6.3.1 Velocity Measurements in a Hypersonic Boundary Layer: Variable Δt, Constant $\dot{m}_{NO_2}$

Figure 6.8 shows several mean streamwise velocity profiles, $\bar{U}$, acquired at several streamwise locations obtained with two Δt settings: 1μs – red data points, 2μs – green data points. These data sets were acquired during Run 5 of Test 481, with the conditions of this run given in Table 3.3 of Chapter 3. The horizontal axes in this figure correspond to streamwise velocity magnitude and the vertical axes correspond to wall-normal *y*-position away from the model surface. The widths of the bars correspond to the uncertainty in the mean streamwise velocity, computed using Eq. 6.18 ($\pm u_{\bar{U}}$). Only streamwise velocities for which the number of single-shot measurements, N, at that location was $N \geq 0.1 \cdot N_{\text{Images}}$ are presented in this figure, where N_{Images} is the total numbers of image pairs. The gain setting of the DiCAM-Pro camera for this study was 20%.

As described in Section 6.1.1, a small physical displacement of the model was observed that presumably is a result of non-uniform thermal loading of the sting. It is estimated that during the Δt = 1 μs and Δt = 2 μs acquisition periods, the model was displaced downward by 0.6 mm and 0.3 mm, respectively.

The heights of the bars in Fig. 6.8 qualitatively convey the uncertainty in *y*-position after correcting the images, but do not represent a quantitative estimate of this uncertainty. This displacement will alter the plate angle. For a displacement of 0.6 mm, the plate angle changes by less than 0.1°, resulting in a change of M_e of less than 0.5%. This is assumed to have a negligible effect on the boundary layer flow.

For both data sets presented in Fig. 6.8, the mean blowing rates were $\dot{m}_{NO_2}$ = 15.6 mg/s (0.501 standard liters per minute, SLPM). The average plate temperature (measured with a thermocouple mounted to the back side of the top surface of the model) for the Δt = 1 μs data was 316 K, and for the Δt = 2 μs data was 373 K. During the Δt = 1 μs acquisition period, either the pump laser beams, probe laser sheets, or both were noticeably shifting relative to each other and relative to the model. This reduced the total number of measurements at a particular location available for analysis in this image set. The pump and probe laser energies were also not uniform over the measurement region during this experiment. As a result, the laser intensity was highest for the profile at *x* = 100.5 mm but visibly diminished for profiles both upstream and downstream of this location. This limited the measurement region to profiles between *x* = 98.4 mm and *x* = 108.2 mm.

Data were also acquired for the Δt = 5 μs setting in Run 5 listed in Table 3.3 of Chapter 3. However, the combination of a relatively low blowing rate ($\dot{m}_{NO_2}$ = 8.8 mg/s, 0.283 SLPM), relatively low SNR, and the inability of the analysis algorithm to distinguish between adjacent profiles prevented analysis. Figure 6.9 provides an averaged delayed image for each Δt setting. This figure highlights the relatively poor quality of the Δt = 5 μs images relative to the Δt = 1 μs and Δt = 2 μs images.

In Fig. 6.8, the streamwise velocity measurements between approximately *y* = 0.05 mm and *y* = 0.60 mm agree relatively well with analytic solutions corresponding to Δt = 1 μs (red curves) and Δt = 2 μs (green curves). These solutions were computed using approximately the lowest and highest wall temperatures measured over the courses of the run. While the measurements do not overlap entirely in this region—that is most likely a result of differing wall temperatures affecting the velocity profiles—they demonstrate two important aspects of the technique. First, the measurement technique is repeatable and nearly independent of Δt. The exception to this being a Δt setting that is too great (i.e. 5 μs), in which case the individual profiles cannot be adequately resolved. Second, a small but noticeable reduction in the uncertainty in the mean streamwise velocity accompanies an increased Δt. Between *y* = 0.05 mm and *y* =

0.60 mm, the average reduction in the uncertainty in the mean streamwise velocity was 10% across the profile at x = 102.4 mm.

Below y = 0.05 mm, the velocity profiles do not tend linearly towards zero as expected (no-slip velocity wall condition). Instead, the measured velocities near the wall are approximately 10% of the estimated freestream value. Figure 6.4 showed a single-shot pair of fluorescence intensity distributions from a sequential image pair (frame 174 from Run 5). These signal distributions are taken just above the model surface for the profile at x = 102.4 mm. The Δt = 2 μs delayed image shows a clear shift relative to the reference image. This corresponds to a streamwise velocity of approximately U =120 m/s.

There are several potential explanations for this behavior. First, some slip velocity at the wall may exist, although analysis of velocity slip using Eqs. 5.1, 5.2, and 5.3 in Chapter 5 shows that this slip should be less than 30 m/s at x = 89.0 mm. Second, a potentially high flux of photoelectrons incident onto the camera's phosphor screen, generated by scattered light from the first probe laser off the quartz window insert, may deplete the phosphor at this particular location. This would result in diminished signal at this location in the delayed image. Third, pixel blooming may occur because of relatively high signal levels at this particular location. At the point where the profile is incident on the quartz window surface, blooming would bias the measured velocity via signal contamination from regions slightly above the plate surface and from reflections off the quartz window surface. Further study is needed to determine the precise cause of this discrepancy between the measured non-zero streamwise velocity near the wall and the analytic solution.

Above y = 0.6 mm, the mean velocity profiles are biased away from the analytic solution, with smaller than expected streamwise velocities relative to the analytic solutions. There are several potential reasons for these discrepancies. First, the estimated edge conditions may not reflect the true edge properties, and therefore the analytic solutions may not be representative of the true velocity boundary layer behavior. Second, the gas seeding (which is not accounted for in the analytic solution) may alter the experimental velocity profile, especially above y = 0.6 mm, resulting in slower streamwise velocity in this region. Third, any significant discrepancies existing between the velocity and concentration boundary layer thicknesses may affect the measured velocity profiles. Analysis of the single-shot images from both acquisition periods (1 μs and 2 μs) indicates that the profiles were, to a limited extent, oscillating irregularly in the y-direction.

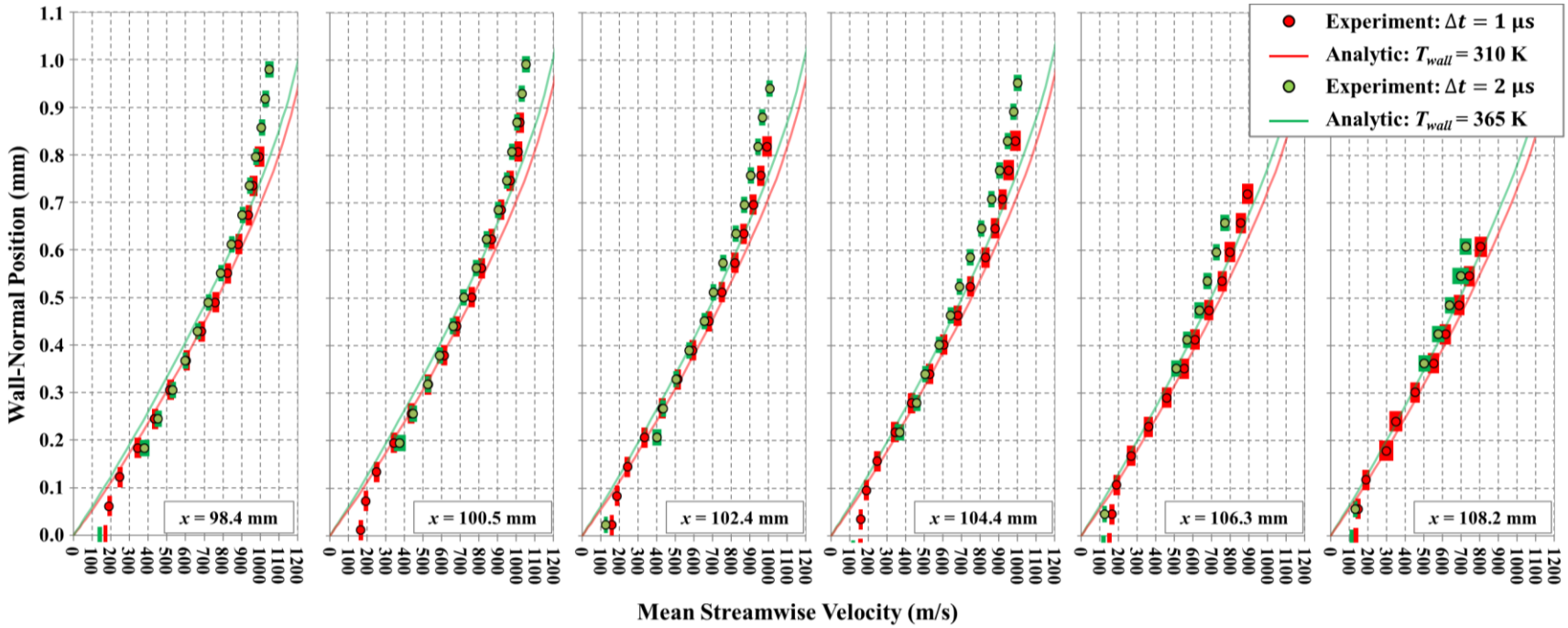

Figure 6.8: Mean velocity profiles ($\overline{U} \pm u_{\overline{U}}$) for Δt settings of 1 μs (red data) and 2 μs (green data). Solid red and green lines correspond to analytic velocity boundary layer solutions for wall temperatures of 310 K and 365 K, respectively. Measured wall temperatures were 315.9 K and 372 K, respectively. Image adapted from Ref. 12.

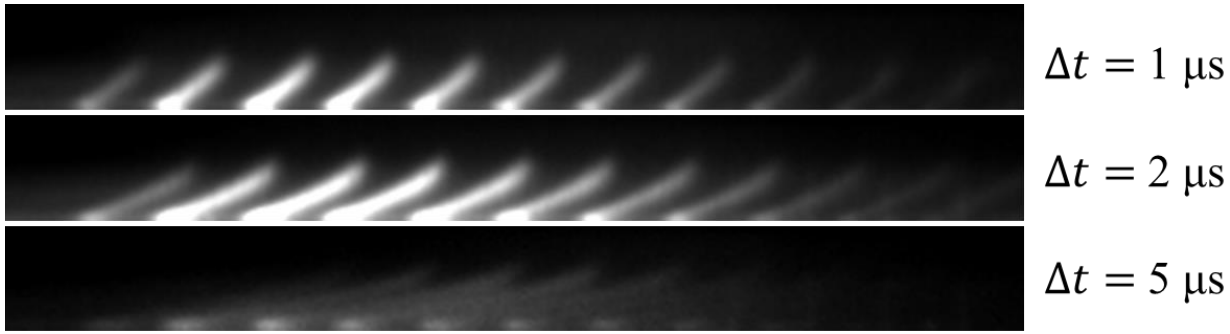

Figure 6.9: Average of raw images with Δt settings of 1 μs (top), 2 μs (middle), and 5μs (bottom). Image adapted from Ref. 12.

In some instances, the upper tips of the profiles in the delayed images bent sharply upward. However, it is unclear if this corresponds to a thickening of the concentration layer – thus providing an intermittent measure of the edge of the velocity layer – or if this was some form of velocity instability. A numerical study of boundary layer behavior for relatively low blowing rates ($\dot{m}_{NO_2} \leq$ 3mg/s) performed in Ref. 16 discussed several consequences of blowing. While the blowing rate and edge conditions of the study in Ref. 16 were more readily applicable to the results presented in Chapters 4 and 5 than for these conditions, the results of that study suggest that an increased blowing rate alters the streamwise velocity profile, resulting in a deficit relative to the expected streamwise velocity profile.

6.3.2 Velocity Measurements in a Hypersonic Boundary Layer: Constant Δt, Variable $\dot{m}_{NO_2}$

Figure 6.10 shows several mean velocity profiles for $\dot{m}_{NO_2}$ = 15.3 mg/s (0.491 SLPM, gray data points) and $\dot{m}_{NO_2}$ = 161.3 mg/s (5.179 SLPM, black data points). The probe delay for these data was Δt = 1 μs. These were the lowest and highest mass flow rates tested for Run 12 of Test 481 (see Table 3.3 of Chapter 3). The plots are organized from left to right according to increasing streamwise location. For these acquisition periods, the measured mean wall temperatures corresponding to the 15.3 mg/s and 161.3 mg/s blowing rates were T_{wall} = 317 K and T_{wall} = 403 K, respectively. As a reference, three analytic compressible velocity boundary layer solutions are superimposed on top of the measurements. The blue, green, and red profiles correspond to wall temperatures of 310 K, 365 K, and 420 K, respectively. These were approximately the lowest, mean, and highest wall temperatures measured over the course of Run 12. The inset plots in the upper left-hand corner of the mean streamwise velocity plots provide an estimate of the fluctuating component of streamwise velocity, U', for each blowing rate tested.

To obtain an estimate of U', the standard deviation of the measured mean streamwise velocity, $\sigma_{\overline{U}}$, must be separated into its constituent components. Specifically, the component arising from systematic error from SNR effects, $\sigma_{\overline{U},\overline{\Delta x}_{\overline{SNR}}}$, must be quantified using Eq. 6.23 assuming that:

$$\sigma_{\overline{U},\overline{\Delta x}_{\overline{SNR}}} = \frac{A+Bexp\left[-\left(C\cdot\{\overline{SNR}-D\}\right)^2\right]}{\Delta t} \tag{6.31}$$

The variance in $\overline{U}$, $\sigma_{\overline{U}}^2$, resulting from random fluctuations in SNR is assumed to be independent of the variance in the $\overline{U}$ resulting from random streamwise velocity fluctuations, $(U')^2$. With the assumption that

each of these quantities are independent of each other and that each can be described by a normal distribution, their sum can be equated with the total variance (or covariance) of $\overline{U}$ such that:[17]

$$\sigma_{\overline{U}}^2 = (U')^2 + \left(\sigma_{\overline{U},\overline{\Delta x}_{\overline{SNR}}}\right)^2 \tag{6.32}$$

This allows for an estimate of the fluctuation in the mean streamwise velocity by solving for U':

$$U' = \sqrt{\max\left\{\left[\sigma_{\overline{U}}^2 - \left(\sigma_{\overline{U},\overline{\Delta x}_{\overline{SNR}}}\right)^2\right], 0\right\}} \tag{6.33}$$

A similar method to estimate U'has previously been applied to the single-laser NO MTV technique in Refs. 6 and 18.

In Fig. 6.10, as in Fig. 6.8, the measurements for $\dot{m}_{NO_2}$ = 15.3 mg/s between y = 0.05 mm and y = 0.60 mm agree relatively well with the T_{wall} = 310 K analytic solution. For the $\dot{m}_{NO_2}$= 161.3 mg/s case, the $\overline{U}$ profiles demonstrate a noticeable deficit away from the analytic solution (which neglects blowing) with increasing x for T_{wall} = 420 K. The higher wall temperature produces an increased velocity boundary layer thickness, and since the accuracy of the T_{wall} measurement is unknown, the observed deficit may be due to an underestimate of T_{wall}.

At the lower blowing rates the U' profiles (inset plots in Fig. 6.10) are parabola-like at some streamwise locations and scattered at others. This is in contrast to the U' measurements at the higher blowing rate, which have a definite parabola-like shape at each streamwise position. In these profiles, the y-position of the peak U' at each streamwise location is denoted by the red square. Generally, the U' magnitudes at the lower blowing rate are a factor of two lower than at the higher blowing rate. That is, higher blowing rates have a greater perturbative effect on the boundary layer, resulting in fluctuations that are larger in magnitude and that penetrate higher into the boundary layer.

Considering both $\overline{U}$ and U' profile plots in Fig. 6.10, there are clearly changes of behavior between the lower and higher $\dot{m}_{NO_2}$. What is unclear, however, is to what extent this behavior is influenced by T_{wall} and to what extent it is influenced by $\dot{m}_{NO_2}$. By comparing the $\overline{U}$ and U' profiles for two similar high $\dot{m}_{NO_2}$ values at two different T_{wall} values and two similar low $\dot{m}_{NO_2}$ values at two different T_{wall} values, the influence of T_{wall} on altering the velocity profiles can be determined. Figure 6.11 provides this comparison. The profiles presented in this figure were each obtained at different times during Run 12, resulting in significantly different (i.e. > 50 K) measured T_{wall} values during each acquisition period.

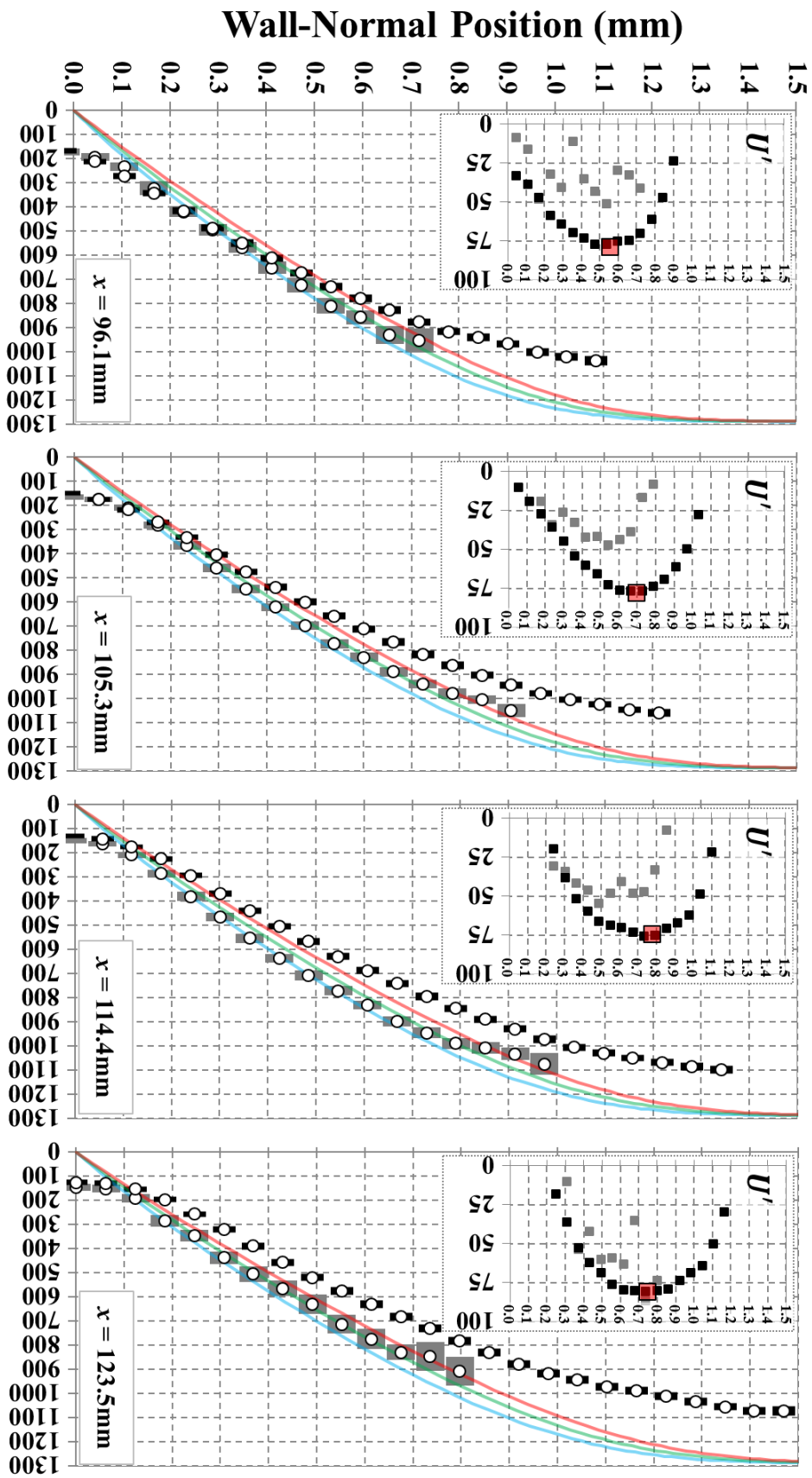

Figure 6.10: Profiles of $\overline{U} \pm u_{IJ}$ for blowing rates of $\dot{m}_{NO_2}$ = 15.3 mg/s (gray data points) and $\dot{m}_{NO_2}$ = 161.3 mg/s (black data points). Solid blue, green, and red profiles correspond to analytic boundary layer solutions for T_{wall} of 310 K, 365 K, and 420 K, respectively. Inset plots represent estimates of U'. Image adapted from Ref. 12.

Two important trends are observed in Fig. 6.11. First, for the 'low' blowing rate, $\dot{m}_{NO_2}$, the $\overline{U}$ profiles obtained with different T_{wall} values fall nearly on top of one another over most of the boundary layer. The profile obtained at higher T_{wall} shows a slightly lower velocity, as expected. Above y = 0.60 mm, the low $\dot{m}_{NO_2}$ = 21.3 mg/s (0.684 SLPM) profile (T_{wall} = 376.6 K) exhibits a slight velocity deficit relative to the $\dot{m}_{NO_2}$ = 22.7 mg/s (0.723 SLPM) blowing rate profile (T_{wall} = 320.8 K). For the high $\dot{m}_{NO_2}$, both $\overline{U}$ profiles fall nearly on top of one another over the extent of the measurement region; the effect of increasing wall temperature appears to be negligible in this case. Second, considering the U' profiles, the two high $\dot{m}_{NO_2}$ profiles exhibit the same general shape and distribution. At the low $\dot{m}_{NO_2}$, the shapes and distributions of U' are also similar to each other. However, the shape of the profile at the lower of the two wall temperatures ($\dot{m}_{NO_2}$ = 22.7 mg/s; T_{wall} = 320.8 K) is more sporadic. In this comparison, it should again be noted that there is some error in the accuracy of the vertical placement of the data with respect to the model surface.

Two conclusions can be made based upon observation of these two trends. First, the influence of the wall temperature on the mean streamwise velocity profiles for this experiment seems to be smaller than that predicted by the analytic solutions. This could potentially be a consequence of the quartz window insert (an insulator being at a different temperature than the rest of the plate) or perhaps localized cooling of the wall resulting from blowing of NO_2. Second, the higher blowing rate has a noticeable effect on the mean streamwise velocity distribution and the intensity of the streamwise velocity fluctuations. This influence of increasing this parameter is significant relative to the minor influence of moderately increasing wall temperature over the course of a wind tunnel run.

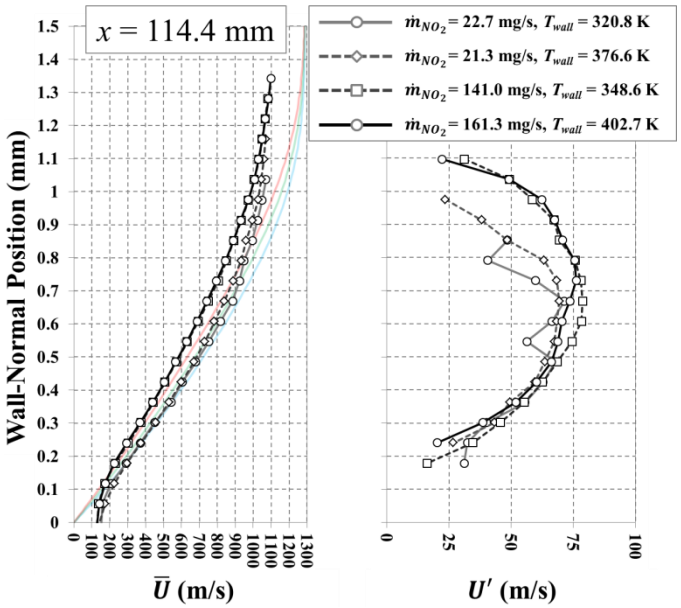

Figure 6.11: Profiles of $\overline{U}$ (left) and U' (right) for both low $\dot{m}_{NO_2}$ (22.7 mg/s and 21.3 mg/s) and high $\dot{m}_{NO_2}$ (141.0 mg/s and 161.3 mg/s), but with different respective measured T_{wall} values for the low $\dot{m}_{NO_2}$ (320.8 K and 376.6 K) and high $\dot{m}_{NO_2}$ (348.6 K and 402.7 K). Image adapted from Ref. 12.

Assuming that the wall temperature has a negligible influence on U over the range considered in this experiment, a functional relationship between $\bar{U}$, U', and $\dot{m}_{NO_2}$ can be developed. Figure 6.12 provides a comparison of measured $\bar{U}$ profiles (left plot) and U' profiles (right plot) for several blowing rates at x = 114.4 mm.

The general effect of increasing $\dot{m}_{NO_2}$ on the measured $\bar{U}$ profiles is an increase in the concentration boundary layer thickness with an accompanying decrease in measured streamwise velocity along the extent of the profiles. This behavior is most pronounced for the profiles with blowing rates above $\dot{m}_{NO_2}$ = 62.6 mg/s (2.01 SLPM), and is a potential result of several factors. First, the presence of the relatively cold, low velocity gas jet issuing from the seeding slot can form a complex separation region just ahead of the jet. A separation shock forms because of this separation region, as well as a primary bow shock.[19] These structures, in turn, create local changes to the streamwise momentum and temperature fields. Once the oncoming boundary layer gas has been processed by these structures, it undergoes some level of mixing with the injected gas and additional momentum and heat transfer processes occur. The gas then proceeds downstream and into the measurement region. In all of the $\bar{U}$ profiles, the magnitude of velocity at the edge of the measurement region is approximately 15% less than that predicted by the analytic solutions.

The general shape of the U' profiles remain the same for all blowing rates. However, the thickness of the profiles appear to be roughly proportional to $\dot{m}_{NO_2}$. As $\dot{m}_{NO_2}$is increased, the profiles also become more parabolic in shape and the smoothness of the profiles becomes more pronounced. A noticeable jump in the thickness of the U' profiles seem to occur when $\dot{m}_{NO_2}$ is increased beyond 62.6 mg/s. At the highest blowing rate ($\dot{m}_{NO_2}$ = 161.3 mg/s), the location of the

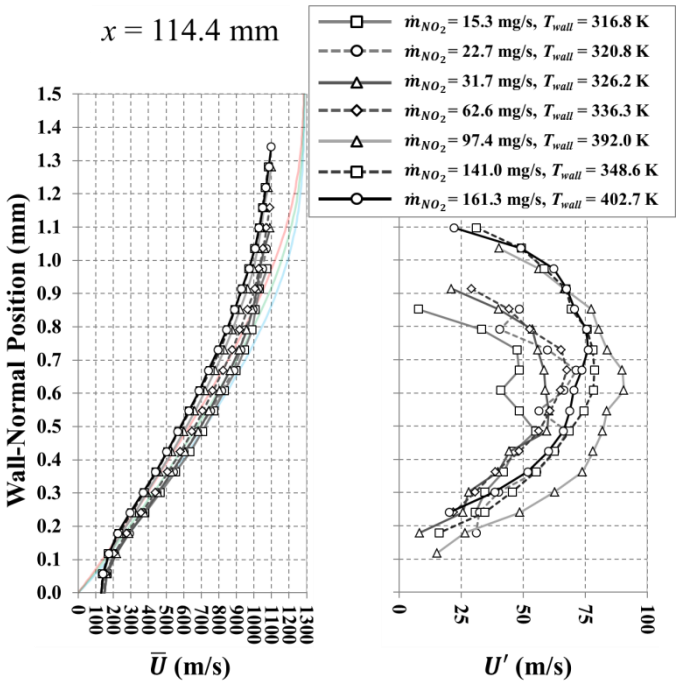

Figure 6.12: Profiles of $\bar{U}$ (left) and U' (right) for several $\dot{m}_{NO_2}$settings. Image adapted from Ref. 12.

peak U' values are at 50% of the velocity boundary layer thickness.

The plots in Fig. 6.12 show that for blowing rates beyond approximately 60 mg/s, and at these specific experimental conditions, both the $\bar{U}$ and U' profiles are noticeably affected by the blowing rate. This observation is important for two reasons. First, the initial motivation for using the NO_2-to-NO photolysis technique was to study hypersonic boundary layer transition-to-turbulence. Figure 6.12 highlights that for $\dot{m}_{NO_2} > 60$, significant changes to the measured velocity boundary layer occur, and these changes may strongly influence the transition-to-turbulence behavior.

Second, as blowing rate is increased, the SNR levels improved across the measurement region. Adequate SNR levels are necessary to make consistent measurements of velocity over the entire measurement region, to ensure relatively low single-shot measurement uncertainty, and allow for a more accurate measure of U'. In the study prior to Ref. 12 (presented in Ref. 13) the relatively low SNR levels limited the overall data yield, both along individual profiles and profiles at streamwise locations away from the peak pump and probe laser intensities. From the perspective of transition-to-turbulence research, it is crucial to be able to provide accurate and precise quantitative information regarding the development of instabilities in both the wall-normal and streamwise directions. This requires sufficient SNR levels across the entire measurement region while at the same time minimizing or removing sources of flow instability. Therefore, a tradeoff between relatively high SNR levels and a low $\dot{m}_{NO_2}$ must occur.

Figure 6.13 plots the average data yield (green points) between y = 0.05 mm and 0.60 mm along the profile at x = 123.5 mm as a function of $\dot{m}_{NO_2}$. The dashed black line represents an exponential-like function, which provides a qualitative fairing of the data. These data were along the profile farthest downstream from the leading edge for which velocity measurements were made in this experiment. From Fig. 6.12, it was determined that blowing rates of $\dot{m}_{NO_2} > 60$ resulted in noticeable

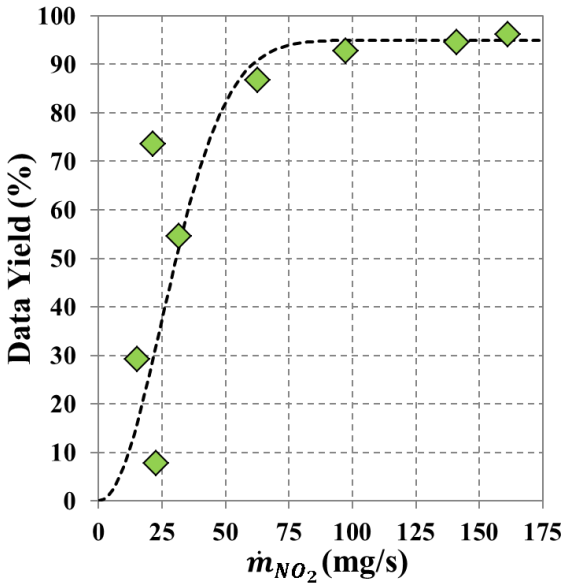

Figure 6.13: Average data yield as a function of $\dot{m}_{NO_2}$. Image adapted from Ref. 12.

changes to both $\overline{U}$ and U' profiles. This corresponds to a data yield of approximately 85% using Fig. 6.13, and using Fig. 6.6, the average SNR that can be expected is approximately 8. From Fig. 6.5, and with a Δt = 2 μs setting, the spatial uncertainty with SNR = 8 is approximately 35 m/s. Figure 6.13 also suggests that blowing rates above 75 mg/s do not appreciably increase the data yield.

Figure 6.14 shows single-shot velocity profiles, U, obtained at the highest blowing rate, $\dot{m}_{NO_2}$ = 161.3 mg/s, with T_{wall} = 402.7 K, and Δt = 1 μs. For reference, $\overline{U}$ profiles (white circle data points with black uncertainty bands) are plotted along with the analytic solution (light red curve) for which T_{wall} = 420 K. The top left-hand plot in Fig. 6.14 combines six instantaneous streamwise velocity profiles (colored data points) with the measured $\overline{U}$ profile and the analytic solution on one graph. The remaining plots show each of the instantaneous U profiles, along with their uncertainty bands corresponding to u_U in Eq. 6.19 (partially determined from the data presented in Fig. 6.5), plotted along with $\overline{U}$.

In Fig. 6.14, both near and far from the wall, the instantaneous U profiles coincide closely with the measured $\overline{U}$ profile. Near the middle portion of the profile, however, noticeable deviations of the U profiles from the $\overline{U}$ profile occur. Observation of the raw instantaneous images shows that on an intermittent basis, relatively sharp bends in the U profiles occur, resulting in significant localized deviations from $\overline{U}$. These images also show that the thickness of the concentration boundary layer oscillates in the *y*-direction. The occurrence of these deviations and oscillations appears to be random when sampled at the 10 Hz pump/probe laser rate.

In Fig. 6.12, the U' profile corresponding to $\dot{m}_{NO_2}$ = 161.3 mg/s at x = 114.4 mm shows, on average, how the instantaneous U profiles behave. Based on observation of the limited number of instantaneous U profiles in Fig. 6.14, it may be that a pattern, consisting of several distinct locations at which velocity peaks occur relative to the mean profile, may exist. One source of such peaks, as described in Chapter 5 and partially shown in Fig. 5.2, may be the presence of a generalized inflection point or an inviscid inflection point (i.e., a point at which $\partial^2 U/\partial y^2 = 0$). For the former, the edge Mach number, M_e, is lower here than that in Chapter 5, and this may promote instability growth. For the latter, the increased blowing rate, $\dot{m}_{NO_2}$, may result in a strong inviscid inflection point. Further analysis, both experimental and computational, may be able to determine if specific *y*-location peaks in U' occur.

One feature of significance in Fig. 6.14 is the magnitude of the instantaneous single-shot uncertainties, u_U. For data between y = 0.05 mm and 0.60 mm along the profile located at x = 114.4 mm (image pair 1051), the average u_U for the profiles shown was 68 m/s. This represents a reduction in u_U by more than a factor of 2.5 compared to the u_U values previously obtained in Ref. 13. Furthermore, some instantaneous measurements showed single-shot uncertainties as low as 44 m/s. Table 6.2 lists the average magnitude of the constituent terms in u_U in the region between y = 0.05 mm and 0.60 mm as a percentage of the edge

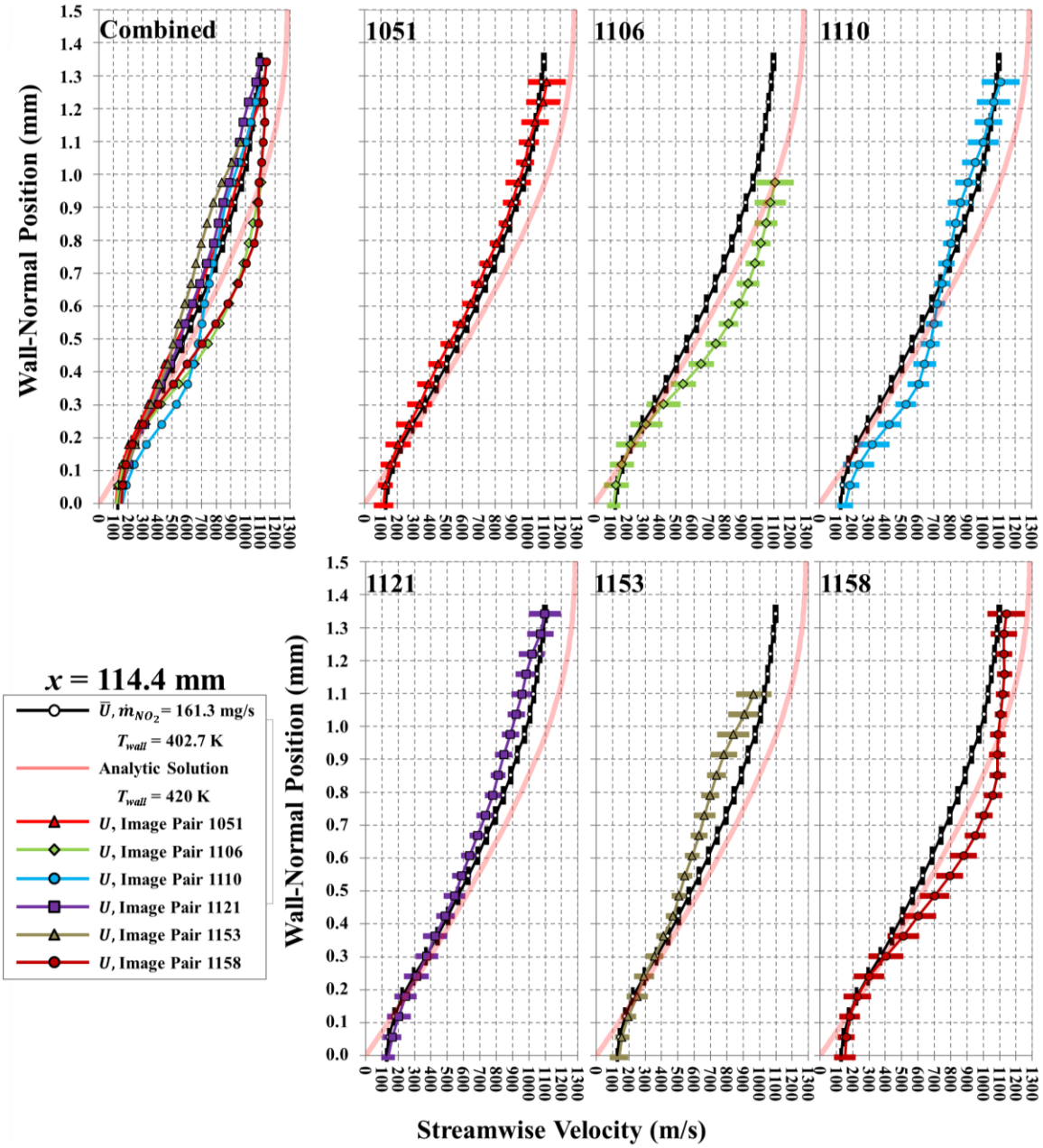

Figure 6.14: Profiles of $\bar{U}$ (black, open circles) and U (colored, filled symbols) obtained at x = 114.4 mm for $\dot{m}_{NO_2}$ = 161.3 mg/s, T_{wall} = 402.7 K, and Δt = 1 µs. Image adapted from Ref. 12.

Table 6.2: Average constituent and total single-shot uncertainties between y = 0.05 mm and y = 0.60 mm at x = 114.4 mm for image pair 1051 as a percentage of edge velocity, U_e.

Uncertainty Term	% of U_e (U_e = 1289 m/s)
$u_{U,Accuracy}$	0.95
$u_{U,\bar{M}}$	0.11
$u_{U,\Delta x}$	4.84
$u_{U,\Delta t}$	0.04
$u_U = \sqrt{u_{U,\Delta x}^2 + u_{U,\Delta t}^2 + u_{U,\bar{M}}^2 + u_{U,Accuracy}^2}$	4.91

velocity, U_e, for the image pair 1051. For this particular image pair, $u_U < 0.05 \cdot U_e$. Further reductions in u_U for this profile could be obtained by increasing the SNR levels and/or increasing Δt. If SNR were increased beyond 14, the resulting u_U values would be reduced by nearly a factor of 2. Increasing the probe laser delay to Δt = 2 μs would result in a further factor of 2 reduction in u_U.

6.4 Discussion

One aspect of the current work that was held constant for each of the experimental analyses was the location of the seeding slot on the model from which the NO_2 was blown into the boundary layer. The location of the slot likely affected the thickness of the concentration boundary layer relative to the velocity boundary layer for all of the experiments. To achieve a concentration layer with a thickness more closely matching that of the velocity boundary layer thickness, experiments could be performed in which the seeding slot location is moved further upstream. Since doing this could potentially affect the stability of the boundary layer itself, an analysis of stability as a function of slot location would need to be performed.

Future velocity measurement experiments should utilize a Δt of 2 μs rather than 1 μs. While this reduces the streamwise spatial resolution of the measurement by a factor of 2, the single-shot uncertainty, u_U, is also reduced by a factor of 2. The reduction of the streamwise spatial resolution is relatively unimportant in the current study because the gradients in the streamwise direction are relatively small (at least well downstream of the roughness element). Efforts should also be made to improve the experimental SNR levels and data yield while using as small a $\dot{m}_{NO_2}$ value as possible to further increase measurement precision. One possible solution is to improve the image processing and data rejection algorithms so that data points with a lower SNR are retained. This is done in the analysis Section 7.1.2 in Chapter 7.

In the experiment, probing the ground state of NO gives relatively strong fluorescence signal across a wide range of temperatures and had been used successfully in previous experiments. Due to the relatively

short test schedule and the number of objectives that had to be met during the test, the excitation of ground state NO was chosen in an effort to maximize the probability of success and minimize the risk associated with unproven alternatives. However, this approach resulted in excitation of ground state NO existing between the profiles, which was prevalent during quiescent gas testing. This may have adversely affected the measured SNR levels, and hence adversely affected the spatial uncertainty reported in Fig. 6.5. To avoid this, an attractive alternative is exciting the first vibrational state of NO, as presented in Ref. 10. This state is relatively well populated for a period after photolysis of NO_2 occurs but not populated at room temperature.

The measured velocity profiles presented in this chapter did not tend toward zero velocity at the wall. By improving the imaging system magnification, the spatial resolution of the experiment was improved so that measurements as close as 0.08 mm to the model surface were made, which is a factor of 4 improvement from the measurements presented in Chapter 5. This allowed for a better-resolved velocity profile, especially near the model surface. Further improvements to the imaging system magnification, such as using extension rings, would allow for measurements even closer to the model surface. This would in turn also make the measurement less susceptible to potential errors caused by pixel blooming.

In this chapter, a primary goal was to analyze how the streamwise velocity profiles behaved as a function of $\dot{m}_{NO_2}$. While performing this analysis, transient behavior at the edge of the concentration layer in the *y*-direction was observed. One hypothesis for this behavior is that these fluctuations in thickness lead to an error that biases measurements near the edge of the boundary layer toward lower values of velocity. While a time-resolved CFD analysis could potentially simulate and account for these errors, any future experimental work should include an analysis of the instantaneous images so that a parameter describing the unsteadiness of the concentration layer thickness may be obtained. This could be done by tracking the upper edge of the zero-delay instantaneous profiles on a frame-by-frame basis.

Future experiments should also include measurements characterizing the flow behavior in the region immediately surrounding the seeding slot. This should be done for a range of blowing rates to determine the kinds of flow structures present, as well as to provide quantitative descriptions of the magnitudes and fluctuating components of both dynamic and thermodynamic properties in this region. Such measurements could then be compared and possibly correlated with flow properties measured downstream of the seeding

region (such as the streamwise velocity behavior measured in this chapter). In this experiment, it was also assumed that the flow did not accelerate or decelerate between the first and second exposures, allowing for the calculation of streamwise velocity using Eq. 6.1. However, as described in Section 4.4.2 of Chapter 4, if the flow is accelerating or decelerating (e.g., because of large a $\dot{m}_{NO_2}$), then the use of Eq. 6.1 is no longer valid. Therefore, CFD computations could be performed to identify to what extent $\dot{m}_{NO_2}$ alters the flowfield to better identify regions of strong velocity gradients (acceleration or deceleration) that may serve as sources of measurement error or instability.

Based on observation of the instantaneous U profiles presented in Fig. 6.14, an analysis could be performed to determine if a predictable pattern exists in the *y*-locations of maximum U' relative to $\overline{U}$. Such a pattern could potentially be related to any oscillatory or instability behavior of the concentration or velocity layer thicknesses. These patterns may indicate which specific instability modes in the boundary layer at these experimental conditions are relevant to the transition-to-turbulence process, absent the presence of an isolated discrete roughness element.

While initial CFD analyses of this experiment should assume a sharp-leading-edge metallic flat plate at a constant T_{wall}, a more detailed analysis could be performed. For instance, a simulation that captures the structure of the model more precisely, such as the mixed material making up the model's top surface, could be performed. In this experiment, the leading edge is solid steel, the top plate is a 1/5-inch thick steel plate, and the quartz window insert is ½-inch thick. These differences in material and thickness may have some influence on the boundary layer behavior. The time history of the model during the run could also be simulated to determine the temperature of the model surface, T_{wall}. In future experiments, temperature sensitive paint could be used to determine the surface temperature of the metal model (and possibly the quartz window) during the run.

Chapter 7 will demonstrate the application of the three-laser NO_2-to-NO photolysis MTV technique described in this chapter to experiments with an isolated cylindrical roughness element which induces transition-to-turbulence.

6.5 Conclusions

A set of experiments using three-laser NO_2-to-NO photolysis MTV have been performed to assess the applicability of the technique to hypersonic boundary layer transition-to-turbulence measurements. Analysis and image processing methodologies have been developed to compute mean and single-shot velocities and associated uncertainties using the experimental MTV images. A methodology was also developed to compute the fluctuating component of streamwise velocity. An analysis was performed to determine how seeding NO_2 from a spanwise slot at various blowing rates from a single streamwise location affects the behavior of the streamwise velocity and the fluctuating component of the streamwise velocity. For the conditions tested in this experiment, a blowing rate threshold has been proposed, above which significant flow perturbations were observed. An effort was made to characterize the single-shot precision and data yield of the measurement technique at varying probe beam delay settings. Data yield and streamwise velocity profile behavior were examined for a range of blowing rates. This work represents the first acquisition of mean and single-shot streamwise velocity profiles in a large-scale hypersonic test facility and in a hypersonic boundary layer using the three-laser NO_2-to-NO photolysis MTV technique. The next chapter uses the methodologies and analysis techniques developed in this chapter to make measurements of velocity in hypersonic boundary layers undergoing roughness-induced transition-to-turbulence.

---

[1] Bathel, B.F., Danehy, P.M., Inman, J.A., Jones, S.B., Ivey, C.B., and Goyne, C.P., "*Multiple Velocity Profile Measurements in Hypersonic Flows Using Sequentially-Imaged Fluorescence Tagging*," AIAA Paper 2010-1404, 48th AIAA Aerospace Sciences Meeting, Orlando, FL, January 4-7, 2010.

[2] Bathel, B.F., Danehy, P.M., Inman, J.A., Jones, S.B., Ivey, C.B., and Goyne, C.P., "*Velocity Profile Measurements in Hypersonic Flows Using Sequentially-Imaged Fluorescence-Based Molecular Tagging Velocimetry*," AIAA Journal, 49(9), September, 2011

[3] Bathel, B.F., Danehy, P.M., Inman, J.A., Watkins, A.N., Jones, S.B., Lipford, W.E., Goodman, K.Z., Ivey, C.B., and Goyne, C.P., "*Hypersonic Laminar Boundary Layer Velocimetry with Discrete Roughness on a Flat Plate*," AIAA Paper 2010-4998, 40th Fluid Dynamics Conference and Exhibit, Chicago, IL, June 28 - July 1, 2010.

[4] Johansen, C.T., Danehy, P.M., Ashcraft, S.W., Bathel, B.F., Inman, J.A., and Jones, S.B., "*PLIF study of Mars Science Laboratory capsule reaction control system jets*," 41st AIAA Fluid Dynamics Conference, AIAA Paper 2011-3890, Honolulu, HI, June 27 – 30, 2011.

[5] Johansen, C.T., Novak, L., Bathel, B.F., Ashcraft, S.W., and Danehy, P.M., "*Comparison of MSL RCS jet computations with flow visualization and velocimetry*," 50th AIAA Aerospace Sciences Meeting, AIAA Paper 2012-594, Nashville, TV, January 9 – 12, 2012.

[6] Inman, J.A., Bathel, B.F., Johansen, C.T., Danehy, P.M., Jones, S.B., Gragg, J.G., and Splinter, S.C., "*Nitric Oxide PLIF Measurements in the Hypersonic Materials Environmental Test System (HYMETS)*," 49th AIAA Aerospace Sciences Meeting, AIAA Paper 2011-1090, Orlando, FL, January 4 – 7, 2011.

[7] Orlemann, C., Schulz, C., and Wolfrum, J., "*NO-flow tagging by photodissociation of NO2. A new approach for measuring small-scale flow structures*," Chem. Phys. Lett., 307, pp. 15-20, 1999.

[8] Shinji, N., Kasahara, M., Tsue, M., and Kono, M., "*Velocity Measurements of Reactive and Non-reactive Flows by NO-LIF Method Using NO_2 Photodissociation*," Heat Transfer – Asian Research, 34 (1), pp. 40-52, 2005.

[9] Hsu, A.G., Srinivasan, R., Bowersox, R.D.W., and North, S.W., "*Two-component molecular tagging velocimetry utilizing NO fluorescence lifetime and NO2 photodissociation techniques in an underexpanded jet flowfield*," Applied Optics, 48 (22), pp. 4414-4423, August, 2009.

[10] Hsu, A.G., Srinivasan, R., Bowersox, R.D.W, and North, S.W., "*Molecular Tagging Using Vibrationally Excited Nitric Oxide in an Underexpanded Jet Flowfield*," AIAA Journal, 47 (11), pp. 2597-2604, November, 2009.

[11] Jiang, N., Nishihara, M., and Lempert, W.R., "*500 kHz NO_2 Molecular Tagging Velocimetry in a Mach 5 Wind Tunnel*," AIAA 2010-4348, 27th AIAA Aerodynamic Measurement Technology and Ground Testing Conference, Chicago, IL, June 28 – July 1, 2010.

[12] Bathel, B.F., Danehy, P.M., Johansen, C.T., Jones, S.B., and Goyne, C.P., "*Hypersonic Boundary Layer Measurements with Variable Blowing Rates Using Molecular Tagging Velocimetry*," 28th AIAA Aerodynamic Measurement Technology, Ground Testing, and Flight Testing Conference, AIAA Paper 2012-2886, New Orleans, LA, June 25 – 28, 2012.

[13] Bathel, B.F., Johansen, C.T., Danehy, P.M., Inman, J.A., Jones, S.B., and Goyne, C.P., "*Hypersonic Boundary Layer Transition Measurements Using $NO_2 \rightarrow NO$ Photo-dissociation Tagging Velocimetry*," 41st AIAA Fluid Dynamics Conference, AIAA Paper 2011-3246, Honolulu, HI, June 27 – 30, 2011.

[14] Sanchez Sorzano, C.O., Thevenaz, P., and Unser, M., "*Elastic Registration of Biological Images Using Vector-Spline Regularization*," IEEE Transactions on Biomedical Engineering, 52 (4), pp. 652-663, April, 2005.

[15] Rasband, W.S., ImageJ, U.S. National Institutes of Health, Bethesda, MD, USA, http://rsb.info.nih.gov/ij, 1997-2009.

[16] Johansen, C.T. and Danehy, P.M., "*Numerical investigation of PLIF gas seeding for hypersonic boundary layer flows*," AIAA 2012-1057, 50th AIAA Aerospace Sciences Meeting, January 9-12, 2012, Nashville, TN.

[17] Kreyszig, E., *Advanced Engineering Mathematics*, 8th ed., pp. 1085 – 1099, John Wiley & Sons, New York, 1999.

[18] Inman, J.A., Bathel, B.F., Johansen, C.T., Danehy, P.M., Jones, S.B., Gragg, J.G., and Splinter, S.C., "*Nitric Oxide Planar Laser-Induced Fluorescence Measurements in the Hypersonic Materials Environmental Test System*," to appear in AIAA Journal.

[19] Berry, S.A., Nowak, R.J., and Horvath, T.J., "*Boundary Layer Control for Hypersonic Airbreathing Vehicles*," 34th AIAA Fluid Dynamics Conference, AIAA Paper 2004-2246, Portland, OR, June 28 – July 1, 2004.

Chapter 7: Application of Three-Laser, Sequentially Imaged NO_2-to-NO Molecular Tagging Velocimetry

The main purpose of this chapter is to provide experimental hypersonic velocity boundary layer data in the wake of an isolated cylindrical roughness element by measuring the streamwise velocity component using a laser-induced fluorescence-based molecular tagging velocimetry (MTV) technique. In this chapter, the three-laser NO_2-to-NO photolysis MTV technique has been used to successfully measure streamwise velocity in a hypersonic boundary layer undergoing transition-to-turbulence in NASA Langley's 31-Inch Mach 10 Air Tunnel. The higher pressure conditions tested in this experiment prevented the application of the single-laser NO MTV technique, which was used to make streamwise velocity measurements in a laminar hypersonic boundary, as described in Chapter 5.

In this experiment, the roughness height relative to boundary layer thickness, k/δ_L, and the roughness Reynolds number, Re_k, were varied, with a constant edge Mach number of M_e = 4.2, to determine their effect on the mean streamwise velocity, $\bar{U}$, and the fluctuating component of streamwise velocity, U'. A comparison with flow visualization images obtained at similar flow conditions to those reported by Danehy et al.[1] is also made. The discussion and results in this chapter have been adapted from Ref. 2.

7.1 Image Analysis

7.1.1 Initial Image Processing

Table 7.1 lists the magnification and magnification uncertainty values used in this experiment.

Three modifications were made to the image processing method described in Chapter 6. The first modification concerned the small physical downward displacement of the model that was observed over the course of a run. Presumably, the displacement is a result of non-uniform thermal loading on the sting, which causes it to bend downward. Using the image processing software *ImageJ* from the National Institutes of Health[3] and the function *Reslice*, the residual laser scatter off a portion of the stainless steel model surface is imaged for each frame in a given data set (as in Fig. 6.1a in Chapter 6). These images are

Table 7.1: Magnification values on centerline (z = 0.0 mm).

Parameter	Value
Mean Magnification, $\bar{M}$	6.07×10^{-2} mm/pixel
Uncertainty in the Mean Magnification, $u_{\bar{M}}$	2.5×10^{-4} mm/pixel

used to generate a single image showing the location of the scatter, and hence location of the model surface, as a function of frame number. As in Chapter 6, a 2nd-order polynomial fit to the location of the laser scatter is then used to characterize the model displacement over the course of a run. Unlike Chapter 6, however, the raw images are then vertically shifted using a bi-cubic image transform function in MATLAB®. By using this function, the plate surface appears stationary in all of the images. In Chapter 6, this correction was accomplished by shifting the images in whole-pixel increments. By using a bi-cubic image transform, spatial errors resulting from shifting the images in whole-pixel increments are avoided. Figure 7.1 shows the current and previous scatter fitting methods used to correct for model displacement.

The second change involves how the signal-to-noise ratio (*SNR*) is calculated. In Chapter 6, the signal in the first ($i = E1$) and second ($i = E2$) camera exposures was computed by taking the difference between the maximum (*peak*, P_i) and minimum (*valley*, V_i) signals within a 21-pixel-wide × 1-pixel-high window centered about P_i of the tagged gas line. The noise, N_i, was then estimated by computing the standard deviation of the signal counts within a 5×5-pixel-square window centered about the location of P_i. This methodology, however, is susceptible to errors because noise from regions above and below the measurement point was included in the SNR computation. Additionally, the curvature about P_i would also result in an increased standard deviation measurement, and hence, N_i estimate.

Since the computed SNR is used to estimate both the single-shot spatial uncertainty, $u_{U,\Delta x}$, and U', any errors associated with the SNR estimate propagate to other calculations. To avoid this error, the SNR in this chapter is computed by fitting a Gaussian-like function, $G_i(x)$, to

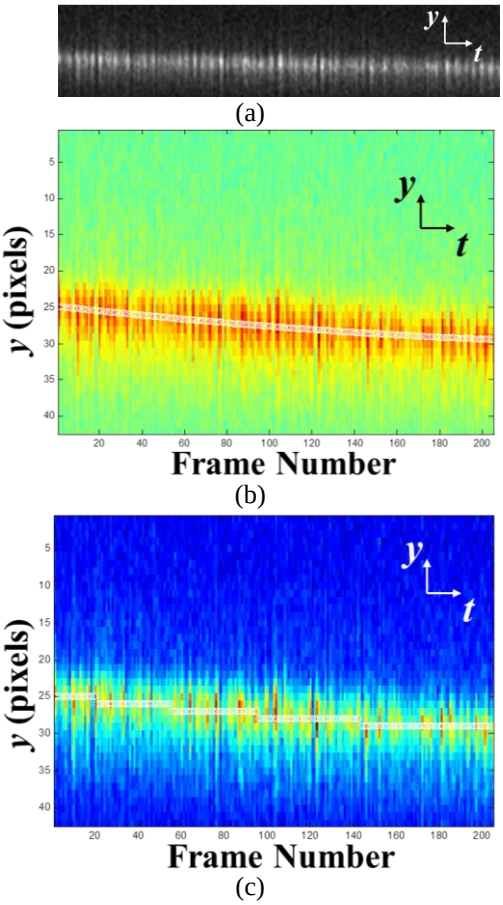

Figure 7.1: Method to correct for model displacement using smooth 2nd-order polynomial fit of laser scatter in (a) to shift images according to the fit shown in (b). Previous method shifted images in whole-pixel increments similar to (c) and Fig. 6.1c in Chapter 6.

the intensity profiles over a 39-pixel-wide × 1-pixel-high window. This window has the same width, W_i, as the window used to correlate intensity profiles captured in the first and second exposures. The window is again centered about the P_i's along each tagged profile. The Gaussian-like function is obtained by using the MATLAB® functions *fminsearch* and *fminbnd* to perform an iterative least-squares fit to the experimental profiles and has the form:

$$G_i(x) = (P_i - V_i) \cdot \exp\left[-\left(x - x_{P_i}\right)^2 / \left(\sqrt{8\ln 2} \cdot FWHM_i\right)^2\right] + B_i \tag{7.1}$$

Here, x_{P_i}, is the center of the experimental intensity distribution, $FWHM_i$ is the full-width at half-maximum of the experimental intensity distribution, and B_i is the number of background counts. The noise, N_i, is computed as twice the standard deviation of the difference between $G_i(x)$ and the experimental signal intensity profile, $S_i(x)$. Prior to computing the noise, any linear trend in this difference is removed using the MATLAB® function *detrend*. The SNR_i for each exposure is computed as:

$$SNR_i = \frac{P_i - V_i}{N_i} = \frac{\max(G_i) - \min(G_i)}{2 \cdot \sigma_{(G_i - S_i)|_{\text{detrend}}}} \tag{7.2}$$

This approach is similar to that outlined in Ref. 4. The composite SNR is then computed using the relation in Eq. 6.21 of Chapter 6.

The third and final change to the image processing procedure involves the data rejection method. In this chapter, a three-step process for accepting or rejecting a data point is used. In the first step, the three parameters returned from the Gaussian-like fit in each image pair to the experimental data are required to be within a specified range of values. The first of these parameters, $(P_i - V_i)$, is assumed to have an acceptable range (in counts) of $1 \leq (P_i - V_i) \leq 2500$. This range is selected so that signal saturation and phosphor artifact effects from the camera (e.g. *ghosting*) are avoided. The acceptable range assumed for the full-width at half-maximum parameter of the fit (in pixels) is $2 \leq FWHM_i \leq W_i/2$, where W_i is the width of the correlation window. This range is chosen to prevent poor fits to the data which have widths that are either much narrower (less than or equal to 2 pixels) or much wider (greater than or equal to half the correlation window size) than what is typically observed in the experimental MTV profiles. The final parameter is x_{P_i} with respect to the center of the correlation window, in pixels. This parameter was assumed to have an acceptable range of $1 \leq x_{P_i} \leq W_i$. This range is chosen to exclude fits to the experimental profiles that are centered outside of the correlation window.

The second rejection step involves the computed composite SNR and the individual SNR_i in the first and second exposures. Analysis of both mean and single-shot velocity data indicate that a lower threshold of SNR > 3.5 and SNR_i > 3.5 are still adequate to ensure that data points obtained from erroneous cross-correlation results are rejected without unnecessarily discarding useable data with low SNR. These first two steps in the rejection process result in a higher data yield at lower SNR levels.

The third and final step in this process rejects data points based on the uncertainty in the mean velocity, $u_{\bar{U}}$. For most runs, measurements with $u_{\bar{U}} >$ ±125 m/s are removed. For measurements from Run 12, any point for which $u_{\bar{U}} >$ ±60 m/s is removed, since there was no roughness present and the seeding was relatively uniform.

7.1.2 Velocity Analysis

Figure 7.2a shows experimental $S_i(x)$ profiles captured in the first (*E1*, blue diamond points) and second (*E2*, red diamond points) exposures that were obtained in nominally quiescent conditions. The corresponding $G_i(x)$ fits to these data (solid blue and red lines) are also shown, as is the difference, $G_i(x) - S_i(x)$ after applying the MATLAB® function *detrend* (circle points). Figure 7.2b shows $S_{E2}(x)$ profile data with an increasing linear trend in intensity (denoted by the dashed line) and the $G_{E2}(x)$ fit to that data. The open circle data points correspond to $(G_{E2} - S_{E2})$ without applying the *detrend*

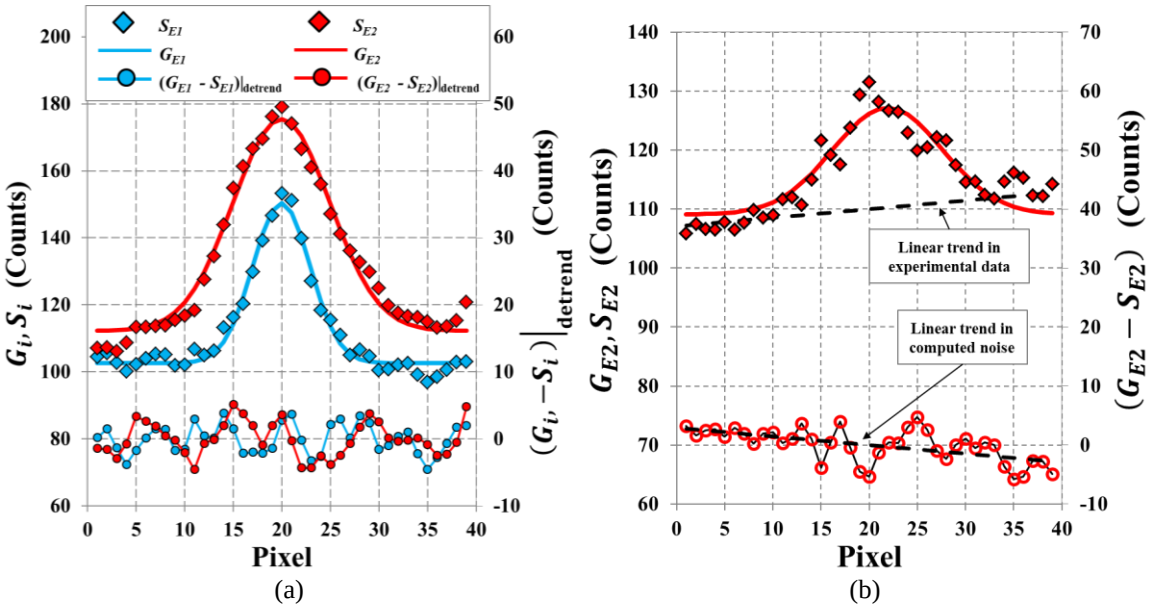

Figure 7.2: (a) Sample experimental intensity profiles, S_i, corresponding to fits, G_i, and the difference, $(G_i - S_i)$ after applying linear detrend function. (b) Profiles of S_{E2}, fit G_{E2}, and difference $(G_{E2} - S_{E2})$ without applying detrend function. Image (a) adapted from Ref. 2.

function. In this example, the noise estimate N_{E2} is approximately 18.5% higher relative to the N_{E2} estimate obtained after applying the *detrend* function.

Figure 7.3 shows the spatial uncertainty, $u_{U,\Delta x}$, as described in Chapter 6 for camera gain settings of 20% (Run 12) and 40% (all other runs) using the new definition of SNR. At the highest SNR levels for the 20% gain setting, a reduction in $u_{U,\Delta x}$ of approximately 5 m/s is observed relative to Fig. 6.5 in Chapter 6 (using the same data), owing to the modified SNR calculation method. The fits to these spatial uncertainty data are given by the solid lines in Fig. 7.3 and have equations of a form similar to Eq. 6.23:

$$u_{U,\Delta x} = \frac{A+Bexp[-(C\cdot\{SNR-D\})^2]}{\Delta t} \tag{7.3}$$

The parameters ***A***, ***B***, ***C***, and ***D*** depend on the probe laser delay, Δt, of Eq. 6.16 and camera gain setting. Table 7.2 provides the values for these parameters.

In Fig. 7.3, $u_{U,\Delta x}$ is reduced significantly as SNR improves. Furthermore, it is reduced by roughly a factor of two when Δt is doubled, though the spatial resolution is decreased by using a longer Δt setting. The lower gain setting also results in a lower $u_{U,\Delta x}$, though higher gain settings are required to study the flows with an isolated roughness element because of the low SNR levels resulting from the lower $\dot{m}_{NO_2}$ used (see Table 3.4 in Chapter 3). The increase in gain is estimated to have increased SNR by as much as a factor of $[\max(SNR)|_{\text{Gain=40\%}}]/[\max(SNR)|_{\text{Gain=20\%}}] = 2.5$ in the quiescent flow images. This assumes constant

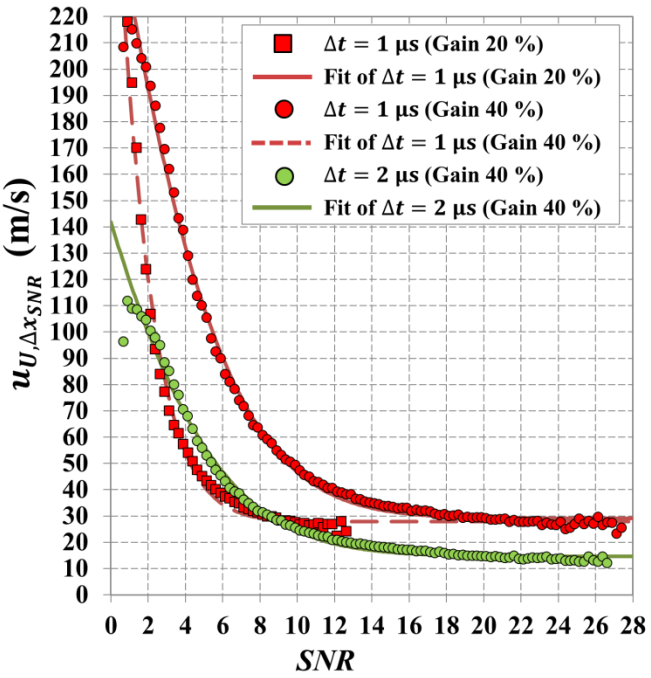

Figure 7.3: Spatial velocity uncertainty, $u_{U,\Delta x}$, and corresponding fit (using Eq. 7.3), as a function of signal-to-noise ratio, SNR. Image adapted from Ref. 2.

Table 7.2: Coefficients for spatial uncertainty relation.

Δt (μs)	Gain	***A*** (μm)	***B*** (μm)	***C***	***D***
1	20%	27.87	14.70×10^{3}	13.14×10^{-2}	-15.13
1	40%	29.09	677.49	8.98×10^{-2}	-11.28
2	40%	29.32	830.65	8.54×10^{-2}	-12.73

laser irradiance and NO_2 concentration. The primary disadvantage of increasing gain is that it makes the images susceptible to increased shot noise (note that this noise is taken into account in the SNR analysis).

7.2 Results

7.2.1 Overview of Streamwise Velocity Measurements

Reference 2 contains a 45-page appendix with mean, fluctuating, and single-shot streamwise velocity measurements. The remainder of this chapter is intended to summarize some of the measurement results originally presented in that paper.

7.2.2 Comparison of Streamwise Velocity Measurements with Flow Visualization

Figures 7.4a and 7.4b show both $\overline{U}$ and U' profiles, respectively, obtained along the centerline (z = 0.0 mm) of the model with no roughness element for $\dot{m}_{NO_2}$ = 31.7 mg/s at Re_∞= 3.3×10^6 m^{-1} (see Run 12 of Test 481 in Table 3.4 of Chapter 3). Data from this same run were presented in Chapter 6 and Ref. 5 and is discussed here briefly in order to compare it with the profiles obtained in the wake of a cylindrical roughness element. The $\overline{U}$ profiles closely match the computed laminar profiles for y less than approximately 0.6 mm. Above this position, the measured profiles still trend with (i.e. have a similar shape to) the computed laminar solution, but a velocity deficit is observed. At its greatest, this deficit is on the order of 125 m/s, and is typically on the order of 100 m/s along the upper extent of the profiles. It is not clear if the velocity deficit was caused by instrument error, by error in estimating the edge conditions, or by the low-velocity gas seeded into the boundary layer altering the boundary layer profile downstream. Computations performed in Ref. 6 for this model at a 5° plate angle and with NO seeding at 3 mg/s showed that deficits on the order of 50 m/s were possible near the edge of the velocity boundary layer, due to the addition of the low-velocity gas. These computations suggest that the method of seeding the boundary layer may have some effect on the measured boundary velocity profiles presented in this chapter. Additional computations are needed to simulate the current 20° plate angle, Reynolds numbers, and blowing rates examined in this chapter to verify that seeding is responsible for the observed distortion of the velocity boundary layer relative to theory.

In Fig. 7.4b, the U' profiles at Re_∞ = 3.3×10^6 m^{-1} exhibit peaks at approximately y = 0.6 mm across all profiles. This is approximately the same location at which the corresponding $\overline{U}$ profiles begin to diverge

from the computed laminar profiles. This behavior was also noted in Chapter 6 and in Ref. 5. The maximum magnitude of U' across all profiles is approximately 75 m/s or about 6% of the edge velocity.

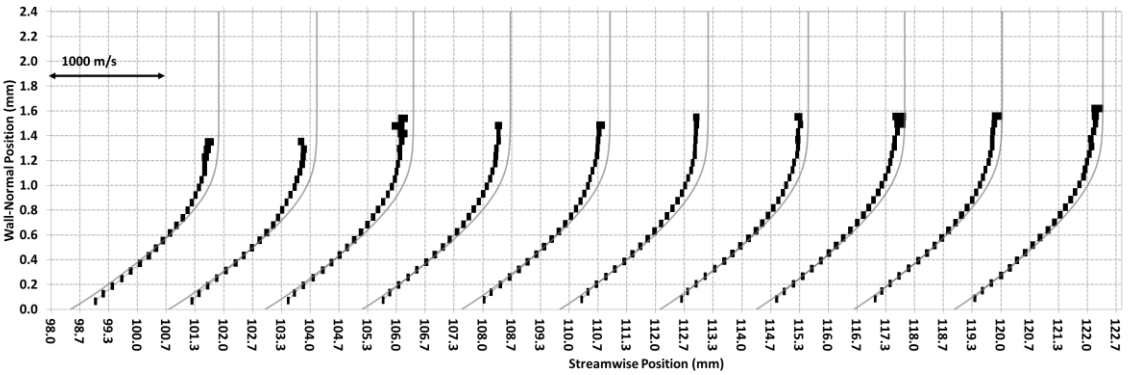

(a)

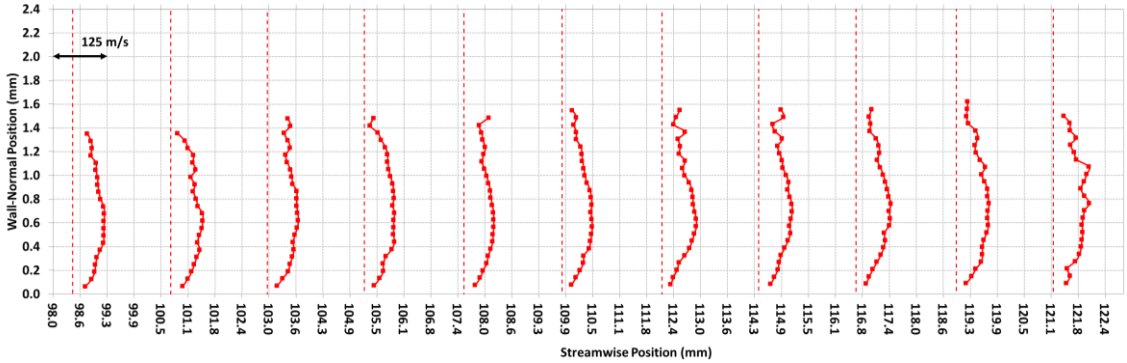

(b)

Figure 7.4: Side-view (a) mean streamwise velocity ($\bar{U}$) profiles and (b) streamwise fluctuating velocity component (U') profiles at z = 0.0 mm (centerline) with no cylindrical roughness element, $\dot{m}_{NO_2}$ = 31.7 mg/s, Re_∞= 3.3×10^6 m^{-1}.

Figures 7.5a – 7.5e show five single-shot flow visualization images (Ref. 1, Fig. 10) for the k = 1.00 mm cylinder using a single-laser NO PLIF flow visualization technique. These images were acquired at flow conditions nominally the same as Run 14 in Test 481 (see Table 3.4 of Chapter 3). The blowing rate of pure NO gas (rather than NO_2, as in this experiment) in Figs. 7.5a – 7.5e was $\dot{m}_{NO}$ = 6.09 mg/s. The laser sheet in these images was oriented parallel to the model surface and was directed from top to bottom in the images. The camera used to acquire these images was oriented perpendicular to the laser sheet and model surface in a plan-view orientation such that it imaged the entire plate surface and accompanying laser-induced fluorescence. In Figs. 7.5a – 7.5e, the position of the laser sheet was varied from y = 0.0 mm to 2.0 mm above the model surface in 0.5 mm increments, respectively. The superimposed transparent blue circle shows the approximate location of the quartz window insert used in this experiment (but not used in the flow visualization experiment). Streamwise velocity measurements

described in this chapter and Chapter 6 were obtained above this window. Also shown in Fig. 7.5a are the approximate spanwise locations of some of the side-view velocity measurement planes in this experiment (dashed white lines). The off-centerline spanwise measurement locations (z = -4.5 mm, -6.0 mm, and -7.5 mm) were chosen because they encompassed a region containing large streamwise streaks observed in the flow visualization images of Ref. 1, including those shown here in Fig. 7.5. An oil flow image, obtained at the same flow condition as the flow visualization images on the model surface, is shown in Figure 7.5f (also taken from Ref. 1). It shows streamline behavior at the model surface and the distortion of the streamlines influenced by the roughness element.

The $\overline{U}$ profiles in Fig. 7.6 (also from Run 14 of Test 481) were acquired at the same nominal flow conditions as the flow-visualization images shown in Fig. 7.5. The spanwise measurement locations in Figs. 7.6a through 7.6d correspond to z = 0.0 mm (centerline), -4.5 mm, -6.0 mm and -7.5 mm, respectively. Along the centerline, an increased $\overline{U}$ velocity relative to the computed laminar solution is observed below approximately y = 0.7 mm, the approximate location at which the measured $\overline{U}$ profiles cross the computed laminar solutions. The increase in profile fullness (i.e. higher velocities) near the wall, relative to the computed laminar profile, resembles that of turbulent boundary layer profiles. This behavior is discussed in detail in section 7.3. Above y = 0.7 mm, the profiles exhibit a velocity deficit relative to the computed laminar profile but begin to trend with this computed profile in the $+y$ direction. This deficit could be caused by the cylindrical roughness element, the seeded low-velocity NO_2 gas that has been injected into the boundary layer, or a combination of these factors.

The off-centerline measurements in Fig. 7.6b through 7.6d are aligned with a large streak running along the model surface that was seen in the flow visualization images taken at these same conditions (Fig. 7.5a). This streak is thought to be indicative of a streamwise vortex emanating from a horseshoe vortex formed in front of the roughness element.[1] In Fig. 7.5c, with the laser sheet at y = 1.0 mm, a secondary streak also appeared at approximately z = -4.5 mm. Approximately halfway between the leading and trailing edges of the window insert, this streak exhibited waviness and started to break down farther downstream. Comparing this plan-view image with the $\overline{U}$ measurements at z = -4.5 mm in Fig. 7.6b, it appears that the profiles exhibit an increased velocity relative to the laminar profiles below approximately y = 0.8 mm. Between approximately y = 0.9 mm and 1.7 mm, a velocity deficit relative to the computed

laminar profiles occurs, possibly influenced by the wake of the roughness element. Above y = 1.7 mm, no mean velocity data were obtained. The flow visualization images in Fig. 7.5 seem to also show that little to no NO gas is present above y = 1.5 mm at z = -4.5 mm.

Moving farther from the centerline, the $\overline{U}$ measurements at z = -6.0 mm (Fig. 7.6c) and -7.5 mm (Fig. 7.6d) appear to trend more with the computed laminar profiles, although each profile has a noticeable velocity deficit compared to the computed laminar profiles. Comparing with the flow visualization results in Figs. 7.5a – 7.5c, the flow at these two locations does appear more laminar than either at the centerline or z = -4.5 mm.

Figures 7.7a – 7.7d show the U' profiles for these same flow conditions at z = 0.0 mm, -4.5 mm, -6.0 mm, and -7.5 mm, respectively. Note that the scale has changed from Fig. 7.6 and that the maximum U' magnitudes along the centerline approach 250 m/s for some profiles (compared to ~80 m/s in the case with no roughness element, as in Fig. 7.4) – about a factor of 3 increase in U'. This corresponds to approximately 20% of the edge velocity, U_e, and is of the same order-of-magnitude as the values listed in Table 2.2 of Chapter 2 for transition downstream of a roughness element and for fully-developed hypersonic turbulent boundary layer flow.

Near the left-hand side of Fig. 7.7a, the centerline U' profiles show a broad, flat peak ranging from approximately y = 0.2 mm to 0.8 mm; that is, fluctuations are greatest in this region above the model surface. Proceeding downstream, the upper y extent of this broad U' feature appears to slowly decrease, with the profiles at the right-hand side of the figure exhibiting a relatively narrower peak centered about y = 0.3 mm. In other words, the region of strong fluctuations is more localized at these locations.

The upstream profiles at z = -4.5 mm in Fig. 7.7b also exhibit a broad, flat peak, ranging from approximately y = 0.2 mm to 0.6 mm. At x = 95.9 mm, the U' profile drops to half of its maximum at approximately y = 0.9 mm (near the height of the cylinder). However, these profiles begin to exhibit a peak U' at y = 0.25 mm, which is approximately 17% of the nominal boundary layer thickness, δ_L, beginning with the profile located at x = 107.3 mm. The maximum U' magnitudes at this spanwise location are approximately 200 m/s – 250 m/s.

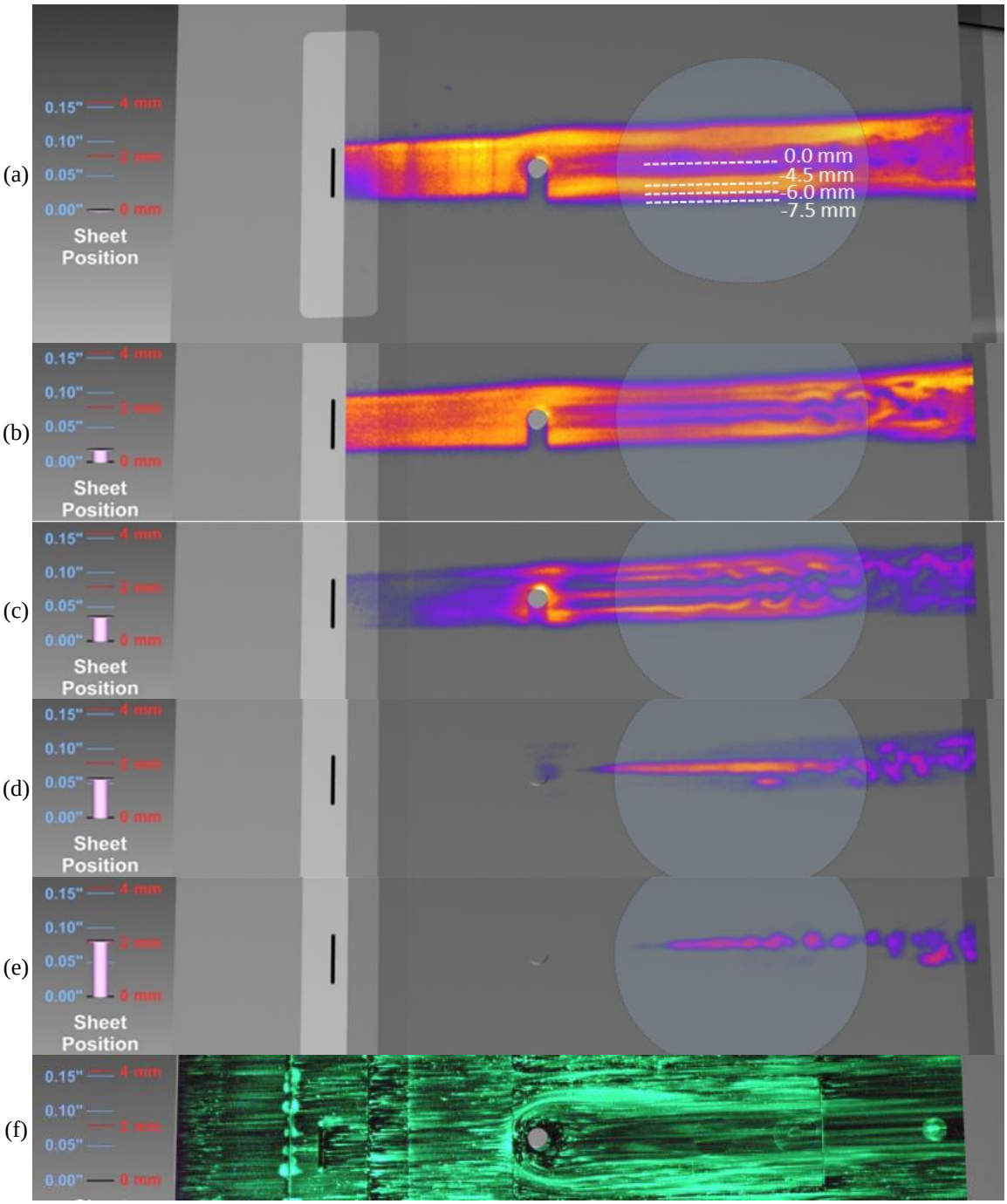

Figure 7.5: Plan-view flow visualization images for a 1-mm-tall × 4-mm-wide cylindrical roughness element, $\dot{m}_{NO}$ = 6.09 mg/s, Re_∞ = $3.3\times10^6 m^{-1}$. Laser sheet *y*-position varies from (a) 0.0 to (e) 2.0 mm above the model surface in 0.5 mm increments. Approximate locations of spanwise MTV measurement planes are shown with white dashed lines in (a). Approximate location of window insert used in MTV runs is shown in (a) through (e). Plan-view oil flow image in (f) for the same run conditions. Images adapted from Ref. 2 and originally taken from Ref. 1.

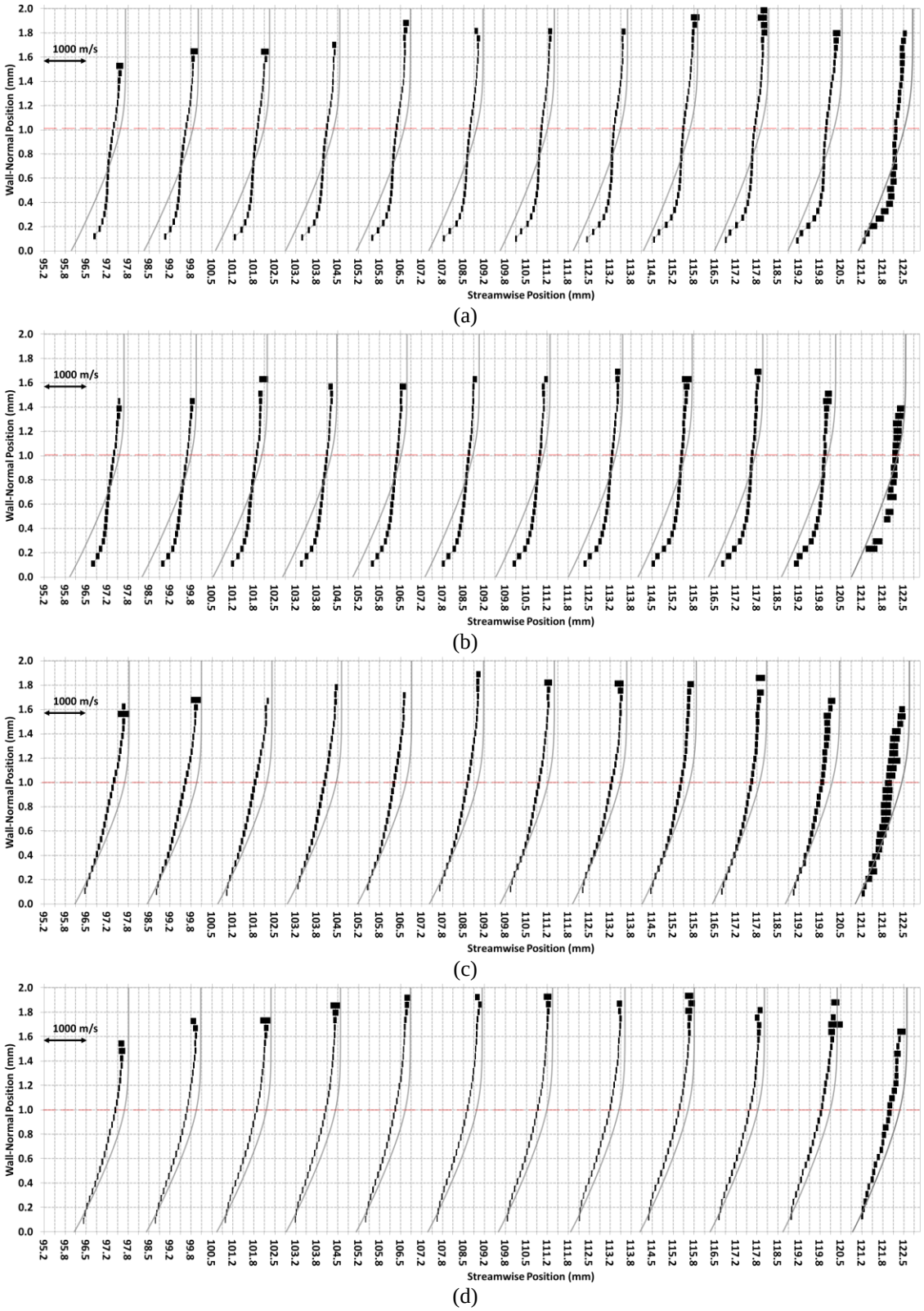

Figure 7.6: Side-view $\overline{U}$ profiles for a 1-mm-tall × 4-mm-wide cylinder (Table 3.4, Run 14, Test 481) at z = (a) 0.0 mm, (b) -4.5 mm, (c) z = -6.0 mm, and (d) z = -7.5 mm. Light gray lines are computed laminar profiles. Dashed horizontal red lines represent roughness height, k (centered at x = 75.4 mm). Images adapted from Ref. 2.

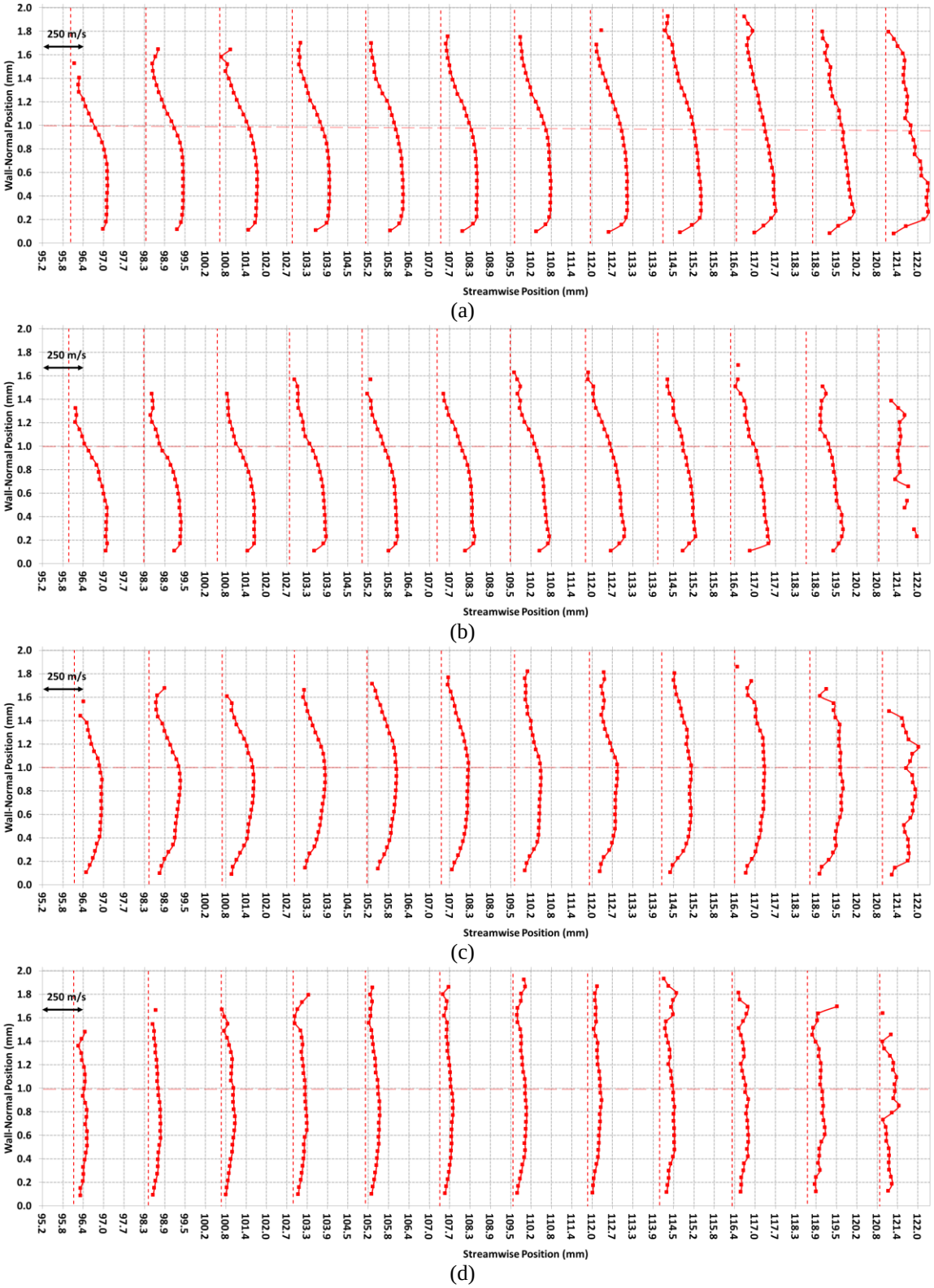

Figure 7.7: Side-view U' profiles for a 1-mm-tall × 4-mm-wide cylinder (Table 3.4, Run 14, Test 481) at z = (a) 0.0 mm, (b) -4.5 mm, (c) z = -6.0 mm, and (d) z = -7.5 mm. Dashed horizontal red lines represent roughness height, k (centered at x = 75.4 mm). Images adapted from Ref. 2.

The profiles measured along z = -6.0 mm in Fig. 7.7c again exhibit a broad, flat U' behavior near the left-hand edge of the measurement region. However, the range of this feature is now between y = 0.4 mm and 1.0 mm. Proceeding downstream, it appears that this U' behavior continues to broaden and never develops a distinguishable peak, with the profiles having maximum magnitudes of less than 200 m/s. At z = -7.5 mm, the magnitudes and shapes of the U' profiles are very similar to those measured for the case with no roughness element shown in Fig. 7.4b, with maximums being located at approximately y = 0.7 mm

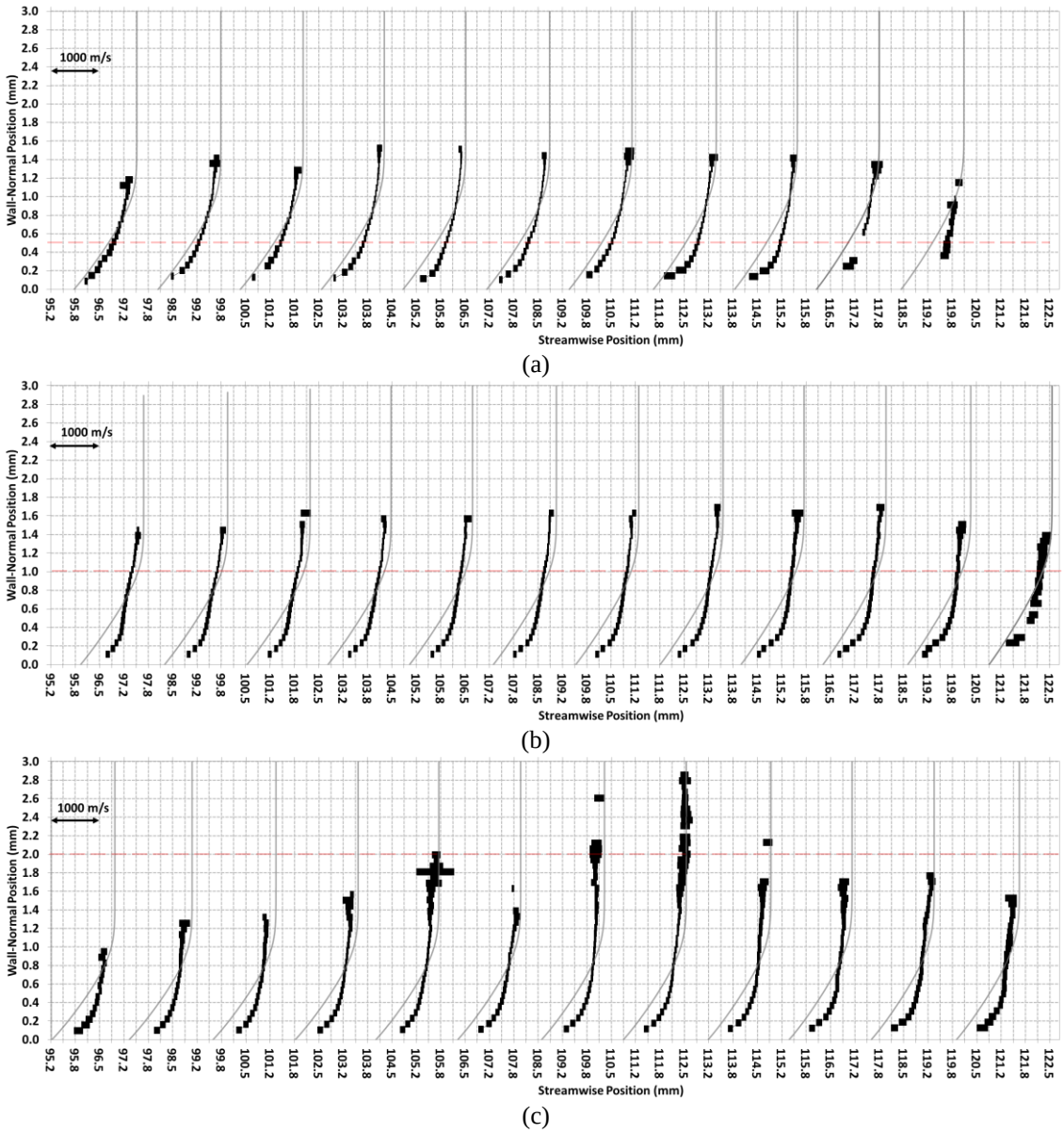

Figure 7.8: Side-view $\overline{U}$ profiles at z = -4.5 mm: (a) k = 0.53 mm cylinder (Test 481, Run 16), (b) k = 1.0 mm cylinder (Test 481, Run 14), and (c) k = 2.0 mm cylinder (Test 481, Run 13). Light gray lines are computed laminar profiles. Dashed horizontal red lines represent roughness height, k (centered at x = 75.4 mm). Images taken from Ref. 2.

and magnitudes less than 100 m/s, confirming that the flow is laminar in this region, as suggested by the flow visualization.

Figures 7.8a – 7.8c show $\overline{U}$ profiles at z = -4.5 mm for roughness heights of k = 0.53 mm, 1.0 mm (also shown in Fig. 7.6b), and 2.0 mm, respectively. This is the same spanwise location at which the secondary streak, shown in Fig. 7.5c, that emanated from the horseshoe vortex in front of the cylinder was observed for k = 1.0 mm. These images correspond to Runs 16, 14, and 13 of Test 481 (see Table 3.4 in Chapter 3).

For k = 0.53 mm (Fig. 7.8a), the $\overline{U}$ profiles, from left to right, initially follow the computed laminar profiles more closely than do the profiles for k = 1.0 mm and 2.0 mm. Proceeding downstream, the profiles develop an increased velocity relative to the computed laminar profile below y = 0.8 mm, as do the k = 1.0 mm and k = 2.0 mm cases. As previously noted, this behavior resembles that of a turbulent boundary layer near the wall. The $\overline{U}$ measurements in this case never extend beyond approximately y = 1.5 mm in the +y direction.

For the k = 2.0 mm case in Fig. 7.8c, the $\overline{U}$ profiles exhibit similar behavior to the $\overline{U}$ profiles measured in the k = 0.53 mm and k = 1.0 mm cases below approximately y = 1.6 mm. The profiles located at x = 104.0 mm, 108.6 mm, and 110.8 mm have several velocity measurements that extend above y = 1.6 mm. Analysis of the standard deviation of the raw delayed single-shot images show that these profiles, in some instances, extended higher above the model surface than surrounding profiles. The raw single-shot images show that this behavior appears to occur more frequently for profiles at spanwise locations of z = -5.5 mm, -6.5 mm, and -7.5 mm. Of particular interest are the measured $\overline{U}$ values near the upper portion of the profiles. Near the upper extent of these profiles, the measured $\overline{U}$ values are approximately equal to the estimated edge velocity, U_e. While the measurements seem to show that $\overline{U} = U_e$ near the upper edge of the boundary layers in this chapter may be a result of flow distortion caused by the roughness element, this result appears to confirm that the M_e values listed in Table 3.4 in Chapter 3, and therefore U_e estimates used to compute theoretical laminar boundary layer profiles, are reasonable.

For comparison, Fig. 7.9 provides plan-view time-resolved flow visualization images (from Ref. 1) for the k = 2 mm case, all taken with the laser sheet at y = 1.1 mm. The images in this figure were acquired with a MHz-rate PLIF imaging system at 1 MHz. Figure 7.9a also shows the approximate location of the quartz window insert and MTV measurement region used in this chapter (denoted by the rectangle). When

compared with the k = 1.0 mm flow visualization image at approximately the same y location (y = 1.0 mm, Fig. 7.5c), two different features are observed. First, it appears that the gas seeded into the boundary layer is deflected by a greater distance in the z-direction for the k = 2.0 mm case than in the k = 1.0 mm case. This is a result of the 2.0 mm cylinder creating a larger flow blockage relative to the 1.0 mm cylinder. Second, three distinct streamwise streaks are observed about the measurement region for the k = 2.0 mm case. In the k = 1.0 mm case, only two streaks were observed about the measurement region at this y location.

Figures 7.10a – 7.10c show the three U' profile measurements corresponding to the $\overline{U}$ measurements (in Fig. 7.8) made at z = -4.5 mm for roughness heights of k = 0.53 mm, k = 1.0 mm (also shown in Fig. 7.7b), and k = 2.0 mm, respectively. In Fig. 7.10a, a peak in U' is apparent at approximately y = 0.2 mm to 0.4 mm for most of the profiles. All of the profiles in the k = 0.53 mm case tend towards $U' = 0$ when moving in the $+y$ direction; that is, fluctuations are larger near the wall and decrease moving toward the upper edge of the boundary layer. For k = 1.0 mm in Fig. 7.10b, the U' peak is broader, peaking at about the same location as the k = 0.53 mm case but extending farther out into the boundary layer. It should be noted that the measurements for k = 0.53 mm were acquired with Δt = 2 μs, while the measurements for k =

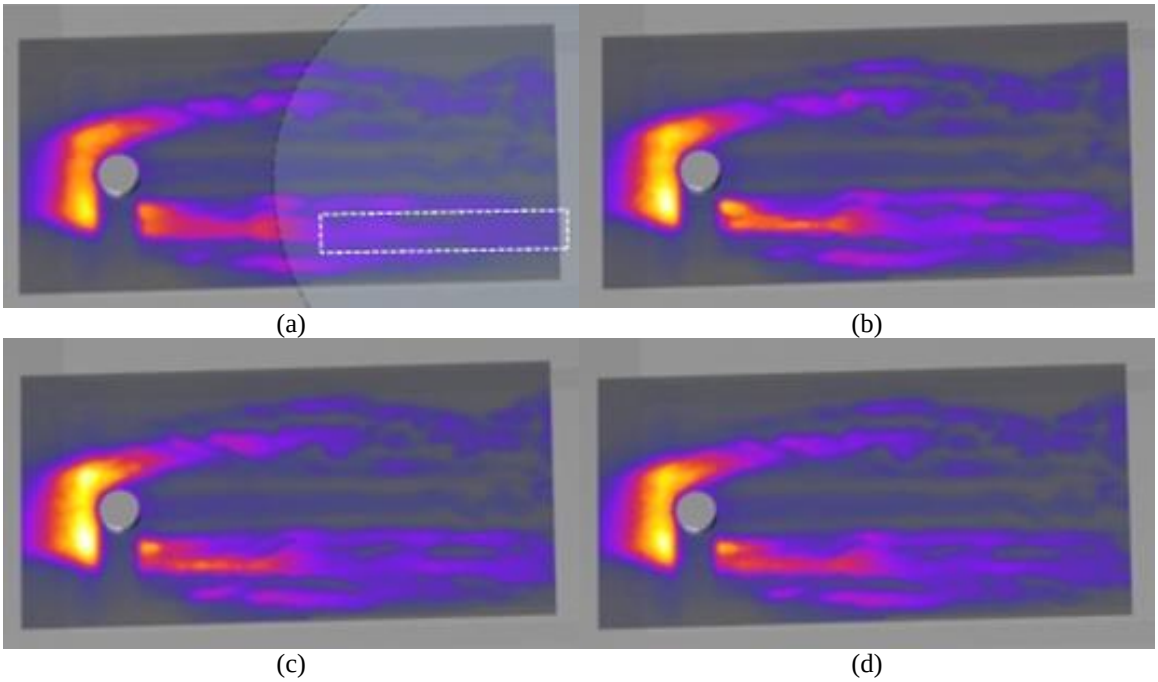

(a) (b)

(c) (d)

Figure 7.9: Plan-view MHz-rate NO PLIF flow visualization sequence for a k = 2 mm cylinder. $\dot{m}_{NO}$ = 6.09 mg/s, Re_∞ = 3.3×10^6 m^{-1}. Laser sheet y = 1.1 mm above model surface. Measurement region for MTV measurement in (a) denoted by white rectangle. Images taken from Ref. 1.

1.0 mm and 2.0 mm were acquired with Δt = 1 μs.

Nearly all of the profiles for the k = 2.0 mm case in Fig. 7.10c have an identifiable U' peak occurring at approximately y = 0.2 mm. For the profile at x = 110.8 mm, the U' profile appears to have a secondary local maximum at approximately y = 2.0 mm, although not as pronounced as that observed near the wall. The raw single-shot images for the k = 2.0 mm case show a greater degree of variability between neighboring profiles in terms of both wall-normal and streamwise distortions. The flow visualization images for k = 2.0 mm in Fig. 7.9 show that, over the extent of the measurement region, the streamwise

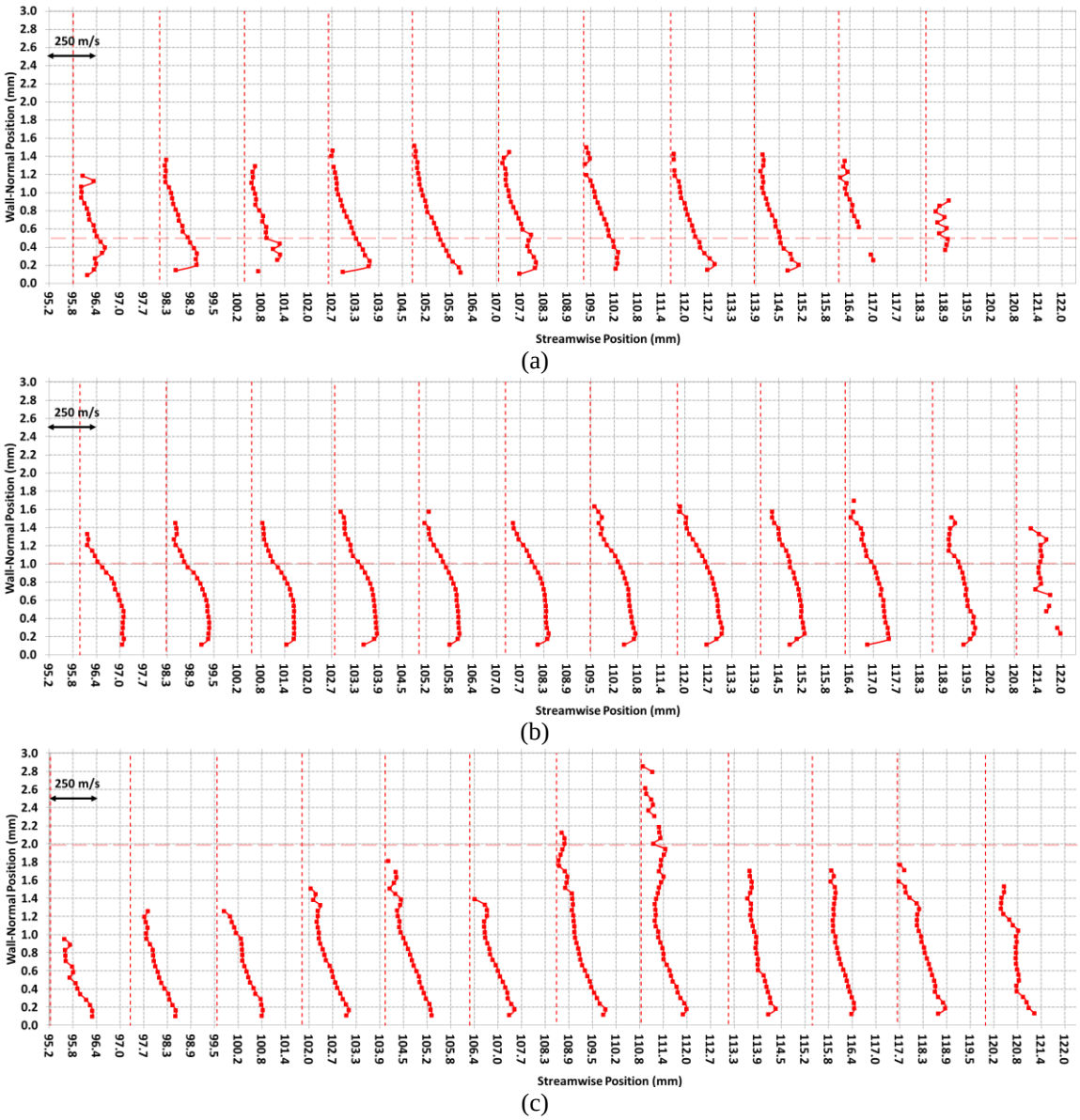

Figure 7.10: Side-view U' profiles at z = -4.5 mm: (a) k = 0.53 mm cylinder (Test 481, Run 16), (b) k = 1.0 mm cylinder (Test 481, Run 14), and (c) k = 2.0 mm cylinder (Test 481, Run 13). Dashed horizontal red lines represent roughness height, k (centered at x = 75.4 mm). Images taken from Ref. 2.

streaks appear to be breaking down.

Figures 7.11a – 7.11d show a comparison between $\overline{U}$ profiles obtained along the centerline (z = 0.0

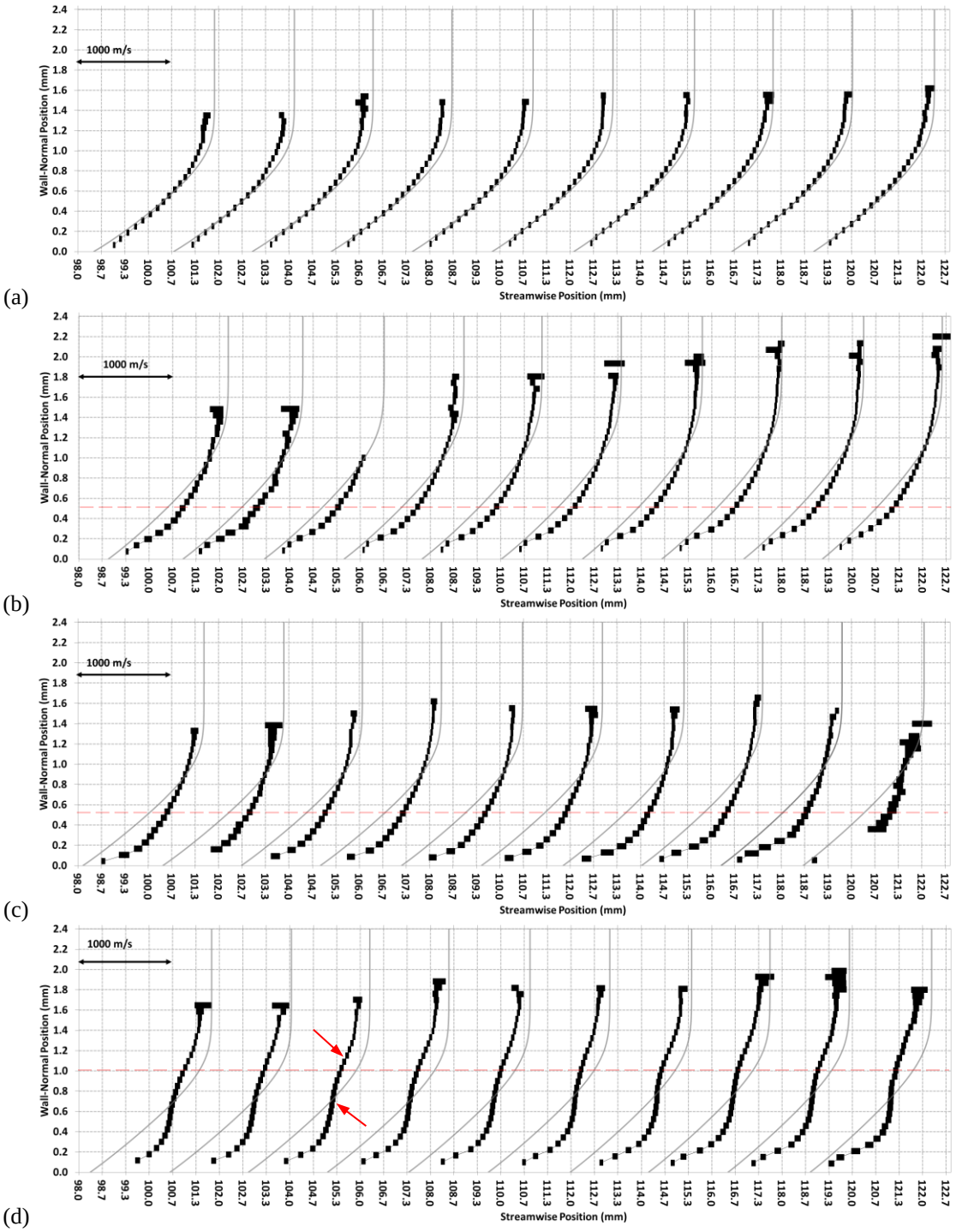

Figure 7.11: Side-view $\overline{U}$ profiles at z = 0.0 mm (centerline): (a) no roughness (Test 481, Run 12); (b) k = 0.53 mm, k/δ_L = 0.41, Re_k = 293 (Test 481, Run 30); (c) k = 0.53 mm, k/δ_L= 0.47, Re_k = 393 (Test 481, Run 16); and (d) k = 1.0 mm, k/δ_L= 0.86, Re_k = 1698 (Test 481, Run 14). Light gray lines are computed laminar profiles. Dashed horizontal red lines represent roughness height, k (centered at x = 75.4 mm). Images taken from Ref. 2.

mm) of the model for no roughness at Re_∞= 3.3×10^6 m^{-1} (also shown in Fig. 7.4a), for the k = 0.53 mm cylinder at Re_∞= 2.4×10^6 m^{-1}, for the k = 0.53 mm cylinder at Re_∞= 3.3×10^6 m^{-1}, and for the k = 1.0 mm cylinder at Re_∞= 3.3×10^6 m^{-1}, respectively. No profiles were obtained along the centerline for the k = 2.0 mm cylinder, since little seeded gas was observed along the centerline wake region for this case, as shown in Fig. 7.9.

For the k = 0.53 mm cylinder cases with differing Reynolds numbers, qualitatively similar $\overline{U}$ behavior is observed. In both cases, an increased velocity relative to the computed laminar profile is observed up to approximately y = 1.0 mm to 1.2 mm. At approximately this height, all of the measured $\overline{U}$ profiles cross the computed laminar profile. However, the maximum velocity relative to the computed laminar profile for the higher Re_∞ = 3.3×10^6 m^{-1} case (Fig. 7.11c) is relatively greater than that observed for the lower Re_∞= 2.4×10^6 m^{-1} case (Fig. 7.11b). Above y = 1.0 mm to 1.2 mm, nearly all of the profiles exhibit a velocity deficit relative to the computed laminar profile.

An interesting feature of the $\overline{U}$ profiles for the k = 1.0 mm cylinder case in Fig. 7.11d is the existence of two inflection points in all of the profiles. As in Chapter 5, these inflection points are characterized by $\partial^2\overline{U}/\partial y^2 = 0$. Two inflection points are also observed along profiles for k = 1.0 mm and 2.0 mm at other locations and conditions (such as in Fig. 7.8c). They are not observed in the k = 0.53 mm cylinder cases, however. The primary inflection point occurs at approximately the same location at which the measured $\overline{U}$ profiles cross the computed laminar profiles. A secondary inflection point occurs between y = 1.0 mm and 2.0 mm, with the location increasing in height with distance downstream. These inflection points are highlighted by red arrows for the profile at x = 102.8 mm in Fig. 7.11d.

Figure 7.12 shows data from this specific profile plotted in a manner similar to that of Fig. 5.4 in Chapter 5. The solid curves in this figure are similar to those in Fig. 5.4, but are generated using a 5-pixel average filter. They show the mean velocity ($\overline{U}$, open circles), smoothed mean velocity ($\overline{U}$, black solid curve), its first derivative ($\partial\overline{U}/\partial y$, dashed black curve), and its second derivative ($\partial^2\overline{U}/\partial y^2$, solid gray curve). Inflection points occur where the second derivative crosses the y-axis. These are denoted by the horizontal dotted red curves in Fig. 7.12. The height of the roughness element is denoted by the horizontal dashed red line. These points of inflection are susceptible to an inviscid instability. Comparing the qualitative trends of these points with those presented in Ref. 7, the highest inflection point is possibly

inviscidly unstable. Unlike Fig. 5.1c, the inflection points along the profiles in Fig. 7.11d persist downstream to the end of the measurement region with no indication that the laminar behavior is being recovered.

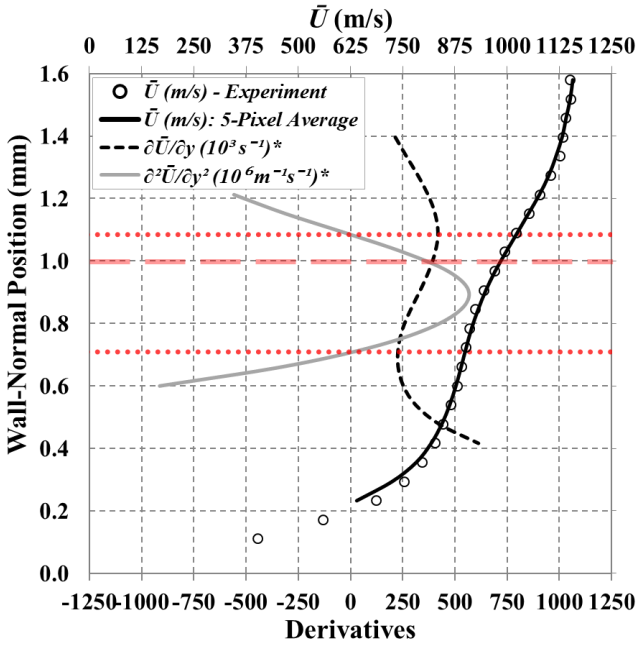

Figure 7.12: Experimental $\bar{U}$ profile data (circles) at x = 102.8 mm from Fig. 7.11d for k = 1 mm. Profiles after applying 5-pixel average filter of $\bar{U}$ (black curve), $\partial\bar{U}/\partial y$ (dashed black curve), and $\partial^2\bar{U}/\partial y^2$ (gray curve). Inflection points and roughness height denoted by horizontal dotted red lines and horizontal dashed red line, respectively.

Figures 7.13a through 7.13d show the centerline (z = 0.0 mm) U' profiles corresponding to the same flow conditions as those presented in Figs. 7.13a – 7.13d, respectively. The U' profiles for the k = 0.53 mm cylinder case at Re_∞ = 2.4×10^6 m^{-1} (Fig. 7.13b) show a peak between y = 0.3 mm to 0.4 mm, both closer to the surface and greater in magnitude than the peak fluctuations of the no-roughness case in Fig. 7.13a. At Re_∞ = 3.3×10^6 m^{-1} for the same roughness height (Fig. 7.13c), the U' profiles exhibit peaks closer to the wall, ranging between y = 0.1 mm to 0.3 mm. The peaks in Fig. 7.13c are less rounded than those at the lower Re_∞ condition of Fig. 7.13b. The magnitudes of the peaks are also, in general, greater than those observed at the lower Re_∞condition. Again, the U' profiles observed for the k = 1.0 mm case (Fig. 7.13d) are broader and extend farther out into the flow than the shorter cylinder cases. The profiles in Fig. 7.13d exhibit peaks between y = 0.2 mm and 0.8 mm, centered initially at approximately y = 0.5 mm on the left-hand-side of the measurement region and moving to approximately y = 0.25 mm on right-hand-side of the measurement region. These peaks are closer to the wall compared to the inflection points computed in Fig. 7.12.

7.3 Discussion

This section investigates a possible cause for the fullness of the $\bar{U}$ profiles in some of the measurements presented in this chapter, as mentioned in Section 7.2. Figure 7.14 shows a $\bar{U}$ profile measured at z = -7.5 mm and x = 113.3 mm for the k = 2.0 mm cylinder case (see Fig. A43a, Ref. 2). The

profile is similar to the profile shown in Fig. 7.8c at x = 110.8 mm, but was chosen because it was a particularly tall profile, with data points acquired nearly 4.8 mm above the model surface. A laminar boundary layer profile computed at the same flow conditions and location is denoted by the solid gray line.

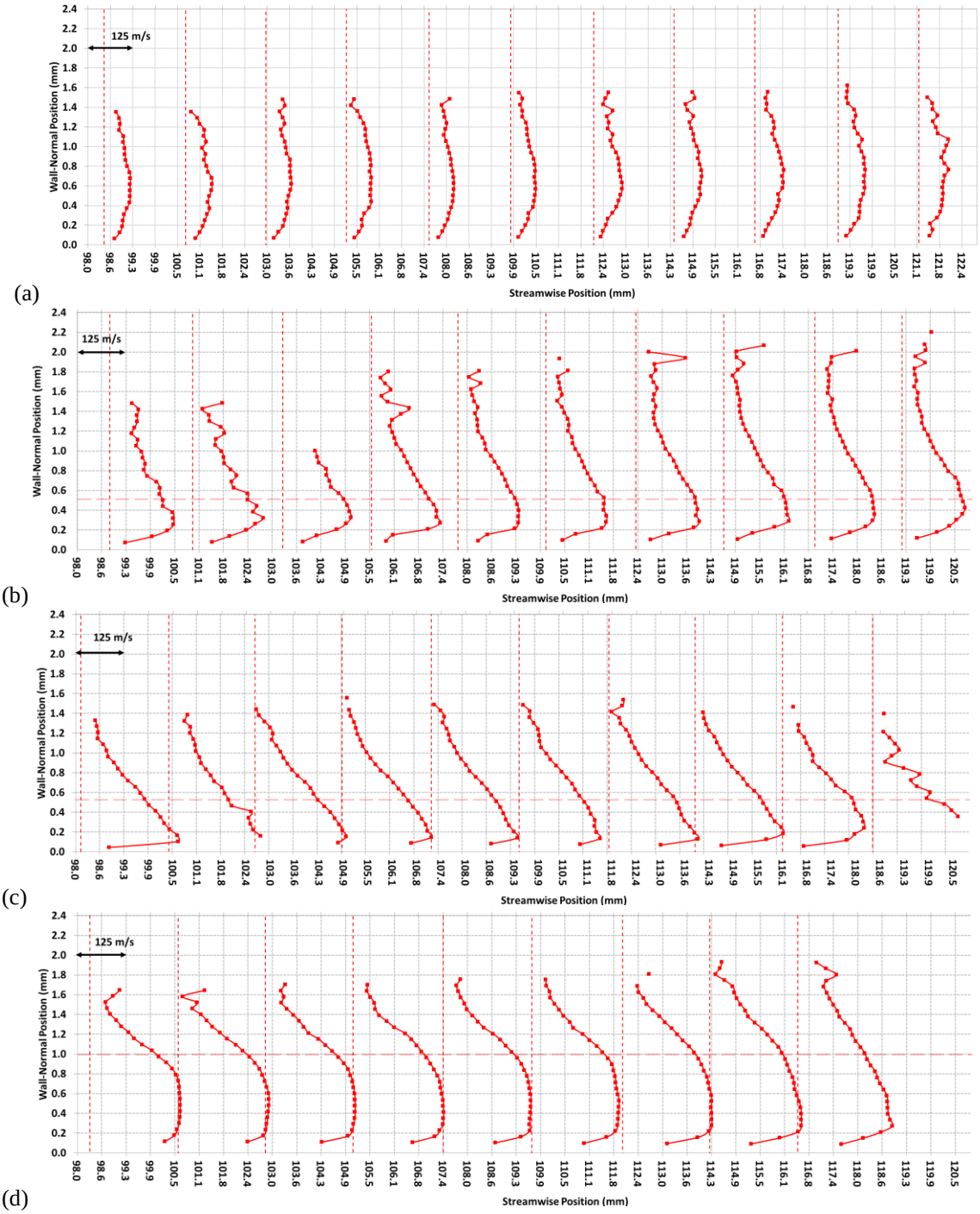

Figure 7.13: Side-view U' profiles at z = 0.0 mm (centerline): (a) no roughness (Test 481, Run 12); (b) k = 0.53 mm, k/δ_L = 0.41, Re_k = 293 (Test 481, Run 30); (c) k = 0.53 mm, k/δ_L= 0.47, Re_k = 393 (Test 481, Run 16); and (d) k = 1.0 mm, k/δ_L= 0.86, Re_k = 1698 (Test 481, Run 14). Dashed horizontal red lines represent roughness height, k (centered at x = 75.4 mm). Images taken from Ref. 2.

For comparison, a turbulent profile was also computed using the Virginia Tech Compressible Turbulent Boundary Layer (CTBL) solver.[8] This profile is denoted by the dashed orange line. The horizontal solid red line denotes the laminar velocity boundary layer thickness (δ_L) at this x location if no cylindrical roughness element were present. For this calculation, the streamwise location at which the turbulent calculation was initiated was set equal to the roughness location, x_T = 75.4 mm, which corresponds to the cylindrical roughness element being *fully effective* (see Section 2.1 in Chapter 2).

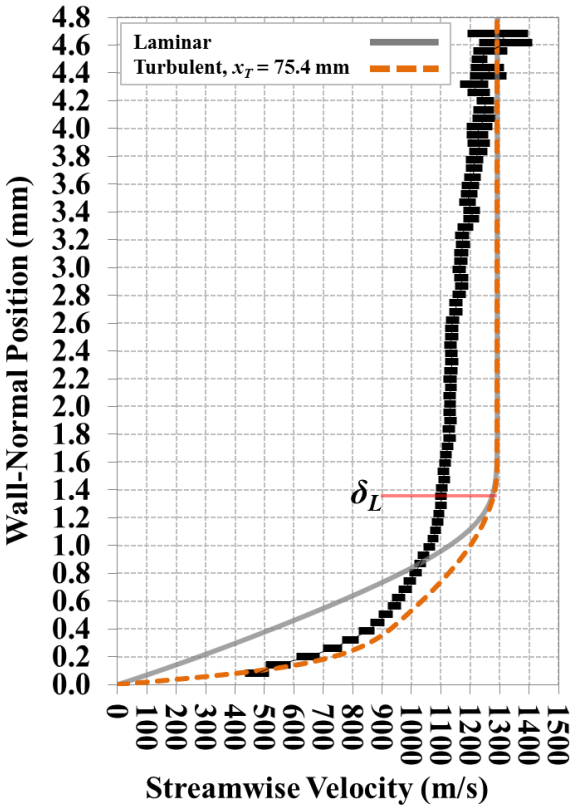

Figure 7.14: Experimental $\bar{U}$ profile for k = 2.0 mm case, x = 113.3 mm, and z = -7.5 mm. Computed laminar profile (gray curve) and computed turbulent profile, computed from the cylindrical roughness location x_T = 75.4 mm (dashed orange curve, Ref. 8). Image from Ref. 2.

While this comparison is meant to be qualitative in nature, a few interesting features associated with the measured $\bar{U}$ profile are observed. Near the wall, the $\bar{U}$ profile closely follows the trend of the turbulent boundary layer profile. At approximately y = 0.2 mm, the magnitude of the slope of $\bar{U}$, that is, ($d\bar{U}/dy$) trends away from that of the computed turbulent profile. At y = 0.9 mm, the measured $\bar{U}$ crosses the computed laminar profile. At approximately $y = \delta_L$, the magnitude of $d\bar{U}/dy$ is approximately zero. This behavior for $y \leq \delta_L$ may be indicative of the transition process. Between approximately $y = \delta_L$ and $y = 2\delta_L$, the measured $\bar{U}$ profile has a nearly constant velocity of 1100 m/s. This deficit relative to the laminar solution is likely a consequence of the wake of the roughness element. Above approximately $y = 2\delta_L$, $\bar{U}$ linearly approaches the edge velocity until approximately y = 4.6 mm where the computed edge velocity is measured experimentally.

The centerline $\bar{U}$ profiles in the wake of a cylindrical roughness element such as in Fig. 7.11b – 7.11d also exhibit augmented velocity near the wall. This is opposed to data acquired at lower Reynolds numbers

but similar k/δ_L values, such as the measurements of $\bar{U}$ in Fig. 5.1c of Chapter 5. In that figure, the profiles downstream of the cylinder appear to recover back to a laminar shape at downstream locations.

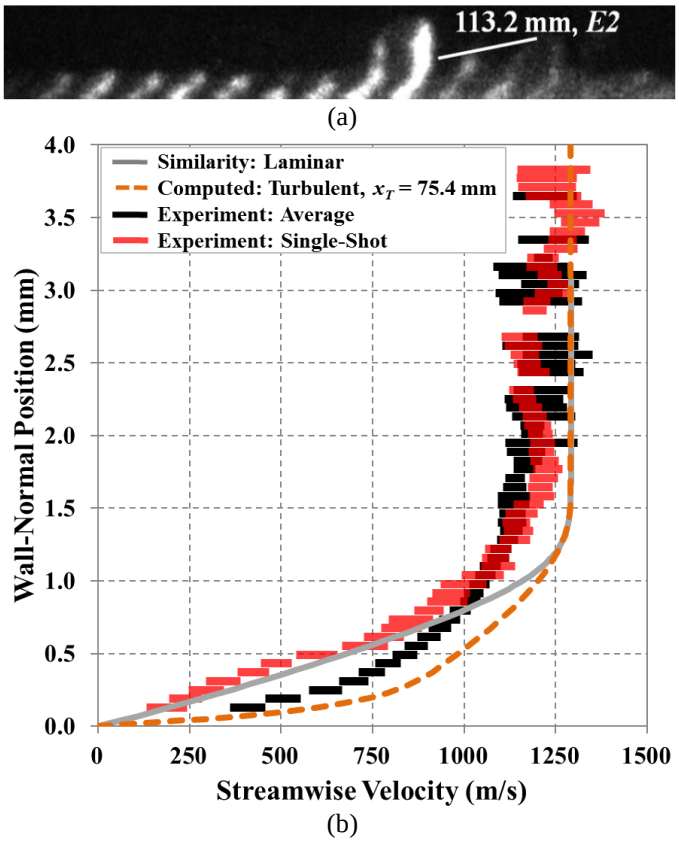

Figure 7.15: (a) Raw single-shot image second exposures. (b) Corresponding $\bar{U}$ (black) and U (red) profiles with uncertainties. Similarity laminar solution (gray) and computed turbulent (dashed orange, Ref. 8) profiles for reference.

Figure 7.15 is intended to provide a sample single-shot velocity measurement for the purpose of quantifying typical single-shot uncertainties achieved using the three-laser NO_2-to-NO photolysis MTV technique. Figure 7.15a shows a single-shot second-exposure image from Run 13 of Test 481 at z = -5.5 mm. Other images from Run 13 had similar intensity and profile shape distributions. Figure 7.15b shows $\bar{U}$ (black bars) and U (red bars) profiles with corresponding uncertainties indicated by the width of the bars. The U profile in Fig. 7.15b corresponds to the profile at x = 113.2 mm shown in Fig. 7.15a. For reference, laminar (gray curve) and turbulent (for fully effective roughness, x_T = 75.4 mm, dashed orange curve, using Ref. 8) profiles have also been computed. Similar to Fig. 7.14, the $\bar{U}$ profile shows an augmented velocity near the wall. The U profile, however, follows the computed laminar solution below approximately y = 0.75 mm. Between y = 0.75 mm and y = 3.0 mm, the U trends with $\bar{U}$ and the computed turbulent profile, although the measured profiles exhibit a velocity deficit relative to the computed turbulent profile. Table 7.3 provides the average and minimum constituent and total single-shot uncertainty values obtained from the U measurement in Fig. 7.15. Note that the average of spatial uncertainty, $u_{U,\Delta x}$, improved by approximately 27% from that reported in Table 6.2 of Chapter 6 and the total uncertainty thus also improved by approximately 28%. The minimum total uncertainty was less than 2.5% of the edge velocity along the same profile.

Table 7.3 also contains an estimate of uncertainty in the mean streamwise velocity, $u_{\bar{U},V}$, resulting from a wall-normal velocity component, V. This was computed in a manner similar to Eq. 4.38 in Chapter 4 (using from Ref. 9) for the $\bar{U}$ profile shown in Fig. 7.15. To see how this uncertainty changes as a function of height above the model surface and in relation to the associated streamwise and vertical velocity profiles, they are plotted together in Fig. 7.16. The $\bar{U}$ profile data are re-plotted in Fig. 7.16 (circles). These data are then smoothed with a 5-pixel average filter (black curve) as in Fig. 7.12. A central difference is then used on the smoothed data to compute $\partial\bar{U}/\partial y$ (dashed black curve). An estimate for V was obtained from the turbulent flow computation shown in Fig. 7.15 using the solver of Ref. 8 (gray curve). The uncertainty $u_{\bar{U},V}$ in Fig. 7.16 (dashed gray curve) is, at most, approximately 0.21% and on average 0.12% of the edge velocity, U_e and is thus negligible compared to the other errors.

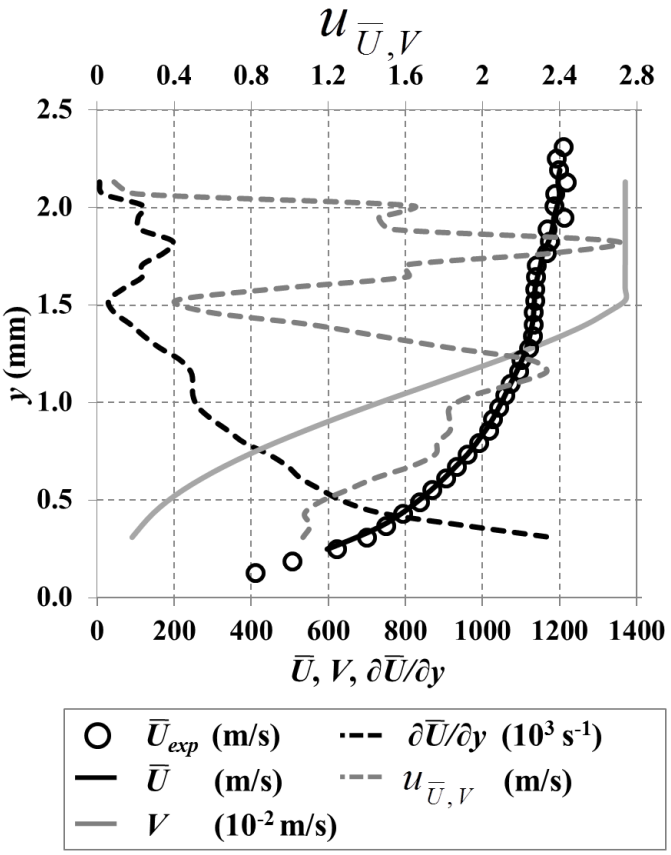

Figure 7.16: Estimate of streamwise velocity uncertainty resulting from *y*-component of velocity (V, gray curve), $u_{\bar{U},V}$ (dashed gray curve). Experimental $\bar{U}$ data ($\bar{U}_{exp}$, circles) and $\bar{U}$ profile (black curve) after applying 5-pixel average filter. Profile of $\partial\bar{U}/\partial y$ computed from smoothed $\bar{U}$ profile.

Table 7.3: Average and minimum constituent and total single-shot uncertainties for image pair 118 of Run 13 of Test 481 at x = 113.2 mm, z = -5.5 mm as a percentage of edge velocity, U_e.

Uncertainty Term	% of U_e (U_e = 1292 m/s)	
	Average	Minimum
$u_{Accuracy}$	0.77	0.77
$u_{U,\bar{M}}$	0.34	0.06
$u_{U,\Delta x}$	3.50	2.31
$u_{U,\Delta t}$	0.12	0.02
$u_{\bar{U},V}$ *	0.12*	0.01*
$u_U = \sqrt{u_{Accuracy}^2 + u_{U,\bar{M}}^2 + u_{U,\Delta x}^2 + u_{U,\Delta t}^2}$	3.62	2.47

* *Not included in u_U or $u_{\bar{U}}$ calculations in this chapter.*

7.4 Conclusions

This chapter presents velocity data acquired in a hypersonic boundary layer undergoing transition-to-turbulence. An NO_2-to-NO photolysis molecular tagging velocimetry technique was used to make the measurements. The measurements were made in the wake of an isolated cylindrical roughness element at several streamwise and spanwise locations. Three different roughness heights were tested: k = 0.53 mm, 1.0 mm, and 2.0 mm. An analysis of the mean streamwise velocity ($\overline{U}$), fluctuating component of streamwise velocity (U'), and instantaneous streamwise velocity profiles (U) was performed, relating the features of these profiles to the roughness heights and Reynolds numbers that were tested. A comparison of the profile data with roughness and with both computed and measured laminar velocity profiles with no roughness was also presented. Analysis showed that along the centerline of the model, the maximum measured U' component increased from approximately ±75 m/s in the no-roughness case to ±225 m/s with a 0.53-mm-tall roughness, and to ±240 m/s with a 1-mm-tall roughness. Near the wall, some of the mean velocity profiles with roughness also exhibited regions of increased velocity relative to the laminar boundary layer measurements and computations. The corresponding profiles of U' exhibited increased magnitudes (i.e. stronger fluctuations) relative to the laminar boundary layer profile measurements.

A measured $\overline{U}$ profile exhibiting relatively high velocity near the wall was compared with computed laminar and turbulent velocity profiles. Based on the analysis of these profiles and the comparison with the computed profiles, this increased velocity region relative to the laminar boundary layer measurements and computations was determined to be likely indicative of transition-to-turbulence. An analysis of the uncertainty in streamwise velocity resulting from a wall-normal velocity component was performed. Based on this analysis, this uncertainty was estimated to be, on average, less than 0.12% of the edge velocity.

---

[1] Danehy, P.M., Ivey, C.B., Inman, J.A., Bathel, B.F., Jones, S.B., McCrea, A.C., Jiang, N., Webster, M., Lempert, W., Miller, J., and Meyer, T., "*High-Speed PLIF Imaging of Hypersonic Transition over Discrete Cylindrical Roughness*," AIAA Paper 2010-703, 48th AIAA Aerospace Sciences Meeting, January 4 – 7, 2010, Orlando, FL.

[2] Bathel, B.F., Danehy, P.M., Jones, S.B., Johansen, C.T., and Goyne, C.P., "*Trip-induced Transition Measurements in a Hypersonic Boundary Layer Using Molecular Tagging Velocimetry*," 51st AIAA Aerospace Sciences Meeting, AIAA Paper 2013-0042, Grapevine, TX, January 4 – 7, 2013.

[3] Rasband, W.S., ImageJ, U.S. National Institutes of Health, Bethesda, MD, USA, http://rsb.info.nih.gov/ij, 1997-2009.

[4] Ramsey, M.C. and Pitz, R.W., "*Template matching for improved accuracy in molecular tagging velocimetry*," Experiments in Fluids, 51(3), pp. 811 – 819, September, 2011.

[5] Bathel, B.F., Danehy, P.M., Johansen, C.T., Jones, S.B., and Goyne, C.P., "*Hypersonic Boundary Layer Measurements with Variable Blowing Rates Using Molecular Tagging Velocimetry*," 28th AIAA Aerodynamic Measurement Technology, Ground Testing, and Flight Testing Conference, AIAA Paper 2012-2886, June 25 – 28, 2012, New Orleans, LA.

[6] Johansen, C.T. and Danehy, P.M., "*Numerical investigation of PLIF gas seeding for hypersonic boundary layer flows*," 50thAIAA Aerospace Sciences Meeting, AIAA Paper 2012-1057, January 9-12, 2012, Nashville, TN.

[7] White, F.M., *Viscous Fluid Flow*, 2nd ed., McGraw-Hill, New York, NY, 1991, pp. 345-348.

[8] Devenport, W.J., and Schetz, J.A., http://www.engapplets.vt.edu/fluids/bls2/ [last accessed June 22, 2013].

[9] Hill, R.B., and Klewicki, J.C., "*Data reduction methods for flow tagging velocity measurements*," Experiments in Fluids, 20(3), pp. 142 – 152, January, 1996.

Chapter 8: Conclusions and Future Work

This chapter provides a summary of this dissertation. Sections 8.1.1 and 8.1.2 highlight the significant results obtained using both the single-laser NO and three-laser NO_2-to-NO photolysis molecular tagging velocimetry (MTV) techniques, respectively. Included in these sections are discussions of the lessons learned while performing the experiments as well as discussions concerning the applicability of these techniques to the study of hypersonic transition-to-turbulence. Sections 8.2.1 and 8.2.2 discuss future work that will need to be carried out in order to make further improvements to the MTV capabilities described in this dissertation and to improve understanding of transition-to-turbulence phenomena. Some of the material presented in this chapter has been adapted from the review in Ref. 1.

8.1 Conclusions

8.1.1 Summary

The design of hypersonic aerospace vehicles requires an understanding of the gas flow passing over a vehicle at Mach numbers on the order of 5 or higher. Particular attention must be paid to the interaction of surface roughness with the hypersonic flow. This includes the interaction between isolated roughness elements and the thin layer of gas that develops around the hypersonic vehicle, known as the boundary layer. The interactions that can occur between the boundary layer and isolated roughness elements on the vehicle have a substantial influence on the vehicle and subsystem designs. These subsystems include the thermal protection system and flight control systems, among many others. Computational fluid dynamic (CFD) simulation capabilities can potentially predict the behavior of hypersonic boundary layers and the underlying physical mechanisms that govern them. However, these simulation tools often rely on models that make certain thermal, chemical, and/or mathematical assumptions about the flowfield. Such assumptions can include the boundary layer being either laminar or fully turbulent to simplify the design process. The complexity of the transition-to-turbulence process from an initially laminar to a fully turbulent boundary layer is often avoided by over-designing a vehicle for the extremes that can be predicted using either a fully laminar or a fully turbulent solution. This option is often chosen, as there is a limited understanding of the mechanisms that govern the transition process for a particular set of conditions. A description of the current understanding of these processes was provided in Chapter 2.

In order to create simulation tools that can address these complexities, experiments are needed to validate the simulation, ensuring that the predicted behavior matches the true physical nature of the boundary layer flowfield. Experiments can also often uncover flow phenomena that are not present or readily apparent in computational studies. This was one of the primary motivations of this dissertation: to develop a measurement tool capable of making quantitative measurements within a laminar hypersonic boundary layer and a hypersonic boundary layer undergoing transition-to-turbulence. This dissertation focused on the characterization, development, implementation, and improvement of two existing MTV techniques that could be applied in hypersonic boundary layer measurements.

In this dissertation, the implementation and application of two planar laser-induced fluorescence-based molecular tagging velocity measurement techniques were explored. The techniques included a single-laser NO MTV technique and a three-laser nitrogen dioxide (NO_2) photolysis and subsequent nitric oxide (NO) probing (NO_2-to-NO) MTV technique. Chapter 2 provided a review of the fundamental aspects of laser-induced fluorescence and reviewed two fluorescence-based velocimetry techniques: Doppler-based velocimetry and MTV. The two MTV techniques were chosen as they provided relatively high measurement precision (as compared to a Doppler-based measurement) and were easier to implement compared to other techniques, especially when considering the laser system, camera system, test facility, and tracer species.

8.1.2 Single-Laser NO MTV

Development of a single-laser NO MTV technique in this dissertation was motivated by the need for quantitative flowfield measurement capabilities that could be applied in a hypersonic test facility to study laminar boundary layer flows and boundary layer flows undergoing transition-to-turbulence. These flows involve both steady and unsteady gas dynamic behavior, which requires that the quantitative measurement technique have the ability to probe the flowfield with relatively high spatial and temporal accuracy and precision. The relatively large mechanical vibrations associated with a large-scale hypersonic facility can result in increased experimental uncertainty. This is especially true when a single-framing camera system or two-camera system is used. Such vibrations can also affect the profile-forming optics and laser system, which can further complicate analysis of experimental images. Additionally, the use of a two-camera system requires that images acquired by each camera be mapped to a common template to correct for

perspective distortion, which can introduce additional errors. Therefore, a decision was made to use a double-framing camera that could provide time-correlated image pairs with a single camera.

Prior to performing any experiments, a timing sequence was adopted with the first exposure completely enveloping the laser pulse using the shortest possible setting Δt_{E1} = 20 ns. The minimum Δt_{D2} = 500 ns interframe delay between the first and second exposures meant that the fluorescence observed in the second exposure would be markedly diminished relative to the first exposure as a result of the exponential decay in signal which occurs after initial excitation of NO with by laser. An approximation of relative signal intensities resulting from exponential fluorescence intensity decay was shown in Fig. 2.6 in Chapter 2. This initially motivated the use of a Δt_{E2} = 300 ns setting to ensure adequate fluorescence was captured in the second exposure.

However, this timing approach resulted in intensities captured by the first exposure that was much greater than intensities captured in the second. Compounding the problem was an issue of overexposure in the first exposure. When the fluorescence signal exceeds approximately 2/3rd of the dynamic range of the camera, artifacts from the first exposure can remain on the intensifier and be observed in the second exposure. This also has an adverse effect on the velocity measurement. Coupled with a lack of an independent gain setting for either the first or second exposure, the development of an alternative camera and laser timing sequence was developed in Chapter 4 to provide comparable signals in both the first and second exposures. This involved timing the end of the first exposure so that it would coincide with the beginning of the laser pulse, thereby limiting the signal collected in the first exposure. The degree of overlap between the first exposure and laser pulse, termed the effective first exposure (or Δt_{eE1}), allowed for a secondary method to control the captured fluorescence intensities apart from the camera gain setting.

The use of a relatively long second exposure (Δt_{E2} = 300 ns) presented another potential issue. While the longer duration was chosen to aid in obtaining signal intensities comparable to those in the first exposure, the high-speed motion of the MTV profiles make the measurement susceptible to motion blurring. An analysis performed in Chapter 4 showed that this motion blurring effect is compounded by the exponential decay of fluorescence with time in a region of uniform collisional quenching (Q_{21} = constant). The combined effect of blurring and fluorescence decay results in a perceived weighting of the measured intensity profiles in the direction opposing the profile motion. By assuming a uniform collisional quenching

environment, a method of correcting the measured velocities for the effects of motion blurring and exponential decay of fluorescence was developed in Chapter 4 using a phenomenological geometric argument based upon camera and laser timing parameters. This analysis suggested that the use of a shorter second exposure would minimize these effects.

In regions of spatially-varying collisional quenching, the velocity measurements are susceptible to biasing to lower or higher velocities if the gradient is positive or negative in the direction of motion, respectively. In a similar manner, the presence of an adverse or favorable pressure gradient potentially biases the measurement to lower or higher velocities, respectively. An analysis of each of these issues was discussed in Chapter 4.

The single-laser NO MTV technique measures a single-component of velocity, namely, the component perpendicular to the tagged lines (i.e. profiles). If a component of velocity exists that is parallel to the MTV profiles, this component can contribute to increased measurement uncertainty. Measurements made in the boundary layer above the surface of a wedge model (in which the top surface effectively served as a flat plate) were performed in Chapters 4 and 5 that accounted for this uncertainty. These measurements were made with the laser sheet parallel to (and a small distance above) the surface of the model. The streamwise component of velocity was measured, with the profiles running in the spanwise direction above the model surface. Regions of the boundary layers in these measurements had a component of velocity in the spanwise direction that was induced by the presence of a cylindrical roughness element. Since the gas in these regions advected in both the streamwise and spanwise directions, the location of a tagged portion of gas along a profile in the first exposure can then be incorrectly correlated with a different portion of gas in the second exposure at the same spanwise location. Chapter 4 provided a methodology for estimating the magnitude of this error source.

Uncertainties in the mean streamwise velocity presented in Chapter 4 varied between approximately 3% and 21% of the measured mean velocity for side-view and plan-view model orientations. Laser scatter on the wall of the flat plate model limited how closely measurements of streamwise velocity could be made to the wall. Based on analysis of the side-view velocity profiles in Chapter 5, it was estimated that the closest a measurement of streamwise velocity could be made to the plate surface was 0.38 mm.

Measurements of streamwise velocity in both side-view and plan-view model orientations were presented in Chapter 5. These measurements were used to characterize the behavior of a laminar hypersonic boundary layer in the presence of an isolated cylindrical roughness element. These measurements were compared with surface heat transfer measurements obtained in experiments performed using temperature sensitive paint. This comparison allowed for a qualitative understanding of the velocity profile behavior resulting from an interaction with the cylindrical roughness element.

The single-laser NO MTV measurement technique described in Chapters 4 and 5 was demonstrated to be capable of providing mean single-component streamwise velocity profiles in a laminar hypersonic boundary layer. One of the primary motivations behind the development and application of this technique was to make quantitative measurements of velocity in large-scale hypersonic wind tunnel facility and in a hypersonic boundary layer undergoing transition-to-turbulence. Unfortunately, as was shown in Chapter 5, the higher Reynolds numbers, higher roughness heights relative to the boundary layer thickness, and lower edge Mach numbers required to achieve transition-to-turbulence on the model used for the experiments in this dissertation requires that the facility stagnation pressure and model plate angle be increased beyond 5°. This results in a higher post-shock static pressure, which in turn proportionally reduces the fluorescence lifetime, and therefore precludes the use of a single-laser NO MTV technique for velocity measurement. This limitation prompted the development of the three-laser NO_2-to-NO photolysis MTV technique, which could be applied independently of the fluorescence lifetime.

8.1.3 Three-Laser NO_2-to-NO Photolysis MTV

The NO_2-to-NO photolysis MTV technique described in Chapters 6 and 7 relied on the dissociation of NO_2, induced by a high-intensity UV laser pulse, to write a pattern of NO profiles into the hypersonic boundary layer gas. By dividing this laser pulse into multiple lines, the spatial pattern of NO could then be probed by two sequential laser pulses that had been formed into laser sheets. This allowed for the excitation of NO fluorescence within the pattern. This fluorescence is captured using the same double-frame camera described in Chapters 4 and 5. The benefit of this technique is that the time delay between the first and second exposures is not limited by the lifetime of NO fluorescence, as was the single-laser NO MTV technique described in Chapters 4 and 5. Rather, the pattern of NO can be probed for as long it remains within the field of view and is not overly dissipated by diffusion, at least for the probe delays used herein.

Over the course of experimentation, some changes were made to the experimental based on lessons learned while performing the single-laser NO MTV technique. Several additional issues arose over the course of testing using the three-laser NO_2-to-NO photolysis MTV technique which affected the data quality and yield. These issues are summarized here.

In order to minimize the undesirable laser scatter encountered in with the single-laser NO MTV technique, the model was modified with a 50.8 mm outer diameter, 6.4 mm thick quartz window centered about the measurement region and mounted flush to the model surface. The use of this UV-transparent window was also intended to prevent damage to the model's black painted surface that would occur from the focused 355 nm pump beams.

The first and second camera exposures, *E1* and *E2*, respectively, were initially timed such that they completely enveloped the first and second probe laser pulses, respectively. This was done to maximize the signal in both exposures, as there was no longer the problem of having unequal intensities between the exposures resulting from fluorescence decay. Unfortunately, scatter from the pump and probe lasers off the bottom metallic surface of the model, observed on and through the quartz window insert, diminished the signal-to-noise ratio (SNR) in both exposures. Inserting a second window into the model allowed light to pass out the bottom of the model, which further reduced laser scatter. Initially, two filters were used to block the remaining scatter, one for the pump laser and one for the two probe lasers. However, the pump laser filter blocked approximately 75% of the NO fluorescence, thus drastically reducing SNR. An alternative approach was then used which required the use of the probe laser filter and delaying both camera exposures to avoid the probe laser scatter. The combination of filter and camera delay worked to reduce the amount of laser scatter captured by the camera exposures while also timing the exposures so that sufficient NO fluorescence could be captured from the NO pattern. A feature of this timing arrangement was that the measurement became insensitive to timing jitter associated with the camera exposures (though sensitivity to timing jitter associated with the probe laser pulses was retained).

Another improvement involved using a series of UV-reflective mirrors to guide both of the probe laser beams from the laser carts to the tunnel test section rather than anti-reflection coated 90° turning prisms, which were used in initial tests. The turning prisms were measured to transmit only 70% – 90% of the incident laser energy per prism. By using 99% reflective dielectric turning mirrors, the laser energies for

the pump, first probe, and second probe (measured at the test section prior to passing through the sheet-forming and profile-forming optics) were approximately 10 mJ/pulse, 3.1 mJ/pulse, and 4.3 mJ/pulse, respectively. Initial experiments using turning prisms resulted in energies of approximately 11-14 mJ/pulse, 0.7 mJ/pulse, and 0.7 mJ/pulse, respectively. This represented an improvement in the transmitted first and second probe laser energies by a factor of 4.4 and 6.1, respectively.

The pump beam alignment relative to the model surface was also modified. Initial experiments were performed using an optical orientation where the angle-of-incidence of the pump laser beams was approximately 75° with respect to the model surface. This was done as a matter of convenience because plate angles of both 5° and 20° were being tested and hence the angle-of-incidence of the pump laser beams were aligned normal (90°) to the plate surface for the 5° plate angle. This made it difficult to analyze the data for time delays that were much greater than Δt = 1μs because a profile in the first exposure could potentially be indistinguishable from a neighboring profile in the second exposure. Experiments in this dissertation were performed with the pump beams at an angle-of-incidence of approximately 90° with respect to the model surface.

The magnification in Chapters 6 and 7 was approximately 6.1 mm/pixel, an improvement of approximately 8% from that in initial experiments. This was accomplished by moving the camera closer to the test section. The horizontal spatial resolution of the measurement is determined by the width of a tagged profile (0.6 mm) and the total shift of the profile (which is largest at the maximum probe laser delay, Δt = 1 μs, and the maximum edge velocity of ~1300 m/s). The resulting spatial resolution ranged from approximately 0.6 mm (where the velocity was low) to 1.3 mm. If a Δt = 2 μs setting is used, the spatial resolution is worsened to 2.6 mm. The vertical spatial resolution was approximately 0.08 mm.

In Chapter 6, a study was performed in nominally quiescent air to help determine the accuracy and precision of the technique. The accuracy in these measurements decreased monotonically with Δt. However, beyond a delay of Δt = 10 μs, measurements of data yield showed no improvement in accuracy. This suggests that the nominally quiescent flow actually had small fluctuations in velocity on the order of 0.3 m/s; any measured velocities above this level are therefore attributable to systematic errors in the measurement system.

In Chapter 7, an analysis of the uncertainty in the measured streamwise velocity because of an unmeasured wall-normal velocity component was performed. This error was assumed relatively negligible in the laminar side-view measurements presented in Chapter 5. However, the unsteady three-dimensional nature of transition-to-turbulence brings such an assumption into question. Therefore, an analysis of a representative velocity profile was performed to determine the magnitude of this error. In this analysis, the derivative of the mean streamwise velocity profile with respect to the wall-normal direction and a turbulent boundary layer computation for the wall-normal velocity distribution were used to provide the uncertainty estimate. Based upon this analysis, it was determined that this uncertainty is insignificant (< 3 m/s) for the conditions of this experiment.

While increasing the time delay of the three-laser NO_2-to-NO photolysis MTV technique resulted in improved accuracy and precision, it diminished the measurement spatial resolution. Additionally, if too long of a time delay is used, it becomes difficult to analyze MTV profiles, as they are nearly indistinguishable from their neighboring profiles. For the experiments described in this dissertation, a setting of Δt = 2 μs serves as an upper limit for ensuring that the image processing techniques described in Chapter 6 can be reliably applied to the MTV images. This tradeoff between the measurement uncertainty and the flow spatial scale must be considered when planning such experiments.

By quantifying the single-shot measurement uncertainty, a methodology to estimate the magnitude of the fluctuating streamwise velocity component was developed. This involved subtracting the contribution of the instrument error as a function of SNR from the measured standard deviation in mean streamwise velocity. This was of particular benefit in Chapter 6 to quantify the effect of blowing rate on boundary layer unsteadiness and in Chapter 7 to quantify the effect of an isolated cylindrical roughness element on boundary layer transition-to-turbulence.

Using this three-laser NO_2-to-NO photolysis MTV technique, uncertainties in the mean streamwise velocity in a laminar boundary layer were as low as approximately 1% to 2% of the measured estimated edge velocity (1289 m/s). Single-shot uncertainties reported in Chapter 7 at points with relatively high SNR were measured to be approximately 3.6% of the edge velocity (1292 m/s). This level of uncertainty is more than sufficient to make measurements of velocity in a transitioning boundary layer and fully turbulent boundary layer at the conditions given in Table 2.2 in Chapter 2. By using a quartz window to minimize the

laser scatter on the model surface, measurements of streamwise velocity as close as 0.08 mm to the model surface were made. This represents a factor of 4 improvement compared to measurements reported in Chapters 4 and 5 using the single-laser NO MTV technique (although the use of a window would probably have allowed the single-laser NO MTV technique to similarly measure velocities closer to the surface).

Measurements of streamwise velocity using a side-view model orientation were presented in Chapter 7. These measurements were used to characterize the behavior of a hypersonic boundary layer undergoing transition-to-turbulence in the wake of an isolated cylindrical roughness element. Particular attention was given to the fluctuating streamwise velocity component. The magnitude and spatial distribution of the fluctuating streamwise velocity component was compared with the cylindrical roughness height at several flow conditions. These measurements were also compared with flow visualization images obtained at the same nominal conditions so that velocity profile behavior could be associated with specific transition-to-turbulence features observed in the flow visualization images.

8.2 Future Work

8.2.1 Single-Laser NO MTV

The analysis methodology presented in Chapter 4 did not include a method for estimating the single-shot uncertainty using the single-laser NO MTV technique. This is partly due to the laminar nature of the boundary layer flow at the experimental conditions in Chapters 4 and 5. When viewing a single-shot image sequence from those experiments, significant unsteady behavior was not observed to compel the development of a comprehensive method for analyzing the single-shot velocity profiles. However, subsequent testing in an arc-heated facility with an unsteady flowfield prompted the development of a method to characterize both single-shot uncertainty and velocity fluctuations. This method was then adapted and refined for use with the three-laser NO_2-to-NO photolysis MTV technique. Additional work will include the development of a method for estimating the SNR-based single-shot spatial uncertainty, as it proved to be the most important parameter in determining single-shot precision. This could then be applied to the data set presented in Chapter 5. Since SNR levels were generally higher than those observed using the three-laser technique, the potential single-shot measurements with uncertainties lower than those obtained with the three-laser technique (~3%) may be achieved. The importance of determining the single-

shot precision is that future experiments at similar pressure and temperature conditions could involve unsteady behavior and it is important to determine the precision with which this technique can resolve those fluctuations.

Transition-to-turbulence was not observed using the wedge model for the conditions tested in Chapters 4 and 5. However, the streamwise length of the model surface (162.5 mm) at the conditions tested in Chapters 4 and 5 limited the distance and time over which disturbances generated by the isolated cylindrical roughness element could grow to amplitudes sufficient for transition to occur. Future experiments should explore the use of longer models that would allow the single-laser NO MTV measurements to be made farther downstream of the roughness element where transition-to-turbulence can occur at the conditions tested in Chapters 4 and 5. For example the use of a long, slender cone, such as that used in Ref. 2, would provide a low-enough pressure, long running length, and high Mach number flowfield that would produce conditions suitable for application of the single-laser NO MTV technique. Advantages of using the single-laser NO MTV technique over the three-laser NO_2-to-NO photolysis MTV technique include ease of setup, improved rate of diffusion of seed material to the edge of the boundary layer, and the lower seeding flow rate required to obtain sufficient SNR, resulting in less perturbation to the flowfield.

A comparison between the velocity profile data in Fig. 5.1c in Chapter 5 and a direct numerical simulation (DNS) were performed in Ref. 3. This was briefly mentioned in Chapter 5. The comparison in Ref. 3 showed relatively good agreement between the measured and predicted streamwise velocity for most of the profiles. However, unpublished comparisons between computations and measurements of the velocity immediately upstream and downstream of the roughness element showed discrepancies, with the measured velocities consistently lower and higher than predicted with DNS, respectively.[*] Based upon this result, it was hypothesized that the presence of a velocity gradient would bias the velocity measurement either low or high if the flow were locally decelerating or accelerating, respectively. By using DNS computations to determine the existence of velocity gradients within a flowfield, a Lagrangian-type analysis of the MTV profile motion (i.e. profile displacements and the associated time delay between image pairs) can be compared with simulation results to estimate the error associated with the mean streamwise

[*] Mahesh, K., University of Minnesota, February 2011 (private communication).

velocity measurement in such regions. An alternate approach would be to compare computed and experimental profile displacements will be compared directly. Computational streamtraces of massless particles released at the location of the initially tagged molecules in the first exposure image can be compared with measured profile displacements. Analysis of wall-normal velocity components using methods described in Section 4.2.4 in Chapter 4 should also be performed to determine if such components have a significant effect on the measured velocity.

For boundary layers studied in Chapters 4 through 7, the presence of an inflection point ($D^2U = 0$) or generalized inflection point ($D(\rho DU) = 0$) in the velocity profile can result in the formation and growth of an instability. Examples of these types of behavior are shown in Figs. 5.3 and 5.2, respectively. While the existence of these points was described in a semi-quantitative fashion in Chapter 5, no analysis of instability potential was performed. Additionally, the effect of seeding NO into the boundary layer on these points was not considered. Future work should include a more in-depth analysis of these points. This should include both simulation and instability analysis, performed both with and without NO mass injection. Such work can potentially determine if the hypersonic boundary layers studied in Chapters 4 and 5 may promote these forms of instability formation and growth and if NO mass injection affects this process, which should avoided when studying high-speed transition-to-turbulence.

As stated in Section 2.2.8 in Chapter 2, the reaction of NO with oxygen (O_2) for the conditions tested in Chapters 4 and 5 was assumed insignificant based upon the calculations performed in Ref. 4. However, this assumption was based on an extrapolation of the reaction rate constant to temperatures well below the valid extent of the reaction rate model used (226 K). Future work can include a comparison of simulated concentration layer thickness with experimental flow visualization images showing the extent of wall-normal NO fluorescence to determine if thicknesses are comparable. A slightly more complex approach would be to implement computation flow imaging (CFI) as was done in Refs. 5 and 6. This would involve simulating the NO fluorescence using the results of a computational fluid dynamic and reaction rate analysis as inputs. This simulated NO fluorescence could then be directly compared to the experimentally imaged NO fluorescence. This would allow for a comparison of both the extent of the signal in the wall-normal direction and the magnitude of the signal intensity. The MTV measurements could also be compared with simulation results to determine if the NO reaction affects velocity profile behavior through

the coupled relation of energy and momentum. Unpublished single-laser NO MTV data obtained during the experiments presented in this dissertation at negative plate angles can provide boundary layer data with extremely low edge temperatures (sub-50 K), which may accelerate NO reactivity with O_2. This unpublished data could also be used to assess the magnitude of velocity slip for the relatively high edge Mach numbers and low static pressure conditions associated with the negative plate angles.

Finally, the lifetime of NO fluorescence in air at the highest stagnation pressures attainable in the 31-Inch Mach 10 Air Tunnel at NASA Langley at the 5° plate angle limited the applicability of the single-laser NO MTV technique to laminar boundary layer measurements. An alternative approach to this lifetime limitation would be to make measurements in a facility for which nitrogen (N_2) was the primary working gas, such as Arnold Engineering and Development Complex (AEDC) Tunnel 9 facility in Silver Spring, Maryland. Figure 2.6 in Chapter 2 showed that much longer lifetimes could be obtained in N_2 environments at the same conditions as those examined in this dissertation, both at the 5° and 20° plate angles.

8.2.2 Three-Laser NO_2-to-NO Photolysis MTV

The blowing rate study presented in Chapter 6 showed that above a blowing rate of approximately 75 mg/s, no gains in data yield were realized and below approximately 45 mg/s, a significant drop off in yield occurs. Additionally, for blowing rates above approximately 60 mg/s, noticeable changes in the mean streamwise boundary layer profiles were observed. These blowing rates were approximately an order of magnitude larger than the blowing rates needed to achieve sufficient SNR levels required to measure velocity using the single-laser NO MTV technique. Future experiments should be performed further optimize the SNR while further decreasing the blowing rate of NO_2 needed to make velocity measurements using the three-laser NO_2-to-NO photolysis MTV technique. This could include further increasing pump laser intensity, using a separate pump laser to increase pump delay, changing the polarization of the pump laser to decrease profile width, increasing probe laser intensities, using an excitation frequency that probes the first vibrational state of NO rather than the ground vibrational state, as was mentioned in Chapter 6. Improvement in the collection optics could also improve SNR, such as using of a faster lens (lower f-number lens) and extension/macro rings.

The relatively high blowing rates had an effect on boundary layer profiles with no roughness, particularly on the fluctuating component of streamwise velocity. Measurements presented in Fig. 6.12 in

Chapter 6 showed that for the range of blowing rates tested, fluctuations of at least 3.9% of the edge velocity were observed. It was not clear from the measurements as to what role the interaction of the mass injection from the seeding slot had on the magnitude and shape of the fluctuating component of streamwise velocity. Future experiments should include flow visualization and velocity measurements near the seeding slot to characterize this interaction. Computations simulating this interaction should also be performed and compared with experimental results.

The use of two quartz windows on the top and bottom surface of the wind tunnel model, which were used to limit the reflection of laser light into the measurement region, also confined the measurement to the wake region behind the cylindrical roughness element. This precluded study of the boundary layer flow immediately upstream or downstream of the roughness element, which plays a significant role in the development of streamwise vortices, which can influence the transition-to-turbulence process, as was determined in Ref. 7. Efforts to apply the three-laser NO_2-to-NO photolysis MTV technique to this region should be made in future experiments. Additionally, a computational analysis of this region should be performed and a comparison with the measured velocity be made.

---

[1] Bathel, B.F., Johansen, C.T., Inman, J.A., Jones, S.B., and Danehy, P.M., "*Review of Fluorescence-Based Velocimetry Techniques to Study High-Speed Compressible Flows (Invited)*," 51st AIAA Aerospace Sciences Meeting, AIAA Paper 2013-0339, Grapevine, TX, January 7 – 10, 2013.

[2] Berridge, D.C., Casper, K.M., Rufer, S.J., Alba, C.R., Lewis, D.R., Beresh, S.J., and Schneider, S.P., "*Measurements and Computations of Second-Mode Instability Waves in Three Hypersonic Wind Tunnels*," 40th AIAA Fluid Dynamics Conference, AIAA Paper 2010-5002, June 28 – July 1, 2010, Chicago, IL.

[3] Iyer, P., Muppidi, S., and Mahesh, K., "*Roughness-Induced Transition in High Speed Flows*," 49th AIAA Aerospace Sciences Meeting, AIAA Paper 2011-566, Orlando, FL, January 4 – 7, 2011.

[4] Arisman, C.J., Johansen, C.T., Galuppo, W.C., and McPhail, A., "*Nitric Oxide Chemistry Effects in Hypersonic Boundary Layers*," 43rd AIAA Fluid Dynamics Conference, AIAA Paper 2013-3104, June 24 – 27, 2013, San Diego, CA.

[5] Wilkes, J.A., Glass, C.E., Danehy, P.M., and Nowak, R.J., "*Fluorescence Imaging of Underexpanded Jets and Comparison with CFD*," 44th AIAA Aerospace Sciences Meeting, AIAA Paper 2006-910, January 9 – 10, 2006, Reno, NV.

[6] Ivey, C.B., Danehy, P.M., Bathel, B.F., Dyakonov, A.A., Inman, J.A., and Jones, S.B., "*Comparison of PLIF and CFD Results for the Orion CEV RCS Jets*," 49th AIAA Aerospace Sciences Meeting, AIAA Paper 2011-713, January 4 – 7, 2011, Orlando, FL.

[7] Wheaton, B.M., Bartkowicz, M.D., Subbareddy, P.K., Schneider, S.P., and Candler, G.V., "*Roughness-Induced Instabilities at Mach 6: A Combined Numerical and Experimental Study*," 41st AIAA Fluid Dynamics Conference, AIAA Paper 2011-3248, June 27-30, 2011, Honolulu, HI.

Appendix: Links to Dissertation-Relevant Documents

This appendix provides links to conference papers and a journal article prepared by the author, which can be found on the NASA Technical Reports Server (NTRS). Please contact Brett Bathel at brett.f.bathel@nasa.gov if you encounter problems with the links provided below.

Chapter 2:

Bathel, B.F., Danehy, P.M., and Cutler, A.D., *Molecular-based optical measurement techniques for transition and turbulence in high-speed flow*, Von Karman Institute Lecture Series Manuscript, Brussels, Belgium, May 27 – 31, 2013. (Document not yet available on NTRS)

Chapter 4:

Bathel, B.F., Danehy, P.M., Inman, J.A., Jones, S.B., Ivey, C.B., and Goyne, C.P., "*Multiple Velocity Profile Measurements in Hypersonic Flows Using Sequentially-Imaged Fluorescence Tagging*," 48th AIAA Aerospace Sciences Meeting, AIAA Paper 2010-1404, January 4-7, 2010, Orlando, FL.

Bathel, B.F., Danehy, P.M., Inman, J.A., Jones, S.B., Ivey, C.B., and Goyne, C.P., "*Velocity Profile Measurements in Hypersonic Flows Using Sequentially-Imaged Fluorescence-Based Molecular Tagging Velocimetry*," AIAA Journal, 49(9), pp. 1183-1896, September, 2011.

Chapter 5:

Bathel, B.F., Danehy, P.M., Inman, J.A., Watkins, A.N., Jones, S.B., Lipford, W.E., Goodman, K.Z., Ivey, C.B., and Goyne, C.P., "*Hypersonic Laminar Boundary Layer Velocimetry with Discrete Roughness on a Flat Plate*," 40th Fluid Dynamics Conference and Exhibit, AIAA Paper 2010-4998, June 28 – July 1, 2010, Chicago, IL.

Chapter 6:

Bathel, B.F., Johansen, C.T., Danehy, P.M., Inman, J.A., Jones, S.B., and Goyne, C.P., "*Hypersonic Boundary Layer Transition Measurements Using $NO_2 \rightarrow NO$ Photo-dissociation Tagging Velocimetry*," 41st AIAA Fluid Dynamics Conference, AIAA Paper 2011-3246, Honolulu, HI, June 27 – 30, 2011.

Bathel, B.F., Danehy, P.M., Johansen, C.T., Jones, S.B., and Goyne, C.P., "*Hypersonic Boundary Layer Measurements with Variable Blowing Rates Using Molecular Tagging Velocimetry*," 28th AIAA Aerodynamic Measurement Technology, Ground Testing, and Flight Testing Conference, AIAA Paper 2012-2886, New Orleans, LA, June 25 – 28, 2012.

Chapter 7:

Bathel, B.F., Danehy, P.M., Jones, S.B., Johansen, C.T., and Goyne, C.P., "*Trip-induced Transition Measurements in a Hypersonic Boundary Layer Using Molecular Tagging Velocimetry*," 51st AIAA Aerospace Sciences Meeting, AIAA Paper 2013-0042, Grapevine, TX, January 4 – 7, 2013.

Chapter 8:

Bathel, B.F., Johansen, C.T., Inman, J.A., Jones, S.B., and Danehy, P.M., "*Review of Fluorescence-Based Velocimetry Techniques to Study High-Speed Compressible Flows (Invited)*," 51st AIAA Aerospace Sciences Meeting, AIAA Paper 2013-0339, Grapevine, TX, January 7 – 10, 2013.